

Electrocatalysis in Protic and Aprotic Ionic Liquids for Energy Applications

By:

Daniel Edward Smith, BSc., MRes.MSET.

Supervisor: Dr. Darren A. Walsh

A thesis submitted to
the School of Chemistry for the
Degree of Doctor of Philosophy

Carbon Neutral Laboratory
University of Nottingham
Nottingham
NG7 2TU
United Kingdom

(26th October 2020)

Abstract

This thesis documents a study of electrocatalytic reactions pertinent to electrochemical energy conversion using protic ionic liquids (PILs) and aprotic ionic liquids (AILs) as electrolytes. The effect of proton-donating and proton-accepting species on electrocatalytic reactions in ionic liquids are investigated, and the implications for the use of PILs as intermediate-temperature fuel-cell electrolytes are considered. A fundamental understanding of proton-shuttling mechanisms in PIL-based fuel cells is presented.

PILs were synthesised and characterised and AILs (used as received) were characterised. A method of synthesising stoichiometric PILs by addition of 0.1 mol dm^{-3} aqueous acid to 0.1 mol dm^{-3} aqueous base with slight excess of base, is presented. The presence of excess neutral acid is detected in PILs voltammetrically, and results from a commonly used synthesis method. The acid does not have a significant effect on PIL ionic conductivity, particularly when compared to the effect of water.

The presence of strong acid in PILs causes the oxygen-reduction reaction (ORR) to shift ≈0.9 V positive, and the presence of a strong base causes the hydrogen-oxidation reaction (HOR) to shift ≈0.9 V negative. Voltammetric experiments show that the fuel-cell half-cell reactions (HOR and ORR) occur at a similar potential in pure stoichiometric PILs, meaning that stoichiometric PILs cannot be used as fuel-cell electrolytes. When acid or base are present in PILs, voltammetric experiments predict a fuel-cell

open-circuit potential (OCP) of around 0.9 V, which is comparable to that in conventional hydrated systems. The presence of acids and bases in PILs changes the mechanism of the ORR and HOR, respectively. Adding acids of increasing strengths (by aqueous pK_a) to O_2-saturated diethylmethylammonium trifluoromethanesulfonate ([dema][TfO]) shifts the ORR half-wave potential positive by ≈ 50 mV per unit decrease in pK_a over the range 10.6 to −3. O_2 reduction can therefore be used to assess relative acidity of protic species added to PILs over this range.

In all AILs tested, the ORR shifts to more positive potentials in the presence of added acid. The greatest shift in ORR to a more positive potential is observed in 1-methyl,1-butylpyrrolidinium bis(trifluoromethanesulfonyl)imide ([pyrr][NTf_2]) in the presence of 0.1 mol dm^{-3} hydrogen bis(trifluoromethanesulfonyl)imide ($HNTf_2$). In the absence of acid, the ORR in [pyrr][NTf_2] occurs at a significantly more negative potential than the HOR indicating that without acid, [pyrr][NTf_2] is not a viable fuel-cell electrolyte. In acidified [pyrr][NTf_2] the difference between the ORR and HOR is around 0.5 V, predicting a lower fuel-cell OCP than in conventional hydrated systems. Voltammetry in O_2-saturated N,N,N,N-tetraoctylammonium bis(trifluoromethanesulfonyl)imide ([N8888][NTf_2]) is similar to that in O_2-saturated N,N,N,N-tetraoctylphosphonium bis(trifluoromethanesulfonyl)imide ([P8888][NTf_2]) in the absence and presence of acid.

Formic acid oxidation (FAO) and water oxidation were studied in [dema][TfO]. FAO was investigated as a probe reaction to assess basicity in

PILs. However, all but one of the bases chosen were found to passivate the platinum electrode used. In the presence of diethylmethylamine (dema), the FAO voltammetric peak magnitude increases, confirming that formate is the active species in direct FAO. Voltammetric evidence for oxygen evolution from water splitting in [dema][TfO] positive of 2.2 V is also presented, along with evidence of the adsorption (on Pt) of a triflic acid-based species at highly oxidising potentials.

Fuel-cell tests confirm the predictions made in Chapter 4, that pure PIL electrolytes cannot sustain a current density because a viable proton shuttling mechanism is not present. When acid or base is added to [dema][TfO], a viable proton shuttling mechanism allowed fuel-cell performance comparable to that of conventional hydrated systems. When base is present at the anode and acid at the cathode, a fuel-cell OCP of around 1.8 V is measured, confirming the understanding of the reaction thermodynamics and mechanisms of the ORR and HOR in PILs presented throughout this thesis. Heating PILs for extended periods at 'intermediate-temperatures' (150 °C), discolours them and generates a protic species, likely triflic acid, which causes the ORR to shift to a more positive potential, which could explain the favourable fuel-cell performance reported in the literature using [dema][TfO] as an electrolyte.

The conclusions of this work, and new understanding of electrocatalytic reactions in ILs, have significant implications for the use of PILs as fuel-cell electrolytes because of the need for added acid or base to provide a viable proton shuttling mechanism. New challenges now arise to identify

electrolyte compositions that retain the advantages offered by PILs (non-volatility and non-corrosivity), while supporting fast proton transport between the anode and cathode of fuel cells.

Declaration

This thesis is the result of my own investigations and is not being concurrently submitted in candidature for any degree.

Signed **(Candidate)**

Date 26th October 2020

University of Nottingham
UK | CHINA | MALAYSIA

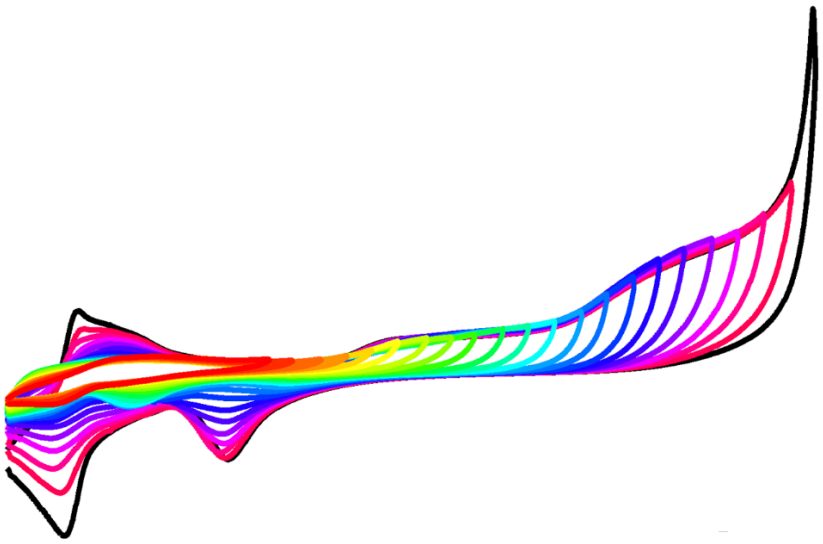
Acknowledgements

My foremost thanks go to Dr. Darren Walsh for his supervision and guidance throughout my studies. I thank Dr. Graham Newton, Professor Peter Licence, and Professor Steve Howdle for their advice and support. Particular thanks go to Professor Peter Licence, former Vice-Chancellor Professor Sir David Greenaway, and Professor Dame Jessica Corner, for supporting my proposal for a piano for the GSK Carbon Neutral Laboratory for Sustainable Chemistry's (CNL) Winter Garden, which has made a significant difference to life at the CNL and School of Chemistry. For their technical support, I thank Neil Barnes, Clive Dixon, Conor Howell-Bennett, James Warren, Shazad Aslan, Pvail Puri, Tom Clayton, Ben Pointer-Gleadhill, and Dr. Mick Cooper. For administrative support, I thank Anne Floyde, Mandy Cordell, Helen Shipman, Amanda Wood, Christine Bexton, John Hooper MBA, Dr. Ahmad Milner-Elkharouf and Dr. David Chambers-Asman. I thank my colleagues at the associated universities of the Centre for Doctoral Training in Fuel Cells and Their Fuels for their friendship and support, and the Engineering and Physical Sciences Research Council for funding my studies. I wish to thank the staff and students of the University of Nottingham School of Chemistry and GSK Carbon Neutral Laboratory for Sustainable Chemistry for providing an academic home during my studies. Especial thanks go to past and current members of the Walsh Electrochemistry Group – in particular, Dr. Sean Goodwin, Dr. Fiona Norten, Dr. Pedro Verdía Barbara, Dr. Saddam Almudhady, Dr. Sayyar Muhammad, Dr. Andinet Ejigu, Peter Greatorex-Davies, Matthew Bird, and Catherine Peake. Additional thanks go to Susan Bamford, Adrian Langham, Dr. Trevor Farren, Canon John Bentham and Professor Philip Moriarty, for the good conversation. Penultimate thanks go to the City of Birmingham Symphony Orchestra for the opportunities provided in respite from my studies. Finally, my profound thanks to my parents; Garry Smith and Lynnda Smith; my Grandma, Beryl Trimmer; my uncle, Professor Barry Trimmer; and all my family and friends, for their love, support and inspiration. I could not have achieved without them.

Dedication

This thesis is dedicated to my parents, Gareth Iain Smith and

Lynnda Ellen Smith, who have lived it with me.



– Cyclic voltammogram recorded in a protic ionic liquid at a platinum electrode

(presented here for artistic purposes).

"*The scientific man does not aim at an immediate result. He does not expect that his advanced ideas will be readily taken up. His work is like that of the planter—for the future. His duty is to lay the foundation for those who are to come, and point the way. He lives and labors and hopes with the poet who says*:

Schaff' das Tagwerk meiner Hände,

Hohes Glück, dass ich's vollende!

Lass, o lass mich nicht ermatten!

Nein, es sind nicht leere Träume:

Jetzt nur Stangen, diese Bäume

Geben einst noch Frucht und Schatten.[1]

[1] Daily work—my hands' employment,

To complete is pure enjoyment!

Let, oh, let me never falter!

No! there is no empty dreaming:

Lo! these trees, but bare poles seeming,

Yet will yield both food and shelter!

Goethe's "Hope"

*Translated by William Gibson, Com. U. S. N.***"**

– Nikola Tesla, taken from "*The Problem of Increasing Human Energy with Special References to the Harnessing of the Sun's Energy*", Century Illustrated Magazine, June 1900.

Abbreviations and Acronyms

Notation	Meaning
[pyrr][NTf_2]	1-methyl 1-butylpyrrolidinium bis(trifluoromethanesulfonyl)imide
ACEIS	Alternating current electrochemical impedance spectroscopy
AILs	Aprotic ionic liquids
[NTf_2]$^-$	Bis(trifluoromethanesulfonyl)imide
C.E.	Counter electrode
CV	Cyclic voltammetry/voltammogram
dema	Diethylmethylamine
[dema]$^+$	Diethylmethylammonium
[dema][NTf_2]	Diethylmethylammonium bis(trifluoromethanesulfonyl)imide
[dema][TfO]	Diethylmethylammonium trifluromethanesulfonate
DSC	Differential scanning calorimetry
[dmba][TfO]	Dimethylbutylammonium trifluoromethanesulfonate
DAFC	Direct alcohol fuel cells
EMIRS	Electrochemically modulated infra-red reflectance spectroscopy
EAN	Ethylammonium nitrate
FA	Formic acid
FAFC	Formic acid fuel cells
FTIR-ATR	Fourier transform infrared spectroscopy by attenuated total reflection
FCs	Fuel cells
GC	Glassy-carbon
HOMO	Highest occupied molecular orbital
$HNTf_2$	Hydrogen bis(trifluoromethanesulfonyl)imide
HER	Hydrogen evolution reaction
HOR	Hydrogen-oxidation reaction
HILIC	Hydrophilic-interaction liquid ion chromatography
IHP	Inner Helmholtz plane
ILs	Ionic liquids
LUMO	Lowest unoccupied molecular orbital
Mass. spec.	Mass spectrometry
[N8888][NTf_2]	N,N,N,N-tetraoctylammonium bis(trifluoromethanesulfonyl)imide
[P8888][NTf_2]	N,N,N,N-tetraoctylphosphonium bis(trifluoromethanesulfonyl)imide
NMR	Nuclear magnetic resonance
OCP	Open-circuit potential
OHP	Outer Helmholtz plane
OER	Oxygen-evolution reaction
ORR	Oxygen-reduction reaction
Pd-H	Palladium hydride
PEEK	Polyether ether ketone
PEM	Polymer electrolyte membrane
PEMFC	Polymer electrolyte membrane fuel cell
PTFE	Polytetrafluoroethylene
PILs	Protic ionic liquids
Ref.	Reference electrode
rpm	Revolutions per minute

RTILs	Room-temperature ionic liquids
RDE	Rotating-disk electrode
RRDE	Rotating-ring disk electrode
SHE	Standard hydrogen electrode
SMR	Steam methane reforming
SEIRAS	Surface-enhanced infra-red absorption spectroscopy
TGA	Thermo-gravimetric analysis
[tea][TfAc]	Triethylammonium trifluoroacetate
$[TfO]^-$	Trifluoromethanesulfonate
TfOH	Trifluoromethanesulfonic acid (triflic acid)
UV-Vis.	Ultra-violet/visible light spectroscopy
H_{upd}	Under-potential deposited hydrogen
W.E.	Working electrode

Symbols

Symbol	Meaning	Units
j_i	$\sqrt{-1}$	
K_a	Acid dissociation / equilibrium constant	
ϵ	Activation energy of viscous flow	kJ mol^{-1}
ω	Angular velocity	rad s^{-1}
i_a	Anodic current	A
$i_p{}^a$	Anodic peak current	A
$E_p{}^a$	Anodic peak potential	V
A	Area	cm^2
T_b	Boiling point	K or °C
k_B	Boltzmann constant (1.380649 × 10^{-23})	J K^{-1}
i_c	Cathodic current	A
$i_p{}^c$	Cathodic peak current	A
$E_p{}^c$	Cathodic peak potential	V
K_{cell}	Cell constant	cm^{-1}
E_{cell}	Cell potential	V
ΔG	Change in Gibbs free energy	kJ mol^{-1}
z	Charge on a dissolved species	
R_{ct}	Charge transfer resistance	Ω
μ	Chemical potential	
δ	Chemical shift	ppm
T_c	Cold crystallisation temperature	°C
N_C	Collection efficiency	
C	Concentration	mol dm^{-3}
i	Current	A
j	Current density	A cm^{-2}
ΔpK_a	Difference in acid dissociation constants of PIL parent acid and PIL cation	
D	Diffusion coefficient	cm^2 s^{-1}
i_d	Disk current	A
x	Displacement	m
C_d	Double layer capacitance	F
η / η^{-1}	Dynamic viscosity / Fluidity	Pa s / Pa^{-1} s^{-1}
ϕ	Electric potential	V
$\bar{\mu}$	Electrochemical potential	
n	Electron transfer number	
α	Electron transfer coefficient	
k_{ox}	Electron transfer rate constant (oxidation)	
k_{red}	Electron transfer rate constant (reduction)	
K_{eq}	Equilibrium constant	
j_0	Exchange current density	A
e	Exponential function	
F	Faraday constant (96485.332)	C mol^{-1}
$J_{B,M}$	Flux to an electrode by charge migration	mol cm^{-2} s^{-1}
$J_{B,D}$	Flux to an electrode by diffusion	mol cm^{-2} s^{-1}

$E^{\theta'}$	Formal potential	V
f	Frequency	s^{-1}
Z_f	Frequency dependent impedance	Ω
$\Delta\Phi$	Galvani potential difference	V
$\Delta_f G$	Gibbs free energy change of formation	kJ mol^{-1}
$\Delta_r G$	Gibbs free energy change of reaction	kJ mol^{-1}
$\Delta G^{\ddagger}$	Gibbs free energy change in reaching transition state	kJ mol^{-1}
T_g	Glass transition temperature	K or °C
$E_{½}$	Half-wave potential	V
Z_{Im}	Imaginary impedance	Ω
Z	Impedance	Ω
u	Ion mobility	$m^2\ V^{-1}\ s^{-1}$
σ	Ionic conductivity	mS cm^{-1}
ν	Kinematic viscosity	$m^2\ s^{-1}$
j_K	Kinetic current density	A cm^{-2}
j_L	Limiting current density	A cm^{-2}
pK_a	Logarithmic acid dissociation constant	
j_{max}	Maximum current density (peak current density)	A cm^{-2}
E_m	Maximum potential amplitude	V
T_m	Melting point	K or °C
R	Molar gas constant (8.314462)	J K^{-1} mol^{-1}
Λ	Molar ionic conductivity	mS cm^{-1} mol^{-1}
E_{onset}	Onset potential	V
η_E	Overpotential	V
i_p	Peak current	A
P	Population of orbitals at a given energy	
E	Potential	V
$E_{p/2}$	Potential at half peak maximum	V
P	Power density	W cm^{-2}
A_F	Pre-exponential factor	
k_d	Rate constant of diffusion	
Z_{Re}	Real impedance	Ω
ρ	Resistivity	Ω cm
i_r	Ring current	A
T_{ss}	Solid-solid crystal transition temperature	K or °C
R_s or R_Ω	Solution resistance	Ω
k^0	Standard electron transfer rate constant	
E^θ	Standard potential	V
T	Temperature	K or °C
T_d	Thermal decomposition temperature	K or °C
l	Thickness of solid electrolyte	cm
t	Time	s
R_u	Uncompensated resistance	Ω
$\Delta\Psi$	Volta potential difference	V
Z_W	Warburg impedance	Ω

Table of Contents

Abstract -i-

Declaration -v-

Acknowledgements -vi-

Dedication -vii-

Abbreviations and Acronyms -ix-

Symbols -xi-

Table of Contents -xiii-

1 Introduction, Literature Review and Project Objectives - 1 -

1.1 Motivation for the Project - 1 -

1.2 Physiochemical Properties of Ionic Liquids - 3 -

1.2.1 Introduction and classification of ionic liquids - 3 -

1.2.2 Physical properties of ionic liquids - 9 -

1.3 Electrochemistry of Ionic liquids - 11 -

1.3.1 Electrochemical properties of ionic liquids - 11 -

1.3.2 Proton activity and affinity in ionic liquids - 15 -

1.3.3 Oxygen-reduction reaction - 17 -

1.3.4 Hydrogen-oxidation reaction - 20 -

1.3.5 Water oxidation - 22 -

1.3.6 Electro-oxidation of small organic molecules - 24 -

1.4 Uses for Protic Ionic Liquids - 31 -

1.5 Project Objectives - 33 -

1.6 References - 34 -

2 Review of Experimental Techniques - 52 -

2.1 Electrochemical Techniques - 52 -
2.1.1 Fundamentals of electrochemistry - 52 -
2.1.2 Mass-transport processes - 59 -
2.1.3 Rates of electrochemical reactions - 61 -
2.1.4 Cyclic voltammetry - 64 -
2.1.5 Rotating-disk electrode voltammetry - 70 -
2.1.6 Electrochemical impedance spectroscopy - 75 -
2.1.7 Fuel cell polarisation curves - 81 -
2.2 References - 83 -

3 Synthesis and Physical Properties of Protic Ionic Liquids - 85 -

3.1 Introduction - 85 -
3.2 Experimental Section - 87 -
3.3 Results and Discussion - 88 -
3.3.1 Nuclear magnetic resonance spectroscopy - 88 -
3.3.2 Fourier-transform infra-red spectroscopy - 88 -
3.3.3 Thermogravimetric analysis - 91 -
3.3.4 Differential scanning calorimetry - 92 -
3.3.5 Ionic conductivity - 95 -
3.4 Conclusions - 98 -
3.5 References - 98 -

4 The Oxygen-Reduction and Hydrogen-Oxidation Reactions in Protic Ionic Liquids - 102 -

4.1 Introduction - 102 -
4.2 Experimental Section - 107 -
4.2.1 Materials and apparatus - 107 -
4.2.2 Synthesis and characterisation of protic ionic liquids - 107 -
4.2.3 Electrode fabrication and electrochemical measurements - 108 -
4.3 Results and Discussion - 110 -
4.3.1 Oxygen-reduction and hydrogen-oxidation in [dema][TfO] - 110 -
4.3.2 Oxygen-reduction and hydrogen-oxidation in [dema][NTf_2] - 143 -
4.4 Conclusions - 149 -
4.5 References - 150 -

5 Oxygen-Reduction and Hydrogen-Oxidation Reactions in Aprotic Ionic Liquids - 155 -

5.1 Introduction - 155 -
5.2 Experimental Section - 156 -
5.2.1 Materials and apparatus - 156 -
5.2.2 Characterisation of aprotic ionic liquids - 158 -
5.2.3 Electrode fabrication and electrochemical measurements - 159 -
5.3 Results and Discussion - 160 -
5.3.1 Oxygen-reduction and hydrogen-oxidation in [pyrr][NTf_2] - 160 -
5.3.2 Oxygen-reduction in [P8888][NTf_2] and [N8888][NTf_2] - 172 -
5.4 Conclusions - 177 -
5.5 References - 178 -

6 Formic Acid Oxidation in Protic Ionic Liquids - 182 -

6.1 Introduction - 182 -
6.2 Experimental Section - 190 -
6.2.1 Materials and apparatus - 190 -
6.2.2 Synthesis and characterisation of [dema][TfO] - 190 -
6.2.3 Electrochemical measurements - 191 -
6.3 Results and Discussion - 192 -
6.3.1 Electrochemical window studies - 192 -
6.3.2 Water oxidation in [dema][TfO] - 197 -
6.3.3 Formic acid oxidation in [dema][TfO] - 209 -
6.3.4 Addition of bases to [dema][TfO] containing formic acid - 224 -
6.4 Conclusions - 239 -
6.5 References - 241 -

7 Protic Ionic Liquids as Fuel-Cell Electrolytes - 246 -

7.1 Introduction - 246 -
7.2 Experimental Section - 248 -
7.2.1 Materials and apparatus - 248 -
7.2.2 Synthesis and characterisation of [dema][TfO] - 248 -
7.2.3 Cell setup and electrochemical measurements - 249 -
7.3 Results and Discussion - 251 -
7.3.1 Polarisation of a PIL-based fuel cell - 251 -
7.3.2 Effect of elevated temperature on [dema][TfO] - 256 -
7.2.3 Determination of PIL impurities formed upon heating - 262 -
7.2.4 Simultaneous acid/base-coupling of ORR/HOR in PIL-based fuel cells - 264 -
7.4 Conclusions - 269 -
7.5 References - 271 -

8 Final Conclusions and Future Outlook - 274 -

8.1 Final Conclusions - 274 -

8.2 Future Work - 278 -

8.3 References - 280 -

Appendix I: Supplementary Characterisation Data - 281 -

Appendix II: List of Publications - 299 -

1 Introduction, Literature Review and Project Objectives

1.1 Motivation for the Project

Ionic liquids (ILs) were first reported at the end of the 19th century but it wasn't until the late 20th century around the time "air and water stable" room-temperature ILs were reported by Wilkes and Zaworotko (1992), that the field greatly expanded.[1,2,3,4,5] Since then ILs have been extensively studied as nonaqueous electrolytes, reaction solvents, lubricants and catalysts.[4,6,7,8] The electrochemical applications of ILs, and protic ionic liquids (PILs) more specifically, have received particular attention because of their reported low-to-negligible volatility, electrochemical stability, thermal stability and high ionic conductivity (especially at elevated temperatures).[9,10] Due to these properties, ILs have been proposed as alternatives to aqueous electrolytes for use in electrochemical energy conversion and storage devices such as batteries, supercapacitors, and fuel cells.[11,12,13,14,15] As such, a great deal of work has concerned understanding electrocatalytic reactions of molecules pertinent to energy applications, such as H_2, O_2, Li, HCOOH, CH_3OH and C_2H_5OH, in ILs.[16,17,18,19,20,21]

The use of PILs as fuel-cell electrolytes has been proposed as a way to increase fuel-cell operating temperatures above 100 °C, simplify cell design, speed up oxygen electrocatalysis at platinum and non-noble metal catalyst materials, and ultimately, reduce cost.[22,23,24,25] The need for decarbonised transport is clear, given the radiative forcing effect of anthropogenic carbon dioxide on the global climate, however, the cost of low/zero-emission vehicles is currently prohibitively

expensive for widespread adoption.[26,27,28] PIL-based fuel-cell electrolytes that can operate under anhydrous conditions at elevated temperatures have shown promising fuel-cell performance.[22,29,30] It has been suggested that the proton shuttling mechanism in PIL-based fuel cells – the regime by which protons are transferred from the fuel-cell anode to the cathode – involves oxidation of H_2 onto neutral base to form the PIL cation (see Figure 1.1); the cation is then reduced at the cathode with O_2 to reform neutral base.[29,31]

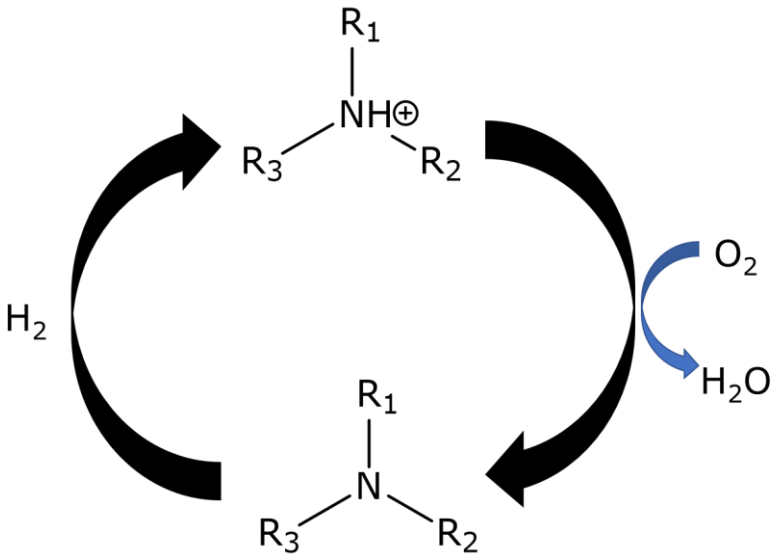


Figure 1.1 Schematic representation of the proposed proton shuttling mechanism in a protic ionic liquid-based fuel cell.

However, the proton shuttling mechanism presented in Figure 1.1 appears flawed, as it requires the presence of neutral base – something that would only exist in trace amounts in a high ionicity PIL, and most likely not enough to sustain fuel-cell reactions.[32] An investigation into viable proton shuttling mechanisms in PIL fuel cells therefore needs to be undertaken. Also, with recent work confirming the presence of excess protic species in PILs, dependent on synthesis method, it is important that the effect of acids and bases on electrocatalytic reactions in ILs is investigated.[33] Furthermore, the commonly used measures of proton activity in

aqueous systems, pK_a and pH, do not necessarily apply accurately to IL systems.[34] Therefore, a fundamental understanding of acidity and basicity in ILs is required to predict how electrocatalytic reactions will be affected by the presence of protic species.

1.2 Physicochemical Properties of Ionic Liquids

1.2.1 Introduction and classification of ionic liquids

ILs comprise entirely ions, except for the presence of varying amounts of water, with some existing in a liquid state at room temperature.[35] The melting point of ILs marks a distinction between room-temperature ILs (RTILs), ILs, and other molten salts; a salt with a melting point (T_m) below 100 °C is generally considered to be an ionic liquid.[5,6] The first reported RTIL was ethylammonium nitrate (EAN) which was reported by Walden in 1914 and the first room-temperature quaternary ammonium-based liquid salt was discovered by Hurley and Wier in 1951.[36,37] ILs are most commonly classified as aprotic (AILs) or protic (PILs); the primary difference between these two types is synthesis method and a labile proton on PIL cations.[6]

PILs are typically synthesised by a neutralisation reaction with a proton transfer from a Brønsted-Lowry acid to a Brønsted-Lowry base (see Equation 1) and, as such, the extent of the proton transfer equilibrium depends on the proton activity and affinity of the acid and base, respectively.[38] By using boiling point (T_b) and thermal decomposition temperature (T_d) as indicators of ionicity, it has been suggested that for the synthesis of high-ionicity PILs, a difference in the aqueous acid dissociation constants of the acid and conjugate acid of the base, needs to be greater than 10 ($\Delta pK_a > 10$).[32,39]

$$HA + B \rightleftharpoons B^+ + A^- \quad (1)$$

The reversible nature of the neutralisation reaction in PIL synthesis requires that there will always be a very low, equilibrium concentration of neutral species dependent on ΔpK_a. However, it has been shown that aqueous pK_a does not provide a perfect description of proton activity/affinity in PILs, and that structure (e.g. primary, secondary or tertiary cations) and hydrogen bonding can also affect proton transfer, and therefore ionicity.[8,40]

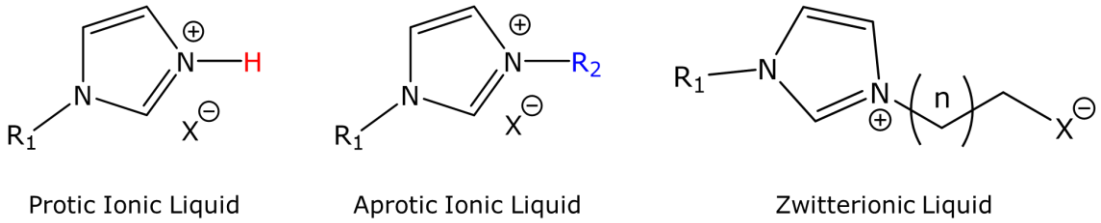


Figure 1.2 Schematic showing different classes of ionic liquid based on alkyl-imidazolium ILs. Adapted from Armand *et al.*[14]

Figure 1.2 depicts the key structural difference between PILs and AILs; here the AIL has an alkyl group, rather than a labile proton, making a quaternary ammonium cation. Also shown is a third type of IL, a zwitterionic liquid, in which both the cation and anion exist on the same species separated by long alkyl chains.[41] Zwitterionic ILs have shown promise as Li-ion conducting electrolytes when polymerised with vinyl groups and Li-bis(trifluoromethanesulfonyl)imide.[14,42,43,]

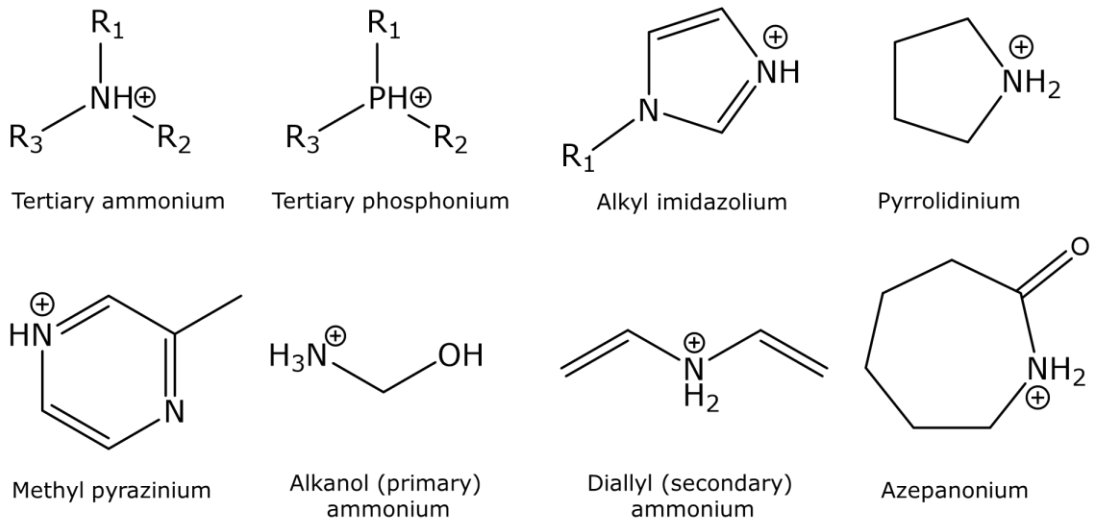


Figure 1.3 Examples of protic ionic liquid cations where 'R' denotes an alkyl group.[11,44,45,46,47,48,49,50]

Figure 1.3 and Figure 1.4 show examples of cations and anions found in PILs, although the anions are also found in AILs.

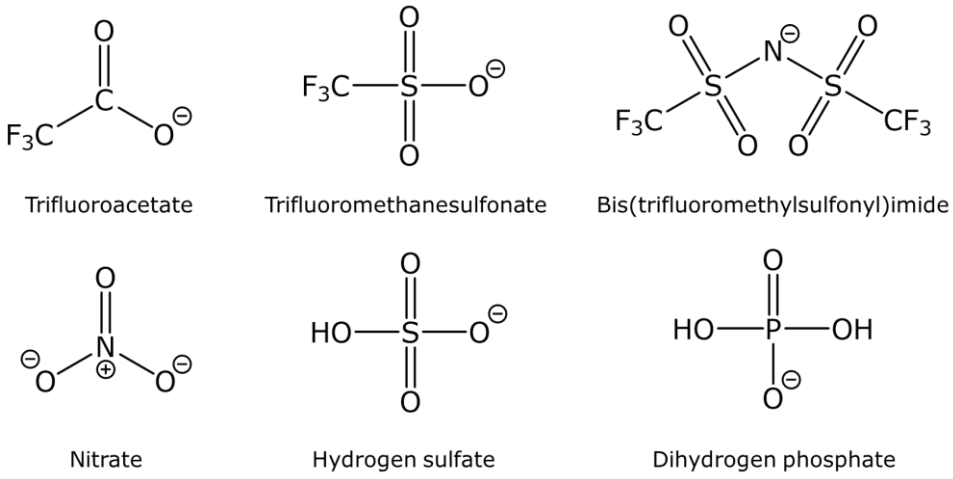


Figure 1.4 Examples of ionic liquid anions.[4,11,36,51]

AILs are commonly synthesised in a multi-step metathetic reaction whereby the cation is formed followed by an anion exchange.[52] AIL cations are generally synthesised by quaternisation where a tertiary amine or phosphine is alkylated with a haloalkane (or dialkylsulfate) by mixing and heating, often in an organic solvent.[52] The halide salt produced forms a separate phase with the reaction

mixture/solvent and can be separated, with the excess solvent then removed by gentle heating under vacuum prior to purification by recrystallisation.[52] Cations and anions commonly found in AILs are shown in Figure 1.5 and Figure 1.6, respectively.

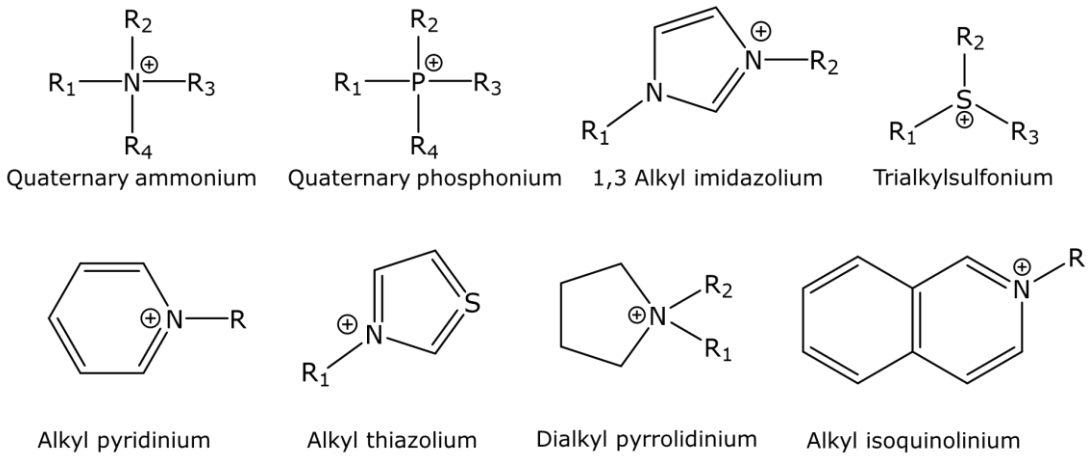


Figure 1.5 Examples of aprotic ionic liquid cations where 'R' denotes an alkyl group.[5,52]

The purified cation-halide salts are either crystalline solids or oils but to make the desired AIL, an anion exchange reaction is required. These reactions either take the form of reactions with Lewis acids, such as trichloroaluminate, or more commonly, a metathesis reaction with the lithium salt, silver salt, or protonated (acidic) form of the desired anion.[3,37,46,53,54] The desired AIL is then formed along with either an acid halide or insoluble Ag/Li-based salt which can be removed by washing with water, filtration or solvent extraction depending on miscibility of the AIL and halide salt.[52]

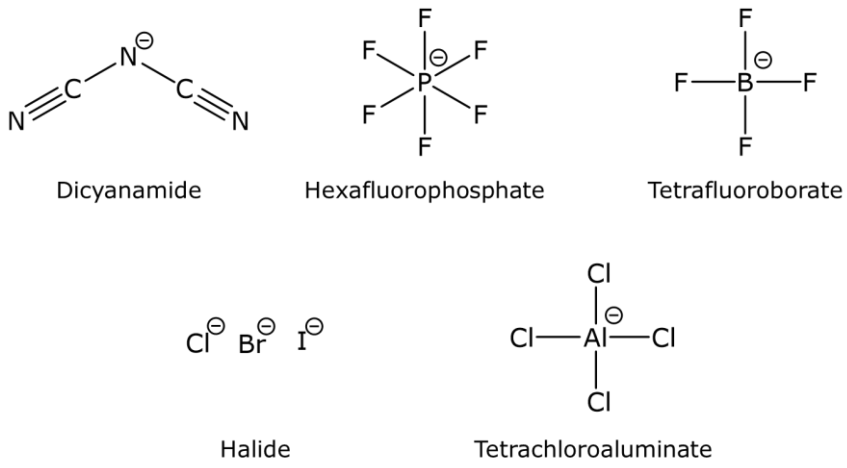


Figure 1.6 Examples of ionic liquid anions common to aprotic ionic liquids.[5]

Purification of PILs is more simple than AILs, as PILs typically only require drying under vacuum to remove water and so do not risk the presence of residual halide salt or solvent impurities from synthesis.[11,32,46,55] It should be noted that neutralisation reactions for PIL synthesis in organic solvents such as ethanol are also reported.[56] Although it cannot be removed completely, PILs are purified primarily to remove water because it has a significant effect on physiochemical and electrochemical properties, and is present either as a reaction solvent or due to the hygroscopicity of the PIL.[33,55,57,58] However, both the PIL synthesis reaction and purification conditions can affect optical and electrochemical properties due to the creation of impurities that are undetectable by normal spectroscopic methods.[33,59,60]

Discolouration of ILs by impurities is commonly observed, and can originate from slight discolouration of starting reagents caused by aerobic oxidation, as occurs in amines, or by overheating during synthesis, of which PILs can be particularly prone due to the highly exothermic neutralisation reaction required.[59,60,61] To remove chromophoric and other impurities from ILs, they can be distilled by strong heating under high vacuum; PILs are more readily distilled than AILs

because of the reversible equilibrium proton transfer between cation and anion.[59,62,63,64] However, by distilling PILs, stoichiometry can be lost, which has a significant effect on their physiochemical and electrochemical properties making it likely undesirable as a purification method, as well as impractical.[33,60] Drying PILs under moderate heat under vacuum to remove water and any excess unreacted base is recommended.[33,61]

While most ILs can be classified as AILs, PILs or zwitterionic, there exists so much variety and potential for functionalisation that subcategories based on structure, properties, or application are often more useful. Hydrophobic ILs with large fluorinated anions such as bis(trifluoromethylsulfonyl)imide are stable in ambient conditions, were first reported in the 1990s, and have been proposed as electrolytes for fuel cells, where water solubility is not desirable.[12,65] Other ILs exhibit optical isomerism with some having both chiral anions and cations.[66,67] Some more recently reported ILs combine structural elements of AILs and PILs that have dications containing both a quaternary ammonium and ternary ammonium with acidic (labile) proton, giving the ILs very low volatility (like AILs), and extended hydrogen bonding and a chemically accessible proton (like PILs).[68] Organometallic ILs such as 1-butyl-3-methylimidazolium cobalt tetracarbonyl have shown catalytic properties.[7] Mixtures of ILs with organic solvents and other ILs to obtain desired properties have also been reported.[29,69,70] The variation in structure, properties and ease of functionalisation has given rise to this now large field of research.[4,5,71]

1.2.2 Physical properties of ionic liquids

As stated above, the properties of ILs are highly dependent on their structure with classifications of protic and aprotic going some way to predict general properties. There is however, great variation in physiochemical properties within each of these two classes, but a low vapour pressure is common to most ILs.[4,72] AILs have been considered to have a near-negligible vapour pressure, and many thermally decompose at elevated temperatures before boiling.[73,74,75] However, distillation of some AILs is possible when heated under high vacuum.[62,73] PILs are more easily distilled under more moderate conditions but could suffer thermal decomposition of the parent acid and/or base species.[61,62,63]

The viscosities of ILs vary greatly but are typically comparable to that of oils – 1 to 2 orders of magnitude greater than those of aqueous or conventional organic solvents.[10,58] IL viscosities are generally dependent on ion size, interionic interaction (hydrogen bonding and van der Waals forces), alkyl chain length on the IL cations, presence of certain functional groups (hydroxyl groups on alky chains increase viscosity), and temperature.[4,49,76] Impurities such as neutral organic species or water decrease IL viscosity by interrupting interionic interactions.[35,77,78]

The physiochemical properties of ILs can be greatly affected by water content which can be problematic given that even hydrophobic ILs are also hygroscopic.[77] The water concentration in ILs under ambient conditions has been attributed to anion identity with more hydrophobic anions ($[FAP]^-$ > $[NTf_2]^-$ > $[PF_6]^-$ > $[CH_3(C_2H_4O)_2SO_4]^-$ > $[C(CN)_3]^-$ > $[BF_4]^-$ > halides) resulting in lower water concentrations and ILs that can be dried to a greater extent.[58,79] Hydrophobicity

has also been shown to increase with increasing cation alkyl chain length.[58,79] Changing water content under ambient conditions provides a challenge to accurate measurement and reporting of IL viscosities.[58]

ILs, especially AILs, typically exhibit high thermal stability with high boiling points and/or thermal decomposition temperatures (>150 °C and < 500 °C).[6,80,81] In PILs, a greater ΔpK_a, results in higher T_b and/or T_d.[32,39] PILs with a very low T_d around 50 °C are secondary and ternary ammonium acetates and formates, which characteristically have low ΔpK_a values around 6.[76] The most thermally stable PILs have a T_d between 400 and 500 °C; an example is 2,3,4,6,7,8,9,10-octahydropyrimido[1,2-a]azepin-1-ium (DBU) bis(trifluoromethanesulfonyl)imide, which has a T_d of 451 °C.[81]

When cooling many liquid ILs, or heating solid salts, a glass transition temperature (T_g) is reached, which is a measure of the mobility of the ionic matrix, and gives an indication of other properties such as viscosity and conductivity.[46,82] A lower T_g means a higher IL matrix mobility, which is indicative of higher fluidity and conductivity, although this is not universally the case.[46] The various phase transitions of ILs (T_m, T_g, transitions between crystalline phases) can be determined by differential scanning calorimetry.[82,83] T_g and T_m are closely related, with most ILs melting within T_g – 1.5 T_g.[9]

T_m of ILs, like many other physiochemical properties, are dependent on structure. Some of the lowest IL melting points are around −80 °C such as 1-methyl-3-octylpyridinium bis(trifluoromethylsulfonyl)imide (an AIL), and ethylammonium formate (a PIL) at −73 °C.[32,84] IL structure affects T_m with larger anions and longer alkyl chains on cations, generally decreasing T_m.[5,82] A significant factor to consider

is symmetry, as a more asymmetric cation sterically hinders efficient packing of the IL, raising the T_m.[4] However, some alkylated imidazolium, pyrrolidinium and quaternary ammonium-based ILs with low cationic asymmetry, are also RTILs.[46] T_m of PILs decreases with increasing ΔpK_a.[4,85] RTILs are the more easily and frequently studied ILs for electrochemical applications for practical reasons.

1.3 Electrochemistry of Ionic Liquids

1.3.1 Electrochemical properties of ionic liquids

Electrochemical stability is a well-documented property of ILs and the 'electrochemical window' of an electrolyte is a measure of its stability. The electrochemical window is the potential range, in which a particular electrode can be held at or scanned to, and in which the electrolyte is neither oxidised nor reduced. An electrolyte's 'negative potential limit' (cathodic limit) is the electrode potential below which the electrolyte is reduced and the electrolyte's 'positive potential limit' (anodic limit) is the electrode potential above which the electrolyte is oxidised. In ILs, the anodic limit is generally determined by the stability of the anion and the cathodic limit is determined by the reduction of the cation.[6] There is currently no standardised current density (j) that anodic or cathodic solvent-electrolysing redox processes are required to reach that define the anodic or cathodic potential limits.

The electrochemical windows of room temperature AILs are typically between 4.5–6.0 V, which reflects the stability of these ILs.[10,86] Some quaternary imidazolium and quaternary phosphonium-cation trifluorotris(pentafluoroethyl)phosphate-anion AILs have electrochemical windows above 6 V.[86] PILs generally have narrower electrochemical windows

than AILs because of a less negative cathodic potential limit due to the comparatively facile reduction of the proton on PIL cations to evolve hydrogen and neutral base.[76] Electrochemical windows of PILs, typically between 1.5 V and 4.3 V, are more susceptible to change with different electrode materials due the fact that the proton reduction overpotential is greatly affected by the choice of electrocatalyst.[76] Glassy-carbon electrodes, are poor proton reduction/hydrogen oxidation catalysts, and provide the widest electrochemical windows in PILs with Pt often providing the narrowest.[76,87] The acidity of the PIL cation has been shown to affect the potential at which it is reduced with more acidic cations being reduced at more positive potentials.[45] However, a general trend of a greater ΔpK_a resulting in a wider electrochemical window has not been established, and the variation in results has been attributed to complex ion-ion interactions and mobility.[76,87] Hydrogen bonding, in particular, between the anion and cation is thought to affect cation reduction potential and, therefore, the potential range (width) of the electrochemical window.[45,87]

The electrochemical windows of ILs are significantly narrowed by the presence of water.[6,9,10,58] In both AILs and PILs, anodic and cathodic potential limits decrease in the presence of water, sometimes halving when containing 12% water by weight, as reported by Schröder *et al*. for AILs.[76,88] It was also found that when dry, alkylated imidazolium AILs were exposed to H_2O-saturated argon, the IL water content increased rapidly from ≈0% to around 5% in 10 minutes, and had levelled at 12% after 60 minutes exposure; this change in water content corresponded to an electrochemical window of 4.10 V (dry) decreasing to

1.95 V (wet).[88] The narrowing of the electrochemical window upon increased water concentration is attributed to water electrolysis.[58,88]

Ionic conductivity (σ) is a measure of the mobility of ions and is principally determined in ILs by ion size, density, molecular weight and number of charges per molecule.[4] ILs with weaker or fewer interactions between ions, or lower charge density (or charge delocalisation), have higher ionic conductivities.[4] The Walden rule applies to ILs in most cases, where a plot of molar ionic conductivity, Λ, against reciprocal dynamic viscosity (fluidity), η^{-1}, produces a straight line of gradient, β (see Equation 2).[9] However, most ILs will fall below the 'ideal ion-conducting electrolyte' of dilute KCl (where β = 1) due to strong interionic forces, such as van der Waals forces and hydrogen bonding, in the concentrated IL electrolyte.[39]

$$\Lambda\eta^{\beta} = \text{constant} \tag{2}$$

IL viscosity decreases as temperature increases, and broadly follows an Arrhenius relationship (see Equation 3), where ϵ is the activation energy of viscous flow, and A_F is the pre-exponential factor.[65] However, in some cases, IL viscosity increases with temperature at a greater rate than Equation 3 predicts, and is related to a low IL T_g and enhanced ionic matrix mobility.[38] It therefore follows that IL conductivity increases with temperature, as IL viscosity decreases.[65]

$$\eta = A_F e^{\epsilon/RT} \tag{3}$$

Ionic conductivity is found generally to increase with a decreasing T_g, as has been reported for $[NTf_2]^-$-based PILs and AILs.[72,89] A comparison of $[NTf_2]^-$ and $[TfO]^-$-based quaternary ammonium AILs found that the $[NTf_2]^-$-based

liquids (≈0.13 mS cm^{-1}) had an ionic conductivity an order of magnitude greater than those of the $[TfO]^-$-based liquids (≈0.017 mS cm^{-1}); this was attributed to greater negative charge delocalisation in $[NTf_2]^-$ and stronger cation-$[TfO]^-$ interactions.[89]

One of the most conductive PILs at room temperature (25 °C) is dimethylammonium formate at 51.1 mS cm^{-2}, which also has a very low viscosity of 8.1 mPa s. However, this IL is likely volatile and low-ionicity due to a ΔpK_a of around 7, which is less than the value of 10 proposed for 'high ionicity' PILs.[38,39] High-ionicity/low-volatility PILs with high conductivity at elevated temperatures have attracted a significant amount of interest, with some reaching 470 mS cm^{-1} at 100 °C.[17,32,81] Ternary ammonium-based PILs containing $[TfO]^-$/$[NTf_2]^-$-anions have received particular attention for their high conductivity (around 30-60 mS cm^{-1} above 120 °C), low T_g and high T_d.[11,22] These PILs have also been incorporated into ion-conducting sulfonated polyimide membranes for use in fuel cells.[23] Like fluidity, IL conductivity increases with increasing water content.[90]

The proton conduction mechanism in PILs is thought to be a combination of the vehicular mechanism, through the net movement of cations, and the Grotthuss mechanism, whereby the presence of a proton acceptor such as neutral base, allows protons to hop between cations and base molecules.[91,92]

Diffusion in ionic liquids is typically slower than in conventional organic solvents due to higher viscosities.[88] However, as stated previously, viscosity is affected by ion size, inter-ionic forces, and temperature which will also affect diffusion.[49] Self-diffusion, a measure of the mobility of anions and cations within the IL, can be determined by pulse-field-gradient spin–echo nuclear magnetic resonance

spectroscopy.[93] The presence of water in ILs has been found to increase diffusion of dissolved ionic species to a greater extent than dissolved neutral species.[88]

1.3.2 Proton activity and affinity in ionic liquids

There have been a number of attempts to determine reliable systems of measuring and reporting proton activity in PILs.[94,95,96,97] In aqueous systems, proton activity is most commonly described by an acid dissociation constant, pK_a, which is the −log of the equilibrium constant of a specific protic species reacting with water.[98] Strong acids have pK_a values close to, and less than 0.[99] The proton activity of proton-accepting species, such as bases, is commonly given as the pK_a of the protonated form of the base (the conjugate acid) which have high pK_as. K_a values can be used to calculate the Gibbs free energy change of proton transfer.[100]

$$\Delta G = -RTlnK_a \tag{4}$$

pH is −log of the concentration of H_3O^+, and is a measure of the bulk proton-donating/-accepting properties of a solution.[98] While pK_a may give an approximation of proton activity in PILs, and an indication in trends of proton activity of dissolved proton-donating/-accepting species, it is clear that pK_a and pH do not have suitable definitions for applying to PILs because existing definitions are based on the role of water and H_3O^+.[16,101,102]

One approach to describing proton activity in PILs is a voltammetric method at platinum electrodes, whereby the potential difference between cation reduction (hydrogen evolution) and hydrogen oxidation onto the PIL anion, are used to obtain a PIL-specific ΔpK_a.[96] These experimentally-determined ΔpK_a values are, in all but one case, less than the aqueous ΔpK_a values by as much as 40.7 %.

However, overall it was concluded that aqueous pK_as are generally appropriate to describe proton activity in PILs.[96] An approach to investigate basicity in PILs involves a potentiometric titration whereby a PIL is acidified with a strong acid, such as triflic acid to a 0.1 mol dm^{-3} concentration, which is titrated against a series of different bases; the potential of a platinized platinum electrode or hydrogen electrode verses a reference, is recorded throughout the titration.[95,103] The PIL is also saturated with H_2 to create a stable equilibrium. The potential-determining equilibrium at the Pt electrode plateaus until the amount of base added in the titration reaches a specific amount, after which the electrode potential decreases rapidly as more base is added, before reaching another plateau at a potential significantly more negative than before the start of the titration. The potentials at each plateau, either side of the 1:1 ratio equivalence of base to acid, and the molar ratio of base to acid at those potentials, were then used to calculate pK_a of the conjugate acid of the base added, using the Nernst equation.[103] A voltammetric method of determining pK_a using the peak separation of acid reduction/H_2-oxidation and cation reduction/H_2-oxidation, was found to produce pK_a values in agreement with the potentiometric titration method.[103]

A different approach to assessing proton activity/affinity in PILs electrochemically is by using voltammetric assessment of the oxidation or reduction of a dissolved molecule such as alcohols or oxygen, in the presence of different proton-accepting or proton-donating species.[16,104] Comminges *et al.* found that the rate of 2,2′6,6′-tetramethylpiperidin-*N*-oxyl (TEMPO)-mediated alcohol oxidation to aldehydes or ketones in an AIL increased as the pK_a of the conjugate acid of the added base increased.[104] Switzer *et al.* found that the

oxygen-reduction reaction onset potential was linearly proportional to the aqueous pK_a of acid added, in the range pK_a ≈15 to −5, in an AIL.[16] The change in oxygen-reduction reaction onset potential changed with aqueous pK_a close to theoretical values of 64 mV decade^{-1}, suggesting that aqueous pK_a is a reasonable indicator of proton activity of ILs.[16] Furthermore, it suggests that redox processes of small probe molecules in ILs can be used to determine trends in proton activity.

Other electrochemical methods of determining pK_a in ILs have used glass pH electrodes for potentiometric measurements to obtain water autoprotolysis constants in water-IL mixtures.[105,106] However, while these measurements might apply to water-IL mixtures, they do not necessarily represent acidity or basicity in pure ILs.[103]

Methods of determining basicity of PIL anions and pK_a in PILs using nuclear magnetic resonance spectroscopy have also been used based on the chemical shift of the acidic proton or a probe molecule in different environments.[81,101,107] Other spectroscopic methods to determine cation acidity or proton activity in ILs more generally include both infra-red spectroscopy and UV-Vis. spectroscopy.[108,109] Criticisms of spectroscopy methods of determining proton activity are the effects of impurities and the efficacy of the probe molecule to accurately describe proton affinity.[101]

1.3.3 Oxygen-reduction reaction

The oxygen-reduction reaction (ORR) is one of the most important electrocatalytic reactions because of its critical role in biological respiration as part of oxidative phosphorylation, and in energy conversion devices such as fuel cells.[110,111] The ORR in acidic aqueous systems proceeds either via a 4-electron (Equation 5) or

2-electron process (Equation 6) to form H_2O or H_2O_2, respectively.[112] H_2O_2 can then be reduced to H_2O in another 2-electron process at a more negative potential (Equation 7), or undergo chemical disproportionation.

$$O_2 + 4HA + 4e^- \rightarrow 2H_2O + 4A^- \qquad (E^0 = 1.229\ V) \qquad (5)$$

$$O_2 + 2HA + 2e^- \rightarrow H_2O_2 + 2A^- \qquad (E^0 = 0.695\ V) \qquad (6)$$

$$H_2O_2 + 2HA + 2e^- \rightarrow 2H_2O + 2A^- \qquad (E^0 = 1.776\ V) \qquad (7)$$

In aqueous alkaline systems, the ORR proceeds either by a 4-electron pathway to form OH^- (Equation 8), or a 2-electron pathway to form HO_2^- (Equation 9), which can then be further reduced in another 2-electron process with H_2O, to form OH^- (Equation 10).[113]

$$O_2 + 2H_2O + 4e^- \rightarrow 4OH^- \qquad (E^0 = 0.401\ V) \qquad (8)$$

$$O_2 + H_2O + 2e^- \rightarrow HO_2^- + OH^- \qquad (E^0 = -0.076\ V) \qquad (9)$$

$$HO_2^- + H_2O + 2e^- \rightarrow 3OH^- \qquad (E^0 = 0.878\ V) \qquad (10)$$

In aprotic organic solvents such as liquid ammonia, a chemically reversible 1-electron reduction of oxygen is observed using Pt and glassy-carbon electrodes, producing superoxide ($O_2^{\bullet -}$).[114] The production of hydroperoxyl anions ($HO_2^{\bullet -}$) in aprotic solvents such as dimethylsulfoxide, has also been reported.[115] In the complete absence of proton-donating species, superoxide can undergo further electrochemical reduction to O_2^{2-} at very negative potentials.[114,116]

In fuel-cell applications, the significant overpotential required for oxygen reduction reduces fuel-cell efficiency, hence methods of enhancing ORR kinetics have received great interest.[117] Pt is the most active metal for the ORR but is very

expensive, generating a need for new ORR electrocatalysts that use less Pt or non-noble metal alternatives.[25,118] Key to ORR electrocatalysis is binding energy of M-O and M-OH intermediates, where 'M' is a metal; too strong or too weak an affinity for the intermediate species will result in large overpotentials at a particular electrocatalyst.[119] Another approach is to increase the operating temperature of fuel-cells in order to improve ORR electrokinetics.[120,121] However, to increase fuel-cell operating temperatures above the boiling point of water, a conducting electrolyte that has low volatility and high thermal stability is required, so ILs have been suggested as candidates.[122]

The ORR has been studied in both AILs and PILs but show significantly different electrochemistry. In dry AILs, the quasi-reversible $O_2/O_2^{\bullet-}$ redox couple is observed, and becomes electrochemically irreversible upon addition of a protic species such as water, as the 1-electron reduction shifts to a 2-/4-electron oxygen reduction.[116,123,124] The addition of acids to AILs shifts the ORR to increasingly positive potentials as the strength of the acid (aqueous pK_a) increases.[16] As the concentration of acid in the AILs increased, the ORR gradually transitions from a 1-electron process to a 4-electron process at both Pt and glassy-carbon electrocatalysts.[16] The ORR in PILs proceeds either via a 2-electron or 4-electron pathway; superoxide is not observed due to protonation by the PIL cation.[125] The ORR in [dema][TfO] proceeds via a 4-electron pathway at a Pt electrode to form H_2O.[126] A more detailed discussion of the ORR is found in the introduction to Chapter 4.

1.3.4 Hydrogen-oxidation reaction

The hydrogen-oxidation reaction (HOR) is one of the most widely studied electrocatalytic reactions in aqueous systems. The HOR is described by the general Equations 11 and 12 in acidic and alkaline aqueous systems, respectively.[96] The HOR, and the coupled reaction, the hydrogen evolution reaction (HER), have very fast electron transfer kinetics and produce electrochemically reversible cyclic voltammograms under most conditions in aqueous media.[127] Pt and Pd remain the most electrocatalytically active metals for the HOR.[128]

$$\text{Acidic: } H_2 + 2H_2O \rightarrow 2H_3O^+ + 2e^- \quad (11)$$

$$\text{Alkaline: } H_2 + 2OH^- \rightarrow 2H_2O + 2e^- \quad (12)$$

The HOR mechanism is thought to involve two of three possible steps in either a Tafel-Volmer or Heyrovský-Volmer configuration. In aqueous alkaline systems, the Tafel step involves the dissociation and adsorption of H_2 , without electron transfer, onto the electrode surface at specific catalytic sites ('*' denotes a catalytic site for hydrogen chemisorption).[129]

$$\text{Tafel: } H_2 + 2* \rightleftharpoons 2*H_{ad} \quad (13)$$

The Heyrovský step involves the dissociation of H_2 by electrooxidation at a specific catalytic site to yield water and an adsorbed hydrogen atom.

$$\text{Heyrovský: } H_2 + * + OH^- \rightleftharpoons *-H_{ad} + H_2O + e^- \quad (14)$$

The Volmer step, common to both pathways, involves the combination of an adsorbed hydrogen atom with OH^- to produce water and an electron.

$$\text{Volmer: } *-H_{ad} + OH^- \rightleftharpoons * + H_2O + e^- \quad (15)$$

In acidic aqueous systems, the Heyrovský and Volmer steps are described as follows.[127]

$$\text{Heyrovský: } H_2 + * + H_2O \rightleftharpoons *-H_{ad} + H_3O^+ + e^- \quad (16)$$

$$\text{Volmer: } *-H_{ad} + H_2O \rightleftharpoons * + H_3O^+ + e^- \quad (17)$$

The rate of the HOR is determined by whichever of the Tafel/Heyrovský/Volmer steps is slowest.

The HOR in both PILs and AILs has been studied.[17,130] It was found that oxidation of H_2 results in protonation of IL anions to produce acid, but it is inhibited by the formation of Pt-oxides from water oxidation at high positive potentials.[17,130] The inhibitory effect of Pt oxides on the HOR has also been observed in aqueous media.[131] After Pt-oxide removal, the Pt electrode is more active to H_2 oxidation in some AILs as a greater mass transport limited current was observed on the reverse potential cycle in voltammetric experiments.[130] In IL electrolytes, HOR/HER voltammetry is typically quasi-reversible or non-reversible depending on the stability of the acid formed.[130] It has been proposed that underpotential deposited hydrogen (H_{upd}) on Pt (see Equation 18) acts as a blocking species inhibiting the dissociative adsorption of H_2 during the HOR.[132]

$$Pt + H^+ + e^- \rightarrow PtH_{upd} \quad (18)$$

Given the importance of the HOR to fuel-cell research, the HOR has been studied in PILs designed for intermediate-temperature (100-200 °C) fuel-cell

applications.[11,12,17,31] The limiting HOR current increases with increasing temperature, due to faster diffusion of H_2 to the electrode surface.[17,96]

1.3.5 Water oxidation

Electrochemical water splitting, encompassing the HER and oxygen-evolution reaction (OER), are integral to producing pure hydrogen from renewable energy sources.[133,134,135] At positive potentials, water is oxidised, first producing a series of metal oxides (m-OH, m-O, m_4OH, m_2OH etc.), before oxygen is evolved.[136] The mechanism for water oxidation in an acidic aqueous system with a metal electrode 'M' is shown below.[137,138]

$$M + H_2O \rightarrow M\text{-}OH_{ads} + H^+ + e^- \quad (19)$$

$$M\text{-}OH_{ads} + OH^- \rightarrow M\text{-}O_{ads} + H_2O + e^- \quad (20)$$

$$2M\text{-}O_{ads} \rightarrow 2M + O_2 \quad (21)$$

$$M\text{-}O_{ads} + H_2O \rightarrow MOOH + H^+ + e^- \quad (22)$$

$$MOOH + H_2O \rightarrow M + O_2 + H^+ + e^- \quad (23)$$

The overall water oxidation reaction is given by,

$$2H_2O \rightarrow 4H^+ + O_2 + 4e^- \quad E = 1.23\ V \quad (24)$$

In alkaline systems, hydroxide is oxidised to hydrogen and water.[138]

Catalysts with a high activity for the OER include RuO_2, IrO_2, Pt and perovskites such as $Ba_{0.5}Sr_{0.5}Co_{0.8}Fe_{0.2}O_{3-\delta}$ and $SrNb_{0.1}Co_{0.7}Fe_{0.2}O_{3-\delta}$.[138,139,140]

The other half-reaction in water splitting is the HER which is described by Equations 25 and 26 below for acidic and alkaline aqueous systems, respectively.

$$4H^+ + 4e^- \rightarrow 2H_2 \quad E = 0\ V \tag{25}$$

$$4H_2O + 4e^- \rightarrow 2H_2 + 4OH^- \quad E = -0.83\ V \tag{26}$$

ILs have been used both as solvents for water splitting, and as solvents for electrosynthesis of water oxidation electrocatalysts.[141] Particular attention has been paid to developing new electrocatalysts for the OER as a significant overpotential of around 450 mV is typically required. Zhou *et al.* have produced highly active manganese oxide water oxidation electrocatalysts by electrodeposition onto a fluorine tin oxide substrate at 120 °C in the PIL ethylammonium nitrate.[142] Manganese oxide film morphology and composition greatly affects catalyst efficacy with Mn_2O_3 greatly out-performing Mn_3O_4.[142] Water oxidation at low overpotentials (≈150 mV) has been reported in a PIL-water mixture with a manganese oxide catalyst.[143] However, the electro-oxidation product was H_2O_2, which decomposes into O_2 after several days in the electrolyte.[143]

The presence of surface oxides on Pt electrodes has previously been detected in a range of PILs, including [dema][TfO], which arise from the oxidation of trace amounts of water always present in PILs.[144] Surface oxides were found to form positive of ≈1.0 V (vs. H_2/H^+ redox couple) at Pt in [dema][TfO] and removed negative of ≈0.8 V. The peak-to-peak separation of oxide formation and removal decreased with increasing temperature, suggesting that the rate of oxide formation and removal increases with temperature. Furthermore, the integrated areas of oxide formation and removal peaks increased with temperature suggesting a thicker oxide layer due to faster kinetics at elevated temperatures. The identities of the Pt-oxide species formed at oxidising potentials in

[dema][TfO] were identified as PtO and PtO_2 using X-ray photoelectron spectroscopy.[144]

1.3.6 Electro-oxidation of small organic molecules

The electro-oxidation of small organic molecules such as HCOOH, CH_3OH and C_2H_5OH have long been studied in aqueous media. Formic acid oxidation (FAO), methanol oxidation and ethanol oxidation are of particular interest because of their critical role as the anodic reactions in formic acid fuel cells (FAFC) and direct alcohol fuel cells (DAFC), respectively.[145,146,147,148] It is only recently however, that these reactions have been investigated in ILs.[18,20,149] Complete methanol electro-oxidation in an aqueous electrolyte is described in Equation 27.

$$CH_3OH + H_2O \rightarrow 6H^+ + 6e^- + CO_2 \qquad (27)$$

Methanol oxidation either proceeds via an adsorbed CO intermediate or via a 2-electron oxidation to formaldehyde which is then oxidised in a 4-electron process to CO_2, or via a 4-electron oxidation to formic acid followed by a 2-electron oxidation to CO_2, depending on catalyst material and pH.[150] Methanol oxidation produces a characteristic cyclic voltammogram (see Figure 1.7) whereby methanol is oxidised on the positive-going potential sweep but is inhibited by Pt-oxide formation at positive potentials. On the negative-going potential sweep, once the Pt-oxide layer is removed, a sharp anodic peak is observed corresponding to direct methanol oxidation to CO_2 on bare Pt.[151] The toxicity of methanol, compared with ethanol, is a significant drawback in using methanol as a fuel.

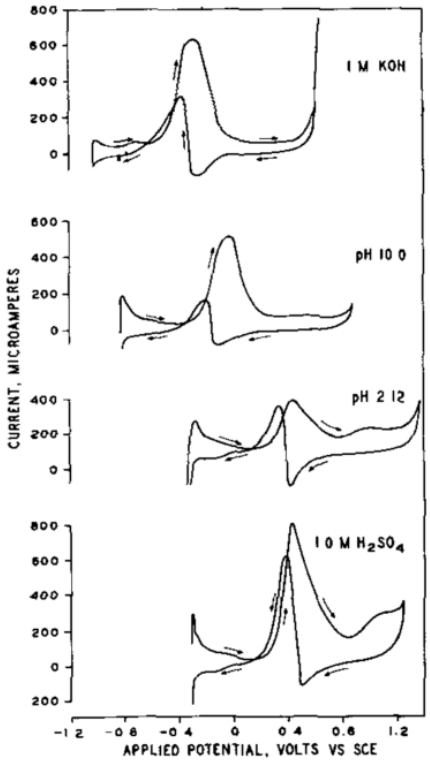


Figure 1.7 Cyclic voltammograms recorded in basic and acidic aqueous electrolytes containing 0.0247 mol dm^{-3} methanol (0.0124 mol dm^{-3} for 1 mol dm^{-3} H_2SO_4), at 8 mV s^{-1}. All sweeps begin at the most positive potentials. Taken from Buck *et al.* (1962).[151]

Methanol oxidation in PILs has been studied at elevated temperatures (above 100 °C) to mitigate the electrode-passivating effects of adsorbed CO intermediates, which reduce the efficiency of conventional direct methanol FCs. The availability of adsorbed OH on Pt was found to determine the onset potential of complete methanol oxidation, described by Equations 28 and 29.[20]

$$Pt + CH_3OH \rightarrow Pt\text{-}CO_{ads} + 4H^+ + 4e^- \quad (28)$$

$$Pt\text{-}CO_{ads} + Pt\text{-}OH_{ads} \rightarrow 2Pt + CO_2 + H^+ + e^- \quad (29)$$

Ethanol oxidation in aqueous systems involves a multi-step pathway, but there is some dispute over the order in which hydrogen atoms on ethanol are

oxidised.[152,153] Equations 30 to 34 show a proposed mechanism of ethanol electro-oxidation at a Pt electrode in acidic aqueous media.

$$nPt + CH_3CH_2OH \rightarrow Pt_n\text{-}CH_3CH_2OH \quad (30)$$

$$Pt_n\text{-}CH_3CH_2OH + H_2O \rightarrow Pt_n\text{-}CH_3CHOH + H_3O^+ + e^- \quad (31)$$

$$Pt_n\text{-}CH_3CHOH + H_2O \rightarrow Pt_n\text{-}CH_3COH + H_3O^+ + e^- \quad (32)$$

$$Pt_n\text{-}CH_3COH + H_2O \rightarrow Pt_n\text{-}CH_3CO + H_3O^+ + e^- \quad (33)$$

$$Pt + Pt_n\text{-}CH_3CO + H_2O \rightarrow Pt_n\text{-}CO + Pt\text{-}CH_3 \quad (34)$$

In alkaline aqueous media, Equations 31 to 33 are replaced by Equations 35 to 37.

$$Pt_n\text{-}CH_3CH_2OH + OH^- \rightarrow Pt_n\text{-}CH_3CHOH + H_2O + e^- \quad (35)$$

$$Pt_n\text{-}CH_3CHOH + OH^- \rightarrow Pt_n\text{-}CH_3COH + H_2O + e^- \quad (36)$$

$$Pt_n\text{-}CH_3COH + OH^- \rightarrow Pt_n\text{-}CH_3CO + H_2O + e^- \quad (37)$$

The complete electro-oxidation of ethanol is a 12-electron process yielding CO_2. However, any of the intermediates, acetaldehyde (CH_3COH) and acetic acid (CH_3COOH), can either diffuse away from the electrode as final products or undergo electro-oxidation themselves to form CO_2.[150] Ethanol oxidation is slower than methanol oxidation due to the presence of the C-C bond. Spectroelectrochemical studies using a Pd electrode showed that the breaking of the C-C bond is dependent on pH of the electrolyte; at a pH greater than 13 only partial ethanol oxidation occurs, producing acetate.[154]

Voltammetry of ethanol in aqueous electrolytes yields a characteristic cyclic voltammogram containing up to four peaks, including a sharp oxidation peak on

the negative-going potential scan after surface oxides are removed (see Figure 1.8).[152] Similar to methanol and formic acid oxidation, adsorbed CO intermediates can passivate Pt electrodes to further ethanol oxidation by competitive binding.[155] Pd is also electroactive for methanol and ethanol oxidation.[148]

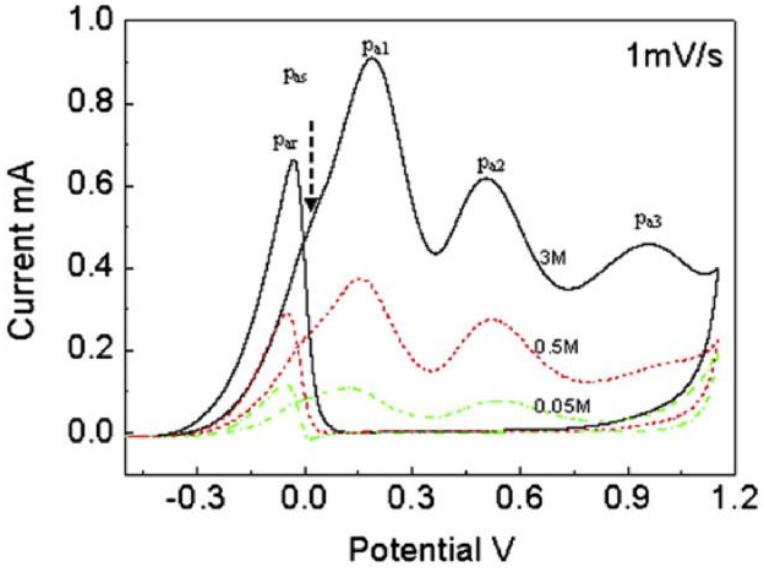


Figure 1.8 Cyclic voltammograms recorded in aqueous 0.1 mol dm^{-3} H_2SO_4 + *x* mol dm^{-3} ethanol, where *x* = 0.05, 0.5 and 3.0, at 1 mV s^{-1}. Taken from Han *et al*. (2012).[152]

Little work has been reported on ethanol electro-oxidation in ILs. However, aprotic imidazolium-based ionic liquids have been used as solvents for chemical oxidations of alcohols, and perylene-based ILs have been incorporated into carbon nanotube electrocatalysts for ethanol oxidation.[21,156] The use of ILs containing a lithium methylsulfonyl group as an electrolyte for electrochemical detection of ethanol using a Ni electrode, has also been reported.[157]

The oxidation of formic acid has been of great interest to electrochemists, as understanding the electro-oxidation mechanism of this most simple carboxylic acid gives insights that could be extended to a whole family of molecules. While

formic acid oxidation (FAO) has been known to progress via two pathways, termed 'direct' (where CO_2 is the product) and 'indirect' (via a chemisorbed passivating intermediate) for some time, the exact nature of the active species and passivating intermediate has been long debated.[158,159,160,161,162] Proposed adsorbed intermediate species have included CO_{ad}, $HCOOH_{ad}$, $HCOO^-_{ad}$, radical carbon species, COH_{ad} and $C(OH)OH_{ad}$.[159,163,164,165] Direct evidence of Pt-adsorbed CO as the electrode-poisoning species in methanol oxidation and indirect FAO has been observed using electrochemically modulated infrared reflectance spectroscopy (EMIRS)[166,167]

The active species in direct FAO had been thought to be adsorbed HCOOH or bridge-bonded formate. However, recent work by Joo *et al.* investigating the effect of pH on FAO has confirmed that $HCOO^-$ is most likely the active species.[162,165,168,169] Electro-oxidation of formate was observed across the pH range 11.7 to 1.1.[169]

$$\text{Direct: } HCOO^- \rightarrow CO_2 + H^+ + 2e^- \quad (38)$$

$$\text{Indirect I: } HCOOH + 2Pt \rightarrow HCOO_{ad}\text{-}Pt + H^+ + e^- \quad (39)$$

$$\text{Indirect II: } HCOO_{ad}\text{-}Pt + H^+ + e^- \rightarrow CO_{ad}\text{-}Pt + H_2O \quad (40)$$

$$\text{Indirect III: } CO_{ad}\text{-}Pt + H_2O \rightarrow Pt + CO_2 + 2H^+ + 2e^- \quad (41)$$

Above are the mechanisms for direct FAO (Equation 38) and indirect FAO (Equations 39-41) as reported by Joo *et al.* and Osawa *et al.*, respectively.[160,169]

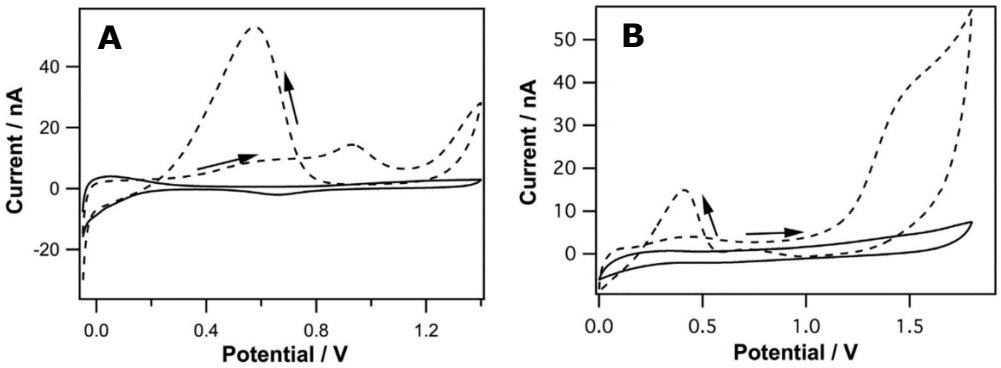


Figure 1.9 Cyclic voltammograms recorded in Ar-saturated (A) aqueous 0.5 mol dm^{-3} H_2SO_4 in the presence and absence of 0.5 mol dm^{-3} ethanol, and (B) [dema][TfO] in the presence and absence of 0.5 mol dm^{-3} ethanol, at 50 mV s^{-1}. Recorded at 50 mV s^{-1} using a 50-μm Pt ultramicroelectrode. Taken and adapted from Goodwin *et al*. (2018).[18]

Cyclic voltammetry of formic acid recorded at a Pt electrode in aqueous acidic media provides four distinct features (see Figure 1.9 (A)).[18] On the positive-going sweep, the first faradaic process is a small/broad anodic peak at around 0.6 V (versus reversible hydrogen electrode (RHE)) that is attributed to direct FAO from $HCOO^-$ (Equation 38); the broad and low current maximum peak is due to adsorbed CO poisoning the electrode surface, reducing the active Pt sites available to formate. At ≈0.9 V on the positive-going potential sweep, a second anodic peak is observed and relates to oxidation of adsorbed CO to CO_2 (Equation 41). A third anodic peak, distinct from water oxidation in blank CVs, is observed at potentials positive of 1.2 V, and is not well understood. However, plausible suggestions are that this peak is direct FAO, but at a high overpotential, that has previously been attributed to specific active Pt-oxide species reacting with formic acid, but more recently that it could be direct $HCOO^-$ oxidation on Pt sites protected from surface oxides by b-COOH.[162,169,170,171] The most defining feature of the FAO CV is observed on the negative-going potential sweep where a large anodic peak is recorded negative of ≈0.8 V, peaking around 0.6 V. This unusual peak is widely

considered to be caused by uninhibited direct FAO (of $HCOO^-$) (Equation 38), uninhibited because any adsorbed CO has been oxidised on the positive-going sweep and is unable to re-form because of Pt-oxides (or b-COOH) blocking access to bare Pt on the electrode surface; once the Pt-oxides are removed leaving bare Pt (peak around 0.8 V), direct formic acid/formate oxidation can occur uninhibited.[18,151,163,168,170,172,173,174] Although considered unlikely due to being less energetically favourable, direct oxidation of HCOOH has not been ruled out. However, any contribution to the total current will be small compared with $HCOO^-$ oxidation. It has also been shown that any b-COOH present on the Pt electrode surface can only form from HCOOH and not $HCOO^-$.[162,169]

Voltammetry of formic acid in [dema][TfO] at a Pt microelectrode (see Figure 1.9 (B)) yields recognisable features of FAO in acidic aqueous systems.[18] The use of microelectrodes allows for rapid diffusion of analyte species to the electrode and reaction products away from the electrode, creating an effect comparable to rotating the electrode very quickly.[175] Goodwin *et al.* found that, on the positive-going potential sweep, a small, broad anodic peak is observed at around 0.4 V and was attributed to direct FAO, inhibited by surface-adsorbed CO.[18] Above 1.0 V a large anodic current was observed and attributed to Pt-oxide formation. On the negative-going potential sweep, a large and defined anodic peak is observed which, like that observed in aqueous systems, was attributed to direct (and uninhibited) FAO. Direct FAO produces a large current density (j) on the negative-going potential sweep because the Pt-oxides formed by water oxidation at positive potentials protect the electrode surface from CO contamination, until they are removed, which allows direct FAO to occur on a clean Pt surface.

1.4 Uses for Protic Ionic Liquids

The electrochemical properties of ILs (ionic conductivity, low volatility, high thermal stability, wide potential window) and the tunability of physiochemical properties as determined by IL structure has led to their use as non-aqueous electrolytes in energy conversion and storage devices such as fuel cells, water electrolysers, batteries, thermocells, CO_2-capture, supercapacitors, and as electrodeposition solvents.[19,83,87,141] While much fundamental research is conducted using PILs as liquid electrolytes, incorporation of PILs into polymer membranes, either by IL-polymerisation, mass uptake/polymer doping, or polymerisation in presence of an IL, has also received significant attention.[23,176,177,178] The polymers chosen vary greatly but include polyethylene oxide, polymethyl methacrylate, Nafion® (perfluoro-sulfonated polytetrafluoroethylene), benzimidazole, and sulfonated polyimide.[23,51,179,180,181,182] Crosslinking in the polymer-IL composites affects ion transport properties as well as physical properties of the membrane, such as brittleness and porosity.[178,183] Co-polymerisation is also used to enhance the properties of poly-IL membranes.[178]

ILs and PILs have been proposed as electrolytes for Li-ion batteries as safe, non-flammable replacements for the flammable organic carbonates currently used. The high electrochemical stability of ILs with an electrochemical window greater than the 5 V required for Li-ion batteries, make some ILs good candidates as Li-ion battery electrolytes. A problem encountered in using IL-electrolytes for battery applications is slow diffusion of Li^+, caused by the electrostatic interaction of the Li-ions and the high Li-ion concentration required increasing IL viscosity.[184]

Li-ion coordination number, the number of IL molecules in the solvation shell, is less in PILs than in AILs, leading to increased Li^+ diffusion in PILs.[184] PILs have also been studied as possible electrolytes for metal/air batteries such as [dema][TfO] in Zn/Air batteries.[141,185] While AILs have more commonly been investigated as battery electrolytes, PILs have shown similar performance with the advantages of being easier to synthesise and less expensive.[186]

PILs have also found applications as electrolytes in electric double-layer capacitors; a type of supercapacitor.[187] Supercapacitors store charge at the electrochemical double layer and have greater charge densities than traditional parallel plate capacitors. Supercapacitors can be charged and discharged quickly, with a high power output for a short time.[141] The high ionic conductivity and charge density of the electrochemical double layer, lend PILs to be used as supercapacitor electrolytes.[188]

One of the main proposed applications for PILs is in intermediate-temperature (100-200 °C) fuel cells and water electrolysers.[189] Increasing the operating temperature of fuel cells increases the rate of the ORR (allowing for lower Pt-catalyst loadings), reduces catalyst poisoning effects of H_2 fuel impurities such as H_2S and CO, and allows for more simple cell designs due to easier water management.[120] Comparatively little work has been reported on PILs as electrolytes for water splitting. However, water splitting has been demonstrated in triethylammonium methanesulfonate with evolved H_2 and O_2 gases being detected by gas chromatography and fluorescence oxygen sensor, respectively.[87] Increasing the operating temperature of water electrolysers provides a

thermodynamic advantage as the electrical energy required to split water lowers as temperature is increased (see Figure 1.10).[190]

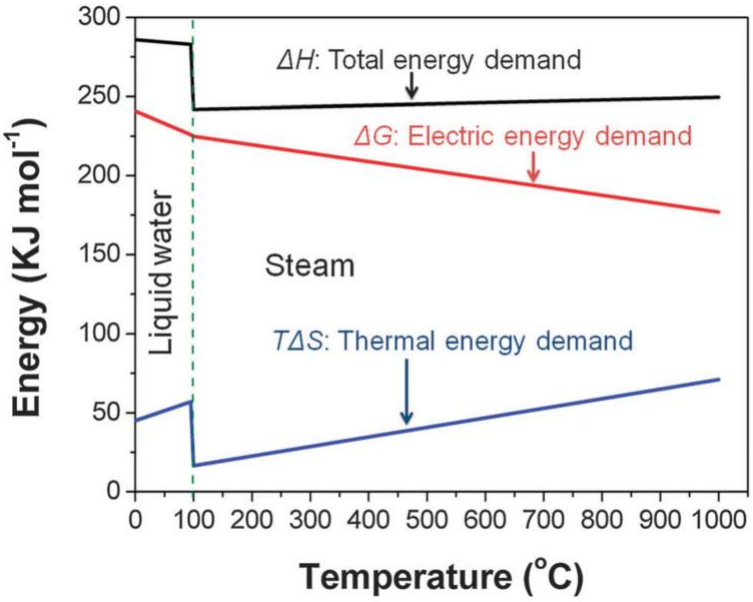


Figure 1.10 Electric, thermal and total energy demand for H_2O electrolysis as a function of temperature. Taken from Bi *et al.* (2014).[185]

PILs have also been used as electrodeposition solvents for metals, for the synthesis of nano-particle electrocatalysts, and synthesis of polymers that require highly protic environments to form, such as polyaniline in ethylammonium nitrate.[191,192]

1.5 Project Objectives

Electrocatalytic reactions of small molecules in ILs have been well documented.[4] The ORR and HOR, in particular, have been well-studied in ILs both at room-temperature and elevated temperature due to their importance in fuel cell applications for decarbonised transport.[11,17,96] However, the significant effect of proton-accepting and/or proton-donating species in PILs on the reduction or oxidation of small key molecules such as H_2O, O_2, H_2 and HCOOH, has only recently

begun to be appreciated.[16,18,33] Furthermore, the apparent electrochemical stability of ILs and the proposed mechanisms for their use as electrolytes in H_2/O_2 fuel-cell applications, appear at odds with the favourable fuel cell performance reported.[22,29,31,76] The origin, role, and effect of proton-donating/-accepting species in ILs, and an understanding of acidity and basicity in ILs is therefore critical.

By studying the ORR and HOR in ILs, both pure stoichiometric PILs and in the presence of proton-donating/-accepting species, this thesis aims to reassess the suitability of PILs as fuel-cell electrolytes as well as provide fundamental insight into the true proton-shuttling mechanisms of these systems.[61] An investigation as to the origins of adventitious protic species and favourable fuel-cell performance as found in the published scientific literature, will also be conducted. Similar to the investigation into the relationship between ORR onset potential and the acidity of protic species in PILs, the formic acid oxidation reaction will be investigated to asses formic acid's suitability as a probe molecule for assessing the basicity of PILs.

Finally, with greater understanding of proton shuttling mechanisms in PILs and the importance of proton thermodynamics on fuel cell performance, a fuel-cell system will be tested which exceeds previously reported performance.[22]

1.6 References

1. Gabriel, S.; Weiner, J. Ueber einige Abkömmlinge des Propylamins. *Ber. Dtsch. Chem. Ges.* **1888,** *21* (2), 2669-2679.

2. Friedel, C.; Crafts, J. M. Sur une nouvelle méthode générale de synthèse d'hydrocarbures, d'acétones. *C. R. Hebd. Seances Acad. Sci.* **1877,** *84*, 1392 and 1450.

3. Wilkes, J. S.; Zaworotko, M. J. Air and Water Stable 1-Ethyl-3-methylimidazolium Based Ionic Liquids. *J. Chem. Soc., Chem. Commun.* **1992,** (13), 965-967.

4. Greaves, T. L.; Drummond, C. J. Protic Ionic Liquids: Properties and Applications. *Chem. Rev.* **2008,** *108* (1), 206-237.

5. Freemantle, M. *An Introduction to Ionic Liquids*. The Royal Society of Chemistry: 2010.

6. Greaves, T. L.; Drummond, C. J. Protic Ionic Liquids: Evolving Structure-Property Relationships and Expanding Applications. *Chem. Rev.* **2015,** *115*, 11379–11448.

7. Brown, R. J. C.; Welton, T.; Dyson, P. J.; Ellis, D. J. 1-Butyl-3-methylimidazolium cobalt tetracarbonyl [bmim][Co(CO)4]: a catalytically active organometallic ionic liquid. *Chem. Commun. (Cambridge, U. K.)* **2001,** (18), 1862-1863.

8. Angell, C. A.; Byrne, N.; Belieres, J.-P. Parallel Developments in Aprotic and Protic Ionic Liquids: Physical Chemistry and Applications. *Acc. Chem. Res.* **2007,** *40* (11), 1228-1236.

9. Ohno, H. *Electrochemical Aspects of Ionic Liquids*. John Wiley & Sons, Inc.: 2005.

10. Silvester, D. S.; Compton, R. G. Electrochemistry in Room Temperature Ionic Liquids: A Review and Some Possible Applications. *Z. Phys. Chem.* **2006,** *220* (10), 1247-1274.

11. Nakamoto, H.; Watanabe, M. Brønsted acid-base ionic liquids for fuel cell electrolytes. *Chem. Commun. (Cambridge, U. K.)* **2007,** (24), 2539-2541.

12. Yasuda, T.; Ogawa, A.; Kanno, M.; Mori, K.; Sakakibara, K.; Watanabe, M. Hydrophobic Protic Ionic Liquid for Nonhumidified Intermediate-temperature Fuel Cells. *Chem. Lett.* **2009,** *38* (7), 692-693.

13. Papageorgiou, N.; Athanassov, Y.; Armand, M.; Bonhôte, P.; Pettersson, H.; Azam, A.; Grätzel, M. The Performance and Stability of Ambient Temperature Molten Salts for Solar Cell Applications. *J. Electrochem. Soc.* **1996,** *143* (10).

14. Armand, M.; Endres, F.; MacFarlane, D. R.; Ohno, H.; Scrosati, B. Ionic-liquid materials for the electrochemical challenges of the future. *Nat. Mater.* **2009,** *8* (8), 621-9.

15. Armand, M.; Tarascon, J.-M. Building better batteries. *Nature (London, U. K.)* **2008,** *451*, 652-657.

16. Switzer, E. E.; Zeller, R.; Chen, Q.; Sieradzki, K.; Buttry, D. A.; Friesen, C. Oxygen Reduction Reaction in Ionic Liquids: The Addition of Protic Species. *J. Phys. Chem. C* **2013,** *117* (17), 8683-8690.

17. Johnson, L.; Ejigu, A.; Licence, P.; Walsh, D. A. Hydrogen Oxidation and Oxygen Reduction at Platinum in Protic Ionic Liquids. *J. Phys. Chem. C* **2012,** *116*, 18048−18056.

18. Goodwin, S. E.; Muhammad, S.; Tuan, L.-P.; Walsh, D. A. The contrasting effects of diethylmethylamine during reduction of protons and oxidation of formic acid in diethylmethylammonium-based protic ionic liquids. *J. Electroanal. Chem.* **2018,** *819*, 187-192.

19. Matsumoto, H.; Sakaebe, H.; Tatsumi, K. Preparation of room temperature ionic liquids based on aliphatic onium cations and asymmetric amide anions and their electrochemical properties as a lithium battery electrolyte. *J. Power Sources* **2005,** *146* (1-2), 45-50.

20. Ejigu, A.; Johnson, L.; Licence, P.; Walsh, D. A. Electrocatalytic oxidation of methanol and carbon monoxide at platinum in protic ionic liquids. *Electrochem. Commun.* **2012,** *23*, 122-124.

21. Farmer, V.; Welton, T. The oxidation of alcohols in substituted imidazolium ionic liquids using ruthenium catalysts. *Green Chem.* **2002,** *4* (2), 97-102.

22. Lee, S. Y.; Ogawa, A.; Kanno, M.; Nakamoto, H.; Yasuda, T.; Watanabe, M. Nonhumidified Intermediate Temperature Fuel Cells Using Protic Ionic Liquids. *J. Am. Chem. Soc.* **2010,** *132* (28), 9764-9773.

23. Lee, S.-Y.; Yasuda, T.; Watanabe, M. Fabrication of protic ionic liquid/sulfonated polyimide composite membranes for non-humidified fuel cells. *J. Power Sources* **2010,** *195* (18), 5909-5914.

24. Colella, W. G.; Jacobson, M. Z.; Golden, D. M. Switching to a U.S. hydrogen fuel cell vehicle fleet: The resultant change in emissions, energy use, and greenhouse gases. *J. Power Sources* **2005,** *150*, 150-181.

25. Chen, Z.; Higgins, D.; Yu, A.; Zhang, L.; Zhang, J. A review on non-precious metal electrocatalysts for PEM fuel cells. *Energy Environ. Sci.* **2011,** *4*, 3167-3192.

26. *Summary for Policymakers - Global Warming of 1.5 °C: an IPCC special report on the impacts of global warming of 1.5 °C above pre-industrial levels and related global greenhouse gas emission pathways, in the context of strengthening the global response to the threat of climate change, sustainable development, and efforts to eradicate poverty*; Intergovernmental Panel on Climate Change (accessed 10 Jun 2018), 2018; pp 1-34.

27. Kiehl, J. T.; Trenberth, K. E. Earth's Annual Global Mean Energy Budget. *Bull. Am. Meteorol. Soc.* **1997,** *78* (2), 197-208.

28. Papageorgopoulos, D. *V.0 Fuel Cells Sub-Program Overview*; United States of America Department of Energy: Online, 2018.

29. Miran, M. S.; Yasuda, T.; Susan, M. A. B. H.; Dokko, K.; Watanabe, M. Binary Protic Ionic Liquid Mixtures as a Proton Conductor: High Fuel Cell Reaction Activity and Facile Proton Transport. *J. Phys. Chem. C* **2014,** *118* (48), 27631-27639.

30. Mitsushima, S.; Shinohara, Y.; Matsuzawa, K.; Ota, K.-i. Mass transportation in diethylmethylammonium trifluoromethanesulfonate for fuel cell applications. *Electrochim. Acta* **2010,** *55* (22), 6639-6644.

31. Miran, M. S.; Yasuda, T.; Susan, M. A. B. H.; Dokko, K.; Watanabe, M. Electrochemical properties of protic ionic liquids: correlation between open circuit potential for H_2/O_2 cells under non-humidified conditions and ΔpK_a. *RSC Adv.* **2013,** *3* (13), 4141-4144.

32. Belieres, J.-P.; Angell, C. A. Protic Ionic Liquids: Preparation, Characterization, and Proton Free Energy Level Representation. *J. Phys. Chem. B* **2007,** *111*, 4926-4937.

33. Goodwin, S. E.; Smith, D. E.; Gibson, J. S.; Jones, R. G.; Walsh, D. A. Electroanalysis of Neutral Precursors in Protic Ionic Liquids and Synthesis of High-Ionicity Ionic Liquids. *Langmuir* **2017,** *33* (34), 8436–8446.

34. Johnson, K. E.; Pagni, R. M.; Bartmess, J. Brønsted Acids in Ionic Liquids: Fundamentals, Organic Reactions, and Comparisons. *Monatsh. Chem.* **2007,** *138* (11), 1077-1101.

35. Cammarata, L.; Kazarian, S. G.; Salter, P. A.; Welton, T. Molecular states of water in room temperature ionic liquids. *Phys. Chem. Chem. Phys.* **2001,** *3* (23), 5192-5200.

36. Walden, P. Ueber die Molekulargrösse und elektrische leitfähigkeit einiger geschmolzenen Salze. *Bull. Acad. Imp. Sci. St.-Pétersbourg* **1914,** *8*, 405-422.

37. Hurley, F. H.; Wier, T. P. Electrodeposition of Metals from Fused Quaternary Ammonium Salts. *J. Electrochem. Soc.* **1951,** *98* (5).

38. Greaves, T. L.; Weerawardena, A.; Krodkiewska, I.; Drummond, C. J., Protic Ionic Liquids: Physicochemical Properties and Behavior as Amphiphile Self-Assembly Solvents. *J. Phys. Chem. B* **2008,** *112* (3), 896-905.

39. Yoshizawa, M.; Xu, W.; Angell, C. A. Ionic Liquids by Proton Transfer: Vapor Pressure, Conductivity, and the Relevance of ΔpK_a from Aqueous Solutions. *J. Am. Chem. Soc.* **2003,** *125*, 15411-15419.

40. Stoimenovski, J.; Izgorodina, E. I.; MacFarlane, D. R. Ionicity and proton transfer in protic ionic liquids. *Phys. Chem. Chem. Phys.* **2010,** *12* (35), 10341-10347.

41. Yoshizawa, M.; Narita, A.; Ohno, H. Design of Ionic Liquids for Electrochemical Applications. *Aust. J. Chem.* **2004,** *57*, 139–144.

42. Byrne, N.; Howlett, P. C.; MacFarlane, D. R.; Forsyth, M. The Zwitterion Effect in Ionic Liquids: Towards Practical Rechargeable Lithium-Metal Batteries. *Adv. Mater.* **2005,** *17* (20), 2497-2501.

43. Yoshizawa, M.; Hirao, M.; Ito-Akita, K.; Ohno, H. Ion conduction in zwitterionic-type molten salts and their polymers. *J. Mater. Chem.* **2001,** *11* (4), 1057-1062.

44. Susan, M. A. B. H.; Noda, A.; Mitsushima, S.; Watanabe, M. Brønsted acid–base ionic liquids and their use as new materials for anhydrous proton conductors. *Chemical Communications (Cambridge, United Kingdom)* **2003**, 938–939.

45. Rana, U. A.; Vijayaraghavan, R.; Walther, M.; Sun, J.; Torriero, A. A. J.; Forsyth, M.; MacFarlane, D. R. Protic ionic liquids based on phosphonium cations: comparison with ammonium analogues. *Chem. Commun. (Cambridge, UK)* **2011,** *47*, 11612–11614.

46. Hirao, M.; Sugimoto, H.; Ohno, H. Preparation of Novel Room-Temperature Molten Salts by Neutralization of Amines. *J. Electrochem. Soc.* **2000,** *147* (11), 4168-4172.

47. Du, Z.; Li, Z.; Guo, S.; Zhang, J.; Zhu, L.; Deng, Y. Investigation of physicochemical properties of lactam-based Brønsted acidic ionic liquids. *J. Phys. Chem. B* **2005,** *109* (41), 19542-6.

48. Anouti, M.; Vigeant, A.; Jacquemin, J.; Brigouleix, C.; Lemordant, D. Volumetric properties, viscosity and refractive index of the protic ionic liquid, pyrrolidinium octanoate, in molecular solvents. *J. Chem. Thermodyn.* **2010,** *42* (7), 834-845.

49. Pinkert, A.; Ang, K. L.; Marsh, K. N.; Pang, S. Density, viscosity and electrical conductivity of protic alkanolammonium ionic liquids. *Phys. Chem. Chem. Phys.* **2011,** *13* (11), 5136-43.

50. Mayrand-Provencher, L.; Rochefort, D. Influence of the Conductivity and Viscosity of Protic Ionic Liquids Electrolytes on the Pseudocapacitance of RuO_2 Electrodes. *J. Phys. Chem. C* **2009,** *113*, 1632–1639.

51. Nakamoto, H.; Noda, A.; Hayamizu, K.; Hayashi, S.; Hamaguchi, H.-o.; Watanabe, M. Proton-Conducting Properties of a Brønsted Acid-Base Ionic Liquid and Ionic Melts Consisting of Bis(trifluoromethanesulfonyl)imide and Benzimidazole for Fuel Cell Electrolytes. *J. Phys. Chem. C* **2007,** *111*, 1541-1548.

52. Anderson, J. L.; Anthony, J. L.; Antonietti, M.; Brennecke, J. F.; Carmichael, A. J.; Carper, W. R.; Chiappe, C.; Cocalia, V. A.; James H. Davis, J.; Popolo, M. G. D.; Dolle, A.; Dreyer, S.; Earle, M.; Eckstein, M.; Abedin, S. Z. E.; Endres, F.; Favre, F.; Fehrmann, R.; Gordon, C. M.; Haddleton, D. M.; Hardacre, C.; Hilgers, C.; Holbrey, J. D.; Hunt, P. A.; Kirschning, A.; Klembt, S.; Kragl, U.; Leuchter, A.; Lynden-Bell, R. M.; Maase, M.; Maginn, E. J.; Mantz, R. A.; Muldoon, M. J.; Olivier-Bourbigou, H.; Palmer, G.; Richter, J.; Riisager, A.; Rogers, R. D.; Schulz, P.; Singh, V.; Smarsly, B.; Trulove, P. C.; Vaultier, M.; Visser, A. E.; Wagner, M.; Wahlbeck, P. G.; Wasserscheid, P.; Welton, T.; Wilkes, J. S.; Zhou, Y. *Ionic Liquids in Synthesis*. 2nd Edition; WILEY-VCH Verlag GmbH & Co. KGaA: 2008; Vol. 1.

53. Wilkes, J. S.; Levisky, J. A.; Wilson, R. A.; Hussey, C. L. Dialkylimidazolium Chloroaluminate Melts: A New Class of Room-Temperature Ionic Liquids for Electrochemistry, Spectroscopy, and Synthesis. *Inorg. Chem.* **1982,** *21* (3), 1263-1264.

54. Chum, H. L.; Koch, V. R.; Miller, L. L.; Osteryoung, R. A. An Electrochemical Scrutiny of Organometallic Iron Complexes and Hexamethylbenzene in a Room Temperature Molten Salt. *J. Am. Chem. Soc.* **1975,** *97* (11), 3264-3265.

55. Mori, K.; Kobayashi, T.; Sakakibara, K.; Ueda, K. Experimental and theoretical investigation of proton exchange reaction between protic ionic liquid diethylmethylammonium trifluoromethanesulfonate and H_2O. *Chem. Phys. Lett.* **2012,** *552*, 58-63.

56. Li, H.; Jiang, F.; Di, Z.; Gu, J. Anhydrous proton-conducting glass membranes doped with ionic liquid for intermediate-temperature fuel cells. *Electrochim. Acta* **2012,** *59*, 86-90.

57. Dahi, A.; Fatyeyeva, K.; Chappey, C.; Langevin, D.; Rogalsky, S. P.; Tarasyuk, O. P.; Marais, S. Water sorption properties of room-temperature ionic liquids over the whole range of water activity and molecular states of water in these media. *RSC Adv.* **2015,** *5* (94), 76927-76938.

58. O'Mahony, A. M.; Silvester, D. S.; Aldous, L.; Hardacre, C.; Compton, R. G. Effect of Water on the Electrochemical Window and Potential Limits of Room-Temperature Ionic Liquids. *J. Chem. Eng. Data* **2008,** *53* (12), 2884-2891.

59. Earle, M. J.; Gordon, C. M.; Plechkova, N. V.; Seddon, K. R.; Welton, T. Decolorization of Ionic Liquids for Spectroscopy. *Anal. Chem. (Washington, DC, U. S.)* **2007,** *79*, 758-764.

60. Mayrand-Provencher, L.; Rochefort, D. Origin and effect of impurities in protic ionic liquids based on 2-methylpyridine and trifluoroacetic acid for applications in electrochemistry. *Electrochim. Acta* **2009,** *54*, 7422–7428.

61. Smith, D. E.; Walsh, D. A. The Nature of Proton Shuttling in Protic Ionic Liquid Fuel Cells. *Adv. Energy Mater.* **2019,** *9* (24).

62. Earle, M. J.; Esperanca, J. M.; Gilea, M. A.; Lopes, J. N.; Rebelo, L. P.; Magee, J. W.; Seddon, K. R.; Widegren, J. A. The distillation and volatility of ionic liquids. *Nature (London, UK)* **2006,** *439* (7078), 831-4.

63. MacFarlane, D. R.; Pringle, J. M.; Johansson, K. M.; Forsyth, S. A.; Forsyth, M. Lewis base ionic liquids. *Chem. Commun. (Cambridge, UK)* **2006,** (18), 1905-17.

64. Taylor, A. W.; Lovelock, K. R. J.; Deyko, A.; Licence, P.; Jones, R. G. High vacuum distillation of ionic liquids and separation of ionic liquid mixtures. *Phys. Chem. Chem. Phys.* **2010,** *12* (8), 1648.

65. Bonhôte, P.; Dias, A.-P.; Armand, M.; Papageorgiou, N.; Kalyanasundaram, K.; Grätzel, M. Hydrophobic, Highly Conductive Ambient-Temperature Molten Salts. *Inorg. Chem.* **1996,** *35* (5), 1168-1178.

66. Howarth, J.; HanIon, K.; Fayne, D.; McCormac, P. Moisture Stable Dialkylimidazolium Salts as Heterogeneous and Homogeneous Lewis Acids in the Diels-Alder Reaction. *Tetrahedron Lett.* **1997,** *38* (17), 3097-3100.

67. Dorta, R.; Machado, M. Synthesis and Characterization of Chiral Imidazolium Salts. *Synthesis* **2005,** *2005* (15), 2473-2475.

68. Mirjafari, A.; Pham, L. N.; McCabe, J. R.; Mobarrez, N.; Salter, E. A.; Wierzbicki, A.; West, K. N.; Sykora, R. E.; Jr., J. H. D. Building a bridge between aprotic and protic ionic liquids. *RSC Adv.* **2013,** *3*, 337-340.

69. Marsh, K. N.; Boxall, J. A.; Lichtenthaler, R. Room temperature ionic liquids and their mixtures—a review. *Fluid Phase Equilib.* **2004,** *219* (1), 93-98.

70. Belieres, J.-P.; Gervasio, D.; Angell, C. A. Binary inorganic salt mixtures as high conductivity liquid electrolytes for >100 °C fuel cells. *Chem. Commun. (Cambridge, UK)* **2006,** (46), 4799-4801.

71. Zhang, S.; Zhang, Q.; Zhang, Y.; Chen, Z.; Watanabe, M.; Deng, Y. Beyond solvents and electrolytes: Ionic liquids-based advanced functional materials. *Prog. Mater Sci.* **2016,** *77*, 80-124.

72. Zhang, S.; Sun, N.; He, X.; Lu, X.; Zhang, X. Physical Properties of Ionic Liquids: Database and Evaluation. *J. Phys. Chem. Ref. Data* **2006,** *35* (4).

73. Rebelo, L. P. N.; Lopes, J. N. C.; Esperança, J. M. S. S.; Filipe, E. On the Critical Temperature, Normal Boiling Point, and Vapor Pressure of Ionic Liquids. *J. Phys. Chem. B* **2005,** *109* (13), 6040-6043.

74. Tokuda, H.; Tsuzuki, S.; Susan, M. A. B. H.; Hayamizu, K.; Watanabe, M. How Ionic Are Room-Temperature Ionic Liquids? An Indicator of the Physicochemical Properties. *J. Phys. Chem. B* **2006,** *110*, 19593-19600.

75. Esperança, J. M. S. S.; Lopes, J. N. C.; Tariq, M.; Santos, L. M. N. B. F.; Magee, J. W.; Rebelo, L. P. N. Volatility of Aprotic Ionic Liquids s A Review. *J. Chem. Eng. Data* **2010,** *55* (1), 3-12.

76. Zhao, C.; Burrell, G.; Torriero, A. A. J.; Separovic, F.; Dunlop, N. F.; MacFarlane, D. R.; Bond, A. M. Electrochemistry of Room Temperature Protic Ionic Liquids. *J. Phys. Chem. B* **2008,** *112*, 6923–6936.

77. Widegren, J. A.; Laesecke, A.; Magee, J. W. The effect of dissolved water on the viscosities of hydrophobic room-temperature ionic liquids. *Chem. Commun. (Cambridge, UK)* **2005,** (12), 1610-2.

78. Kelkar, M. S.; Maginn, E. J. Effect of Temperature and Water Content on the Shear Viscosity of the Ionic Liquid 1-Ethyl-3-methylimidazolium Bis(trifluoromethanesulfonyl)imide As Studied by Atomistic Simulations. *J. Phys. Chem. B* **2007,** *111* (18), 4867-4876.

79. Freire, M. G.; Santos, L. M. N. B. F.; Fernandes, A. M.; Coutinho, J. A. P.; Marrucho, I. M. An overview of the mutual solubilities of water–imidazolium-based ionic liquids systems. *Fluid Phase Equilib.* **2007,** *261* (1-2), 449-454.

80. Holbrey, J. D.; Seddon, K. R. The phase behaviour of 1-alkyl-3-methylimidazolium tetrafluoroborates; ionic liquids and ionic liquid crystals. *J. Chem. Soc., Dalton Trans.* **1999,** (13), 2133–2139.

81. Miran, M. S.; Kinoshita, H.; Yasuda, T.; Susan, M. A.; Watanabe, M. Physicochemical properties determined by ΔpK_a for protic ionic liquids based on an organic super-strong base with various Brønsted acids. *Phys. Chem. Chem. Phys.* **2012,** *14* (15), 5178-86.

82. MacFarlane, D. R.; Meakin, P.; Sun, J.; Amini, N.; Forsyth, M. Pyrrolidinium Imides: A New Family of Molten Salts and Conductive Plastic Crystal Phases. *J. Phys. Chem. B* **1999,** *103* (20), 4164-4170.

83. McEwen, A. B.; Ngo, H. L.; LeCompte, K.; Goldman, J. L. Electrochemical Properties of Imidazolium Salt Electrolytes for Electrochemical Capacitor Applications. *J. Electrochem. Soc.* **1999,** *146* (5), 1687-1695.

84. CRC, *CRC Handbook of Chemistry and Physics*. 96th ed.; CRC Press: 2015; p 2677.

85. Ohno, H.; Yoshizawa, M. Ion conductive characteristics of ionic liquids prepared by neutralization of alkylimidazoles. *Solid State Ionics* **2002,** *154–155*, 303–309.

86. Buzzeo, M. C.; Hardacre, C.; Compton, R. G. Extended electrochemical windows made accessible by room temperature ionic liquid/organic solvent electrolyte systems. *ChemPhysChem* **2006,** *7* (1), 176-80.

87. Lu, X.; Burrell, G.; Separovic, F.; Zhao, C. Electrochemistry of Room Temperature Protic Ionic Liquids: A Critical Assessment for Use as Electrolytes in Electrochemical Applications. *J. Phys. Chem. B* **2012,** *116* (30), 9160-70.

88. Schröder, U.; Wadhawan, J. D.; Compton, R. G.; Marken, F.; Suarez, P. A. Z.; Consorti, C. S.; de Souza, R. F.; Dupont, J. Water-induced accelerated ion diffusion: voltammetric studies in 1-methyl-3-[2,6-(S)-dimethylocten-2-yl]imidazolium tetrafluoroborate, 1-butyl-3-methylimidazolium tetrafluoroborate and hexafluorophosphate ionic liquids. *New J. Chem.* **2000,** *24* (12), 1009-1015.

89. Sun, J.; Forsyth, M.; MacFarlane, D. R. Room-Temperature Molten Salts Based on the Quaternary Ammonium Ion. *J. Phys. Chem. B* **1998,** *102*, 8858-8864.

90. Widegren, J. A.; Saurer, E. M.; Marsh, K. N.; Magee, J. W. Electrolytic conductivity of four imidazolium-based room-temperature ionic liquids and the effect of a water impurity. *J. Chem. Thermodyn.* **2005,** *37* (6), 569-575.

91. Noda, A.; Susan, M. A. B. H.; Kudo, K.; Mitsushima, S.; Hayamizu, K.; Watanabe, M. Brønsted Acid-Base Ionic Liquids as Proton-Conducting Nonaqueous Electrolytes. *J. Phys. Chem. B* **2003,** *107*, 4024-4033.

92. Watanabe, H.; Umecky, T.; Arai, N.; Nazet, A.; Takamuku, T.; Harris, K. R.; Kameda, Y.; Buchner, R.; Umebayashi, Y. Possible Proton Conduction Mechanism in Pseudo-Protic Ionic Liquids: A Concept of Specific Proton Conduction. *J. Phys. Chem. B* **2019,** *123* (29), 6244-6252.

93. Ueno, K.; Tokuda, H.; Watanabe, M. Ionicity in ionic liquids: correlation with ionic structure and physicochemical properties. *Phys. Chem. Chem. Phys.* **2010,** *12* (8), 1648.

94. Bentley, C. L.; Bond, A. M.; Zhang, J. Voltammetric Perspectives on the Acidity Scale and H^+/H_2 Process in Ionic Liquid Media. *Annu. Rev. Anal. Chem.* **2018,** *11* (1), 397-419.

95. Kanzaki, R.; Kodamatani, H.; Tomiyasu, T.; Watanabe, H.; Umebayashi, Y. A pH Scale for the Protic Ionic Liquid Ethylammonium Nitrate. *Angew. Chem., Int. Ed. Engl.* **2016,** *55* (21), 6266-6269.

96. Bautista-Martinez, J. A.; Tang, L.; Belieres, J.-P.; Zeller, R.; Angell, C. A.; Friesen, C. Hydrogen Redox in Protic Ionic Liquids and a Direct Measurement of Proton Thermodynamics. *J. Phys. Chem. C* **2009,** *113*, 12586–12593.

97. Abbott, A. P.; Alabdullah, S. S. M.; Al-Murshedi, A. Y. M.; Ryder, K. S. Bronsted acidity in deep eutectic solvents and ionic liquids. *Faraday Discuss.* **2018,** *206*, 365-377.

98. Atkins, P. W.; De Paula, J. *Atkin's Physical Chemistry*. Eighth ed.; W.H. Freeman and Company: 2006.

99. Ripin, D. H.; Evans, D. A. pK_as of Inorganic and Oxo-Acids. http://evans.rc.fas.harvard.edu/pdf/evans_pKa_table.pdf.

100. Harvey, D. *Modern Analytical Chemistry*. Second ed.; McGraw-Hill Companies: 2009.

101. Hasani, M.; Yarger, J. L.; Angell, C. A. On the Use of a Protic Ionic Liquid with a Novel Cation To Study Anion Basicity. *Chem. - Eur. J.* **2016,** *22* (37), 13312-9.

102. Trummal, A.; Lipping, L.; Kaljurand, I.; Koppel, I. A.; Leito, I. Acidity of Strong Acids in Water and Dimethyl Sulfoxide. *J. Phys. Chem. A* **2016,** *120* (20), 3663-9.

103. Barhdadi, R.; Troupel, M.; Comminges, C.; Laurent, M.; Doherty, A. Electrochemical determination of pKa of N-bases in ionic liquid media. *J. Phys. Chem. B* **2012,** *116* (1), 277-82.

104. Comminges, C.; Barhdadi, R.; Doherty, A. P.; O'Toole, S.; Troupel, M. Mechanism of 2,2′6,6′-Tetramethylpiperidin-N-oxyl-Mediated Oxidation of Alcohols in Ionic Liquids. *J. Phys. Chem. A* **2008,** *112* (34), 7848–7855.

105. Bou Malham, I.; Letellier, P.; Turmine, M. Application of the Bahe's pseudolattice-theory to water-1-butyl-3-methylimidazolium tetrafluoroborate (bmimBF(4)) mixtures at 298.15K Part I. Autoprotolysis constants. *Talanta* **2007,** *72* (1), 155-64.

106. Malham, I. B.; Letellier, P.; Turmine, M. Application of the Bahe's pseudolattice theory to water-1-butyl-3-methylimidazolium tetrafluoroborate (bmimBF4) mixtures at 298.15K: Part II. Acidity scales. *Talanta* **2008,** *77* (1), 48-52.

107. Scholz, F.; Himmel, D.; Eisele, L.; Unkrig, W.; Martens, A.; Schluter, P.; Krossing, I. The Acidity of the HBr/AlBr3 System: Stabilization of Crystalline Protonated Arenes and Their Acidity in Bromoaluminate Ionic Liquids. *Chem. - Eur. J.* **2015,** *21* (20), 7489-502.

108. Holzweber, M.; Lungwitz, R.; Doerfler, D.; Spange, S.; Koel, M.; Hutter, H.; Linert, W. Mutual Lewis acid-base interactions of cations and anions in ionic liquids. *Chem. - Eur. J.* **2013,** *19* (1), 288-93.

109. Stoyanov, E. S.; Stoyanova, I. V.; Reed, C. A. The basicity of unsaturated hydrocarbons as probed by hydrogen-bond-acceptor ability: bifurcated N-H^+...pi hydrogen bonding. *Chem. - Eur. J.* **2008,** *14* (26), 7880-91.

110. Bacon, F. T. Fuel Cells, Past, Present And Future. *Electrochim. Acta* **1969,** *14*, 569-585.

111. Berg, J. M.; Tymoczko, J. L.; Stryer, L. *Biochemistry: International Edition*. Sixth (Revised) ed.; W. H. Freeman & Co Ltd.: 2006.

112. Song, C.; Zhang, J. Electrocatalytic Oxygen Reduction Reaction. In *PEM Fuel Cell Electrocatalysts and Catalyst Layers*, Springer: 2008; pp 89-134.

113. Ge, X.; Sumboja, A.; Wuu, D.; An, T.; Li, B.; Goh, F. W. T.; Hor, T. S. A.; Zong, Y.; Liu, Z. Oxygen Reduction in Alkaline Media: From Mechanisms to Recent Advances of Catalysts. *ACS Catal.* **2015,** *5* (8), 4643-4667.

114. Uribe, F. A.; Bard, A. J. Electrochemistry in liquid ammonia. 5. Electroreduction of oxygen. *Inorg. Chem.* **1982,** *21* (8), 3160-3163.

115. Morrison, M. M.; Roberts, J. L.; Sawyer, D. T. Oxidation-reduction chemistry of hydrogen peroxide in aprotic and aqueous solutions. *Inorg. Chem.* **1979,** *18* (7), 1971-1973.

116. René, A.; Hauchard, D.; Lagrost, C.; Hapiot, P. Superoxide Protonation by Weak Acids in Imidazolium Based Ionic Liquids. *J. Phys. Chem. B* **2009,** *113* (9), 2826–2831.

117. Song, C.; Tang, Y.; Zhang, J. L.; Zhang, J.; Wang, H.; Shen, J.; McDermid, S.; Li, J.; Kozak, P. PEM fuel cell reaction kinetics in the temperature range of 23–120 °C. *Electrochim. Acta* **2007,** *52* (7), 2552-2561.

118. Shao, M.; Chang, Q.; Dodelet, J. P.; Chenitz, R. Recent Advances in Electrocatalysts for Oxygen Reduction Reaction. *Chem. Rev.* **2016,** *116* (6), 3594-657.

119. Nørskov, J. K.; Rossmeisl, J.; Logadottir, A.; Lindqvist, L.; Kitchin, J. R.; Bligaard, T.; Jonsson, H. Origin of the Overpotential for Oxygen Reduction at a Fuel-Cell Cathode. *J. Phys. Chem. B* **2004,** *108*, 17886-17892.

120. Chandan, A.; Hattenberger, M.; El-Kharouf, A.; Du, S.; Dhir, A.; Self, V.; Pollet, B. G.; Ingram, A.; Bujalski, W. High temperature (HT) polymer electrolyte membrane fuel cells (PEMFC)–A review. *J. Power Sources* **2013,** *231*, 264-278.

121. Kongstein, O. E.; Berning, T.; Børresen, B.; Seland, F.; Tunold, R. Polymer electrolyte fuel cells based on phosphoric acid doped polybenzimidazole (PBI) membranes. *Energy* **2007,** *32* (4), 418-422.

122. Yasuda, T.; Nakamura, S.-i.; Lee, S.-Y.; Watanabe, M. Performance of Nonhumidified Intermediate-temperature Fuel Cells Based on Protic Ionic Liquids Prepared from Oxo and Amide Acids. *Chem. Lett.* **2010,** *39*, 678-679.

123. Zhang, Y.; Pozo-Gonzalo, C. Variations and applications of the oxygen reduction reaction in ionic liquids. *Chem. Commun. (Cambridge, UK)* **2018,** *54* (31), 3800-3810.

124. Katayama, Y.; Onodera, H.; Yamagata, M.; Miura, T. Electrochemical Reduction of Oxygen in Some Hydrophobic Room-Temperature Molten Salt Systems. *J. Electrochem. Soc.* **2004,** *151* (1), A59.

125. Khan, A.; Lu, X.; Aldous, L.; Zhao, C. Oxygen Reduction Reaction in Room Temperature Protic Ionic Liquids. *J. Phys. Chem. C* **2013,** *117* (36), 18334-18342.

126. Walsh, D. A.; Ejigu, A.; Smith, J.; Licence, P. Kinetics and mechanism of oxygen reduction in a protic ionic liquid. *Phys. Chem. Chem. Phys.* **2013,** *15* (20), 7548.

127. Sheng, W.; Gasteiger, H. A.; Shao-Horn, Y. Hydrogen Oxidation and Evolution Reaction Kinetics on Platinum: Acid vs Alkaline Electrolytes. *J. Electrochem. Soc.* **2010,** *157* (11), B1529.

128. Sheng, W.; Myint, M.; Chen, J. G.; Yan, Y. Correlating the hydrogen evolution reaction activity in alkaline electrolytes with the hydrogen binding energy on monometallic surfaces. *Energy Environ. Sci.* **2013,** *6* (5).
129. Campos-Roldán, C. A.; Alonso-Vante, N. The Hydrogen Oxidation Reaction in Alkaline Medium: An Overview. *Electrochem. Energy Rev.* **2019,** *2* (2), 312-331.

130. Silvester, D. S.; Aldous, L.; Hardacre, C.; Compton, R. G. An Electrochemical Study of the Oxidation of Hydrogen at Platinum Electrodes in Several Room Temperature Ionic Liquids. *J. Phys. Chem. B* **2007,** *111*, 5000-5007.

131. Varela, H.; Krischer, K. Nonlinear phenomena during electrochemical oxidation of hydrogen on platinum electrodes. *Catal. Today* **2001,** *70*, 411–425.

132. Goodwin, S. E.; Walsh, D. A. Hydrogen Electrooxidation under Conditions of High Mass Transport in Room-Temperature Ionic Liquids and the Role of Underpotential-Deposited Hydrogen. *J. Phys. Chem. C* **2016,** *120*, 11498–11507.

133. Marbán, G.; Valdés-Solís, T. Towards the hydrogen economy? *Int. J. Hydrogen Energy* **2007,** *32* (12), 1625-1637.

134. Jensen, S. H.; Larsen, P. H.; Mogensen, M. Hydrogen and synthetic fuel production from renewable energy sources. *Int. J. Hydrogen Energy* **2007,** *32* (15), 3253-3257.

135. Holladay, J. D.; Hu, J.; King, D. L.; Wang, Y. An overview of hydrogen production technologies. *Catal. Today* **2009,** *139* (4), 244-260.

136. Angerstein-Kozlowska, H.; Conway, B. E.; Sharp, W. B. A. The Real Condition Of Electrochemically Oxidized Platinum Surfaces Part I. Resolution Of Component Processes. *J. Electroanal. Chem. Interfacial Electrochem.* **1973,** *43*, 9-36.

137. Song, S. D.; Zhang, H. M.; Ma, X. P.; Shao, Z. G.; Baker, R. T.; Yi, B. L. Electrochemical investigation of electrocatalysts for the oxygen evolution reaction in PEM water electrolyzers. *Int. J. Hydrogen Energy* **2008,** *33* (19), 4955-4961.

138. Suen, N. T.; Hung, S. F.; Quan, Q.; Zhang, N.; Xu, Y. J.; Chen, H. M. Electrocatalysis for the oxygen evolution reaction: recent development and future perspectives. *Chem. Soc. Rev.* **2017,** *46* (2), 337-365.

139. Suntivich, J.; May, K. J.; A.Gasteiger, H.; Goodenough, J. B.; Shao-Horn, Y. A Perovskite Oxide Optimized for Oxygen Evolution Catalysis from Molecular Orbital Principles. *Science (Washington, DC, U. S.)* **2011,** *334*, 1383-1385.

140. Zhu, Y.; Zhou, W.; Zhong, Y.; Bu, Y.; Chen, X.; Zhong, Q.; Liu, M.; Shao, Z. A Perovskite Nanorod as Bifunctional Electrocatalyst for Overall Water Splitting. *Adv. Energy Mater.* **2017,** *7* (8), 1602122.

141. MacFarlane, D. R.; Tachikawa, N.; Forsyth, M.; Pringle, J. M.; Howlett, P. C.; Elliott, G. D.; Davis, J. H.; Watanabe, M.; Simon, P.; Angell, C. A. Energy applications of ionic liquids. *Energy Environ. Sci.* **2014,** *7* (1), 232.

142. Zhou, F.; Izgorodin, A.; Hocking, R. K.; Spiccia, L.; MacFarlane, D. R. Electrodeposited MnOx Films from Ionic Liquid for Electrocatalytic Water Oxidation. *Adv. Energy Mater.* **2012,** *2* (8), 1013-1021.

143. Izgorodin, A.; Izgorodina, E.; MacFarlane, D. R. Low overpotential water oxidation to hydrogen peroxide on a MnOx catalyst. *Energy Environ. Sci.* **2012,** *5* (11).

144. Walsh, D. A.; Ejigu, A.; Muhammad, S.; Licence, P. The Formation and Role of Oxide Layers on Pt during Hydrazine Oxidation in Protic Ionic Liquids. *ChemElectroChem* **2014,** *1* (1), 281-288.

145. DeLuca, N. W.; Elabd, Y. A. Polymer Electrolyte Membranes for the Direct Methanol Fuel Cell: A Review. *J. Polym. Sci., Part B: Polym. Phys.* **2006,** *44* (16), 2201-2225.

146. Park, K.-W.; Choi, J.-H.; Sung, Y.-E. Structural, Chemical, and Electronic Properties of Pt/Ni Thin Film Electrodes for Methanol Electrooxidation. *J. Phys. Chem. B* **2003,** *107*, 5851-5856.

147. Cuesta, A.; Cabello, G.; Osawa, M.; Gutiérrez, C. Mechanism of the Electrocatalytic Oxidation of Formic Acid on Metals. *ACS Catal.* **2012,** *2* (5), 728-738.

148. Xu, C.; Cheng, L.; Shen, P.; Liu, Y. Methanol and ethanol electrooxidation on Pt and Pd supported on carbon microspheres in alkaline media. *Electrochem. Commun.* **2007,** *9* (5), 997-1001.

149. Feng, Y.-Y.; Yin, Q.-Y.; Lu, G.-P.; Yang, H.-F.; Zhu, X.; Kong, D.-S.; You, J.-M. Enhanced catalytic performance of Pd catalyst for formic acid electrooxidation in ionic liquid aqueous solution. *J. Power Sources* **2014,** *272*, 606-613.

150. Ozoemena, K. I. Nanostructured platinum-free electrocatalysts in alkaline direct alcohol fuel cells: catalyst design, principles and applications. *RSC Adv.* **2016,** *6* (92), 89523-89550.

151. Buck, R. P.; Griffith, L. R. Voltammetric and Chronopotentiometric Study of the Anodic Oxidation of Methanol, Formaldehyde, and Formic Acid. *J. Electrochem. Soc.* **1962**.

152. Han, L.; Ju, H.; Xu, Y. Ethanol electro-oxidation: Cyclic voltammetry, electrochemical impedance spectroscopy and galvanostatic oscillation. *Int. J. Hydrogen Energy* **2012,** *37* (20), 15156-15163.

153. Wang, Y.; Zou, S.; Cai, W.-B. Recent Advances on Electro-Oxidation of Ethanol on Pt- and Pd-Based Catalysts: From Reaction Mechanisms to Catalytic Materials. *Catalysts* **2015,** *5* (3), 1507-1534.

154. Fang, X.; Wang, L.; Shen, P. K.; Cui, G.; Bianchini, C. An in situ Fourier transform infrared spectroelectrochemical study on ethanol electrooxidation on Pd in alkaline solution. *J. Power Sources* **2010,** *195* (5), 1375-1378.

155. Parreira, L. S.; Antoniassi, R. M.; Freitas, I. C.; de Oliveira, D. C.; Spinacé, E. V.; Camargo, P. H. C.; dos Santos, M. C. MWCNT-COOH supported PtSnNi electrocatalysts for direct ethanol fuel cells: Low Pt content, selectivity and chemical stability. *Renewable Energy* **2019,** *143*, 1397-1405.

156. Li, S.; Ma, J.; Huo, H.; Jin, J.; Ma, J.; Yang, H. Ionic liquids-noncovalently functionalized multi-walled carbon nanotubes decorated with palladium nanoparticles: A promising electrocatalyst for ethanol electrooxidation. *Int. J. Hydrogen Energy* **2016,** *41* (28), 12358-12368.

157. Lee, Y. G.; Chou, T. C. Ionic liquid ethanol sensor. *Biosens. Bioelectron.* **2004,** *20* (1), 33-40.

158. Müller, E. Die Elektrolytische Oxydation Der Ameisensäure. *Z. Elektrochem. Angew. Phys. Chem.* **1923,** *23*, 264-274.

159. Capon, A.; Parsons, R. The Oxidation Of Formic Acid On Noble Metal Electrodes I. Review Of Previous Work. *J. Electroanal. Chem. Interfacial Electrochem.* **1973,** *44*, 1-7.

160. Cuesta, A.; Cabello, G.; Gutierrez, C.; Osawa, M. Adsorbed formate: the key intermediate in the oxidation of formic acid on platinum electrodes. *Phys. Chem. Chem. Phys.* **2011,** *13* (45), 20091-5.

161. Chen, Y.-X.; Heinen, M.; Jusys, Z.; Behm, R. J. Bridge-Bonded Formate: Active Intermediate or Spectator Species in Formic Acid Oxidation on a Pt Film Electrode? *Langmuir* **2006,** *22*, 10399-10408.

162. Joo, J.; Uchida, T.; Cuesta, A.; Koper, M. T.; Osawa, M. Importance of acid-base equilibrium in electrocatalytic oxidation of formic acid on platinum. *J. Am. Chem. Soc.* **2013,** *135* (27), 9991-4.

163. Breiter, M. W. Anodic Oxidation Of Formic Acid On Platinum-I. Adsorption Of Formic Acid, Oxygen, And Hydrogen In Perchloric Acid Solutions. *Electrochim. Acta* **1963,** *8*, 447-456.

164. Brummer, S. B.; Makrides, A. C. Adsorption and Oxidation of Formic Acid on Smooth Platinum Electrodes in Perchloric Acid Solutions. *J. Phys. Chem.* **1964,** *68* (6).

165. Chen, Y. X.; Heinen, M.; Jusys, Z.; Behm, R. J. Kinetics and mechanism of the electrooxidation of formic acid--spectroelectrochemical studies in a flow cell. *Angew. Chem. Int. Ed. Engl.* **2006,** *45* (6), 981-5.

166. Beden, B.; C., L. Electrosorption Of Methanol On A Platinum Electrode. IR Spectroscopic Evidence For Adsorbed CO Species. *J. Electroanal. Chem.* **1981,** *121*, 343-347.

167. Beden, B.; Bewick, A.; Lamy, C. A Study By Electrochemically Modulated Infrared Reflectance Spectroscopy Of The Electrosorption Of Formic Acid At A Platinum Electrode. *J. Electroanal. Chem.* **1983,** *148*, 147-160.

168. Samjeské, G.; Miki, A.; Ye, S.; Osawa, M. Mechanistic Study of Electrocatalytic Oxidation of Formic Acid at Platinum in Acidic Solution by Time-Resolved Surface-Enhanced Infrared Absorption Spectroscopy. *J. Phys. Chem. B* **2006,** *110* (33), 16559-16566.

169. Joo, J.; Uchida, T.; Cuesta, A.; Koper, M. T. M.; Osawa, M. The effect of pH on the electrocatalytic oxidation of formic acid/formate on platinum: A mechanistic study by surface-enhanced infrared spectroscopy coupled with cyclic voltammetry. *Electrochim. Acta* **2014,** *129*, 127-136.

170. Capon, A.; Parsons, R. The Oxidation Of Formic Acid On Noble Metal Electrodes II. A Comparison Of The Behaviour Of Pure Electrodes. *J. Electroanal. Chem. Interfacial Electrochem.* **1973,** *44*, 239-554.

171. Tyurikova, O. G.; Miller, N. B.; Yakovleva, A. A.; Veselovskii, V. I. *Elektrokhimiya* **1971,** *7*, 690.

172. Giner, J. The Anodic Oxidation Of Methanol And Formic Acid And The Reductive Adsorption Of CO_2. *Electrochim. Acta* **1964,** *9*, 63-77.

173. Capon, A.; Parsons, R. The Oxidation Of Formic Acid On Noble Metal Electrodes III. Intermediates And Mechanism On Platinum Electrodes. *Electroanal. Chem. Interfacial Electrochem.* **1973,** *45*, 205-231.

174. Chen, W.; Kim, J.; Sun, S.; Chen, S. Electro-oxidation of formic acid catalyzed by FePt nanoparticles. *Phys. Chem. Chem. Phys.* **2006,** *8* (23), 2779-86.

175. Bard, A. J.; Faulkner, L. R. *Electrochemical Methods: Fundamentals and Applications*. Second Edition; John Wiley & Sons, Inc.: 2001.

176. Park, M. J.; Choi, I.; Hong, J.; Kim, O. Polymer Electrolytes Integrated with Ionic Liquids for Future Electrochemical Devices. *J. Appl. Polym. Sci.* **2013,** *129* (5), 2363-2376.

177. Iojoiu, C.; Hana, M.; Molmeret, Y.; Martinez, M.; Cointeaux, L.; El Kissi, N.; Teles, J.; Lepretre, J. C.; Judeinstein, P.; Sanchez, J. Y. Ionic Liquids and Their Hosting by Polymers for HT-PEMFC Membranes. *Fuel Cells* **2010,** *10* (5), 778-789.

178. Yuana, J.; Mecerreyes, D.; Antonietti, M. Poly(ionic liquid)s: An update. *Prog. Polym. Sci.* **2013,** *38*, 1009– 1036.

179. Simonetti, E.; Carewska, M.; Maresca, G.; De Francesco, M.; Appetecchia, G. B. Highly Conductive, Ionic Liquid-Based Polymer Electrolytes. *J. Electrochem. Soc.* **2017,** *164* (1), A6213-A6219.

180. Di Noto, V.; Negro, E.; Sanchez, J. Y.; Iojoiu, C. Structure-Relaxation Interplay of a New Nanostructured Membrane Based on Tetraethylammonium Trifluoromethanesulfonate Ionic Liquid and Neutralized Nafion 117 for High-Temperature Fuel Cells. *J. Am. Chem. Soc.* **2010,** *132* (7), 2183-2195.

181. Wang, L.; Advani, S. G.; Prasad, A. K. Ionic Liquid-Based Composite Membrane for PEMFCs Operating under Low Relative Humidity Conditions. *Electrochem. Solid-State Lett.* **2012,** *15* (4), B44.

182. Sood, R.; Iojoiu, C.; Espuche, E.; Gouanvé, F.; Gebel, G.; Mendil-Jakani, H.; Lyonnard, S.; Jestin, J. Proton Conducting Ionic Liquid Doped Nafion Membranes: Nano-Structuration, Transport Properties and Water Sorption. *J. Phys. Chem. C* **2012,** *116* (46), 24413-24423.

183. Snedden, P.; Cooper, A. I.; Scott, K.; Winterton, N. Cross-Linked Polymer-Ionic Liquid Composite Materials. *Macromolecules* **2003,** *36* (12), 4549-4556.

184. Eftekhari, A.; Liu, Y.; Chen, P. Different roles of ionic liquids in lithium batteries. *J. Power Sources* **2016,** *334*, 221-239.

185. Ingale, P.; Sakthivel, M.; Drillet, J.-F. Test of Diethylmethylammonium Trifluoromethanesulfonate Ionic Liquid as Electrolyte in Electrically Rechargeable Zn/Air Battery. *J. Electrochem. Soc.* **2017,** *164* (8), H5224-H5229.

186. Menne, S.; Pires, J.; Anouti, M.; Balducci, A. Protic ionic liquids as electrolytes for lithium-ion batteries. *Electrochem. Commun.* **2013,** *31*, 39-41.

187. Anouti, M.; Couadou, E.; Timperman, L.; Galiano, H. Protic ionic liquid as electrolyte for high-densities electrochemical double layer capacitors with activated carbon electrode material. *Electrochim. Acta* **2012,** *64*, 110-117.

188. Anouti, M.; Timperman, L. A pyrrolidinium nitrate protic ionic liquid-based electrolyte for very low-temperature electrical double-layer capacitors. *Phys. Chem. Chem. Phys.* **2013,** *15* (17), 6539-6548.

189. Yasuda, T.; Ogawa, A.; Lee, S.-Y.; Watanabe, M. Protic Ionic Liquid as an Electrolyte for Non-humidified Intermediate Temperature Fuel Cells. *Electrochemical Society Meeting Abstracts* **2008,** *MA2008-02 3043*.

190. Bi, L.; Boulfrad, S.; Traversa, E. Steam electrolysis by solid oxide electrolysis cells (SOECs) with proton-conducting oxides. *Chem. Soc. Rev.* **2014,** *43* (24), 8255-70.

191. Suryanto, B. H. R.; Gunawan, C. A.; Lu, X.; Zhao, C. Tuning the electrodeposition parameters of silver to yield micro/nano structures from room temperature protic ionic liquids. *Electrochim. Acta* **2012,** *81*, 98-105.

192. Snook, G. A.; Greaves, T. L.; Best, A. S. A comparative study of the electrodeposition of polyaniline from a protic ionic liquid, an aprotic ionic liquid and neutral aqueous solution using anilinium nitrate. *J. Mater. Chem.* **2011,** *21* (21).

2 Review of Experimental Techniques

2.1 Electrochemical Techniques

2.1.1 Fundamentals of electrochemistry

Electrochemistry has been described as "…the science of structures and processes at and through the interface between an electronic (electrode) and an ionic conductor (electrolyte) or between two ionic conductors".[1] The "electrochemical double layer" is a description of the interface between a metal electrode and the surrounding electrolyte. 'Double' in this context refers to two charged layers each of opposite polarities held $\approx 10^{-10}$ m apart.[2]

Figure 2.1 is a schematic representation of the electrode-electrolyte interface in an aqueous system containing KCl as the electrolyte. At the inner Helmholtz plane (IHP), the double layer is established such that the positive electrode (in the example shown) induces orientation of the polar solvent water molecules. Also shown is a partially de-solvated, specifically adsorbed anion (Cl^-), and fully solvated supporting electrolyte cation (K^+) in the outer Helmholtz plane (OHP). The double layer resembles a parallel plate capacitor, the charging of which during voltammetric experiments is the origin of the non-zero, non-faradaic (no transfer of electrons) current over potential ranges determined by the electrolyte and analyte present.[3,4]

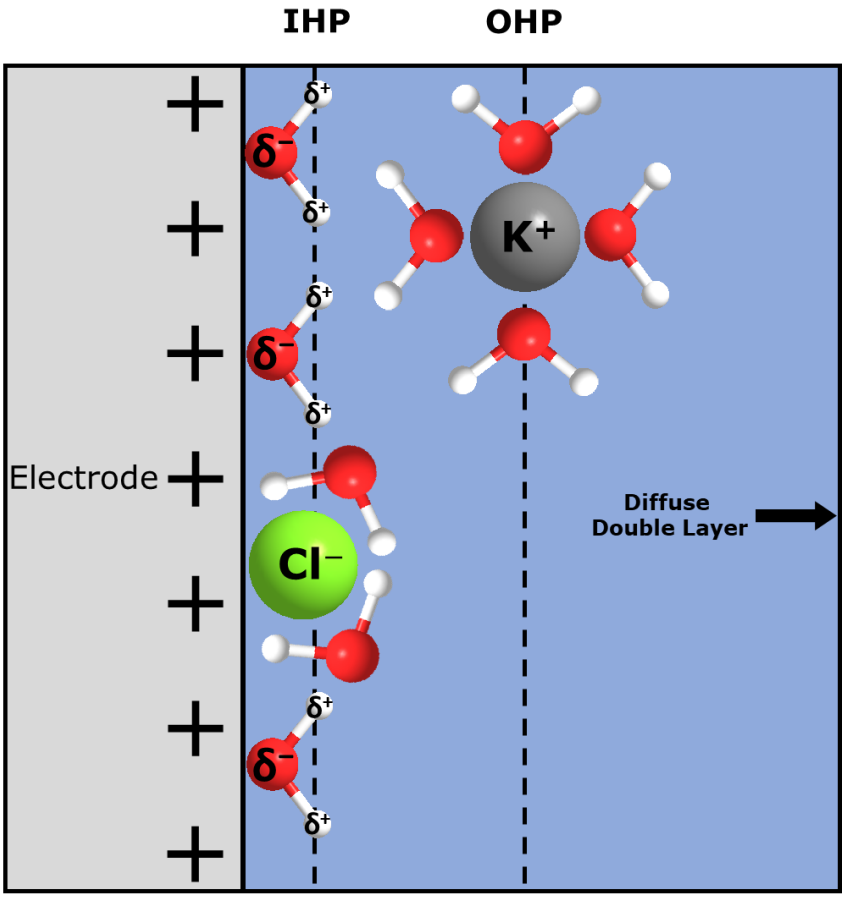


Figure 2.1 Schematic representation of the electrode-electrolyte interface and the electrochemical double layer. The electrolyte is aqueous with KCL supporting electrolyte. Adapted from Hamann *et al.* and Ramaswamy *et al.*[3,5]

It is important to consider the different potentials that can arise at electrode surfaces, and what it is possible to measure experimentally. An electrode potential is established by the difference in the electric potentials (ϕ) of two distinct phases, the metal and solution.

$$^{M}\Delta^{S}\phi = \phi_{M} - \phi_{S} \qquad (1)$$

The electric potential ϕ, of the metal and electrolyte respectively, can be thought of as the work done to move a unit test charge along a fixed axis from an infinite distance through a vacuum to the electrode or electrolyte.[6] However, it is the point to which the test charge is brought that creates an important distinction; either

the charge is brought to the surface of the electrode or electrolyte, or it is brought to a point inside the phase of the electrode or electrolyte. These differences are shown in Figure 2.2 and are termed the Volta potential difference ($\Delta\Psi$), the potential difference between the outer electric potentials of the electrode and electrolyte, and the Galvani potential difference ($\Delta\Phi$), the potential difference between the inner electric potentials of the electrode and electrolyte.

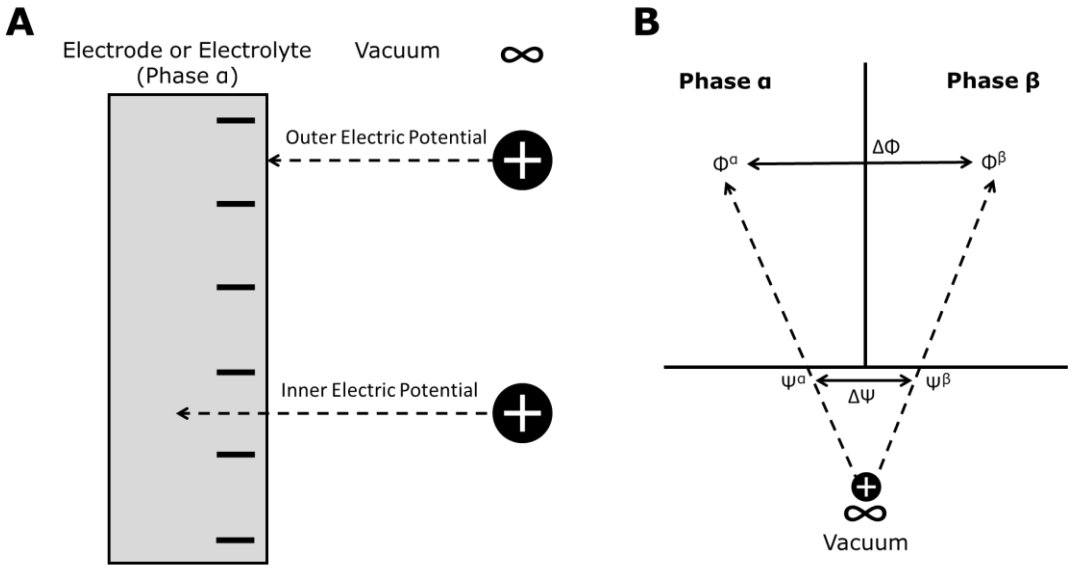


Figure 2.2 (A) Schematic representation of the definition of electric potential in an electrochemical context. (B) Schematic representation of the Volta ($\Delta\Psi$) and Galvani ($\Delta\Phi$) potential differences. Adapted from Scholz.[7]

It is not possible to measure the absolute electric potential or the potential difference between phases at a single interface because an attempt to do so would introduce a further interface and change that being measured.[4] However, it is possible to measure the potential difference between two interfaces but requires the concept of electrochemical potential, $\bar{\mu}$.

For a charged species 'i' in solution, the electrochemical potential is a combination of the chemical potential μ_i of the species in solution (relates to the Gibbs free energy) and the electric potential ϕ_i as discussed (in Volts) multiplied by the Faraday constant (in Coulombs per mole) and the charge (z) on the dissolved species (see Equation 2).

$$\bar{\mu}_i = \mu_i + zF\phi_i \tag{2}$$

The chemical potential of a species in solution is related to a standard chemical potential (μ_i^θ) by Equation 3, where a is the activity of i.

$$\mu_i = \mu_i^\theta + RTlna_i \tag{3}$$

Introducing a metal electrode to an electrolyte containing an ionic species that exists in oxidised and reduced forms, establishes an equilibrium at the electrode. An example of this equilibrium showing the reduction of a general analyte is shown in Equation 4.

$$O + e^-_{Metal} \rightleftharpoons R \tag{4}$$

At equilibrium, the electrochemical potential of the reduced species is equal to the sum of the electrochemical potentials of the oxidised species and the electron in the metal electrode.

$$\bar{\mu}_R = \bar{\mu}_O + \bar{\mu}_{e^-_{Metal/Solution}} \tag{5}$$

$$\bar{\mu}_{e^-_{Metal/Solution}} = \mu_{e^-_{M/S}} - F\phi_{M/S} \tag{6}$$

Incorporating Equations 2, 3 and 6, into 5 yields,

$$\mu_{\mathrm{R}}^{\theta} + RTlna_{\mathrm{R}} + z_{\mathrm{R}}F\phi_S = \mu_{\mathrm{O}}^{\theta} + RTlna_{\mathrm{O}} + z_{\mathrm{O}}F\phi_S + \mu_{e_M^-}^{\theta} + z_{e^-}F\phi_M \qquad (7)$$

An activity term for electrons in a metal is not required because the electron concentration remains effectively constant.[4] However, since,

$$z_{\mathrm{R}} - z_{\mathrm{O}} = -n \qquad (8)$$

where n = number of electrons transferred, Equation 7 can be expressed as,

$$\begin{aligned} z_{e^-}F(\phi_M - \phi_S) = z_{e^-}F\phi_M + z_{\mathrm{O}}F\phi_S - z_{\mathrm{R}}F\phi_S = -nF(\phi_M - \phi_S) \\ = \mu_{\mathrm{R}}^{\theta} - \mu_{\mathrm{O}}^{\theta} + RTlna_{\mathrm{R}} - RTlna_{\mathrm{O}} - \mu_{e_M^-}^{\theta} \end{aligned} \qquad (9)$$

and rearranged to,

$$\phi_M - \phi_S = \frac{\mu_{\mathrm{O}}^{\theta} - \mu_{\mathrm{R}}^{\theta} + \mu_{e_M^-}^{\theta}}{nF} + \frac{RT}{nF} ln \frac{a_{\mathrm{O}}}{a_{\mathrm{R}}} \qquad (10)$$

which because,

$${}^{\mathrm{M}}\Delta^{\mathrm{S}}\phi \equiv \Delta E \qquad (11)$$

can be finally expressed as a recognisable form of the Nernst equation.

$$\Delta E = \Delta E_{\mathrm{O/R}}^{\theta} + \frac{RT}{nF} ln \frac{a_{\mathrm{O}}}{a_{\mathrm{R}}} \qquad (12)$$

More commonly used is the formal potential ($\Delta E^{\theta'}$) which considers the concentration of the ionic species, rather than activity.

$$\Delta E = \Delta E_{\mathrm{O/R}}^{\theta'} + \frac{RT}{nF} ln \frac{[\mathrm{O}]}{[\mathrm{R}]} \qquad (13)$$

As previously stated, it is only possible to measure ΔE between two electrode-electrolyte interfaces, which is solved experimentally by introducing a reference

electrode that has a known potential. This standard reference electrode is called the standard hydrogen electrode (SHE) and relies on the following equilibrium.

$$H^{+}_{(aq)} + e^{-}_{Metal} \rightleftharpoons \tfrac{1}{2}H_{2(g)} \qquad E^{\theta} = 0\ V \tag{14}$$

The SHE itself consists of a platinised Pt electrode, over which H_2 gas is flowed at standard pressure (1 atm), immersed in an HCl aqueous solution with a proton activity of 1.[4] The potential of the SHE is zero volts by convention and so the potential difference of a redox process can be measured between the electrode-electrolyte interface of the SHE and that at another electrode-electrolyte interface. However, because the conditions required to make an SHE are experimentally demanding, alternative reference electrodes that are easier to assemble are commonly used. Some examples of other reference electrodes are Ag/AgCl, saturated calomel, and palladium hydride (Pd-H) reference electrodes. The experimental setup required to measure onset potentials of redox processes is described in the cyclic voltammetry section of this chapter.

As previously mentioned, electrochemists are concerned with processes at electrode-electrolyte interfaces, and these often involve a transfer of electrons either from the metal to the solution or from the solution to the metal. There are two types of electron transfer reactions: inner-sphere and outer-sphere. Inner-sphere reactions involve a strong interaction between the analyte and the electrode with adsorption often occurring in order for electron transfer and rearrangement of the adsorbed molecule to occur.[8] Outer-sphere reactions do not require the analyte to adsorb onto the electrode and electrons quantum tunnel across a layer of solvent in the IHP.[4] A well-studied outer-sphere reaction is the oxidation of the organometallic compound ferrocene to ferrocenium.[9]

Inner-sphere reactions include the oxygen-reduction reaction, which is essential to fuel-cell operation.[5,10] Formic-acid oxidation, which involves both weakly and strongly adsorbed intermediates, is also an inner-sphere reaction.[11,12]

Figure 2.3 depicts electro-oxidation and electro-reduction processes in (A) and (B), respectively. The simplest oxidations involve the transfer of an electron from the highest occupied molecular orbital (HOMO) of a species in solution, to the metal electrode when the electrochemical potential ($\bar{\mu}$) of the electrode is lower than the energy of the HOMO. Conversely, reduction involves the transfer of an electron from the metal electrode to the lowest unoccupied molecular orbital (LUMO) of a species in solution, when the electrochemical potential ($\bar{\mu}$) of the electrode is higher than the energy of the LUMO.

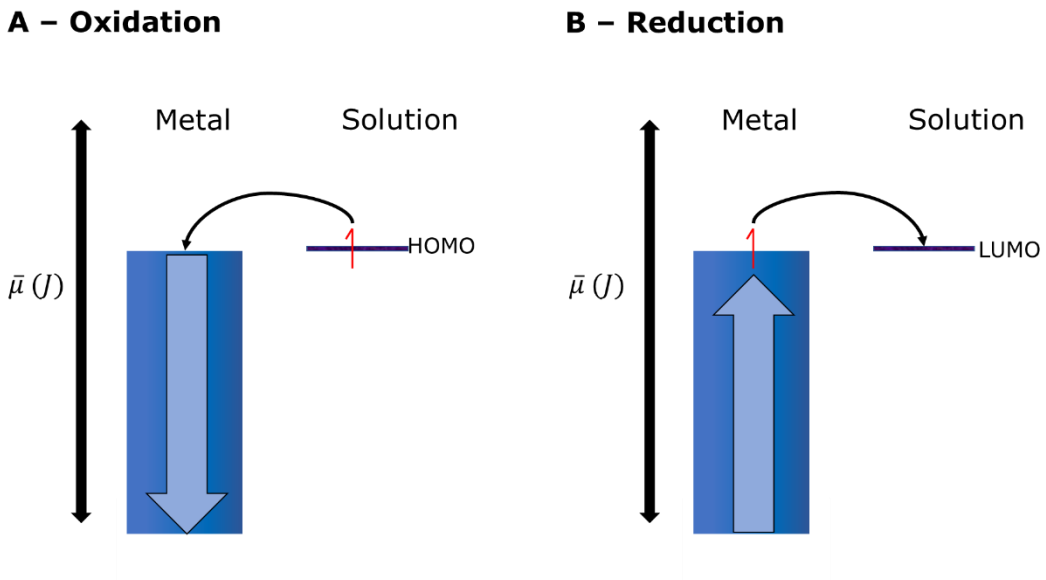


Figure 2.3 (A) Depiction of an electro-oxidation whereby an electron is transferred from a chemical species in solution to the electrode by lowering the electrochemical potential of the electrode. (B) Depiction of an electro-reduction whereby an electron is transferred from the electrode to a chemical species in solution by raising the electrochemical potential of the electrode.

The electrochemical potential of electrons in a given phase is called a Fermi level and represents the average energy available to those electrons.[4] The Fermi level is described by the Fermi-Dirac distribution, shown below.

$$P = \frac{1}{e^{(E-\mu)/k_B T} + 1} \tag{15}$$

P is the population of orbitals at a given energy, E. μ is chemical potential (in Joules) at which energy level P = ½, k_B is the Boltzmann constant, e is the exponential function, T is absolute temperature.[13] The Fermi-Dirac distribution applies a Boltzmann distribution to the Pauli exclusion principle, that no two electrons in a solid can have the same quantum state.

2.1.2 Mass-transport processes

There are three processes by which the analyte moves in solution with respect to the electrode. The first is migration whereby a charged ion in solution will move away from regions of like-charges though electrostatic repulsion or move in response to an electric field. Equation 16 describes the flux of ions in solution (species B) in an electric field where u is the ion mobility, $[B]$ is the concentration of ions in solution, and $\frac{\partial \phi}{\partial x}$ is the infinistessimally small change in electric potential over an infinitesimally small distance.[3,14,15]

$$J_{B,M} = -u[B]\frac{\partial \phi}{\partial x} \tag{16}$$

The flux of ions to an electrode is mitigated in electrochemical experiments by introducing a non-electroactive supporting electrolyte with similar sized anions and cations such as KCl.[15] The supporting electrolyte also serves to ensure the potential drop at the electrode-electrolyte interface is limited to within

10-20 Angstroms of the surface of the electrode, so that the driving force for any electron transfer reaction is maximised over this distance.[16]

The second factor affecting mass transport is diffusion, by which a chemical species in solution will move from a region of high concentration to low concentration. This is especially important in electrochemical reactions as products will diffuse away from the electrode, and reactants to it, across a region next to the electrode called the diffusion layer. The thickness of the diffusion layer depends on the diffusion coefficient of the analyte and, in voltammetric measurements, the rate at which the potential of the working electrode is changed with faster scan rates producing thinner diffusion layers.[4]

Diffusion of a chemical species in solution across a concentration gradient is described by Fick's laws of diffusion; the first law is shown in Equation 17 where J_B is the flux of species B across a concentration gradient (in mols s^{-1} cm^{-2}), D_B is a constant of proportionality called the diffusion coefficient (in cm^2 s^{-1}), and $\frac{\partial c_B}{\partial x}$ is the infinitesimal change in concentration over an infinitesimally small distance at a given time.

$$J_{B,D} = -D_B \frac{\partial c_B}{\partial x} \tag{17}$$

Oxidation or reduction of an electroactive species at an electrode causes the generation of a diffusion layer, and the current, *i*, that flows as a function of time, *t*, when the species is electrolysed at the diffusion-controlled rate, is described by the Cottrell equation (Equation 18),[17] where *F* is Faraday's constant, C_{bulk} is the bulk concentration of the electroactive species. *D* is the diffusion coefficient of the

electroactive species, n is the number of electrons transferred according to the reaction stoichiometry, and t is the time at which current is recorded.

$$i = nFAJ = \frac{nFAD^{\frac{1}{2}}C_{bulk}}{(\pi t)^{\frac{1}{2}}} \quad (18)$$

The third type of analyte movement is convection. Convection naturally occurs due to temperature or density gradients in the electrolyte. However, these variables are easily controlled in electrochemical experiments such that diffusion is the overwhelmingly dominant mode of mass transport to the electrode. Artificially forced convention using hydrodynamic techniques such as rotating the working electrode or ultrasonic vibration (sonoelectrochemistry), control the rate of mass-transport to the electrode and is discussed in greater detail later in this chapter.[4]

2.1.3 Rates of electrochemical reactions

The rate of an electrochemical process depends on two key parameters. The first parameter is the rate constant of electron transfer at the electrode surface (denoted k_{ox} or k_{red} for an oxidation or reduction, respectively), which encompasses a rearrangement of the ionic atmosphere, reorientation of the solvent dipoles, changes in the distance between the central ion and any ligands and finally, electron transfer itself followed by a repeat of the three steps prior to electron transfer to accommodate the newly oxidised or reduced species.[15] The second parameter is the rate constant of diffusion of electroactive species to the electrode surface (denoted k_d). Other factors that affect the rate of an electrochemical reaction are chemical reactions either before or after the electron

transfer, and adsorption/desorption or crystallisation processes on the electrode.[4]

For the simple one-electron transfer reaction below, where the concentration of O and R are equal,

$$O_{(aq)} + ne_M^- \underset{k_{ox}}{\overset{k_{red}}{\rightleftharpoons}} R_{(aq)} \quad (19)$$

the cathodic (reduction) current is given by,

$$i_c = -FAk_{red}[O] \quad (20)$$

and the anodic (oxidation) current is given by,

$$i_a = -FAk_{ox}[R] \quad (21)$$

At equilibrium the net current is zero as the rate of the reduction is equal to the rate of oxidation. The current at equilibrium is called the exchange current, i_0.

In a case where the redox system in Equation 19 is not in equilibrium, by changing the electrode potential of the working electrode, a net current flows and i in Equation 22 is non-zero.

$$i = i_a + i_c \quad (22)$$

The rate constants k_{red} and k_{ox} are dependent on electrode potential and increase or decrease exponentially as electrode potential is changed.[15] This is because the electrode behaves as a catalyst and raises or lowers the free energy of the

transition state, $\Delta G^{\ddagger}$, between oxidised and reduced forms of the electroactive species.[14]

$$\Delta G_{red}^{\ddagger} = \Delta G_{red,o}^{\ddagger} + \alpha_{red} nF(E_{eq} - E^{\theta}') \quad (23)$$

$$\Delta G_{ox}^{\ddagger} = \Delta G_{ox,o}^{\ddagger} - \alpha_{ox} nF(E_{eq} - E^{\theta}') \quad (24)$$

where $\Delta G_{o}^{\ddagger}$ is the free energy change of the transition state when the electrode potential is at the standard electrode potential E^{θ}, $(E_{eq} - E^{\theta}')$ is the overpotential, and α, is the electron transfer coefficient.[14] The electron transfer coefficient (dimensionless) of α_{red} and α_{ox} varies between 0 and 1 and describes how the free energy of the transition state varies with potential, and to what degree the transition state's structure resembles the reactants or products.[15] In metals, α is around 0.5, suggesting that the structure of the transition state equally reflects products and reactants.[15]

By introducing a standard rate constant of electron transfer, k^0, the rate constant of a reduction or oxidation at a given overpotential can be given by,

$$k_{red} = k_{red}^{0} \exp\left(\frac{-\alpha nF\left(E - E^{\theta}'\right)}{RT}\right) \quad (25)$$

for a reduction and,

$$k_{ox} = k_{ox}^{0} \exp\left(\frac{\alpha nF\left(E - E^{\theta}'\right)}{RT}\right) \quad (26)$$

for an oxidation.

Overpotential η_E, is the deviation in electrode potential from the equilibrium potential E_{eq}.

$$\eta_E = E - E_{eq} \tag{27}$$

Combining Equations 25 and 26 with the rate of mass flux to the electrode in Equations 20 and 21, gives the Butler-Volmer equation below, which expresses the current density recorded at an electrode in terms of the mass transport to the electrode and the deviation of the electrode potential from equilibrium conditions (where j is zero).

$$j = j_0 \left(\frac{[\mathrm{R}]_\mathrm{o}}{[\mathrm{R}]_\mathrm{bulk}} \exp\left\{ \frac{(1-\alpha F\eta)}{RT} \right\} - \frac{[\mathrm{O}]_\mathrm{o}}{[\mathrm{O}]_\mathrm{bulk}} \exp\left\{ \frac{-\alpha F\eta}{RT} \right\} \right) \tag{28}$$

The mass transport terms $\frac{[\mathrm{R}]_\mathrm{o}}{[\mathrm{R}]_\mathrm{bulk}}$ and $\frac{[\mathrm{O}]_\mathrm{o}}{[\mathrm{O}]_\mathrm{bulk}}$ can be eliminated by using hydrodynamic techniques, such as mechanical stirring or rotation of the electrode, that ensure a constant flux of analyte to the electrode.[14]

2.1.4 Cyclic voltammetry

The invention of the potentiostat by Archie Hickling in 1942 enabled the development of reliable potential sweep electrochemical techniques such as cyclic voltammetry.[18] In voltammetry, the electrode potential of a 'working electrode' (W.E.) is shifted positive and/or negative with respect to a reference electrode (Ref.) of known, fixed potential. For a current to flow, a third electrode is required and is referred to in this study as a counter-electrode (C.E.). Without the counter-electrode a current flow between the working electrode and reference electrode would change the potential-determining equilibrium of the reference electrode, rendering it unreliable.[16] In this 'three-electrode system', a high resistance is maintained between the working and reference electrodes to prevent any appreciable current flowing between them, causing current to flow between the

counter and working electrodes. It is good practice to place the counter-electrode away from the working and reference electrodes in the electrolyte, or isolate it behind a porous frit, so that the redox products do not interfere with measurements at the working electrode or the potential-determining equilibrium at the reference electrode.[16] However, a compromise on electrode placement is often required as an increase in distance between W.E. and C.E. increases solution resistance.[4]

The potentiostatic control of electrode potentials and the recording of current and electrode potential in a three-electrode cell, is more complex than the simple description provided here. However, a useful and simple schematic is provided in Figure 2.4.[3]

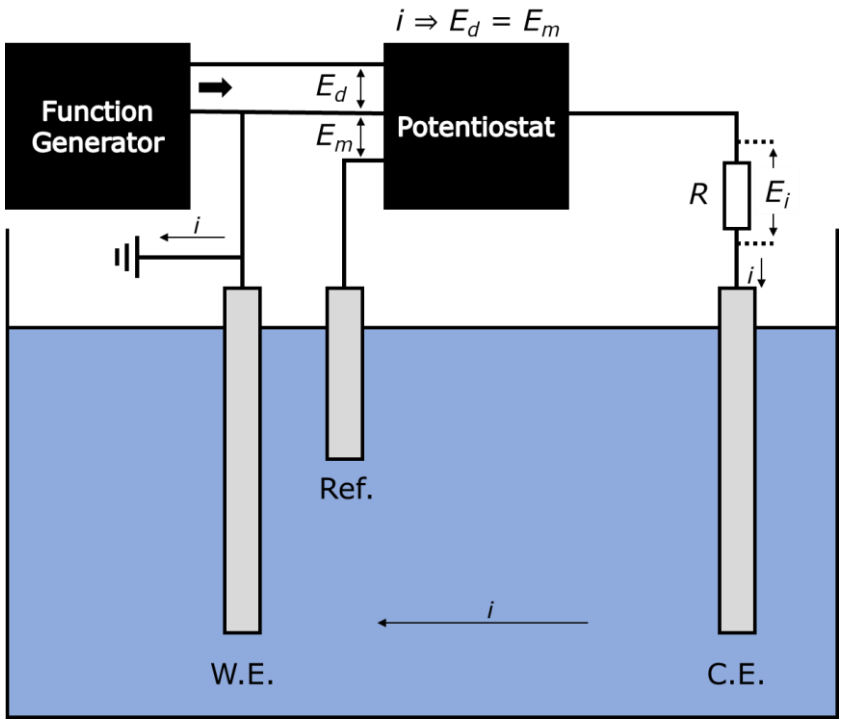


Figure 2.4 Schematic representation of a three-electrode cell with potentiostatic circuit. Components are a working electrode (W.E.), reference electrode (Ref.) and counter-electrode (C.E.), function generator and potentiostat. Adapted from Hamann *et al*.[3]

Here the working electrode is connected to ground and a potential is applied (E_d) between the ground and one of the voltage inputs of the operational amplifier (op-amp) inside the potentiostat. A second voltage input (E_m) is between the second voltage input of the op-amp and the reference electrode. The potentiostat ensures that the potential applied to the working electrode is the same as the potential difference between the W.E. and the Ref. ($E_d = E_m$), while a high-input impedance prevents current flow to the Ref. The output of the op-amp is connected to the C.E. and has a low impedance to allow current to flow between the W.E. and C.E. This current passes through a shunt resistor and the drop in potential (E_i) is measured by a second op-amp, and is compared with the voltage input (E_d) in order to determine current.[3]

An example of a cyclic voltammogram (CV) is found in Figure 2.5 showing the 1-electron oxidation of ferrocene to ferrocenium and the coupled reverse process, the reduction of ferrocenium to ferrocene, in a dry non-aqueous solvent. The potential sweep starts at 0.3 V (versus a reference electrode) in a positive-going direction and a oxidation current is observed positive of 0.4 V (E_{onset}). As the potential of the W.E. becomes more positive, the concentration of ferrocene at the electrode surface decreases as it is oxidised, thus a concentration gradient is established in a diffusion layer, increasing the flux of ferrocene to the electrode surface. The maximum flux of ferrocene to the electrode occurs at E_p^a at which potential the current is maximum (i_p^a); beyond this potential, higher currents cannot be sustained due to depletion of ferrocene in the diffusion layer, causing the current to decrease.[4] The current recorded past E_p^a is therefore limited by mass transport.

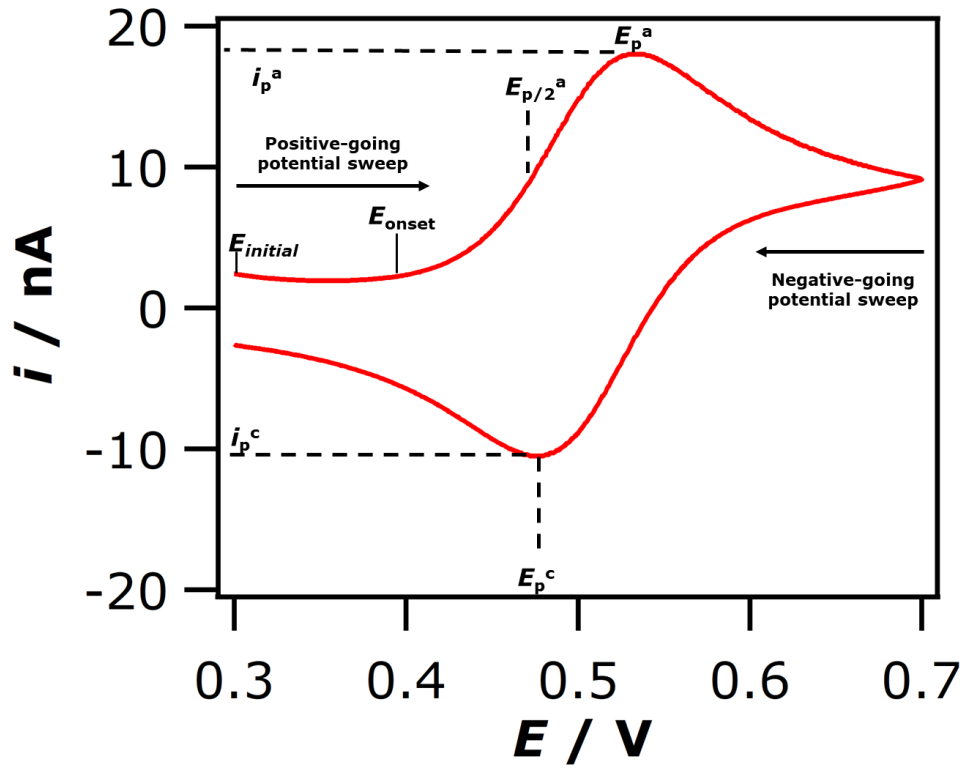


Figure 2.5 Example cyclic voltammogram recorded at a Pt electrode in a dry ionic liquid containing dissolved ferrocene. The potential scan rate was 0.01 mV s^{-1}.

At around 0.7 V, the potential sweep changes direction to be negative-going, and at around 0.6 V a reduction of the oxidation product, ferrocenium, begins. The reduction occurs because ferrocenium is still present at the electrode surface and in the diffusion layer, and has not been removed by forced convection/stirring or given the time to diffuse away from the electrode. A reduction peak (E_p^c) is observed at around 0.48 V, at which potential, the reduction current is at a maximum (i_p^c). The separation in potential between cathodic and anodic peaks, (ΔE_p), is important in determining whether a redox process behaves in a thermodynamically reversible or irreversible way.

A system is chemically reversible if a chemical reaction can take place in both directions i.e. that reaction products can return to the reactant species. An

example of this in an electrochemical context is the oxidation of ferrocene to ferrocenium and the subsequent reduction of ferrocenium to ferrocene, shown by the example CV in Figure 2.5. Thermodynamic reversibility however, is a specific and exacting term, where a change in a system can be reversed by an infinitesimal change in a variable.[13] In electrochemistry the key variable is the driving force for the reaction, potential (E), and so for a perfectly electrochemically reversible system any infinitesimal change in potential must be accompanied by the reaction reaching equilibrium conditions; in other words, the Nernst equation (Equation 12) must be satisfied at all times.[1] In reality, electrochemical systems can never achieve true thermodynamic reversibility because of the non-instantaneous rate of electron transfer however, they can approximate it to a greater or lesser extent depending on the kinetics of electron transfer.

In systems where the standard electron transfer rate constant (k^0) of a redox process is much greater than the rate constant of mass transport to the electrode (k_d), then the reaction is considered reversible and therefore Nernstian, where current is limited only by mass transport to the electrode.[17] When $k^0 << k_d$, the reaction is considered irreversible in which case, as the standard redox potential of a redox process is reached and current starts to flow, the rate of electron transfer is dominant on the reaction rate (and current recorded) until higher overpotentials are reached.[17] Since the ratio of k^0 and k_d (or diffusion coefficient) is a continuum along which all possible electrochemical reactions could sit, ranges of this ratio were proposed by Matsuda and Ayabe to more clearly define reversible and irreversible reactions.[19] To encompass the transition between reversible and irreversible, a third term 'quasi-reversible' was created to describe

redox processes that behave close to a reversible system at slower scan rates.[16] A slower scan rate allows more time for a reaction equilibrium to be established, partially compensating for a slower rate of electron transfer, as potential is changed, and if slow enough, the Nernst equation applies.[4] However, even a 'reversible' redox process can be made 'irreversible' at extremely high scan rates where k_d approaches k^0.[16]

The voltammetry of a reversible redox system produces a ΔE_p of 57 mV at 298 K which remains constant as scan rate changes, and a potential at half peak maximum ($E_{p/2}$) independent of the concentrations of redox species.[16,17] Also, in reversible systems i_p^c is equal to i_p^a. The peak current, i_p, of a reversible system can be expressed as a function of concentration of redox species, scan rate and diffusion coefficient, in the Randles-Ševčík equation.[16,20]

$$i_p^{rev.} = 0.446\, nFAC_{bulk}\left(\frac{nF\nu D}{RT}\right)^{1/2} \qquad (29)$$

i_p increases with scan rate because, as shown in Equations 17 and 18, current is proportional to the flux of electroactive species to the electrode and a faster potential sweep results in a thinner diffusion layer, creating a steeper concentration gradient and increasing flux of electroactive species to the electrode.[14]

In irreversible or 'slow electron transfer' redox processes, ΔE_p deviates from 57 mV and is dependent on scan rate, and $E_{p/2}$ is dependent on the rate constant of mass transport to the electrode (k_d).[17] In simple 1-electron irreversible redox processes, E_p decreases by 60 mV per decade of the log of scan rate. For

irreversible redox processes, the relationship between i_p and scan rate and diffusion coefficient is as follows:[16]

$$i_p^{irr.} = 0.496\sqrt{\alpha}\, nFAC_{bulk}\left(\frac{nF\nu D}{RT}\right)^{1/2} \quad (30)$$

In practice, and especially when using non-aqueous solvents, a significant resistance between the W.E. and C.E. can exist (R_s), caused by a lack of charge-carrying ions, or ions without sufficient mobility to compensate for the charge transfers occurring at the electrode-solution interfaces. Since there will always be some distance between the Ref. and W.E., a fraction of R_s will remain, called the uncompensated resistance (R_u), which will affect the measured potential.[1] The *iR* drop between W.E. and reference electrode is minimised by using a 3-electrode system, so current flows though the C.E., and by placing the reference close to the W.E.[14] R_u, if not reduced by adding supporting electrolyte such as KCl for aqueous systems or tetrabutylammonium hexafluorophosphate for non-aqueous ones, can be compensated for electronically by the potentiostat using 'positive feedback [*iR*] compensation'.[4] Most of the voltammetry presented in the experimental chapters of this thesis are *iR* corrected.

2.1.5 Rotating-disk electrode voltammetry

Rotating-disk electrode voltammetry involves rotating a working electrode at a fixed angular velocity (ω) in s^{-1}, often given in revolutions per minute (rpm), in order to control mass transport of the analyte to the electrode surface while the electrode is polarised. Angular velocity is given by Equation 31 where *f* is frequency.

$$\omega = 2\pi f \tag{31}$$

A schematic of a rotating-disk electrode (RDE) and electrolyte flow profile of electrolyte over an RDE is shown in Figure 2.6 (A) and (B) respectively. Not shown is the modulated speed rotator which controls the rotation rate of the electrode. The insulating shrouds around the electrodes are typically polytetrafluoroethylene (PTFE), or polyether ether ketone (PEEK) for use at elevated temperatures.[21]

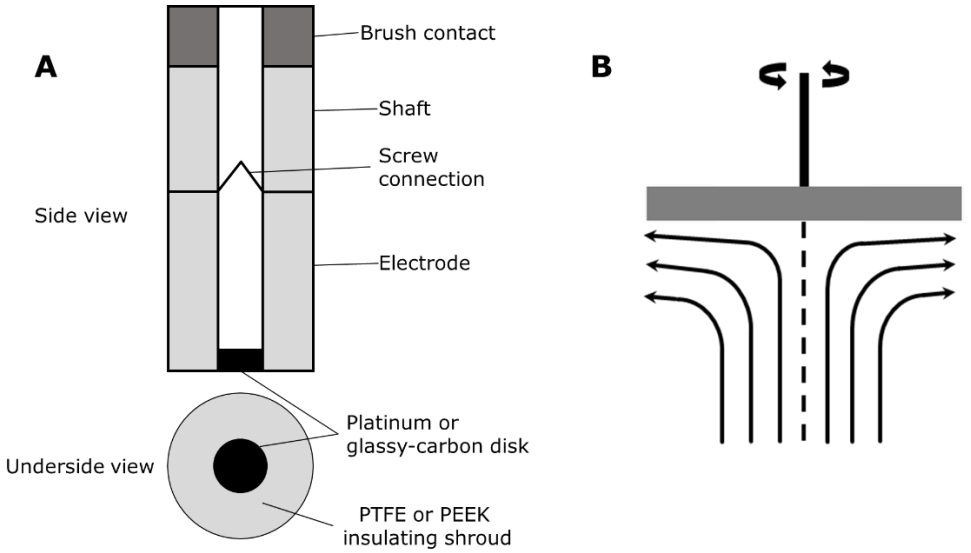


Figure 2.6 (A) Schematic of a rotating-disk electrode showing a side view and underside view. (B) Schematic of electrolyte flow over the surface of a rotating electrode. Adapted from Bard *et al*.[4]

The current recorded at a rotating electrode, from the reduction or oxidation of an analyte species in the bulk electrolyte, is constant because unreacted analyte is being hydrodynamically forced to the electrode surface which then reacts instantaneously. Exceptions where a constant current is not observed at a rotating electrode are common in cases where the reacting species adsorbs to the electrode, passivating the surface, and inhibiting further electrochemical reactions. The concentration of the analyte at an electrode surface when a

constant current is achieved, is zero, meaning that the steady-state current recorded is overwhelmingly caused by the forced convection of the rotating electrode rather than diffusion. The mass transport to the electrode, and the steady-state current recorded, is therefore proportional to the rotation rate of the electrode. The relationship between mass-transport limited steady-state current and rotation rate is formalised in the Levich equation, shown in Equation 32 normalised for electrode surface area where j_{L} is the Levich current density, D_{m} is the diffusion coefficient of species m, ν is the kinematic viscosity of the electrolyte, and C_m is the concentration of species m in the bulk electrolyte.

$$j_L = 0.62nFD_{\mathrm{m}}^{\frac{2}{3}}\omega^{\frac{1}{2}}\nu^{-\frac{1}{6}}C_{\mathrm{m}} \tag{32}$$

As discussed in section 2.1.1, the current recorded at a W.E. depends on the rate constant of mass transport to the electrode (k_d) and the rate constant of electron transfer at the electrode (k^0). If a redox process is reversible, the current recorded is linearly proportional the square root of rotation rate. However, any deviation from this linearity as rotation rate increases, causing k_d to approach k^0, means that a kinetic limitation on i has been reached. The separation of the kinetic current (i_{k}), the current that would be recorded if mass transport was so efficient that the concentration of the electroactive species at the electrode was maintained equal to the bulk concentration, and the mass transport limited current achieved where $k_d << k_0$ (i_{L}), is expressed in the Koutecký-Levich equation shown below normalised for electrode area.

$$j^{-1} = j_L^{-1} + j_K^{-1} \tag{33}$$

By plotting j^{-1}, the recorded current density, against $1/\sqrt{\omega}$, a straight line is obtained where any non-zero y-intercept is due to sluggish electron transfer (see E_1 and E_2 in Figure 2.7).

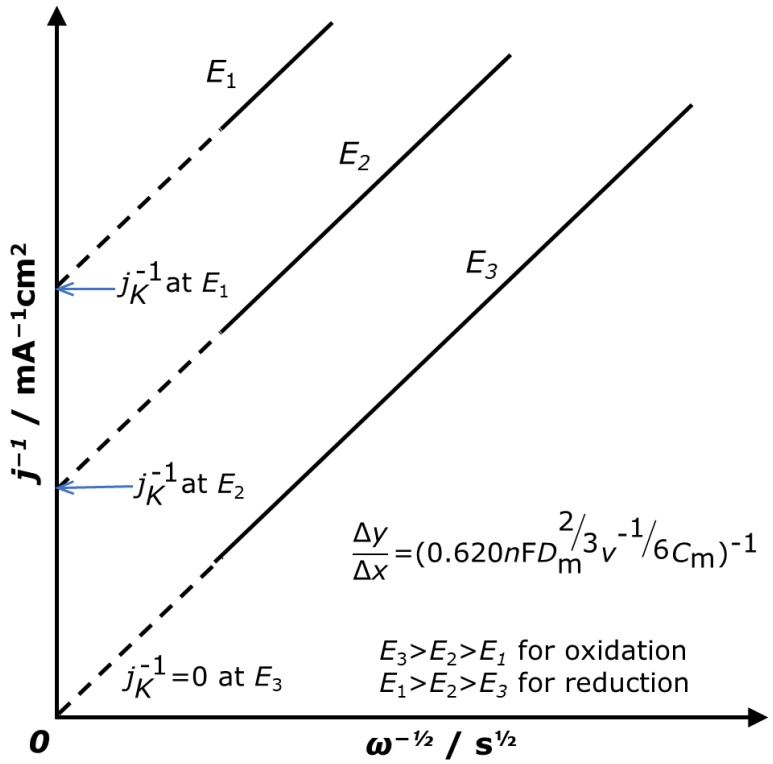


Figure 2.7 Koutechý-Levich plot of a general, hypothetical system at three different potentials. Adapted from Bard *et al.*[4]

The gradient of a Koutecký-Levich plot is given by the bracketed terms in Equation 34, which shows the Koutecký-Levich equation expressed in the form of a straight line equation, $y = mx + c$.

$$j^{-1} = (0.620nFD_m^{\frac{2}{3}}\nu^{-\frac{1}{6}}C_m)^{-1}\omega^{-\frac{1}{2}} + j_K^{-1} \qquad (34)$$

From the gradient of the Koutecký-Levich plot, useful electrochemical parameters can be obtained such as n, D, or C.

Another hydrodynamic technique to determine *n* is rotating-ring-disk electrode (RRDE) voltammetry. An RRDE has both a central disk electrode, like that in Figure 2.6 (A), but also has a ring electrode (typically Pt) outside the central disk over which the product of any reduction or oxidation at the disk, flows over due to the forced convection of the rotating electrode. By holding the ring at a fixed potential and sweeping the potential of the disk using a bipotentiostat, reaction products at the disk can be reduced or oxidised at the ring, and the currents at each electrode can be recorded simultaneously. The currents at the disk and ring are denoted i_d and i_r, respectively. The equation for calculating the stoichiometric electron transfer number from RRDE experiments for the oxygen-reduction reaction is given in Equation 35, where *n* is between 2 and 4 and N_C is the collection efficiency of the RRDE.[22]

$$n = 4 \times \frac{i_d}{i_d + \frac{i_r}{N_C}} \tag{35}$$

N_C of an RRDE is a measure of the proportion of electroactive species made at the disk that arrives at the ring and is dependent on the geometry of the RRDE (ring radius and spacing between disk and ring etc.). N_C is often provided by the manufacturer and/or supplier of the RRDE however, N_C can be determined experimentally by the ratio $-i_r:i_d$.[4]

2.1.6 Electrochemical impedance spectroscopy

Alternating current electrochemical impedance spectroscopy (ACEIS) is a technique used to investigate the properties of the phases, and interfaces between phases, in an electrochemical cell.[14] To probe these properties, a sinusoidally oscillating potential of specified (but small) amplitude is applied to the system over a wide frequency spectrum most commonly in the mHz to kHz range.[1] Equation 36 describes how potential varies with angular frequency over time,

$$E(t) = E_m \sin(\omega t) \tag{36}$$

where E_m is the maximum amplitude of E, and where angular frequency is given by Equation 31 (see previous section).

The sinusoidally oscillating current that flows in response to the oscillating potential is out of phase (θ) with the applied potential, to a greater or lesser extent, over the range of frequencies used and gives rise to the impedance of the system, (Z) (see Equation 42).

$$Z_f = \frac{E(t)}{i(t)} \tag{37}$$

Figure 2.8 shows the phase separation between an applied alternating potential and corresponding alternating current.

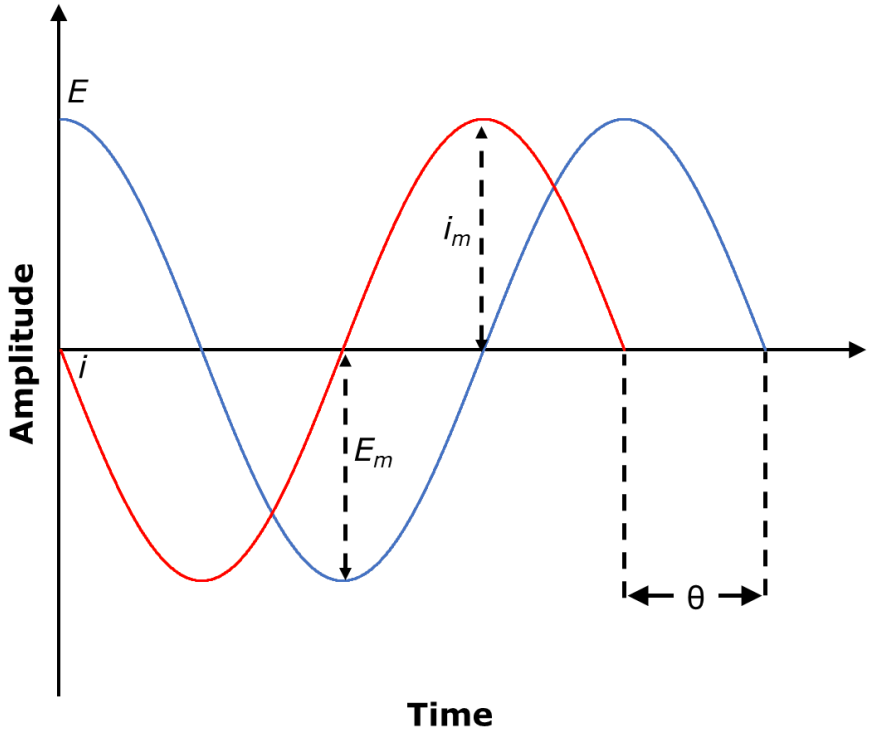


Figure 2.8 Sinusoidal potential oscillation and the corresponding current with phase difference, θ, at a single frequency. Potential and current amplitudes are denoted E_m and i_m, respectively. Adapted from Fisher.[14]

The current is related to potential where potential is oscillating through a frequency-dependent impedance (Z_f) which, recorded across a range of frequencies, is complex and consists of a real component (Z_{Re}) and an imaginary component (Z_{Im}), where,

$$Z_f = Z_{\mathrm{Re}} - j_i Z_{\mathrm{Im}} \tag{38}$$

and,

$$j_i = \sqrt{-1} \tag{39}$$

making Z_f a vector quantity dependent on frequency (or, more correctly, angular frequency (see Equation 31)).[4]

Across the electrochemical cell there exist many sources of resistance that contribute to the impedance measurement such as charge transfer resistance for a faradic electron transfer, R_{ct}, and the solution resistance of the electrolyte, R_{Ω}. There is also the impedance associated with the charging current of the electrochemical double-layer which has an associated capacitance (C_d) (see section 2.1.1), and of diffusional effects on charge transfer called the Warburg impedance (Z_W).[3,4] These resistances, along with the double-layer capacitance, can be considered as components in an electrical circuit which behave as analogues to the various interfaces, phases, and processes in the cell.[23]

By plotting Z_{Re} against $-Z_{\mathrm{Im}}$, a Nyquist plot (Figure 2.9) is obtained, where the different resistances present in the electrochemical system can be found by the x-intercepts, Z_{Re}, of the hemisphere produced over the frequency range. The Nyquist plot in Figure 2.9 represents a hypothetical dataset of an electrochemical system where the impedance is dominated by R_{ct}, so the capacitive effects implied by Z_W at low frequencies are negligible. A Randles equivalent circuit of the Nyquist plot is also included in Figure 2.9, showing R_{Ω}, in series with C_d and R_{ct}, in parallel.

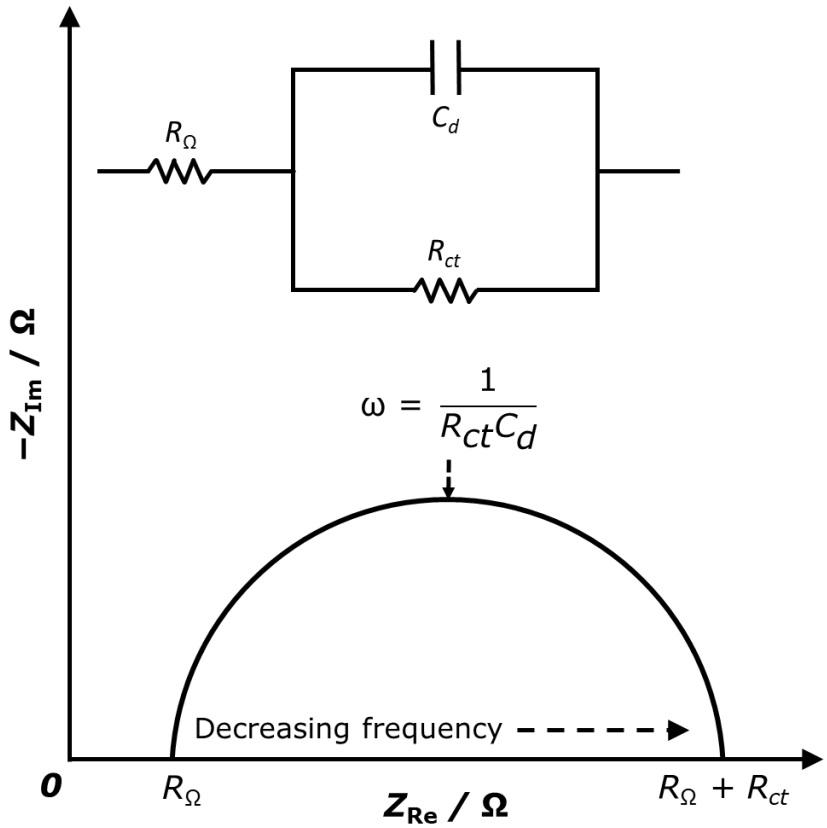


Figure 2.9 Nyquist plot with accompanying 'Randles' equivalent circuit for a system with negligible Warburg impedance (R_{ct} is dominant). Adapted from Bard[4] and Hamann.[3]

R_Ω, can be found at the high frequency x-intercept of a Nyquist plot. Measuring R_Ω is important to determining the ionic conductivity, σ, of an electrolyte.

Ionic conductivity is a measure of the ease that an ion, in a unit area, moves through a unit length (measured in S cm^{-1}, where S ≡ Ω^{-1}) in response to an electric field or local electrostatic attraction/repulsion, and is an intrinsic property of solid and liquid electrolytes. Conductivity is the inverse of resistivity, ρ, (measured in Ω cm).[24]

$$\sigma = \frac{1}{\rho} \tag{40}$$

Resistivity, an intrinsic property, relates to resistance through the introduction of area (A) and length (l) terms.

$$\rho = \frac{R \times A}{l} \tag{41}$$

The ionic conductivity of an electrolyte is therefore given by Equation 42 as defined by the relationship in Equation 40.[3]

$$\sigma = \frac{l}{R_\Omega \times A} \tag{42}$$

To calculate the ionic conductivity, R_Ω must be measured, and l and A determined. As shown above R_Ω can be measured using ACEIS however, determining l and A varies in ease depending on whether the ionically-conducting electrolyte is solid or liquid. For solid electrolytes the area term can be measured as the area of the electrode in contact with the electrolyte, and the length term is the distance through the electrolyte between the two electrodes. However, for liquid electrolytes, l and A are not easily accessible and cannot be measured independently. An alternative approach is required where l and A can be combined into a constant,[3] K_{cell} such that

$$\sigma = \frac{K_{cell}}{R_\Omega} \tag{43}$$

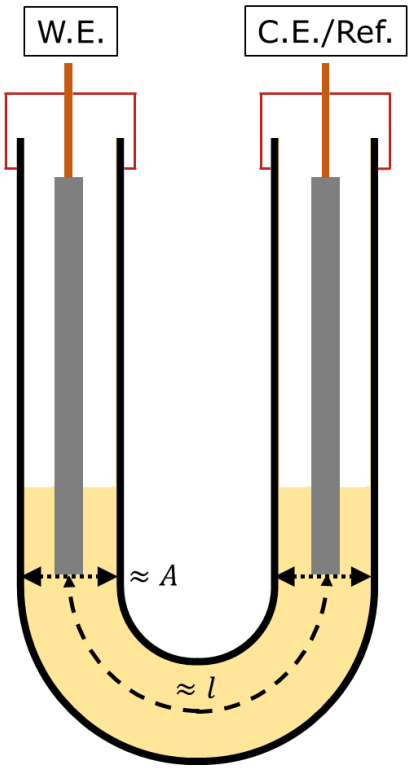


Figure 2.10 Diagram of experimental apparatus to measure the ionic conductivity of a liquid.

Figure 2.10 shows a diagram of the experimental setup used to measure K_{cell} and σ. By filling the U-shaped glassware with a volume of standard KCl solution of known conductivity (σ_{std}) – for example, 0.117 mol dm^{-3} KCl with a conductivity of 15 mS cm^{-1} at 25 °C – the solution resistance of the of the standard solution can be measured by ACEIS and K_{cell} calculated by Equation 44.

$$K_{cell} = \sigma_{std} \times R_{\Omega} \tag{44}$$

Once K_{cell} is known, a volume, equal to that of the conductivity standard, of the electrolyte under investigation is pipetted into the same (washed and dried) U-shaped glassware, ensuring that the electrodes remain in the same position. R_{Ω} is then measured by ACEIS and the ionic conductivity of the electrolyte calculated using Equation 43.

2.1.7 Fuel-cell polarisation curves

The performance of hydrogen fuel cells is most commonly assessed by recording a polarisation curve whereby the current density (j) of a cell is increased from zero at a fixed rate and the cell potential (E_{cell}) is recorded.[10,25] Figure 2.11 shows a hypothetical fuel-cell polarisation curve and the effect on E_{cell} of the various kinetic and mass transport limitations as j increases.

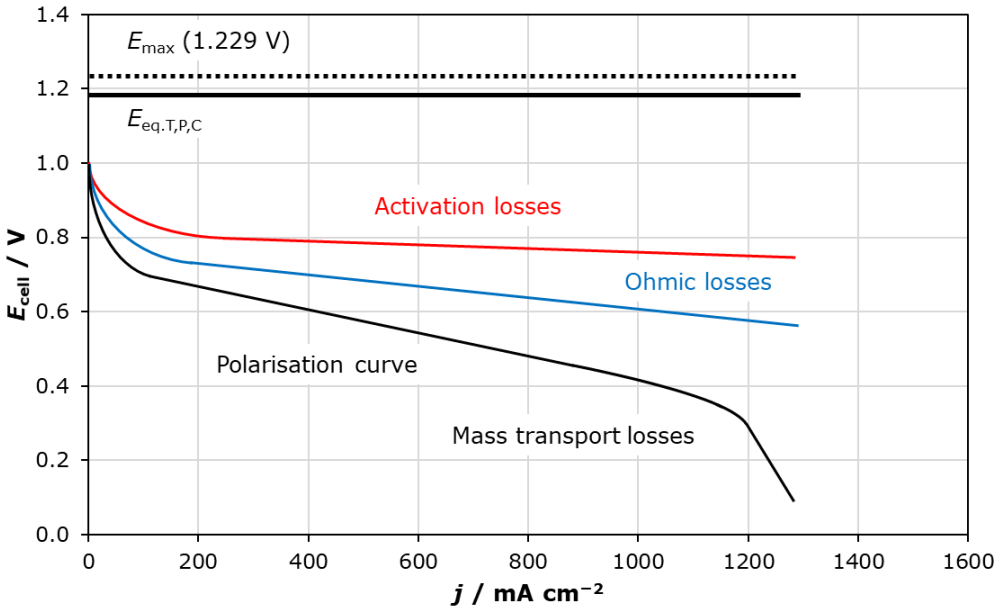


Figure 2.11 Hypothetical H_2/O_2 fuel-cell polarisation curve showing the lossless, theoretical maximum cell potential (E_{max}), the equilibrium potential ($E_{eq.}$) at the temperature, pressure and reactant concentrations used in the hypothetical system, the individual contribution of the activation and ohmic losses on potential (E_{cell}) as current density (j) is increased, and the hypothetic fuel-cell polarisation curve as influenced by the different potential losses. Adapted from Barbir.[10]

The shape of the fuel-cell polarisation curve provides much information about how the fuel cell performs and is typically divided into three successive regions as j increases and E_{cell} decreases. The first is the 'activation' or kinetic loss region whereby small a increase in j is accompanied by a significant loss in E_{cell} and is caused by the kinetic limitations of the oxygen-reduction reaction (and hydrogen-oxidation reaction to a much lesser extent) requiring a large overpotential (η), typically around 300 mV, to sustain a particular rate of electron transfer (or

current density), even at Pt-based catalyst materials.[10,26] Increasing the operating temperature of fuel cells decreases this overpotential by increasing the rate of electron transfer.[26] The second polarisation curve region is the 'ohmic region' wherein the E_{cell} decreases linearly with increasing j because of Ohm's Law, and is caused by resistance to the movement of ions in the electrolyte, charge (electron) transfer resistance and resistance across any of the cell interfaces.[25] Like Ohm's law (Equation 45), the product of the combined resistances of the cell (R_{cell}) and the cell current (i_{cell}) gives rise to the ohmic losses (E_{ohmic}) in the overall E_{cell}.[25,27]

$$V = IR \quad \equiv \quad E_{\text{ohmic}} = i_{\text{cell}} \times R_{\text{cell}} \tag{45}$$

The linearity of the ohmic region is lost at higher current densities because reactants cannot get to the electrode surface fast enough to maintain the current density, resulting in a rapid loss in E_{cell}. This final region is known as the mass-transport limited region and the resulting losses in E_{cell} are known as mass-transport losses. In H_2/O_2 fuel-cell systems it is typically the slower diffusion of oxygen to the cathode that is responsible for the onset of mass-transport limited E_{cell}.[25]

Fuel-cell polarisation curves can be recorded in systems where H_2 and O_2 are supplied to the HOR (anode) and ORR (cathode) electrode respectively, which are separated by a membrane through which ions can move. Polarisation curves to investigate electrolyte or catalyst materials can therefore be recorded with a simplified cell setup without the need for a complete fuel-cell device. Such a cell or 'Grove-type cell' has been used to study the ORR and HOR, and record fuel-cell polarisation curves in PILs.[28] The exact details of the experimental apparatus and conditions used to record fuel cell polarisation curves can be found in Chapter 7.

2.2 References

1. Bard, A. J.; Inzelt, G.; Scholz, F. *Electrochemical Dictionary*; Springer-Verlag: Berlin, 2008.

2. Sparnaay, M. J. The Electrical Double Layer. In *The International Encyclopedia of Physical Chemistry and Chemical Physics*, First ed.; Everett, D. H., Ed.; Pergamon Press: Glasgow, 1972; Vol. 4, pp 1-415.

3. Hamann, C. H.; Hamnett, A.; Vielstich, W., *Electrochemistry*. Second ed.; Wiley-Vch Verlag GmbH & Co.: 2007.

4. Bard, A. J.; Faulkner, L. R. *Electrochemical Methods: Fundamentals and Applications*. Second ed.; John Wiley & Sons, Inc.: 2001.

5. Ramaswamy, N.; Mukerjee, S. Influence of Inner- and Outer-Sphere Electron Transfer Mechanisms during Electrocatalysis of Oxygen Reduction in Alkaline Media. *J. Phys. Chem. C* **2011,** *115* (36), 18015-18026.

6. Bockris, J. O. M.; Reddy, A. K.; Gamboa-Aldeco, M. *Modern Electrochemistry - Volume 2A: Fundamentals of Electrodics*. Second ed.; Kluwer Academic Publishers: 2002; Vol. 2A.

7. Scholz, F. Thermodynamics of Electrochemical Reactions. In *Electroanalytical Methods Guide to Experiments and Applications*, Second ed.; 2010; pp 11-31.

8. Taube, H.; Myers, H.; Rich, R. L., Observations on the Mechanism of Electron Transfer in Solution. *J. Am. Chem. Soc.* **1953,** *75* (16), 4118-4119.

9. Cuharuc, A. S.; Zhang, G.; Unwin, P. R. Electrochemistry of ferrocene derivatives on highly oriented pyrolytic graphite (HOPG): quantification and impacts of surface adsorption. *Phys. Chem. Chem. Phys.* **2016,** *18* (6), 4966-4977.

10. Barbir, F. *PEM Fuel Cells Theory and Practice*. Second ed.; Elsevier: United States of America, 2013.

11. Bard, A. J. Inner-Sphere Heterogeneous Electrode Reactions. Electrocatalysis and Photocatalysis: The Challenge. *J. Am. Chem. Soc.* **2010,** *132*, 7559–7567.

12. Joo, J.; Uchida, T.; Cuesta, A.; Koper, M. T.; Osawa, M. Importance of acid-base equilibrium in electrocatalytic oxidation of formic acid on platinum. *J. Am. Chem. Soc.* **2013,** *135* (27), 9991-9994.

13. Atkins, P. W.; De Paula, J. *Atkins' Physical Chemistry*. Ninth ed.; Oxford University Press: 2010.

14. Fisher, A. C. *Electrode Dynamics*. Oxford University Press: 1996.

15. Brett, C. M. A.; Brett, A. M. O. *Electrochemistry Principles, Methods, & Applications*. First ed.; Oxford University Press: 1992.

16. Compton, R. G.; Banks, C. E. *Understanding Voltammetry*. Second ed.; Imperial College Press: 2011.

17. Brett, C. M. A.; Brett, A. M. O. *Electroanalysis*. Oxford University Press: 1998.

18. Hickling, A. Studies in electrode polarisation. Part IV.—The automatic control of the potential of a working electrode. *Trans. Faraday Soc.* **1942,** *38* (0), 27-33.

19. Matsuda, H.; Ayabe, Y. Zur Theorie der Randles-Sevčikschen Kathodenstrahl-Polarographie. *Z. Elektrochem.* **1955,** *59* (6), 494-503.

20. Ševčík, A. Oscillographic polarography with periodical triangular voltage. *Collect. Czech. Chem. Commun.* **1948,** *13*, 349–377.

21. PINE Research Instrumentation Product Page. https://pineresearch.com/shop/product-category/electrodes/rde/ (accessed Sep 27, 2019).

22. Zhou, R.; Zheng, Y.; Jaroniec, M.; Qiao, S.-Z. Determination of the Electron Transfer Number for the Oxygen Reduction Reaction: From Theory to Experiment. *ACS Catal.* **2016,** *6* (7), 4720-4728.

23. Randles, J. E. B. Kinetics of Rapid Electrode Reactions. *Discuss. Faraday Soc.* **1947,** *1*, 11-19.

24. Compton, R. G.; Sanders, H. W., *Electrode Potentials*. Oxford University Press: 1996.

25. Peighambardoust, S. J.; Rowshanzamir, S.; Amjadi, M. Review of the proton exchange membranes for fuel cell applications. *Int. J. Hydrogen Energy* **2010,** *35* (17), 9349-9384.

26. Tse, E. C.; Gewirth, A. A. Effect of temperature and pressure on the kinetics of the oxygen reduction reaction. *J. Phys. Chem. A* **2015,** *119* (8), 1246-1255.

27. Woan, G., *The Cambridge Handbook of Physics Formulas*. Cambridge University Press: 2003.

28. Noda, A.; Susan, M. A. B. H.; Kudo, K.; Mitsushima, S.; Hayamizu, K.; Watanabe, M. Brønsted Acid-Base Ionic Liquids as Proton-Conducting Nonaqueous Electrolytes. *J. Phys. Chem. B* **2003,** *107*, 4024-4033.

3 Synthesis and Characterisation of Ionic Liquids

3.1 Introduction

Protic ionic liquids (PILs) are synthesised most commonly by the addition of a Brønsted acid to a Brønsted base in a neutralisation reaction.[1] Occasionally an ion exchange reaction with a metal salt of the anion is used, where the conjugate acid of the anion is expensive or difficult to obtain e.g. hydrogen bis(trifluoromethanesulfonyl)imide $HNTf_2$.[2] To synthesise a high-ionicity PIL (where the reaction equilibrium is entirely in favour of the ionic species), it was found that a difference in the acid dissociation constant (pK_a) between the acid and conjugate acid of the base (ΔpK_a) needs to be greater than 10.[2,3] Figure 3.1 shows the neutralisation reaction of diethylmethylamine (dema) and trifluoromethanesulfonic acid (TfOH) to make [dema][TfO].

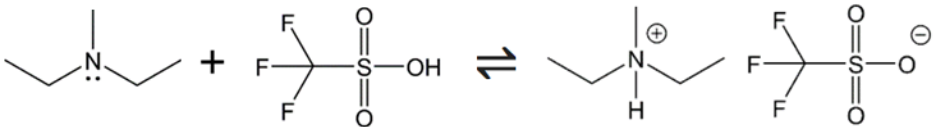


Figure 3.1 Synthesis of diethylmethylamine trifluoromethanesulfonate ([dema][TfO]).

Despite the simplicity of the PIL synthesis reaction, the reaction conditions and purification steps vary greatly in published literature. Some syntheses use an equimolar ratio of acid and base,[2,4,5,6,7] where others use a slight molar excess of amine to be evaporated off in the drying process.[8,9,10] While most syntheses involve the addition of concentrated acid to concentrated base,[2,4,5,6,8,9,11] some syntheses use either aqueous solvents[7,10] or ethanol[12] to better control the heat of the reaction. In all cases, the highly exothermic addition of acid to base requires

cooling in an ice bath or dry ice/acetone bath to prevent evaporation or thermal decomposition of the amine.[5,9,13] There are instances of PIL synthesis taking place inside gloveboxes to prevent amine oxidation.[4]

Drying regimes vary greatly with high to moderate heating under a strong vacuum. The table below shows a number of different drying regimes for [dema][TfO]. It has been shown that drying [dema][TfO] above 60 °C causes discolouration, likely due to thermal decomposition of the base.[14]

Table 3.1 – Protic ionic liquid drying regimes from the literature.

Temperature	Vacuum	Duration	Reference
150 °C	Yes	12 hours	Watanabe (2007)[4]
80 °C	Vacuum oven with P_2O_5	48 hours	Angell (2007)[7]
80 °C	Yes	24 hours	Watanabe (2010)[5]
100 °C	Yes	24 hours	Mori (2012)[11]
180 °C	Yes	12 hours	Gu (2012)[12]
80 °C	Yes	48 hours	Watanabe (2013)[8]
70 °C	Yes	48 hours	Goodwin (2017)[10]
40 °C	Yes	1 week	Smith (2019)[14]

This chapter provides a detailed description of the synthesis of the protic ionic liquids (PILs) used throughout this thesis as well as provide characterisation data for all the ionic liquids (ILs) reported in this thesis. Also provided is an electrochemical assessment of conductivity in PILs containing different concentrations of water and acid.

3.2 Experimental Section

Diethylmethylamine (98%), dimethylbutylamine (99%), triethylamine (99.5%), trifluoromethanesulfonic acid (99%) and trifluoroacetic acid (99%), were purchased from Sigma Aldrich or Fischer Scientific and used as received. PILs were prepared by the dropwise addition of 0.1 mol dm^{-3} aqueous acid to 0.1 mol dm^{-3} aqueous base with a 5% molar excess of the base. The reaction mixture was cooled in an ice bath. Excess water was removed using rotary evaporation. The product was then either, held under vacuum at 70 °C for 48 h at 5×10^{-2} mbar, or held under vacuum at 40 °C for 1 week at 5×10^{-2} mbar, to remove residual water and base. The liquid was then transferred under vacuum to a glovebox containing a dry N_2 atmosphere (<0.1 ppm O_2 and <0.4 ppm H_2O). PILs were characterized by ^{1}H, ^{13}C and ^{19}F nuclear magnetic resonance (NMR) spectroscopy (Bruker Ascend™ 400 MHz NMR Spectrometer) using a hexadeuterodimethyl sulfoxide solvent. NMR spectra of ILs are presented in Appendix I. Attenuated total reflection Fourier-transform infrared spectroscopy was carried out using a Bruker Alpha Platinum-ATR FTIR spectrometer at 30 °C. Thermogravimetric analysis (TGA) and differential scanning calorimetry (DSC) was carried out using a TA Instruments Discovery instrument under a N_2 atmosphere, and residual water contents were determined using Karl-Fischer titrations (Mitsubishi CA-200 Moisturemeter). The kinematic viscosity of the liquid was measured at 40 °C using an SVM 3000 Stabinger Viscometer from Anton Paar. Residual water contents after synthesis and drying were below 100 ppm. diethylmethylammonium bis(trifluoromethanesulfonyl)imide, [dema][NTf_2], was synthesised using a metathesis reaction described in reference.[15] Aprotic ionic liquids were used and characterised as received.

The ionic conductivity of the PILs was measured by a 2-probe alternating-current electrochemical impedance spectroscopy (ACEIS) method using a U-shaped glass cell and two silver electrodes. A standard 0.117 mol dm^{-3} KCl solution (Alfa Aesar) of 15 mS cm^{-1} at 25 °C was used to obtain a cell constant (see Chapter 2 for more detail). The ionic conductivities of [dema][TfO], [dmba][TfO] and [tea][TfAc] were obtained using an ACEIS method at 40 °C. Variable temperature conductivity measurements were recorded by submersing the U-shaped cell in a silicone oil bath on a hot plate. PIL water contents before and after conductivity measurements were obtained by Karl Fischer titration.

3.3 Results and Discussion

3.3.1 Nuclear magnetic resonance spectroscopy

^{1}H, ^{13}C and ^{19}F NMR spectra of [dema][TfO], [dema][NTf_2], [dmba][TfO], [tea][TfAc], [pyrr][NTf_2], [N8888][NTf_2] and [P8888][NTf_2] are presented in Appendix I. The peaks, peak assignments and splitting patterns are consistent with those in the literature.

3.3.2 Fourier-transform infra-red spectroscopy

The FTIR-ATR absorbance spectrum of [dema][TfO] is shown in Figure 3.2 (A) and shows the characteristic N-H stretches at ≈3050 and 2700 cm^{-1}, C-F stretches (≈1200 and 1250 cm^{-1}), C-N stretch (≈1000 cm^{-1}) and O-S-O bending (≈650 cm^{-1}).[6] O-H stretching (≈3500 cm^{-1}) and bending (≈1630 cm^{-1}) are also observed in the ILs with absorbance increasing with increasing H_2O concentrations.[16] FTIR-ATR spectra of the other PILs used in this thesis are presented in Figure 3.2 (B), (C) and (D), and show the expected peaks.[17,18,19,20,21]

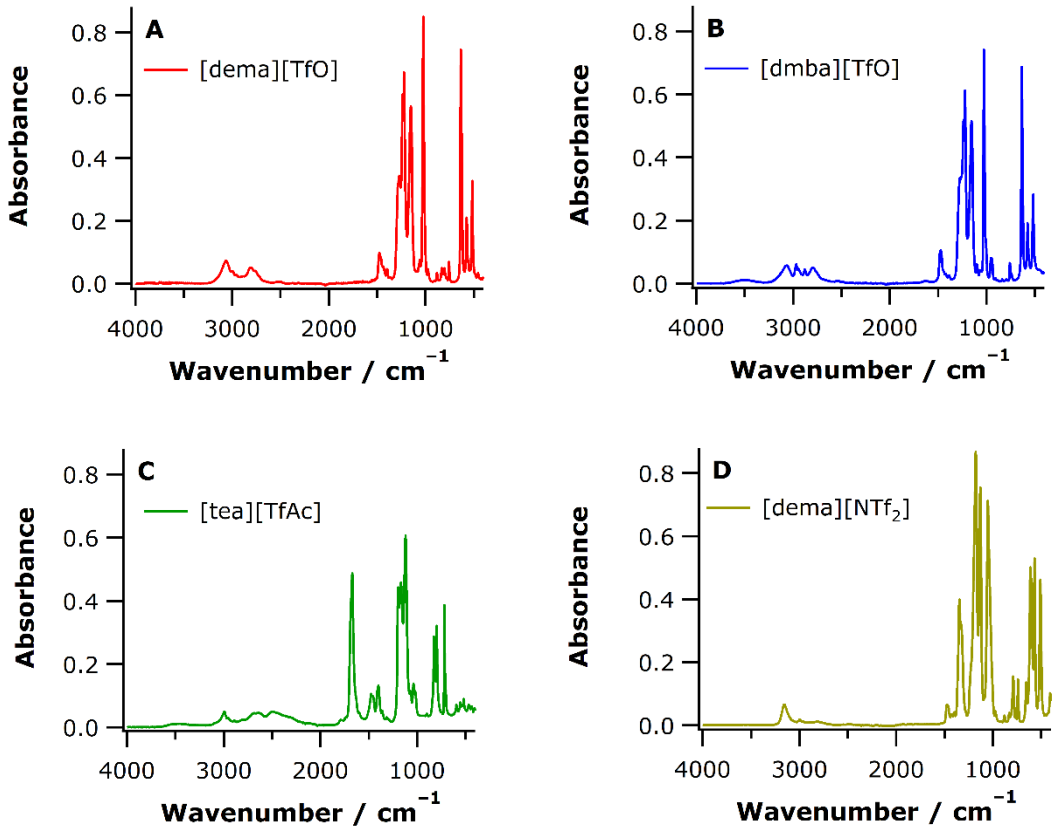


Figure 3.2 FTIR-ATR absorbance spectra of protic ionic liquids. (A) [dema][TfO] (≈11.7 ppm H_2O), (B) [dmba][TfO] (≈9351.3 ppm H_2O), (C) [tea][TfAc] (≈1896.2 ppm H_2O), and (D) [dema][NTf_2] (≈187.1 ppm H_2O), recorded at 30 °C. Water contents provided are those of the ILs in a glovebox; in reality, the water contents will be higher than those presented as the FTIR-ATR instrument is outside a glovebox.

The FTIR-ATR absorbance spectrum of AILs used in this thesis are shown in Figure 3.3 and show the characteristic peaks expected.[19,22,23]

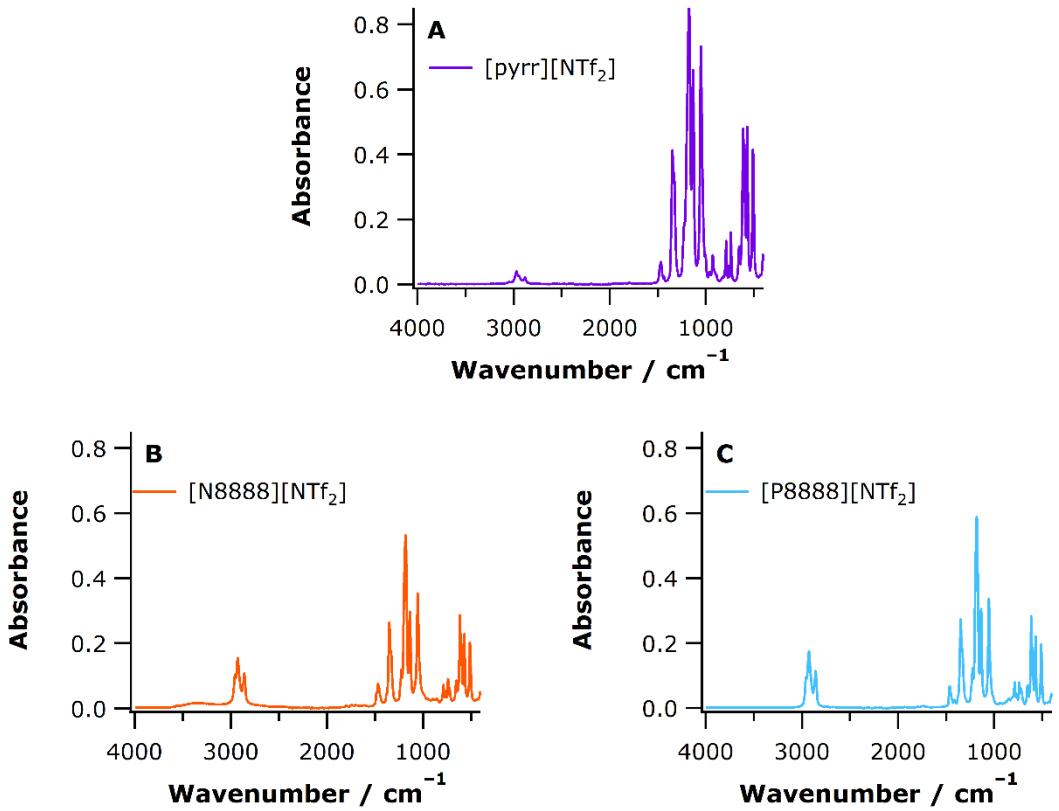


Figure 3.3 FTIR-ATR absorbance spectrum of aprotic ionic liquids. (A) [pyrr][NTf$_2$] (≈146.3 ppm H_2O), (B) [N8888][NTf$_2$], and (C) [P8888][NTf$_2$], recorded at 30 °C.

Figure 3.4 compares the FTIR-ATR spectra of [dema][TfO] and acidified [dema][TfO], and demonstrates that there is no spectroscopic difference (apart from an increase in water content) upon acidification of the IL.

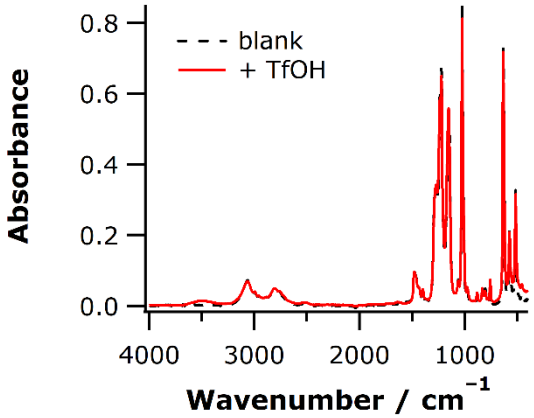


Figure 3.4 FTIR-ATR absorbance spectrum of [dema][TfO] (≈11.7 ppm H_2O) and [dema][TfO] containing 0.1 mol dm^{-1} triflic acid (≈8699.3 ppm H_2O recorded at 30 °C.

3.3.3 Thermogravimetric analysis

Thermogravimetric curves of PILs are presented in Figure 3.5. [dema][NTf_2] and [dmba][TfO] are the most thermally stable, with decomposition temperatures around 330 °C. [tea][TfAc] is the least thermally stable with a significant mass loss at around 190 °C; this is consistent with the literature boiling point of [tea][TfAc] of 190°C.[24,25] [dema][TfO] behaves as reported in the literature and thermally decomposes at around 300 °C, with complete mass loss by 400 °C.[5]

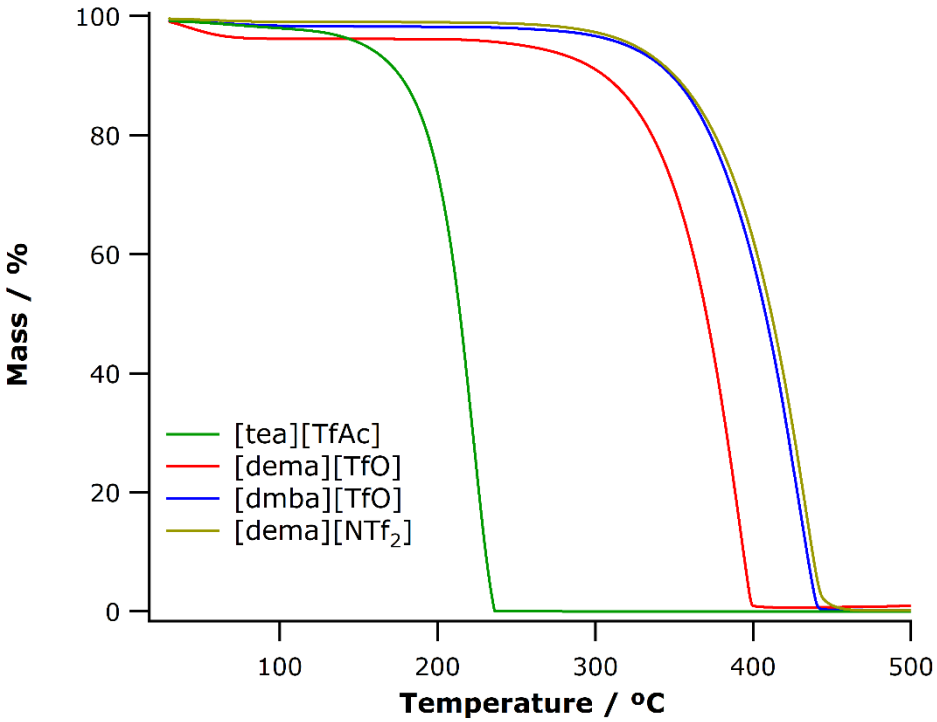


Figure 3.5 TGA curves of protic ionic liquids use in this thesis recorded in a nitrogen atmosphere a 5 °C min^{-1} heating rate.

Thermogravimetric curves of AILs are presented in Figure 3.6. [pyrr][NTf_2] is the most thermally stable, with a decomposition temperature of around 390 °C. [P8888][NTf_2] was found to have a slightly higher decomposition temperature than its ammonium analogue (around 360 °C), which has been previously demonstrated in comparisons of the physical properties of phosphonium and ammonium-based ILs.[26]

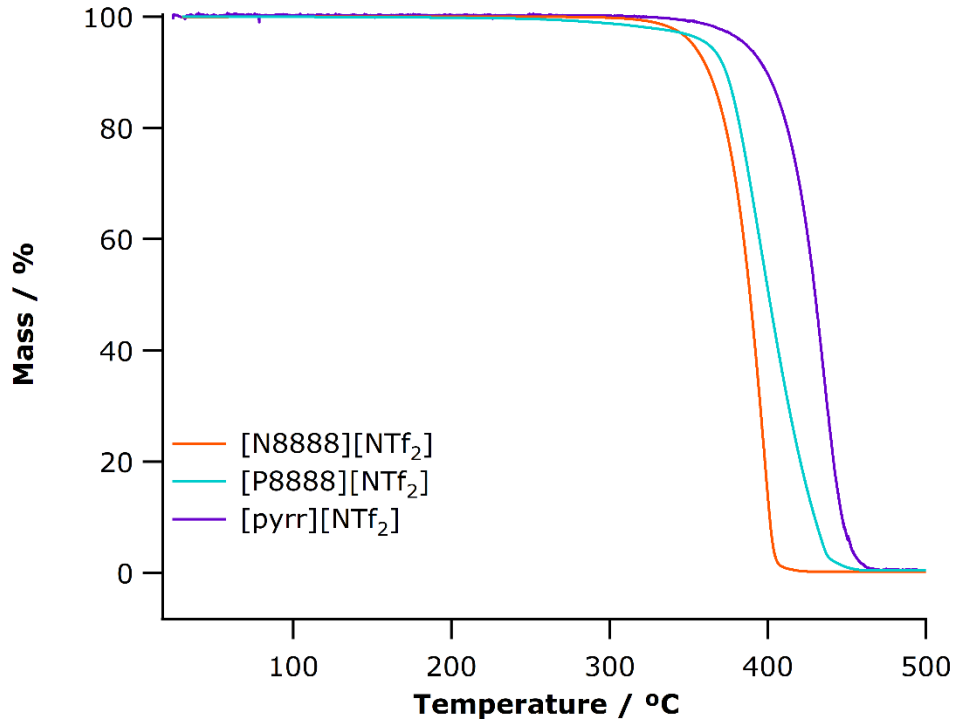


Figure 3.6 TGA curves of aprotic ionic liquids use in this thesis recorded in a nitrogen atmosphere a 5 °C min^{-1} heating rate.

3.3.4 Differential scanning calorimetry

DSC traces of PILs are shown in Figure 3.7. The cold crystallisation temperature (T_c) of [dema][TfO], [dmba][TfO] and [tea][TfAc] were found to be similar and around −24 °C. The T_c of [dema][NTf_2] was found to be higher than in [dema][TfO], at 3 °C, and is a consequence of the larger [NTf_2]$^-$ anion. The melting points of all PILs are close to those reported in the literature.[4,25,27] A glass transition was observed in [dema][NTf_2] at around −30 °C. However, this is higher than the value of −67 °C previously reported.[4] An unknown endothermic peak in [dema][NTf_2], labelled $T_?$, is possibly the melting point of water in the ionic liquid.

Table 3.2 Physiochemical properties of ionic liquids; crystallisation temperature (T_c), melting point (T_m), and thermal decomposition temperature (T_d). *At 5% mass loss (after water mass loss).

Ionic liquid	T_c (°C)	T_m (°C)	T_{other} (°C)	T_d* (°C)
[dema][TfO]	−23	−5	N/A	298
[dmba][TfO]	−24	9	N/A	334
[TEA][TfAc]	−24	16	N/A	166
[dema][NTf_2]	3	25	T_g = −30 $T_?$ = −9	332
[pyrr][NTf_2]	−50	−18	T_{ss} = −28	386
[N8888][NTf_2]	−47	31	T_{ss} = −1	353
[P8888][NTf_2]	N/A	N/A	N/A	362

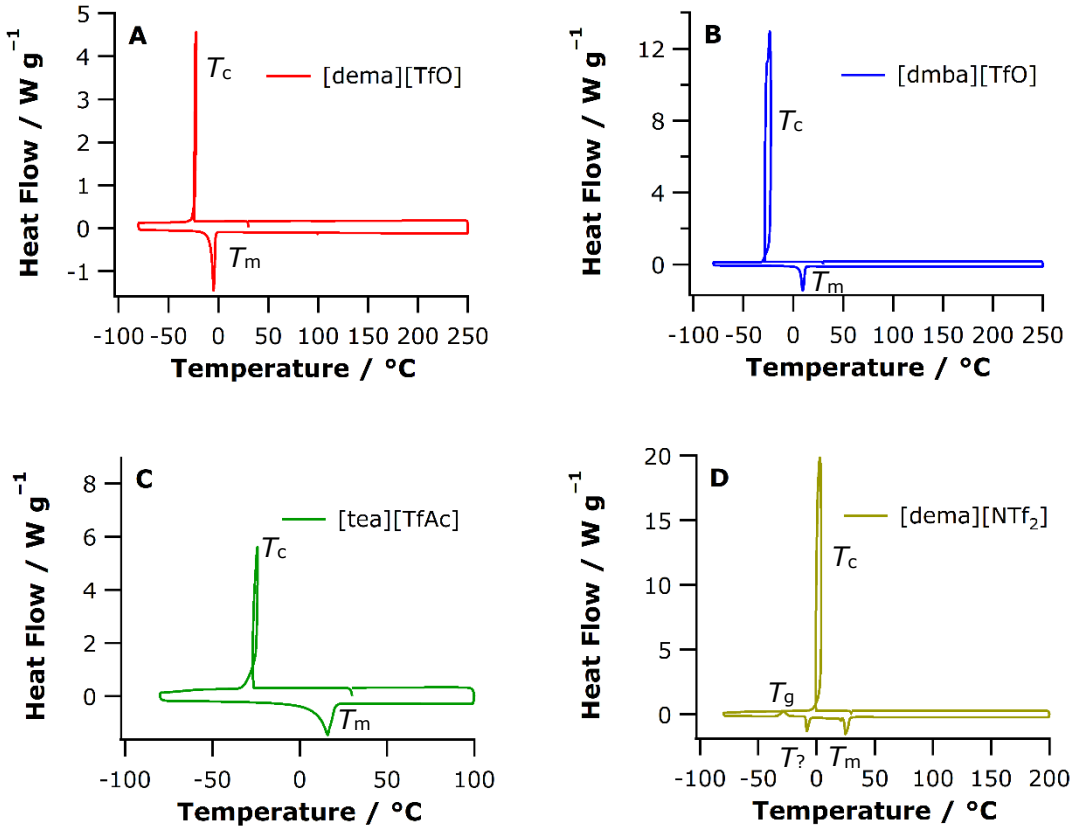


Figure 3.7 DSC traces of protic ionic liquids (exothermic heat flow upward). (A) [dema][TfO] (11.7 ppm H_2O), (B) [dmba][TfO] (9351.3 ppm H_2O), (C) [tea][TfAc] (1896.2 ppm H_2O), and (D) [dema][NTf_2] (187.1 ppm H_2O), recorded at a 5 °C min^{-1} heating/cooling rate. Samples prepared and hermetically sealed in a nitrogen-atmosphere glovebox.

DSC traces of AILs are presented in Figure 3.8. The T_c, solid-solid crystal transition (T_{ss}) and T_m of [pyrr][NTf_2] at −50, −28, and −18 °C are close to those reported in the literature (−60, −29, and −21 °C).[28] A T_g at −88 °C was not observed. The DSC trace of [N8888][NTf_2] in Figure 3.8 (B) provides a T_c, T_{ss} and T_m of −47, −1 and 31 °C, respectively. The DSC trace of [P8888][NTf_2] appears somewhat anomalous as no exothermic or endothermic peaks are observed (see Figure 3.8 C). [P8888][NTf_2] has a glass transition at 184.7 K (-88.45 °C), and crystallisation at 284.3 K (11.15 °C).[29]

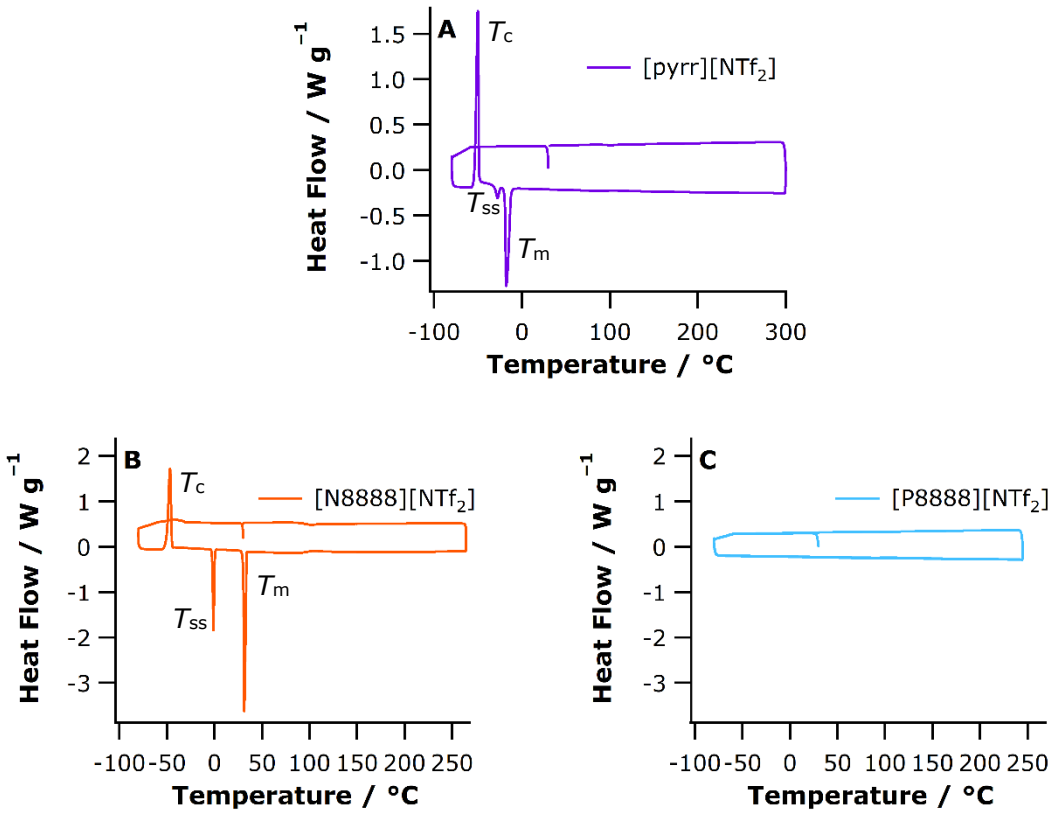


Figure 3.8 DSC traces of aprotic ionic liquids (exothermic heat flow upward). (A) [pyrr][NTf_2] (146.3 ppm H_2O), (B) [N8888][NTf_2], and (C) [P8888][NTf_2], recorded at 5 °C min^{-1}. Samples prepared and hermetically sealed in a nitrogen-atmosphere glovebox.

3.3.5 Ionic conductivity

Work by Goodwin *et al*. established that the method of PIL synthesis used can lead to PILs with up to 0.23 mol dm^{-3} of excess neutral acid.[10] Methods where concentrated acid is added to concentrated base produced PILs with excess acid due to evaporation/thermal decomposition of the base. To test the effect of the presence of acid on PIL ionic conductivity, stoichiometric PILs were synthesised by slow addition of 1 mol dm^{-3} aqueous acid to 1 mol dm^{-3} aqueous base, and the ionic conductivity, viscosity and water content measured. The ionic conductivities of PILs containing 0.25 and 0.50 mol dm^{-3} of the parent acids of the respective PILs, were then measured. As a further comparison, water was added to the PILs to determine the extent of the effect of water on ionic conductivity and viscosity. The data presented as a Walden plot in Figure 3.9 suggests that the presence of acid has a limited effect on the ionic conductivity and viscosity of [dema][TfO] and [dmba][TfO] compared with the effect of the presence of water. The 'scatter' in data points 1–3 and 6–8 as acid is added indicates a negligible effect of the added neutral acid on conductivity and viscosity. The significant increase in ionic conductivity decrease in viscosity upon addition of increasing amounts of water to [dema][TfO] and [dmba][TfO] in data points 4–5 and 9–10, respectively, confirms water content, rather than acid content, as having the greater effect on the ionic conductivity of PILs. Ionic conductivity was calculated by dividing conductivity by the concentration of the IL; concentration of the IL was calculated by diving the density of the IL by its relative molecular mass. Only the molar concentration of the IL anions and cations were considered in calculating molar conductivity.

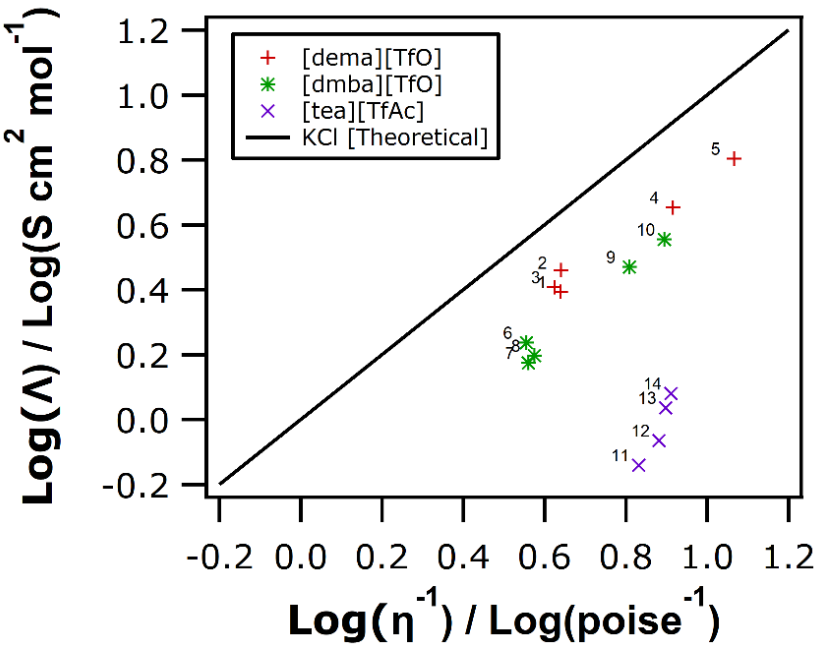


Figure 3.9 Walden Plot of [dema][TfO], [dema][TfO] and [tea][TfAc] in Dry, Acidified and Wet-Acidified Forms. Data points 1, 6 and 11 are pure PILs. Points 2, 3, 7, 8, 12, 13 and 14 contain added acid only. Points 4, 5, 9 and 10 and contain added acid and water. Numbered data points are described in more detail in Table 3.3.

Table 3.3 Water and acid contents of numbered data points presented in Figure 3.9.

Data Point	Chemical Identity	Water content (mol dm^{-3})	
		Λ	η
1	[dema][TfO]	0.013	0.010
2	[dema][TfO] + 0.25 M TfOH	1.054	1.022
3	[dema][TfO] + 0.50 M TfOH	1.053	1.017
4	[dema][TfO] + 0.50 M TfOH + H_2O	5.063	5.004
5	[dema][TfO] + 0.50 M TfOH + 2× H_2O	7.876	7.822
6	[dmba][TfO]	0.093	0.098
7	[dmba][TfO] + 0.25 M TfOH	0.165	0.171
8	[dmba][TfO] + 0.50 M TfOH	0.702	0.670
9	[dmba][TfO] + 0.50 M TfOH + H_2O	3.502	3.477
10	[dmba][TfO] + 0.50 M TfOH + 2× H_2O	4.593	4.621
11	[tea][TfAc]	0.035	0.031
12	[tea][TfAc] + 0.25 M HTfAc	0.099	0.064
13	[tea][TfAc] + 0.50 M HTfAc	0.641	0.586
14	[tea][TfAc] + 0.50 M HTfAc (lower H_2O)	0.126	0.099

The [tea][TfAc] data points (11–14) suggest a greater effect of acid on ionic conductivity, however, the water content also increased notably upon acid addition so firm conclusions cannot be made. In all cases, the shift upward and to the right on the Walden plot upon addition of water (see Table 3.3), follows a broadly straight line parallel with the ideal, fully dissociated, dilute KCl electrolyte line, suggesting that a change in conduction mechanism is not observed and that the increase in conductivity is a result of the presence of water decreasing viscosity.[3,30]

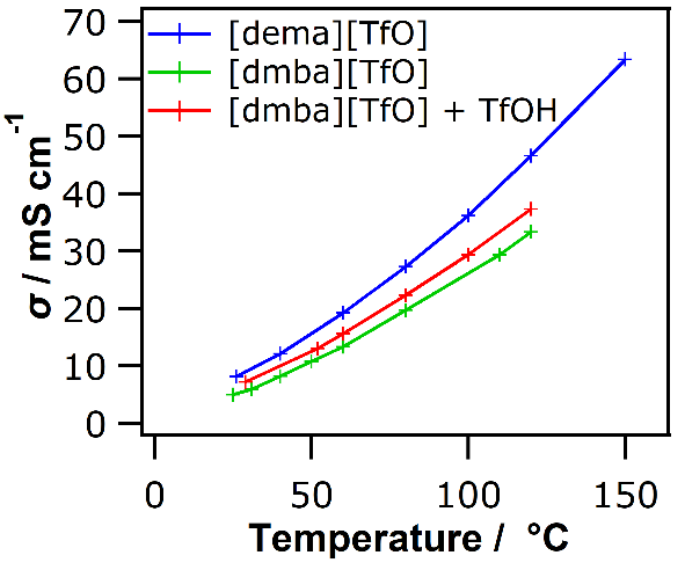


Figure 3.10 Plot of ionic conductivity against temperature of wet [dema][TfO], [dmba][TfO] (56 ppm H_2O) and [dmba][TfO] + 0.04 mol dm^{-3} TfOH

The effect of temperature on the ionic conductivity of [dema][TfO] and [dmba][TfO] is presented in Figure 3.10 and clearly shows the broadly linear increase in ionic conductivity with temperature and is close to the ionic conductivity of PILs reported in the literature.[4,5] The presence of acid in [dmba][TfO] appears to slightly increase the ionic conductivity over the temperature range 25–120 °C by about 2 mS cm^{-1}. However, this effect could also be due to an increased water content in the acidified PIL.

3.4 Conclusions

ILs were successfully synthesized and characterised, or characterised as received, by NMR spectroscopy, FTIR-ATR spectroscopy, TGA and DSC. The effect of the presence of acid and water on the ionic conductivity of PILs has also been determined, with the later having a greater effect in increasing ionic conductivity upon increased concentration. The synthesis method of PILs can produce non-stoichiometric ILs with an excess of parent acid being present. To avoid a non-stoichiometric PIL, the recommended synthesis method is the slow addition of 1 mol dm^{-3} aqueous base to 1 mol dm^{-3} aqueous acid with a slight molar excess of base, chilled in an ice bath, followed by drying at moderate temperatures (40 °C) under vacuum for a week. The effect of the presence of acid on electrocatalytic reactions will be explored in subsequent chapters.

3.5 References

1. Anderson, J. L.; Anthony, J. L.; Antonietti, M.; Brennecke, J. F.; Carmichael, A. J.; Carper, W. R.; Chiappe, C.; Cocalia, V. A.; James H. Davis, J.; Popolo, M. G. D.; Dolle, A.; Dreyer, S.; Earle, M.; Eckstein, M.; Abedin, S. Z. E.; Endres, F.; Favre, F.; Fehrmann, R.; Gordon, C. M.; Haddleton, D. M.; Hardacre, C.; Hilgers, C.; Holbrey, J. D.; Hunt, P. A.; Kirschning, A.; Klembt, S.; Kragl, U.; Leuchter, A.; Lynden-Bell, R. M.; Maase, M.; Maginn, E. J.; Mantz, R. A.; Muldoon, M. J.; Olivier-Bourbigou, H.; Palmer, G.; Richter, J.; Riisager, A.; Rogers, R. D.; Schulz, P.; Singh, V.; Smarsly, B.; Trulove, P. C.; Vaultier, M.; Visser, A. E.; Wagner, M.; Wahlbeck, P. G.; Wasserscheid, P.; Welton, T.; Wilkes, J. S.; Zhou, Y. *Ionic Liquids in Synthesis*. 2nd Edition; WILEY-VCH Verlag GmbH & Co. KGaA: 2008; Vol. 1.

2. Miran, M. S.; Kinoshita, H.; Yasuda, T.; Susan, M. A.; Watanabe, M. Physicochemical properties determined by ΔpK_a for protic ionic liquids based on an organic super-strong base with various Brønsted acids. *Phys. Chem. Chem. Phys.* **2012,** *14* (15), 5178-86.

3. Yoshizawa, M.; Xu, W.; Angell, C. A. Ionic Liquids by Proton Transfer: Vapor Pressure, Conductivity, and the Relevance of ΔpK_a from Aqueous Solutions. *J. Am. Chem. Soc.* **2003,** *125*, 15411-15419.

4. Nakamoto, H.; Watanabe, M. Brønsted acid-base ionic liquids for fuel cell electrolytes. *Chem. Commun. (Cambridge, UK)* **2007,** (24), 2539-2541.

5. Lee, S. Y.; Ogawa, A.; Kanno, M.; Nakamoto, H.; Yasuda, T.; Watanabe, M. Nonhumidified Intermediate Temperature Fuel Cells Using Protic Ionic Liquids. *J. Am. Chem. Soc.* **2010,** *132* (28), 9764-9773.

6. Mori, K.; Hashimoto, S.; Yuzuri, T.; Sakakibara, K. Structural and Spectroscopic Characteristics of a Proton-Conductive Ionic Liquid Diethylmethylammonium Trifluoromethanesulfonate [dema][TfOH]. *Bull. Chem. Soc. Jpn.* **2010,** *83* (4), 328-334.

7. Belieres, J.-P.; Angell, C. A. Protic Ionic Liquids: Preparation, Characterization, and Proton Free Energy Level Representation. *J. Phys. Chem. B* **2007,** *111*, 4926-4937.

8. Miran, M. S.; Yasuda, T.; Susan, M. A. B. H.; Dokko, K.; Watanabe, M. Electrochemical properties of protic ionic liquids: correlation between open circuit potential for H_2/O_2 cells under non-humidified conditions and ΔpK_a. *RSC Adv.* **2013,** *3* (13), 4141-4144.

9. Thomson, J.; Dunn, P.; Holmes, L.; Belieres, J.-P.; Angell, C. A.; Gervasio, D. A Fluorinated Ionic Liquid as a High-Performance Fuel Cell Electrolyte. *ECS Trans.* **2008,** *13* (28), 21-29.

10. Goodwin, S. E.; Smith, D. E.; Gibson, J. S.; Jones, R. G.; Walsh, D. A. Electroanalysis of Neutral Precursors in Protic Ionic Liquids and Synthesis of High-Ionicity Ionic Liquids. *Langmuir* **2017,** *33* (34), 8436−8446.

11. Mori, K.; Kobayashi, T.; Sakakibara, K.; Ueda, K. Experimental and theoretical investigation of proton exchange reaction between protic ionic liquid diethylmethylammonium trifluoromethanesulfonate and H_2O. *Chem. Phys. Lett.* **2012,** *552*, 58-63.

12. Li, H.; Jiang, F.; Di, Z.; Gu, J. Anhydrous proton-conducting glass membranes doped with ionic liquid for intermediate-temperature fuel cells. *Electrochim. Acta* **2012,** *59*, 86-90.

13. Walsh, D. A.; Ejigu, A.; Smith, J.; Licence, P. Kinetics and mechanism of oxygen reduction in a protic ionic liquid. *Phys. Chem. CHem. Phys.* **2013,** *15* (20), 7548.

14. Smith, D. E.; Walsh, D. A. The Nature of Proton Shuttling in Protic Ionic Liquid Fuel Cells. *Adv. Energy Mater.* **2019,** *9* (24).

15. Bautista-Martinez, J. A.; Tang, L.; Belieres, J.-P.; Zeller, R.; Angell, C. A.; Friesen, C. Hydrogen Redox in Protic Ionic Liquids and a Direct Measurement of Proton Thermodynamics. *J. Phys. Chem. C* **2009,** *113*, 12586–12593.

16. Williams, D. H.; Fleming, I. *Spectroscopic Methods in Organic Chemistry*. Fifth Edition; McGraw-Hill: 1995.

17. Bio-Rad Laboratories, Inc. SpectraBase: 2016. http://spectrabase.com/spectrum/5ZWKtnQ2oH?a=SPECTRUM_5ZWKtnQ2oH (accessed Oct 09, 2019)

18. Bio-Rad Laboratories, Inc. SpectraBase: 2016. http://spectrabase.com/spectrum/JfEDDQL6SiQ?a=SPECTRUM_JfEDDQL6SiQ (accessed Oct 09, 2019)

19. Bio-Rad Laboratories, Inc. SpectraBase: 2018. http://spectrabase.com/spectrum/KRue8iW85wH?a=SPECTRUM_KRue8iW85wH (accessed Oct 09, 2019)

20. Bio-Rad Laboratories, Inc. SpectraBase: 2014. http://spectrabase.com/spectrum/EylZKdzReDy?a=SPECTRUM_EylZKdzReDy (accessed Oct 09, 2019)

21. Di Noto, V.; Negro, E.; Sanchez, J. Y.; Iojoiu, C. Structure-Relaxation Interplay of a New Nanostructured Membrane Based on Tetraethylammonium Trifluoromethanesulfonate Ionic Liquid and Neutralized Nafion 117 for High-Temperature Fuel Cells. *J. Am. Chem. Soc.* **2010,** *132* (7), 2183-2195.

22. Bio-Rad Laboratories, Inc. SpectraBase: 2014. http://spectrabase.com/spectrum/7ETxrTqOGnB?a=SPECTRUM_7ETxrTqOGnB (accessed Oct 09, 2019)

23. Bio-Rad Laboratories, Inc. SpectraBase: 2014. http://spectrabase.com/spectrum/KF8keo0bxsI?a=SPECTRUM_KF8keo0bxsI (accessed Oct 09, 2019)

24. Martinez, M.; Molmeret, Y.; Cointeaux, L.; Iojoiu, C.; Lepretre, J. C.; El Kissi, N.; Judeinstein, P.; Sanchez, J. Y. Proton-conducting ionic liquid-based Proton Exchange Membrane Fuel Cell membranes: The key role of ionomer-ionic liquid interaction. *J. Power Sources* **2010,** *195* (18), 5829-5839.

25. Shmukler, L. E.; Gruzdev, M. S.; Kudryakova, N. O.; Fadeeva, Y. A.; Kolker, A. M.; Safonova, L. P. Thermal behavior and electrochemistry of protic ionic liquids based on triethylamine with different acids. *RSC Adv.* **2016,** *6* (111), 109664-109671.

26. Tsunashima, K.; Sugiya, M. Physical and electrochemical properties of low-viscosity phosphonium ionic liquids as potential electrolytes. *Electrochem. Commun.* **2007,** *9*, 2353-2358.

27. Yasuda, T.; Nakamura, S.; Honda, Y.; Kinugawa, K.; Lee, S. Y.; Watanabe, M. Effects of polymer structure on properties of sulfonated polyimide/protic ionic liquid composite membranes for nonhumidified fuel cell applications. *ACS Appl. Mater. Interfaces* **2012,** *4* (3), 1783-90.

28. Gómez, E.; Calvar, N.; Domínguez, Á.; Macedo, E. A. Thermal behavior and heat capacities of pyrrolidinium-based ionic liquids by DSC. *Fluid Phase Equilib.* **2018,** *470*, 51-59.

29. Domańska, U.; Wlazło, M.; Karpińska, M.; Zawadzki, M. High selective water/butan-1-ol separation on investigation of limiting activity coefficients with $[P_{8,8,8,8}][NTf_2]$ ionic liquid. *Fluid Phase Equilib.* **2017,** *449*, 1-9.

30. MacFarlane, D. R.; Forsyth, M.; Izgorodina, E. I.; Abbott, A. P.; Annat, G.; Fraser, K. On the concept of ionicity in ionic liquids. *Phys. Chem. Chem. Phys.* **2009,** *11* (25), 4962-7.

4 The Oxygen-Reduction and Hydrogen-Oxidation Reactions in Protic Ionic Liquids

4.1 Introduction

The electrocatalytic oxygen-reduction reaction (ORR) is one of the most widely studied electrocatalytic reactions, due in large part to its role in electrochemical energy conversion devices such as fuel-cells.[1] In acidic and alkaline aqueous electrolytes, the 4-electron ORR proceeds according to Equations 1 and 2, respectively (where HA is a generalized Brønsted acid).[2] Potentials reported in Equations 1–4, 6 and 7 are versus the standard hydrogen electrode (SHE).

$$O_2 + 4HA + 4e^- \rightarrow 2H_2O + 4A^- \qquad (E^0 = 1.229\ V) \qquad (1)$$

$$O_2 + 2H_2O + 4e^- \rightarrow 4OH^- \qquad (E^0 = 0.401\ V) \qquad (2)$$

In acidic electrolytes, a 2-electron ORR yielding H_2O_2 can also occur, depending on electrode material, and proceeds according to Equation 3, which may be followed by electro-reduction (Equation 4) or disproportionation of H_2O_2 (Equation 5).

$$O_2 + 2HA + 2e^- \rightarrow H_2O_2 + 2A^- \qquad (E^0 = 0.695\ V) \qquad (3)$$

$$H_2O_2 + 2HA + 2e^- \rightarrow 2H_2O \qquad (E^0 = 1.776\ V) \qquad (4)$$

$$2H_2O_2 \rightarrow 2H_2O + O_2 \qquad (5)$$

In alkaline electrolytes, a 2-electron ORR yielding HO_2^- also occurs and proceeds according to Equation 6, which may be followed by electro-reduction (Equation 7) or disproportionation of $2HO_2^-$ (Equation 8).

$$O_2 + H_2O + 2e^- \rightarrow HO_2^- + OH^- \qquad (E^0 = -0.076\ V) \qquad (6)$$

$$HO_2^- + H_2O + 2e^- \rightarrow 3OH^- \qquad (E^0 = 0.878\ V) \qquad (7)$$

$$2HO_2^- \rightarrow 2OH^- + O_2 \qquad (8)$$

The reactions shown in Equations 1–8 are complex and the rate determining step is generally considered to be electro-reduction of adsorbed oxygen on the electrode surface, $O_{2,ads}$:[2]

$$O_2 + e^- \rightarrow O_2^{\bullet -} \qquad (9)$$

The hydrogen-oxidation reaction (HOR) is perhaps the single most studied electrocatalytic reaction and underpins the definition of 0 V at the SHE because of its very fast kinetics and electrochemical reversibility.[3] The SHE is described more fully in Chapter 2. As well as being of use as a reference tool and the reverse process, the hydrogen-evolution reaction (HER) is used for determining the electrochemically active surface area of electrodes,[4] and is the anodic reaction of H_2/O_2 fuel cells.[1a] The general HOR is described in an acidic and alkaline aqueous electrolyte by Equations 10 and 11 respectively.[5]

$$H_2 + 2H_2O \rightarrow 2H_3O^+ + 2e^- \qquad (10)$$

$$H_2 + 2OH^- \rightarrow 2H_2O + 2e^- \qquad (11)$$

The HOR and HER are electrochemically reversible at Pt electrodes in acidic and alkaline aqueous media.[6]

The widespread adoption of hydrogen as an energy vector has been proposed, whereby hydrogen is produced from thermo/electro/photo-lysis of water (utilising renewable energy) or from steam-methane reformation of fossil fuels.[7]

The produced hydrogen could then be consumed in fuel cells, for either stationary or mobile (vehicular) applications, resulting in the production of electrical energy and water.[8] This "Hydrogen Economy" could ultimately result in significant (or even total) decarbonisation of the transport system and domestic heating, providing that the hydrogen is produced by water splitting via renewable energy sources, as well as provide a practical solution to the energy storage problem.[9]

In recent years, a number of researchers have begun to study the ORR and HOR[5] in room-temperature ionic liquids (RTILs), salts that are liquid below 100 °C.[10,11,12] Chemically-reversible cyclic voltammograms (CVs) have been recorded in O_2-containing aprotic RTILs and attributed to the $O_2/O_2^{\bullet-}$ redox couple.[13] Some quaternary ammonium cation, bis(trifluoromethanesulfonyl)imide anion aprotic ionic liquids (AILs) display quasi-reversible $O_2/O_2^{\bullet-}$ voltammetry which becomes irreversible upon the addition of water.[14] The $O_2/O_2^{\bullet-}$ redox couple becomes increasingly (electrochemically) irreversible upon addition of weakly protonating species, such as phenol, as the 1-electron reduction becomes a 2-electron reduction (via disproportionation) to produce H_2O_2.[15]

Recent work by Switzer *et al*. has considered the effects of adding various protic species to aprotic ionic liquids to assess how the potential at which the ORR occurs is affected.[16] A positive shift of the ORR potential of about 1.8 V was observed at a Pt electrode when the pK_a of the proton-donating species was changed from 10.6 to −14. It was proposed that $O_2^{\bullet-}$ generated during the ORR (Equation 9) is protonated by the protic species, HA, yielding $HO^{2\bullet}$ (Equation 12):

$$O_2^{\bullet-} + HA \rightarrow HO_2^{\bullet} + A^- \qquad (12)$$

which can be followed by either disproportionation or electro-reduction of $HO_2^{\bullet}$:

$$2HO_2^{\bullet} \rightarrow H_2O_2 + O_2 \quad (13)$$

$$HO_2^{\bullet} + e^- \rightarrow HO_2^{\bullet -} \quad (14)$$

Chemical protonation of $HO_2^{\bullet -}$ can then occur yielding H_2O_2:

$$HO_2^{\bullet -} + HA \rightarrow H_2O_2 + A^- \quad (15)$$

Protic ionic liquids (PILs) are ionic liquids that are synthesised by proton transfer from Brønsted acids to Brønsted bases. It is generally accepted that a difference in pK_a between the acid and the base larger than 10 (that is, $\Delta pK_a > 10$) is necessary for complete proton transfer and the formation of "high ionicity" PILs.[17] It has been proposed that the high ionic conductivity, low volatility and thermal stability of PILs means they can be used as electrolytes at temperatures greater than 100 °C.[18]

A proposed mechanism for the ORR at glassy-carbon (GC) and gold electrodes in ammonium-based PILs follows the mechanism of the ORR in an aprotic solvent containing a strong acid (see Equations 9–15).[19] The proposed mechanism begins with the electrochemical reduction of dioxygen to superoxide (Equation 9), followed by the chemical protonation of the superoxide radical by the proton on the PIL cation resulting in the hydroperoxyl radical (Equation 12). The hydroperoxyl radical is then electrochemically reduced to the hydroperoxyl anion (Equation 14), which can then accept a further proton from the PIL cation to produce hydrogen peroxide (Equation 15) resulting, overall, in an ECEC ORR scheme.

The PIL [dema][TfO] has been proposed as a good electrolyte for polymer electrolyte membrane fuel cells (PEMFCs) operating at >100 °C operation because of its high proton conductivity of 68.0 mS cm^{-1} at 150 °C, thermal stability up to 360 °C, and high open circuit potential (OCP) (greater than 1.0 V at 150 °C).[12,18,20,21,22,23] The high OCP reported by Watanabe and co-workers was attributed to fast ORR and HOR kinetics in the PIL.[20] Operating PEM fuel cells at temperatures greater than >100 °C is desirable as it increases the rate of the otherwise slow ORR, meaning that lower platinum catalyst loadings can be used, or even allow for non-precious metal alternatives to replace platinum, greatly reducing the cost of PEM devices.[1a,24] Conventional PEM fuel cells are limited to operating below 100 °C because the perfluorosulfonic acid electrolyte membrane (Nafion®) requires hydration to facilitate proton transport;[25,26] something that is not possible above the boiling point of water at atmospheric pressure. Other approaches to intermediate-temperature (120 to 200 °C) PEMFCs involve the use of proton-conducting acid-containing polymers such as phosphoric acid-doped polybenzimidazole, but these have encountered problems of the acid leaching from the membrane resulting in reduced fuel-cell performance.[27,28]

This chapter focusses on the effects of acidification on the ORR in the PIL, [dema][TfO], as well as the effect of adding base on the HOR in [dema][TfO]. The ORR and HOR in another PIL, [dema][NTf_2], is also investigated. As described below, the onset potential of the ORR in [dema][TfO] depends on the presence of acid in the PIL, but more so, is dependent on the strength (aqueous pK_a) of the acid added to [dema][TfO], something that has been shown previously in aprotic ionic liquids.[16] Irrespective of whether or not a strong acid is present, the ORR at Pt

follows a 4-electron pathway to produce water, whereas the ORR at a GC electrode follows a 2-electron pathway (producing hydrogen peroxide), and at more negative potentials by a 4-electron pathway to produce water.

In addition, the onset potential of the HOR is affected by the presence of base in [dema][TfO]. From the studies of ORR and HOR, the cell potential of a fuel cell containing acid-free [dema][TfO] or [dema][NTf_2] as an electrolyte is estimated and compared with that in acidified [dema][TfO] or [dema][NTf_2].

4.2 Experimental Section

4.2.1 Materials and apparatus

All chemicals were obtained from Acros Organics, Sigma Aldrich, Merck, VWR Chemicals, or Fischer Scientific, and were used as received. O_2 (99.95%) and H_2 (99.999%), were from BOC gases (Nottingham, UK). Ar (99.999%) was from CryoService (Worcester, UK). Pd wire (0.5 mm diameter, 99.99%) was from Alfa Aesar. A modulated speed rotator and platinum and glassy-carbon rotating disk electrodes (RDEs) and rotating ring-disk electrodes (RRDEs) were from Pine Research Instrumentation, Inc (Durham, NC, USA). Platinum (2 mm diameter), glassy-carbon (3 mm) and gold (2 mm) stationary electrodes were purchased from CH Instruments and a stationary palladium (1.6 mm) electrode was purchased from ALS Co. Ltd. Electrochemical measurements were performed using a model CHI760C potentiostat from CH Instruments, Austin, TX, USA.

4.2.2 Synthesis and characterisation of protic ionic liquids

Diethylmethylammonium trifluoromethanesulfonate, [dema][TfO], was prepared by the dropwise addition of 1 mol dm^{-3} aqueous trifluoromethanesulfonic acid (abbreviated to triflic acid or sometimes TfOH) to 1 mol dm^{-3} aqueous

N,N-diethylmethylamine (dema) with a 5% molar excess of the base. The reaction mixture was cooled in an ice bath. Excess water was removed using rotary evaporation. The product was then either held under vacuum (5×10^{-2} mbar) at room temperature for 72 h and then at 70 °C for 24 h, or held under vacuum (5×10^{-2} mbar) at 40 °C for between 5 and 10 days, to remove residual water and base. The liquid was then transferred under vacuum to a glovebox containing a dry N_2 atmosphere (<0.1 ppm O_2 and <0.4 ppm H_2O). [dema][TfO] was characterized by ^{1}H, ^{13}C and ^{19}F NMR spectroscopy (Bruker Ascend™ 400 MHz NMR Spectrometer) using a hexadeuterodimethyl sulfoxide solvent. Attenuated total reflection Fourier-transform infrared spectroscopy was carried out using a Bruker Alpha Platinum-ATR FTIR spectrometer at 30 °C. Thermogravimetric analysis (TGA) was carried out using a TA Instruments Discovery instrument under a N_2 atmosphere, and residual water contents were determined using Karl-Fischer titrations (Mitsubishi CA-200 Moisturemeter). The kinematic viscosity of the liquid was measured at 40 °C using an SVM 3000 Stabinger Viscometer from Anton Paar. Residual water contents were below 100 ppm. Diethylmethylammonium bis(trifluoromethanesulfonyl)imide, [dema][NTf_2], was synthesised using a metathesis reaction described in reference 5. PIL characterisation data is presented in Chapter 3 and Appendix I.

4.2.3 Electrode fabrication and electrochemical measurements

The use of Pd-H reference electrodes for electrochemistry in PILs was introduced by Angell.[5] Pd-H electrodes provide stable potentials in PILs, which are defined by the hydrogen-redox equilibrium at the interface between Pd and the PIL. A Pd-H reference electrode was fabricated by sealing a 0.5 mm diameter Pd wire

(≈2.7 cm long) into borosilicate glass using a butane flame. Approximately 1.5 cm of the Pd wire was left protruding from the glass sheath to form a Pd rod electrode. A polished Ag contact wire was attached to the Pd wire inside the glass sheath using Ag epoxy (Chemtronics, Kennesaw, GA, USA). The Pd rod was then annealed in a butane flame and immersed in water before H_2 was bubbled over the Pd metal surface for 30 minutes. The rod was then rinsed with deionised water and either dried under a flow of N_2 or Ar, or left covered in air until dry.

A three-electrode electrochemical cell containing either a 4.6 mm diameter Pt disk or 5.6 mm diameter glassy-carbon working electrode, a Pt flag counter electrode (A ≈0.70 cm^2) and a Pd-H reference electrode, were used for all electrochemical measurements, unless otherwise stated. Prior to use, the Pt or GC disk electrode was polished using an aqueous suspension of 0.05 μm α-alumina (Buehler, Lake Bluff, Illinois) on felt polishing pads, and rinsed thoroughly with deionized water. The Pt flag counter electrode was flame annealed in a butane flame before being rinsed with deionised water. All working and counter electrodes were dried in a glassware oven before use. The cell was charged with 5 mL of PIL, sealed using rubber septa and bubbled with O_2, H_2 or Ar through a needle for a minimum of 40 minutes, while being stirred by a magnetic stirrer. During voltammetric measurements, a blanket of the appropriate gas was maintained above the PIL. All voltammograms were *iR*-corrected unless otherwise stated. To mitigate for changes in the potential of the Pd-H reference electrode upon addition of acid, base or gases to the PILs, potentials were adjusted, such that the electrochemical window was the same during each analysis.

4.3 Results and Discussion

4.3.1 Oxygen-reduction and hydrogen-oxidation in [dema][TfO]

The voltammetry of O_2-saturated [dema][TfO] at Pt and GC electrodes is shown in Figure 4.1. The onset of oxygen reduction at Pt is at around 0.3 V compared with −0.2 V at GC, which is expected given the poorer electrocatalytic activity for O_2-reduction at GC. The relative magnitudes of the peak ORR current densities at stationary Pt and GC electrodes is 2:1 suggesting the number of electrons transferred per molecule O_2 is twice that at Pt than at GC. When rotating the electrodes at 1,600 rpm, the magnitudes of the steady-state mass-transport limited current densities (j_L) recorded at Pt and GC are, initially, again in an approximately 2:1 ratio. However, at potentials negative of around −1.0 V at GC, a secondary reaction mechanism takes over resulting in j_L doubling, such that it is similar to Pt (an approximately 1:1 j_L ratio is observed).

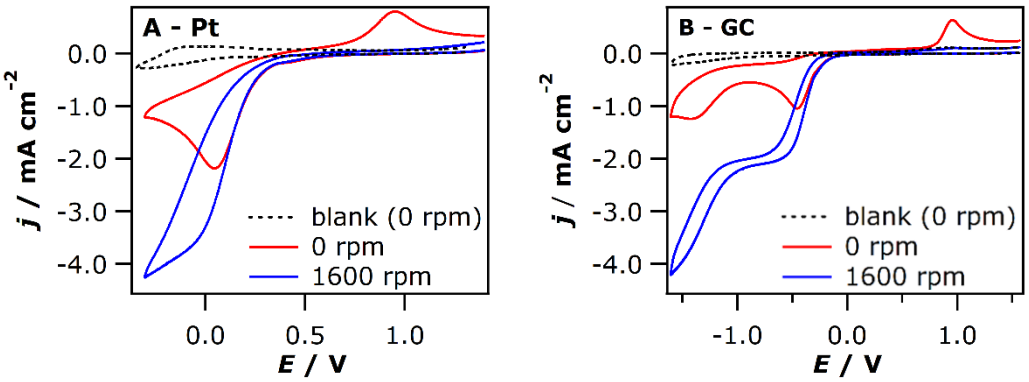


Figure 4.1 Cyclic voltammograms of [dema][TfO] recorded using stationary and rotating (A) Pt and (B) glassy-carbon electrodes. The voltammograms were recorded at 100 mV s^{-1} and the initial sweep was in the negative direction. The rotation rate was 1,600 rpm.

The peak-to-peak separation between O_2-reduction and the subsequent oxidation indicates that the reaction is electrochemically irreversible and is therefore unlikely to be superoxide formation/oxidation observed in dry AILs in the absence

of a proton donor (see Equation 9), which is electrochemically reversible. The reduction of O_2 is less reversible at a GC electrode than at Pt.

At stationary Pt and GC electrodes, oxidation of an ORR product is observed around 1.0 V at both electrodes, suggest that one of the ORR products produced at both electrode materials is the same in each case. Furthermore, at a GC electrode, if the potential is scanned to −0.9 V (before the second ORR process takes over negative of −0.9 V) then the oxidation peak at 1.0 V is half the current density than that observed at the Pt electrode. If the potential is swept to −1.6 V at a GC electrode, the oxidation peak current density is around 0.6 mA cm^{-2}, double that when only scanning negative enough to include the first ORR peak; this also means that at the peak oxidation current of the ORR product is similar to that observed at a Pt electrode. It can be further concluded that the number of electrons transferred from the one ORR process at Pt and the two at GC are very similar, meaning that possible ORR mechanisms at each electrode can be suggested. The proposed reaction mechanisms for ORR at Pt and GC carbon electrodes in [dema][TfO] are as follows:

At Pt:

$$O_2 + 4[dema]^+ + 4e^- \rightarrow 2H_2O + 4dema \quad (16)$$

At GC:

$$O_2 + 2[dema]^+ + 2e^- \rightarrow H_2O_2 + 2dema \quad (17)$$

followed by:

$$2[dema]^+ + H_2O_2 + 2e^- \rightarrow 2H_2O \quad (18)$$

The voltammetry in Figure 4.2 shows the effect of the presence of added triflic acid on the ORR potential at Pt and GC electrodes both rotating and stationary. A clear shift in ORR potential of ≈0.9 V at Pt and GC to a more positive potential is observed upon addition of triflic acid. Figure 4.2 (C) shows a similar j_L of approximately 3.5 mA cm^{-1} for the ORR both in the presence and absence of added acid at a Pt electrode, suggesting that the number of electrons transferred is the similar in both cases. At a rotating GC electrode, see Figure 4.2 (D), the ORR j_L recorded is nearly the same in the presence and absence of acid, and is similar to Pt in this regard. While the ORR onset potential occurs at more positive potentials at GC upon acidification of the PIL, the second ORR process (attributed to H_2O_2 reduction to H_2O) is not similarly shifted to a more positive potential. At stationary Pt and GC electrodes, see Figure 4.2 (A) and Figure 4.2 (B), the oxidation of the ORR product at ≈1.0 V is lost when acid is added to [dema][TfO]. The proposed reaction mechanisms for the ORR in [dema][TfO] containing triflic acid are as follows.

At Pt:

$$O_2 + 4TfOH + 4e^- \rightarrow 2H_2O + 4[TfO]^- \quad (19)$$

At GC:

$$O_2 + 2TfOH + 2e^- \rightarrow H_2O_2 + 2[TfO]^- \quad (20)$$

followed by Equation 17 at more negative potentials.

The positive shift in the ORR upon addition of triflic acid can be explained by the relative strengths of the available proton donors. The aqueous pK_a of the PIL cation ($[dema]^+$) is 10.6 whereas the pK_a of triflic acid is −14 (≈ 24 orders of

magnitude more proton-donating) meaning that where triflic acid is present the thermodynamic requirement for the ORR is significantly reduced and the ORR onset potential is much more positive.

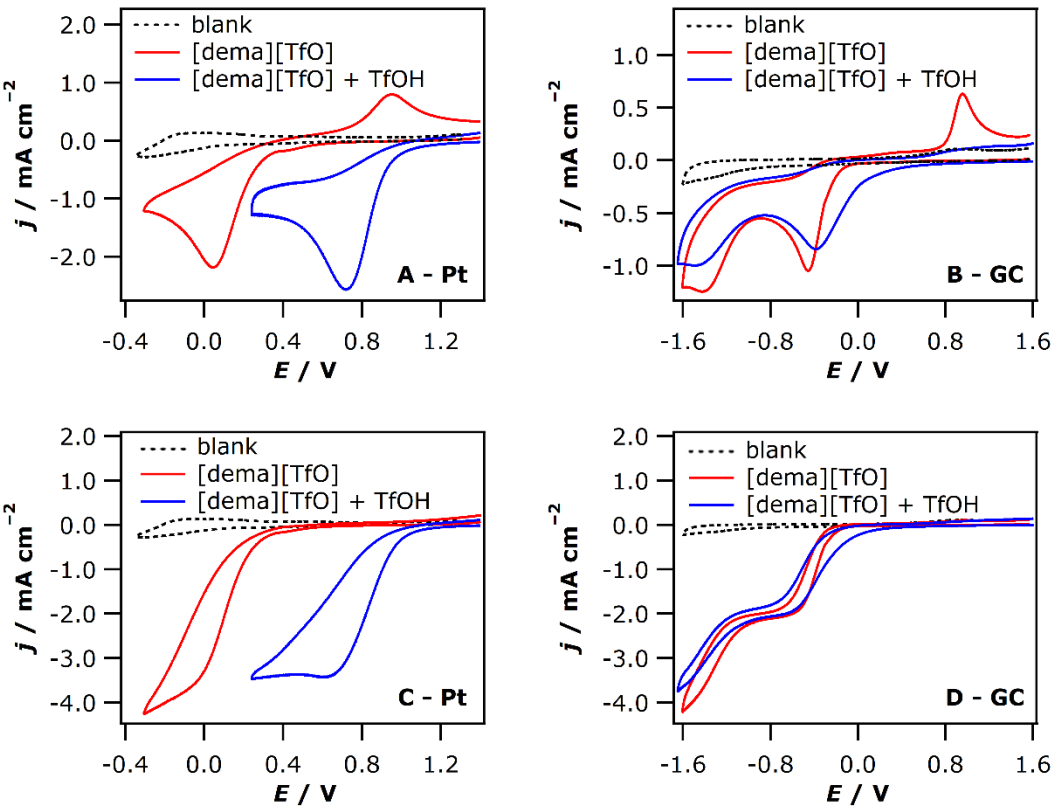


Figure 4.2 Cyclic voltammograms recorded in O_2-saturated [dema][TfO] and O_2-saturated [dema][TfO] containing 0.1 mol dm^{-3} TfOH using Pt and glassy-carbon rotating-disk electrodes at 100 mV s^{-1}. (A) and (B) are recorded at 0 rpm, and (C) and (D) at 1,600 rpm. The initial sweeps were in the negative direction.

To further support the ORR mechanisms in [dema][TfO] proposed in Equations 16–20, a hydrodynamic study of the ORR in pure and acidified [dema][TfO] was undertaken. Unfortunately, the Koutecký-Levich analysis on the linear sweep voltammograms (LSVs) showing the ORR at Pt and GC electrodes rotating to achieve a j_L proportional to the rotation rate, provided no fixed gradient over all rotation rates from which an electron transfer number (n) could be determined with any certainty. It does suggest that the ORR in [dema][TfO] (acidified or otherwise) at Pt and GC, does not conform to Koutecký-Levich

analysis. All the LSVs and rotation rate data points obtained are presented in Figure 4.3 and Figure 4.4, but where an electron transport number has been posited, the data points used to calculate it will be stated.

The method for calculating the number of electrons transferred by Koutecký-Levich analysis is as follows. The gradient of the Koutecký-Levich plot (normalised for electrode area) is equal to the following equation, which can be rearranged for *n*.

$$\text{gradient} = (0.620n\text{F}D_{O_2}^{\frac{2}{3}}\nu^{-\frac{1}{6}}C_{O_2})^{-1} \quad (21)$$

where *n* is the electron transfer number, F is Faraday's constant, *D* is the diffusion coefficient of oxygen in [dema][TfO], ν is the kinematic viscosity of the PIL and *C* is the saturation concentration of oxygen in [dema][TfO].[3] This equation then forms part of the Koutecký-Levich equation normalised for electrode area:

$$j^{-1}=j_L^{-1}+j_K^{-1} \quad (22)$$

$$j^{-1}=(0.620n\text{F}D_{O_2}^{\frac{2}{3}}\nu^{-\frac{1}{6}}C_{O_2})^{-1}\omega^{-\frac{1}{2}}+j_K^{-1} \quad (23)$$

Figure 4.3 shows how the ORR current changes with the rotation rate of a Pt electrode in O_2-saturated [dema][TfO], either in the absence (plots A and B) or presence (plots C and D) of triflic acid. The ORR j_L in [dema][TfO], in both the presence and absence of triflic acid, increases with rotation rate as expected. The Koutecký-Levich analysis of the ORR in [dema][TfO] with and without acidification at a Pt electrode, over the rotation rates chosen, do not provide a constant gradient as potential changes. In addition, none of the Koutecký-Levich plot gradients have a *y*-intercept of 0 or less, meaning that there are kinetic

limitations over the potential range used and that the measured currents were not truly a result of mass transport limitations only. Therefore, a value of *n* could not be determined with any certainty.

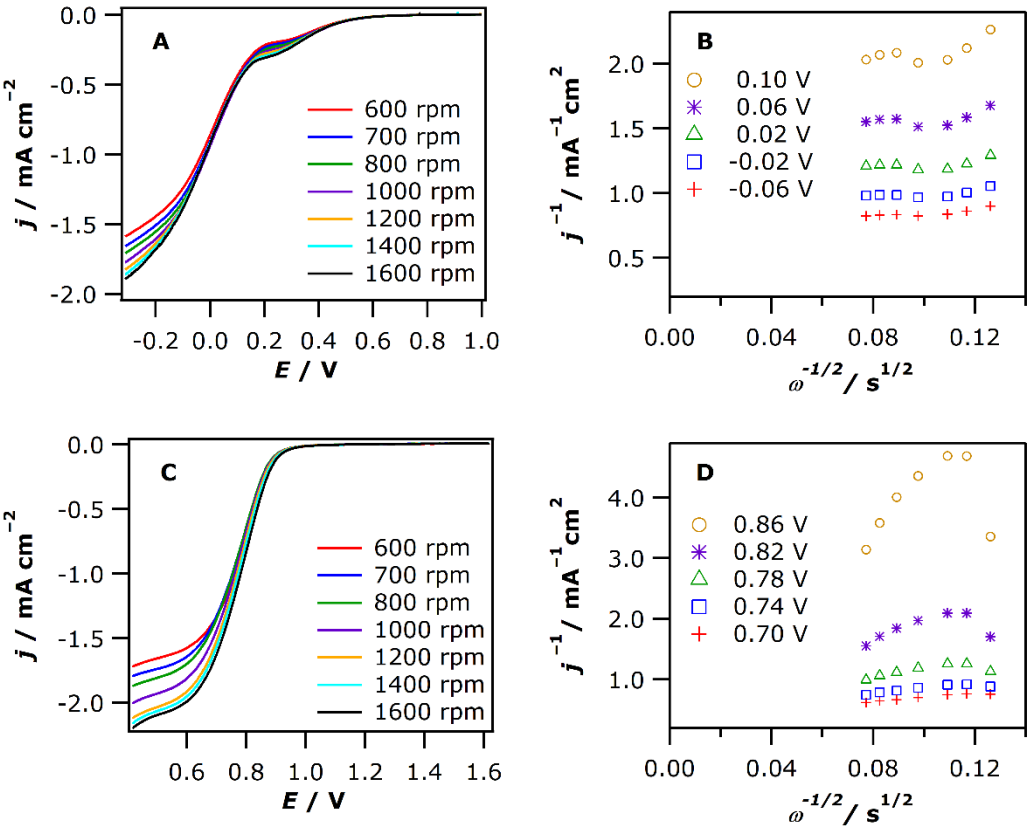


Figure 4.3 (A,C) Hydrodynamic linear sweep voltammograms (LSVs) of O_2-saturated [dema][TfO] and O_2-saturated [dema][TfO] containing 0.1 mol dm^{-3} triflic acid recorded at a Pt working electrode. LSVs in plot A are recorded in O_2-saturated [dema][TfO] without any added acid and B is the associated Koutecký-Levich plot. LSVs in plot C are recorded in O_2-saturated [dema][TfO] with triflic acid added to achieve a concentration of 0.1 mol dm^{-3} and D is the associated Koutecký-Levich plot. All LSVs are recorded at a 5 mV s^{-1} scan rate. The potential sweeps all begin in a negative-going direction.

Figure 4.4 shows how the ORR current changes with the rotation rate of a GC electrode in O_2-saturated [dema][TfO], either in the absence (plots A and B) or presence (plots C and D) of triflic acid. The ORR j_L in acid-free [dema][TfO] at a GC electrode also increases with rotation rate as it does at a Pt electrode. The same can be said for the ORR in [dema][TfO] containing 0.1 mol dm^{-3} recorded at a GC electrode rotating up to 1,200 rpm, after which, the j_L anomalously decreases

slightly at higher rotation rates. The Koutecký-Levich analysis of the ORR in [dema][TfO] with and without acidification at a GC electrode, over the rotation rates chosen, do not provide a constant gradient as potential changes (as also observed at a Pt electrode).

Similar to the comparable studies at a Pt electrode, none of the Koutecký-Levich plot gradients have a *y*-intercept of 0 or less, meaning that there are kinetic limitations over the potential range used and that the measured currents were not truly a result of mass transport limitations only. Therefore, a value of *n* could not be determined with any certainty. Recent work by Zhou *et al*. on the ORR in alkaline aqueous systems suggests that Koutecký-Levich analysis is not suitable for studying the ORR and that rotating-ring disk (RRDE) voltammetry is preferable.[29] An alternative to either RRDE or Koutecký-Levich analysis for determining *n* and studying ORR kinetics is proposed by Liu and Bard[30] through the use of a scanning electrochemical microscope, although their efforts were confined to aqueous alkaline media and remains untested in ILs.

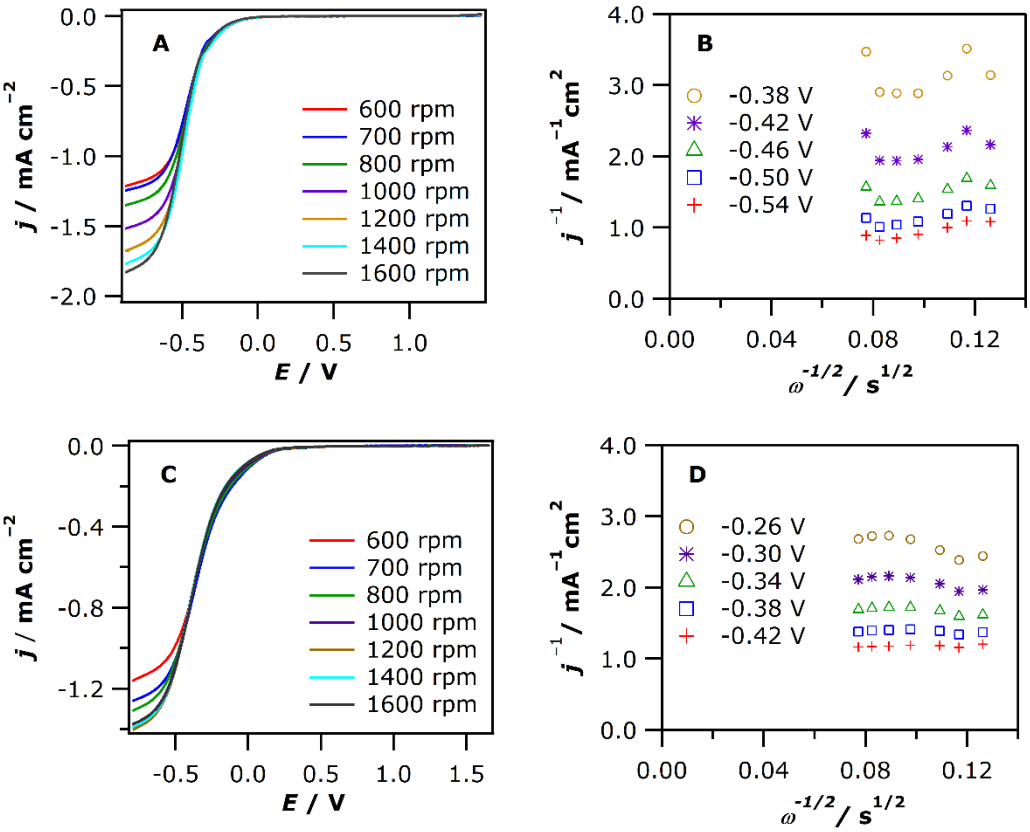


Figure 4.4 (A,C) Hydrodynamic Linear sweep voltammograms (LSVs) of O_2-saturated [dema][TfO] in the presence and absence of 0.1 mol dm^{-3} triflic acid at a glassy-carbon working electrode. LSVs in plot A are recorded in O_2-saturated [dema][TfO] without any added acid and B is the associated Koutecký-Levich plot. LSVs in plot C are recorded in O_2-saturated [dema][TfO] with triflic acid added to achieve a concentration of 0.1 mol dm^{-3} and D is the associated Koutecký-Levich plot. All LSVs are recorded at a 5 mV s^{-1} scan rate. The potential sweeps all begin in a negative-going direction.

Since Koutecký-Levich analysis was unsuccessful, an attempt to calculate the ORR electron transfer number using rotating ring-disk electrode (RRDE) voltammetry[29] was made, where n can be found by simultaneously recording the ORR current at the disk and the ORR product oxidation current at the ring (see Figure 4.5) according to the following equations:

$$n = 4 \times \frac{i_d}{i_d + \frac{i_r}{N_C}} \qquad (24)$$

$$p = 2 \times \frac{\frac{i_r}{N_C}}{i_d + \frac{i_r}{N_C}} \quad (25)$$

$$n = 4 - 2p \quad (26)$$

where n is the electron transfer number, p is the fraction of O_2 reduced to hydrogen peroxide, i_r is the current recorded at the ring, i_d is the current recorded at the disk, and N_C is the collection efficiency of the RRDE. The collection efficiencies of the Pt and glassy-carbon RRDEs are 21.8% and 37.0% respectively, as provided by the RRDE manufacturer, PINE Research Instrumentation. Unfortunately, the values for n calculated using this method (n = 2.8 for acid-free [dema][TfO] at Pt and GC electrodes) were not consistent with the voltammetry and previous studies of the ORR mechanism in [dema][TfO] which conclude that H_2O is the dominant ORR product at Pt electrodes.[10]

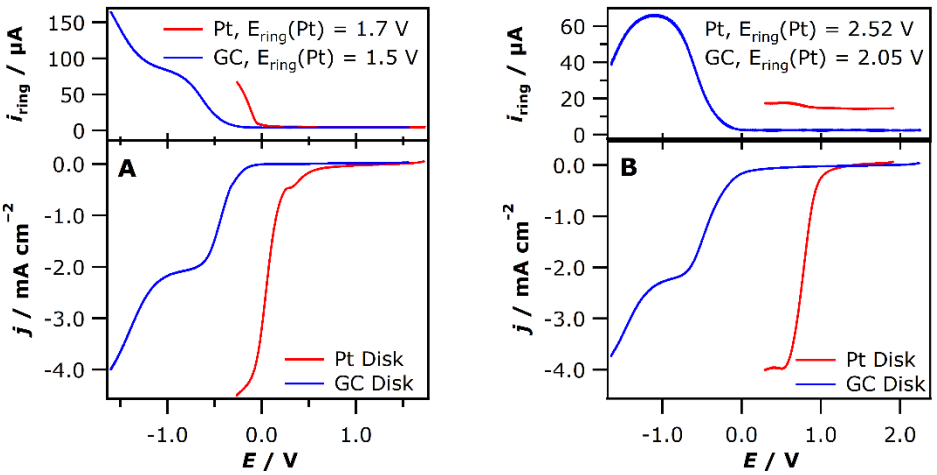


Figure 4.5 Linear sweep voltammograms recorded in O_2-saturated [dema][TfO] in the absence (A) and presence (B) of added triflic acid to a 0.1 mol dm^{-3} concentration recorded at either a Pt-ring/Pt-disk or Pt-ring/GC-disk rotating ring disk electrode (RRDE). A fixed potential of 1.7 V and 1.5 V was maintained at the Pt rings of the Pt and GC-disk RRDEs respectively, such that the ORR product at the Pt and GC disk electrodes, is oxidised. Pt/GC disk LSVs, are recorded at 4.57 mm diameter Pt and 5.61 mm diameter GC disks. The Pt ring of the Pt RRDE has an area of 0.037 cm^2 and the Pt ring of the GC RRDE has an area of 0.1866 cm^2. All LSVs are recorded at a 100 mV s^{-1} scan rate with the electrodes rotating at 1,600 rpm. The potential sweeps begin in a negative-going direction.

Since exact determination of the electron transport number by hydrodynamic methods were unsuccessful, another approach was needed to investigate the ORR mechanism. To determine whether H_2O_2 was an ORR reaction product in unacidified [dema][TfO], as Figure 4.5 (A) would erroneously suggest, and to explore the cause of the oxidation peak observed at ≈1.0 V, H_2O_2 was added to [dema][TfO] in a 0.05 mol dm^{-3} concentration to determine its oxidation potential. Figure 4.6 (A) shows a CV of H_2O_2 added to [dema][TfO] recorded at a Pt electrode alongside CVs of O_2-saturated [dema][TfO] in the presence and absence of added triflic acid. The H_2O_2 oxidation peak is observed at ≈1.4 V and is 0.4 V more positive than the peak observed for oxidation of the ORR product at ≈1.0 V; this suggests that H_2O_2 is not an ORR product at a Pt electrode in [dema][TfO]. A proposed mechanism for the oxidation of H_2O_2 in [dema][TfO] is shown in Equation 27.

$$H_2O_2 + 2[TfO]^- \rightarrow O_2 + 2TfOH + 2e^- \quad (27)$$

After H_2O_2 is oxidised, a corresponding reduction peak is observed at ≈ 0.8 V which is most likely O_2 reduction but coupled with the proton on the TfOH present at the electrode surface from the recent oxidation of H_2O_2, instead of the $[dema]^+$ cation, because the ORR potential is very close to that observed for ORR in presence of triflic acid when added to [dema][TfO] (see Equation 19).

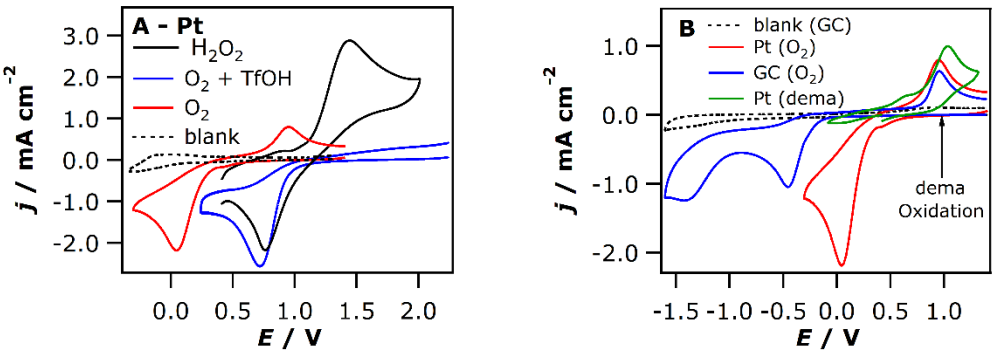


Figure 4.6 (A) – Voltammograms recorded at a stationary Pt electrode in either deaerated [dema][TfO] containing 0.05 mol dm^{-3} H_2O_2 or O_2-saturated [dema][TfO] with or without 0.1 mol dm^{-3} TfOH. (B) – Voltammograms recorded in O_2-saturated pure [dema][TfO] at stationary Pt and GC electrodes and deaerated [dema][TfO] containing 0.1 mol dm^{-3} dema at a Pt electrode. The blank is recorded in deaerated [dema][TfO] at a GC electrode. The scan rates are 100 mV s^{-1}. The blanks are recorded in deaerated [dema][TfO].

In the absence of acid in [dema][TfO] the ORR product, other than water (at Pt) or hydrogen peroxide (at GC), is dema, since it is the proton on the PIL cation ([dema]$^+$) that is consumed by the ORR. Figure 4.6 (B) shows the CVs of O_2-saturated [dema][TfO] recorded at both Pt and GC electrodes. The positive current density observed at both Pt and GC at ≈1.0 V is attributed to the oxidation of dema. This is confirmed by the green CV and the oxidation current density at a very similar potential recorded at a Pt electrode in deaerated [dema][TfO] containing ≈0.1 mol dm^{-3} of added dema. The conclusions from the addition of H_2O_2 and dema, respectively, to [dema][TfO] are that the mechanisms for the ORR in acidified and non-acidified [dema][TfO] at Pt and GC electrodes proceed according to Equations 16 to 20.

To investigate the nature of the shift between [dema]$^+$-coupled ORR and TfOH-coupled ORR a series of CVs were recorded with increasing concentrations of added TfOH. From Figure 4.7 (A), at a Pt electrode, we see that the ORR onset potential shifts to the more positive potentials associated with TfOH-coupled ORR

even when low concentrations of TfOH are present, further confirming the importance of any acid present in PILs on the ORR. As concentrations of acid increase, Figure 4.7 (A) shows the j_L also increasing. Once TfOH has been added to a concentration of 88 mM the j_L at 3.5 mA cm^{-2} is similar to that shown in Figure 4.2 of O_2-saturated [dema][TfO] containing 100 mM TfOH, meaning that at >88 mM acid the ORR is entirely dominated by acid-coupled ORR rather than any contribution of PIL-cation-coupled ORR at more negative potentials. In other words, the acid-coupled ORR current density, at more positive potentials, has reached parity with the flux of [dema]$^+$ to the electrode.

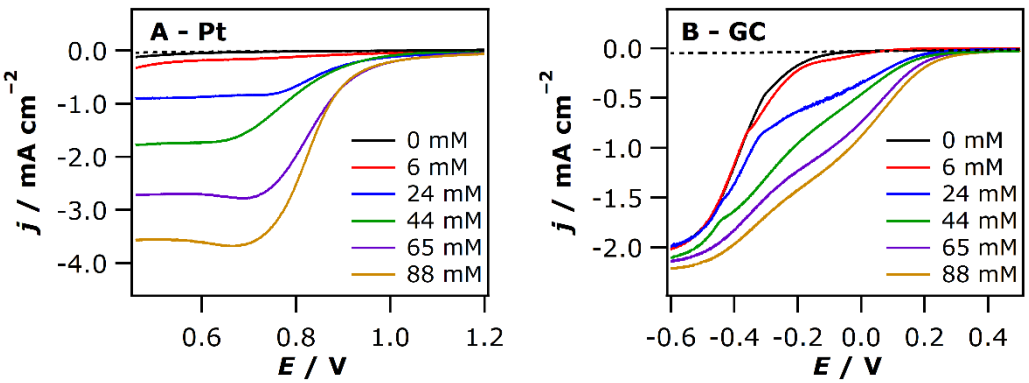


Figure 4.7 Linear sweep voltammograms (LSVs) of O_2-saturated [dema][TfO] with increasing concentrations of added TfOH recorded at Pt and GC electrodes. All LSVs were recorded at 100 mV s^{-1} and the initial sweep was in the negative direction. The rotation rate for all LSVs was 1,600 rpm except for the blank at 0 rpm. The blank experiments are represented by the black dotted voltammograms.

The effect of increasing concentration of triflic acid on the ORR potential at a GC electrode is shown in Figure 4.7 (B). Similar to that observed at a Pt electrode, the presence of even a small concentration of triflic acid results in an ORR onset at a significantly more positive potential where the ORR current density increases with acid concentration. Figure 4.7 (B) also shows TfOH-coupled ORR (at positive potentials) and [dema]$^+$-coupled ORR (at more negative potentials) in the same

voltammogram, when concentrations of TfOH are 6, 24 and 44 mmol dm^{-3}. This indicates that at lower concentrations of TfOH, at higher potentials the ORR current density is limited by availability of acid at the electrode surface until the potential is scanned negative enough for the $[dema]^+$ PIL cation to take part in the reaction, after which the ORR current density is limited by the availability of any proton donor at the electrode surface, given that the diffusion (and effective concentration) of O_2 is far greater than the proton donors at the electrode surface. Furthermore, the reaction stoichiometry requires double the number of moles of protons to O_2 at a GC electrode and quadruple at Pt. In the case of GC, the ORR shown in Figure 4.7 (B) is the reduction of O_2 to H_2O_2 rather than H_2O.

The effect of different concentrations of triflic acid on the ORR in PILs at Pt and GC electrodes is now known, but what of different acid species with different proton affinities? To investigate this, acid-free [dema][TfO] was acidified with acids covering a large range of pK_as to a concentration of 0.1 mol dm^{-3} and oxygenated to saturation concentrations (1.79 ± 0.04 mmol dm^{-3})[11] before voltammetry in the various acidified-PIL electrolytes was carried out. The acids and aqueous pK_as are as follows: ethanoic acid (4.76),[31] formic acid (3.77),[31] trifluoroacetic acid (−0.25),[32] sulfuric acid (−3.0),[31] perchloric acid (−10.00),[31] and trifluoromethanesulfonic acid (−14);[32] the aqueous pK_a of the $[dema]^+$ cation in acid-free [dema][TfO] is 10.6.[16] Figure 4.8 shows the effect of acids of different strengths in O_2-[dema][TfO] on the potential at which the ORR occurs at a Pt electrode rotating at 1,600 rpm. The LSVs in plot A show the onset potential of the ORR becoming more positive as the pK_a of the acid added to [dema][TfO] decreases (acid gets stronger). The most negative ORR potential at half the

current density maximum ($E_{½}$) is observed in acid-free [dema][TfO] (red voltammogram) at $E_{½}$ = 0.04 V and the most positive ORR potential at half current density maximum is that of perchloric acid acidified [dema][TfO] (light blue voltammogram) at $E_{½}$ = 0.74 V. All j_Ls were around 3.5 mA cm^{-2} suggesting that the reaction mechanism for all acids used is the same and proceeds according to Equation 1 at a Pt electrode (equation also shown in the blue box in Figure 4.8 (A)).

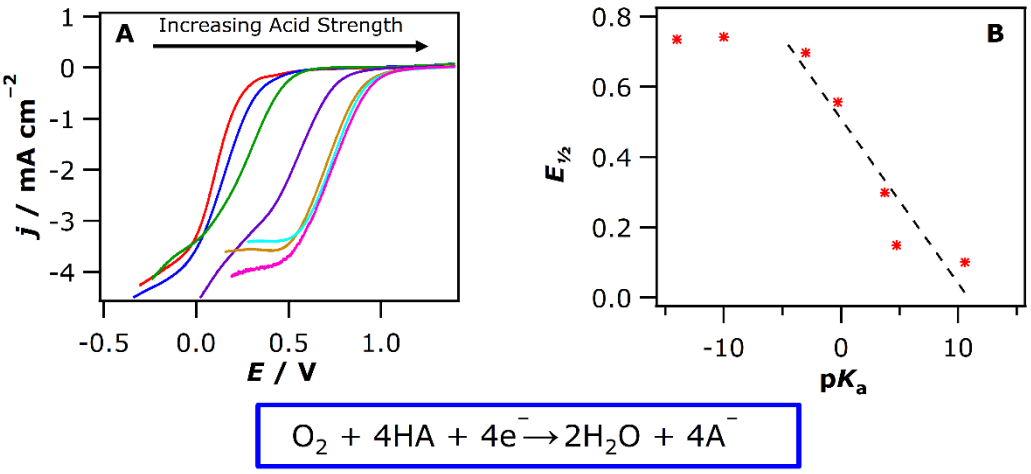


Figure 4.8 (A) Linear-sweep voltammograms of O_2-saturated of [dema][TfO] containing (from left to right) no added acid, ethanoic acid, formic acid, trifluoroacetic acid, sulfuric acid, perchloric acid, and triflic acid. All voltammograms were recorded using a Pt electrode rotating at 1,600 rpm and at a scan rate of 100 mV s^{-1}. The acid concentration was 0.1 mol dm^{-3} in each case and all potential sweeps began in the negative direction. (B) The ORR potential at half the maximum current versus the pK_a of the added acid. The acids are (from left to right) triflic acid, perchloric acid, sulfuric acid, trifluoroacetic acid, formic acid, ethanoic acid, [dema][TfO] (no added acid).

Figure 4.8 (B) directly shows the effect of the strength of the acid used to acidify [dema][TfO] as aqueous pK_a, on the potential at which ORR occurs, here represented by the potential at half the current density maximum ($E_{½}$) at a Pt electrode rotating at 1,600 rpm. Between ethanoic acid-acidified [dema][TfO], with a pK_a of 4.76, and sulfuric acid-acidified [dema][TfO], with a pK_a of −3, the positive shift of $E_{½}$ is linear with ORR shifting positive by ≈50 mV for every decrease in pK_a by 1, which is close to the value obtained for the ORR with a general proton donor and that observed for the ORR in an aprotic ionic liquid.[16]

When [dema][TfO] is acidified with acids of pK_as lower than sulfuric acid (−3), there is minimal change in ORR ($E_{½}$); this suggests that acids of strengths equal to or greater than sulfuric acid are required to acidify [dema][TfO] if a suitable high PEM cell potential is to be achieved. However, it should be noted that sulfuric acid is diprotic with the second proton of pK_a of 1.99 being weakly acidic which could contribute to the recorded ORR current density at a sufficiently negative potential. This effect is likely caused by solvent levelling in the PIL, where water or the IL anion acts as a buffer, as has been suggested for aprotic ionic liquids.[16]

So far, the studies of the ORR presented in this chapter have been limited to Pt and GC electrodes. To investigate the effect of the electrode material on the ORR mechanism and overpotential in [dema][TfO], voltammetric measurements were made at stationary Pt, GC, Au and Pd disk electrodes in O_2-saturated [dema][TfO]. Figure 4.9 (A) shows very similar ORR behaviour between Pd and Pt electrodes with peaks at ≈0.1 V. The onset potential of the ORR is only slightly more positive at Pt (≈0.4 V) than Pd (≈0.3 V) as would be expected given previous studies of the electrocatalytic activity of unalloyed metals for oxygen-reduction demonstrating that Pt is the best (lowest overpotential) ORR electrocatalyst in aqueous media and is closely follow by Pd.[33] The mechanism for the ORR also appears to be the same at Pd and Pt electrodes, due to the respective voltammetric peak areas being similar, indicating that the amount of charge transferred is similar in both cases. Voltammetry at both Pt and Pd electrodes also showed an oxidation at ≈0.6 V, corresponding to irreversible dema oxidation. Blanks recorded in deaerated [dema][TfO] in a dry N_2-atmosphere glovebox are not presented in order to preserve clarity.

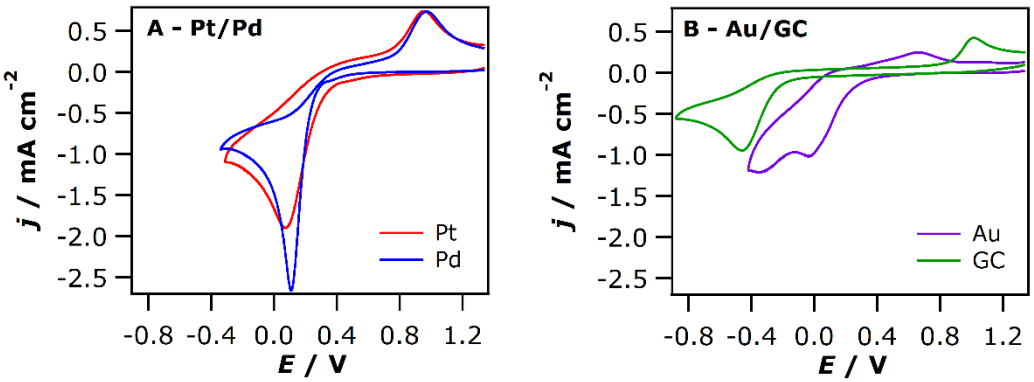


Figure 4.9 Cyclic voltammograms recorded in O_2-saturated [dema][TfO] at stationary Pt, GC, Au and Pd electrodes at 100 mV s^{-1}. All potential sweeps begin in a negative-going direction. (A) compares Pt and Pd electrodes. (B) compares Au and GC electrodes. Axes of both plots (A) and (B) are the same to aid comparison while maintaining clarity.

Experimental voltammetry and computer simulation by Khan *et al.* to elucidate the ORR mechanism in protic ionic liquids at different electrode materials, suggest the following mechanism for the ORR in PILs, which has been adapted for the 2-electron ORR in pure [dema][TfO].[19]

E $O_2 + e^- \rightarrow O_2^{\bullet -}$ (28)

C $O_2^{\bullet -} + [dema]^+ \rightarrow HO_2^{\bullet} + dema$ (29)

E $HO_2^{\bullet} + e^- \rightarrow HO_2^{\bullet -}$ (30)

C $HO_2^{\bullet -} + [dema]^+ \rightarrow H_2O_2 + dema$ (31)

In their work with ethylammonium nitrate (EAN) Khan *et al.* demonstrated that for this particular PIL the ORR favoured the 2-electron pathway to produce H_2O_2 at Au, GC and Pt electrodes.[19] The ECEC process they propose fits the voltammetric observations of the ORR in [dema][TfO] recorded at GC and Au electrodes (see Figure 4.9 (B)), whereby O_2 is first reduced to superoxide (Equation 28), a chemical protonation from the PIL cation then occurs producing a hydroperoxyl radical (Equation 29), which can then be

electrochemically reduced to the hydroperoxyl anion (Equation 30), followed by another chemical protonation by the PIL cation (Equation 31), to make hydrogen peroxide as the final ORR product. Contrary to Khan *et al.*'s observations in EAN,[19] at Pt and Pd electrodes in [dema][TfO] the ORR favours the 4-electron process to form H_2O. However, their proposed mechanism could be adapted to accommodate a 4-electron ORR, and is described by Equations 32–36, but it should be noted that this is a purely speculative pathway.[19,34]

E $O_2 + e^- \rightarrow O_2^{\bullet -}$ (32)

C $O_2^{\bullet -} + [dema]^+ \rightarrow HO_2^{\bullet} + dema$ (33)

E $HO_2^{\bullet} + e^- \rightarrow HO_2^{\bullet -}$ (34)

C $HO_2^{\bullet -} + [dema]^+ \rightarrow H_2O_2 + dema$ (35)

E $H_2O_2 + 2[dema]^+ + 2e^- \rightarrow 2H_2O$ (36)

The ECEC mechanism, Equations 28–31, is represented by one single peak, rather than one peak for each electrochemical reduction at different potentials, at Pt, Pd and GC electrodes because the values of the electron transfer constants of the two electrochemical steps, were found to be of similar magnitudes in EAN as is likely the case in [dema][TfO].[19] The purple CV presented in Figure 4.9 (B) shows the ORR recorded at an Au electrode where two clear ORR peaks are observed and closely resembles previous work on Au-ORR voltammetry in PILs other than [dema][TfO].[19] The two peaks at Au can be understood because previous studies have shown the electron transfer rate constant of the first electrochemical ORR step in Equation 28 is an order of magnitude larger than the electrochemical second electrochemical step in Equation 30 at an Au electrode.[19] An oxidation

concomitant with the ORR is observed at an Au electrode at ≈0.7 V and could be dema oxidation, although if this is dema oxidation, it occurs about 0.2 V more negative than at Pt, Pd and GC, all at ≈ 1.0 V.

Figure 4.10 shows voltammetry of H_2-saturated [dema][TfO] recorded at Pt and GC electrodes. The H_2 saturation concentration of [dema][TfO] at room temperature has previously been shown to be 0.23 ± 0.01 mM dm^{-3}.[11] The red CV in (A) shows the oxidation of hydrogen and concomitant anion protonation (positive current), $[TfO]^-$ as the only available proton acceptor, to give triflic acid (TfOH) (see equation 37).

$$2[TfO]^- + H_2 \rightarrow 2TfOH + 2e^- \quad (37)$$

$$2TfOH + 2e^- \rightarrow 2[TfO]^- + H_2 \quad (38)$$

The potential at which dema is oxidised appears notably less positive at an Au electrode, around 0.6 V, than any of the other electrode materials, including Pt. This can be explained by gold's notably strong electrocatalytic activity toward amine oxidation.[35]

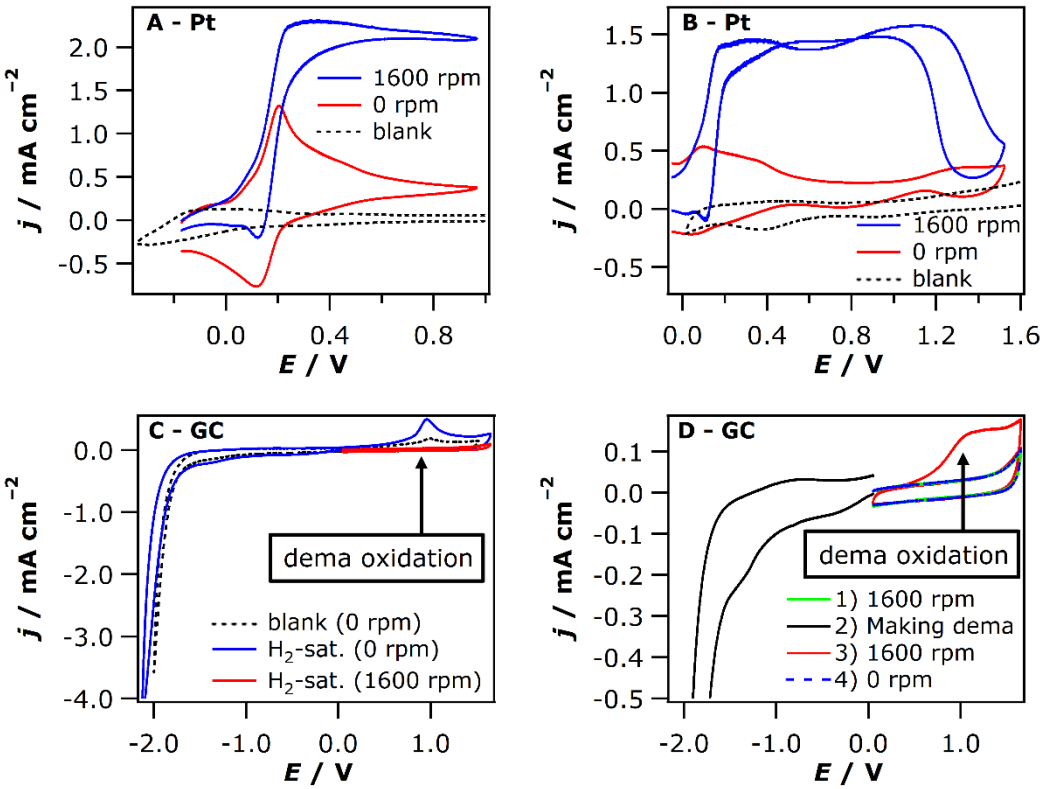


Figure 4.10 Cyclic voltammograms (CVs) recorded in H_2-saturated [dema][TfO] at stationary and rotating Pt and GC electrodes, at 100 mV s^{-1}. **(A)** CVs at rotating and stationary Pt electrodes. **(B)** CVs recorded at rotating and stationary Pt electrodes up to a higher potential of ≈1.55 V. **(C)** CVs recorded at stationary and rotating GC electrodes. **(D)** CVs recorded at stationary and rotating GC electrodes numbered in order that the consecutive CVs were recorded. 1) is recorded rotating at 1,600 rpm over dema oxidation potentials, 2) is recorded at a stationary electrode over PIL-cation reduction potentials to make dema at the electrode surface, 3) is recorded at a rotating electrode over dema oxidation potentials after the electrode has been rotated at 1,600 rpm for 10 minutes prior to recording the CV, 4) is recorded at a stationary electrode over dema oxidation potentials. Blank CVs are recorded in deaerated [dema][TfO] at either a stationary Pt or GC electrode.

After H_2 is oxidised in the positive sweep, TfOH is then reduced back to $[TfO]^-$ and H_2 on the negative sweep when using a stationary Pt electrode (see Equation 38). The H_2/TfOH redox process is reversible in [dema][TfO][11], as it is in the similar redox couple H_2/$HNTf_2$ in triethylammonium NTf_2 ([tea][NTf_2])[36]. The blue voltammogram in Figure 4.10 (A) shows the oxidation of hydrogen as described

by Equation 37 but at a Pt electrode rotating at 1,600 rpm which reaches a j_L of 2.3 mA cm^{-2} at a potential positive of ≈0.3 V. The HOR onset potential is approximately 0.0 V. An HOR j_L is recorded at a Pt electrode up to ≈1.3 V but rapidly decreases as the potential is swept more positive (see Figure 4.10 (B) blue voltammogram). This loss of HOR activity is attributed to the oxidation of low concentrations of H_2O in the PIL forming an HOR-inhibiting Pt-oxide layer on the electrode surface,[11, 37] although this has previously been attributed to inhibition by $[TfO]^-$ anion oxidation to form platinum(II) triflate complexes on the electrode surface.[5] The red voltammogram in Figure 4.10 (B) recorded at a stationary Pt electrode in H_2-saturated [dema][TfO] shows an increase in positive current density coinciding with loss of HOR current density confirming a new oxidation process (oxide-layer formation) occurs at this potential and inhibits the HOR. The formation of the Pt-O_2 layer and its effect on the HOR is further confirmed by the rapid increase in the HOR current density in the negative-going sweep from ≈1.3 V as the oxide layer is removed from the electrode surface once again making the Pt accessible to H_2. The pre-Pt-O_2 formation HOR j_L in Figure 4.10 (B) of ≈1.5 mA cm^{-2} on the forward going sweep is achieved once again on the negative-going sweep after Pt-O_2 removal negative of ≈1.0 V. The loss of HOR current in the potential region between 1.0 V and 1.5 V has shown H_2 to be a fairly good probe molecule for indirect detection of oxide formation and removal in [dema][TfO] with oxide formation between ca. 1.3 V and 1.5 V and oxide removal between ca. 1.3 V and 1.0 V. The lower HOR current densities observed between Figure 4.10 (A) and (B) are likely the result of a loss of H_2 from [dema][TfO] in (B), deviating from the saturation concentration due to fast H_2 diffusion in [dema][TfO]. Oxide formation and removal in PILs is discussed further in Chapter 6.

Glassy-carbon is known to be a very poor electrocatalyst for hydrogen oxidation generally however, to determine whether this is the case in PILs, CVs were recorded in H_2-saturated [dema][TfO] using a GC electrode. The CVs in Figure 4.10 (C), recorded using a GC electrode, show a number of redox processes but none of them are H_2 oxidation. Firstly, the blank CV recorded in deaerated [dema][TfO] at a stationary GC electrode shows a large current density negative of ≈−1.5 V which corresponds to the electrolytic breakdown of the PIL cation to make neutral dema and H_2 (Equation 39). If the H_2 near the electrode surface could be oxidised back onto neutral dema (Equation 40), a positive current around −1.5 V should occur on the positive sweep, but it is absent, meaning that H_2 is not oxidised.

$$2[dema]^+ + 2e^- \rightarrow 2dema + H_2 \quad (39)$$

$$2dema + H_2 \rightarrow 2[dema]^+ + 2e^- \quad (40)$$

H_2 oxidation and concomitant anion protonation, as observed at Pt and described by Equation 37, is also not observed at GC. The blue and red voltammograms in Figure 4.10 (C) of H_2-saturated [dema][TfO] confirm the absence of hydrogen oxidation since the only oxidation observed (at ≈1.0 V, blue voltammogram) occurs only after $[dema]^+$ has been reduced to dema. The absence of HOR at GC strongly indicates that the oxidation at 1.0 V in Figure 4.10 (C) is dema oxidation and, in conjunction with Figure 4.6 (B) and Figure 4.1, that the dema resulting from ORR is responsible for the oxidation observed at ≈1.0 V in voltammetry in O_2-saturated [dema][TfO] recorded using both Pt and GC electrodes. The product of dema oxidation is unknown but given that it is chemically irreversible, it is likely that a radical species forms which quickly reacts chemically to form a stable

molecule such that a reduction of the dema oxidation product is not observed in voltammetric experiments.

The sequence of CVs presented in Figure 4.10 (D) recorded at a GC electrode demonstrate the physisorption of neutral dema on the GC surface. Firstly, a CV was recorded at a rotating electrode at dema-oxidising potentials and showed no evidence of dema oxidation (CV 1). Then a CV was recorded at a stationary GC electrode in a negative-going direction from 0 V to around −1.8 V, so that $[dema]^+$ is reduced to give neutral dema (Equation 39), which is left near the electrode surface and is not oxidised (CV 2). Next, the electrode, starting with a high concentration of neutral dema near to it, was rotated at 1,600 rpm for 10 minutes to remove any dema from the diffusion layer preventing the oxidation of any dema in solution being observed. Another CV was recorded, again at a rotating GC electrode, but swept positive of 0 V over dema oxidation potentials (CV 3). A clear oxidation with a peak at ≈1.0 V corresponding to dema oxidation is visible, meaning that neutral dema must have been adsorbed to the electrode. CV 4 shows a return to the same CV shape recorded before the generation of dema next to the electrode and after the dema stuck to the electrode was oxidised, suggesting that the electrode is now free of dema contamination. The adsorption of dema on Pt electrodes will be shown to impact fuel-cell performance in Chapter 7.

The HOR and ORR have thus far been studied in [dema][TfO] in isolation, so it is now appropriate to consider them together as the anodic and cathodic reactions in a PIL-PEM fuel cell. The maximum cell potential of (E_{cell}) of a single H_2/O_2 fuel cell is the potential difference between the HOR and the ORR, sometimes called the open-circuit potential (OCP). While the theoretical maximum E_{cell} can be

calculated by thermodynamic values of the reactants and products, in a real system the slow kinetics of the fuel cell reactions, especially of the ORR brought about by poor electrocatalysts, result in a much lower overall E_{cell}. This is due to the high overpotential required for the ORR and HOR, but especially for the ORR.[1a] By comparing the voltammetrically-determined potentials at which the ORR and HOR occur at Pt electrodes, the best known unalloyed metal for oxygen electrocatalysis,[33] the likely E_{cell} of a H_2/O_2 [dema][TfO]-electrolyte fuel cell can be obtained. Furthermore, the effect of the presence of acid or base in the electrolyte on likely E_{cell} values can also be investigated.

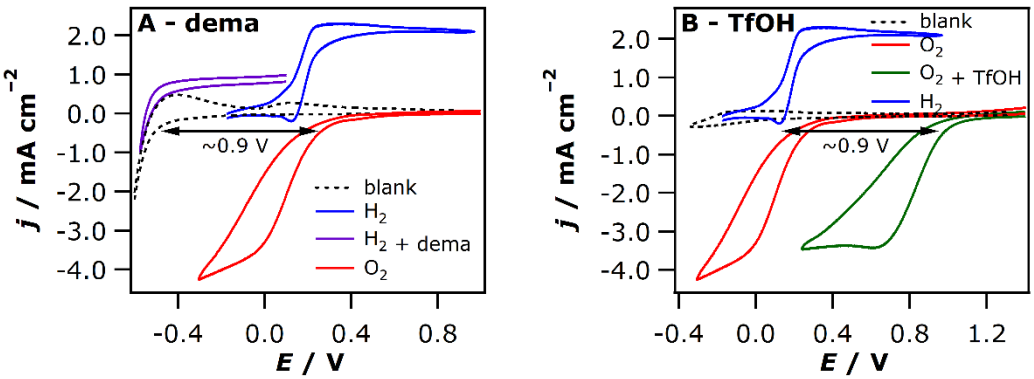


Figure 4.11 Cyclic voltammograms recorded in O_2-saturated [dema][TfO] and O_2-saturated [dema][TfO] containing 0.1 mol dm^{-3} TfOH using Pt and glassy-carbon rotating-disk electrodes at 100 mV s^{-1}. (A) and (B) are recorded at 1,600 rpm, and (C) and (D) at 0 rpm. The initial sweeps were in the negative direction.

The CVs in Figure 4.11 (A) show the ORR in O_2-saturated [dema][TfO] (red CV), the HOR in H_2-saturated [dema][TfO] (blue CV), and the HOR in H_2-saturated [dema][TfO] containing 0.1 mol dm^{-3} dema. The potential at which the HOR occurs shifts by about 0.9 V to a significantly more negative potential upon addition of dema. This is because the proton acceptor in the HOR has changed from $[TfO]^-$, a poor base (see Equation 37), to dema, a strong base (see Equation 39). This negative shift in the HOR upon the addition of dema versus the ORR, results in a potential difference, and likely E_{cell}, of about 0.9 V. The other

notable difference in the HOR upon addition of dema is that j_L decreased from 2.3 mA cm^{-2} in the pure PIL to ≈0.8 mA cm^{-2} in the presence of dema; this is likely due to the aforementioned electrode poisoning effect of dema sticking on Pt and GC electrode surfaces. Similarly, the CVs in Figure 4.11 (B) also show a likely E_{cell} of about 0.9 V but only when the ORR has shifted to more positive potentials because of the presence of 0.1 mol dm^{-3} triflic acid, a strong proton donor (see Equation 19) rather than the weakly proton-donating [dema]$^+$ in the pure PIL (see Equation 16). The presence of additional proton donors or acceptors has a significant effect on the reaction mechanism and potentials at which the HOR and ORR occur in PILs.

The voltammetrically determined likely maximum E_{cell} of a PIL-PEM system with either added acid or base, or pure [dema][TfO], is presented in Figure 4.12 with accompanying schematics depicting how protons are shuttled between the fuel cell anode and cathode in each of the systems. Figure 4.12 (A) shows voltammetry of O_2-saturated [dema][TfO] containing 0.1 mol dm^{-3} triflic acid and H_2-saturated [dema][TfO]. The potential difference between the onset potentials of the ORR and HOR is ≈0.9 V. Figure 4.12 (B) shows the schematic of a fuel cell system containing triflic acid where [TfO]$^-$/TfOH act as the proton shuttles between the fuel cell anode and cathode (see Equation 41 for the overall reaction).

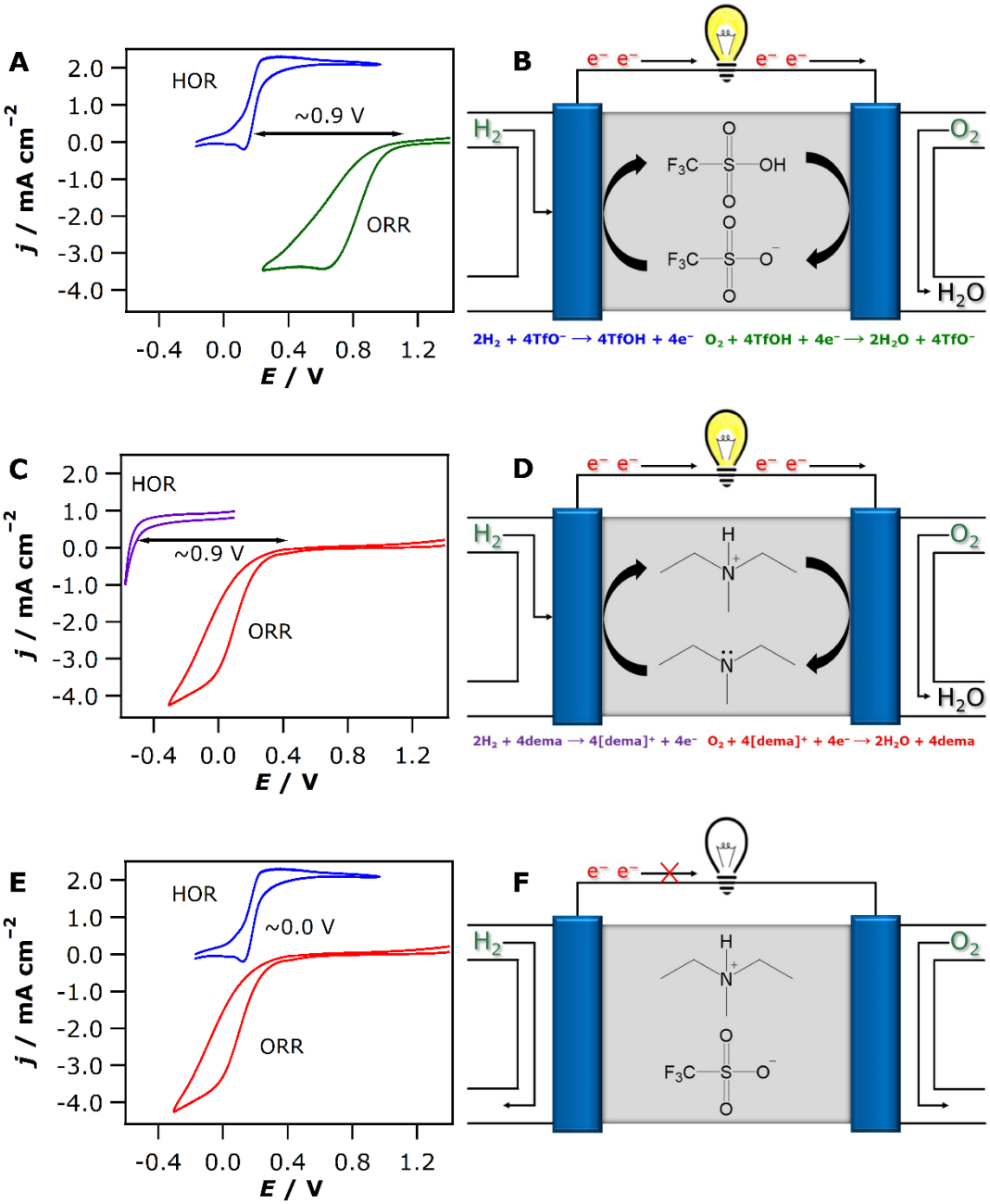


Figure 4.12 Cyclic voltammograms of (A) H_2-saturated [dema][TfO] and O_2-saturated [dema][TfO] containing 0.1 mol dm^{-3} TfOH, (C) O_2-saturated [dema][TfO] and H_2-saturated [dema][TfO] containing 0.1 mol dm^{-3} dema, and (E) H_2- and O_2-saturated [dema][TfO], respectively. Voltammograms were recorded using a 5-mm diameter Pt electrode rotating at 1,600 rpm and at 100 mV s^{-1}. The arrow in each frame shows the approximate difference between the ORR and HOR onset potential. B and D show the proposed operation of [dema][TfO]-based fuel cells containing triflic acid and diethylmethylamine, respectively, as electrolyte additive. F shows that, in the absence of added triflic acid or diethylmethylamine, the cell containing [dema][TfO] cannot sustain current flow.

Figure 4.12 (C) shows voltammetry of H_2-saturated [dema][TfO] containing 0.1 mol dm^{-3} dema and O_2-saturated [dema][TfO]. The potential difference between the onset potentials of the ORR and HOR is again ≈0.9 V. Figure 4.12 (D) shows

the schematic of a fuel-cell system containing dema where dema/[dema]$^+$ act as the proton shuttles between the fuel cell anode and cathode, which is the proton conduction vehicle proposed by Watanabe *et al*. in pure PILs (see Equation 41 for the overall reaction).[12]

The voltammetry of H_2- and O_2-saturated [dema][TfO], respectively, is shown in Figure 4.12 (E). In pure [dema][TfO] the onset potentials of the HOR and ORR are very close together, almost overlapping, giving an E_{cell} of ≈0 V; meaning that a pure [dema][TfO] system could not be used as fuel cell electrolyte. To explore why this 0 V potential difference is observed in the voltammetry presented, reveals fundamental flaws with [dema][TfO] as a fuel cell electrolyte and improves our understanding of PILs generally as fuel cell electrolytes. For example, Figure 4.12 (F) shows the schematic of a pure [dema][TfO] fuel cell and would require H_2 to be oxidised onto $[TfO]^-$ to give TfOH at the anode and O_2 to be reduced proton-coupled with $[dema]^+$ to give dema and H_2O, which means that protons are not shuttled across from anode to cathode. In effect, were the fuel cell to run, the PIL would be electrochemically broken down into the parent acid and base species, with TfOH formed at the anode and dema at the cathode (see Equation 42). Eventually, the dema and TfOH would react chemically to produce [dema][TfO] and heat. The pure [dema][TfO] fuel cell cannot operate as proposed by Watanabe *et al*., with dema/$[dema]^+$ as the proton shuttle, because in order for H_2 to be oxidised onto dema to make $[dema]^+$ there must already exist a bulk concentration of dema at the anode, which cannot be the case because the ORR at the cathode (making dema) requires the electrons from the HOR; consequently, the only available HOR reaction is H_2 and $[TfO]^-$ being oxidised to TfOH, as shown

in the Figure 4.12 (F) schematic. For a viable PIL-PEM fuel cell to operate, additional proton shuttles must be added to the PIL.

$$2H_2 + O_2 \rightarrow 2H_2O \qquad \Delta G^{\ominus} = -237.13 \text{ kJ mol}^{-1} \quad (41)$$

$$2H_2 + O_2 + 4[\text{dema}][\text{TfO}] \rightarrow 4\text{dema} + 4\text{TfOH} + 2H_2O \qquad \Delta G^{\ominus} = ? \quad (42)$$

In addition to the absence of a suitable proton shuttle in pure [dema][TfO], the 0 V potential difference between the HOR and the ORR can be explained by the thermodynamics of Equation 42. In order for the HOR and ORR to proceed in pure [dema][TfO], making water in an exergonic process,[38] energy also has to be supplied to return [dema][TfO] to its parent acid and base in an endergonic process that offsets the energy released in the reaction of H_2 and O_2 to make water. The $\Delta_r G^{\ominus}$ of H_2 and O_2 to make water, as occurs in a conventional humidified fuel cell, is shown in Equation 41 and can be calculated as follows under standard conditions.

$$\begin{aligned} \Delta_r G^{\ominus} &= \sum_{products} \nu \Delta_f G^{\ominus} - \sum_{reactants} \nu \Delta_f G^{\ominus} \\ \Delta_r G^{\ominus} &= (2 \times -237.13) - (2 \times 0 + 1 \times 0) \\ \Delta_r G^{\ominus} &= -237.13 \; kJmol^{-1} \\ N.B.\ \Delta_r G^{\ominus} &= \Delta_f G^{\ominus}_{H_2O}, because\ \Delta_f G^{\ominus}\ of\ all\ reactants\ is\ zero \end{aligned} \quad (43)$$

However, according to Equation 42, in a pure PIL electrolyte, the PIL must return to its parent acid and base species for the formation of H_2O to occur because $[\text{dema}]^+$ and $[\text{TfO}]^-$ are reactants. Since $\Delta_r G^{\ominus}$ for a reaction is proportional to the equilibrium constant (under standard conditions), $K_{eq}^{\ominus}$, as described by

Equation 44, and $K_{eq}^{\ominus}$ can be calculated from the pK_a values from the acid/base reaction of PIL synthesis using Equation 45, the $\Delta_r G^{\ominus}$ of a [dema][TfO]-coupled water formation reaction can be calculated (shown by Equation 47)

$$\Delta_r G^{\ominus} = -RTLnK_{eq}^{\ominus} \tag{44}$$

$$\text{p}K_{eq} = \text{p}K_{a(\text{parent acid})} - \text{p}K_{a(\text{conjugate acid of the parent base})}$$

$$\text{p}K_{eq} = \text{p}K_{a(\text{TfOH})} - \text{p}K_{a([\text{dema}]^+)}$$

$$\text{p}K_{eq} = -14 - 10.6 \tag{45}$$

$$\text{p}K_{eq} = -24.6$$

$$K_{eq} = 3.98 \times 10^{24}$$

$$\Delta_r G^{\ominus} = -8.31441 \times 298.15 \times Ln(3.98 \times 10^{24}) \tag{46}$$

$$\Delta_r G^{\ominus} = -140.41615\ kJmol^{-1}$$

$$\Delta_r G_{Total}^{\ominus} = \nu\Delta_r G_{H_2O\ formation}^{\ominus} - \nu\Delta_r G_{[dema][TfO]\ formation}^{\ominus}$$

$$\Delta_r G_{Total}^{\ominus} = (2 \times -237.13) - (4 \times -140.41615) \tag{47}$$

$$\Delta_r G_{Total}^{\ominus} = 87.40458\ kJmol^{-1}$$

The positive $\Delta_r G^{\ominus}$ of the [dema][TfO]-coupled fuel-cell reaction shown in Equations 42 and 47 means that 87.4 kJ per mole O_2 has to be provided to the system in order for the reaction to proceed. In other words, a galvanic system that provides 474.6 kJ per mole O_2 of energy through the exergonic reaction of H_2 and O_2 in a traditional fuel cell would become an electrolytic system, requiring ≈87.4 kJ per mole O_2 of energy, because of the highly endergonic formation of parent acid and base from the PIL. The above calculations, along with the lack of a viable proton shuttle, explain the ORR and HOR redox potentials occurring at approximately the same potential in the voltammetry of pure [dema][TfO] in Figure 4.12 (E) and the predicted lack of a cell potential in such a system.

Furthermore, because of the relationship between the cell potential and the change in Gibbs free energy of reaction described in Equation 48, an E_{cell} can be calculated for a [dema][TfO]-coupled fuel cell. The calculated E_{cell} of a [dema][TfO]-coupled fuel cell was found to be ≈−0.23 V, meaning that a potential has to be applied for the fuel cell reaction to proceed due to the negative potential, and it is also a value close to the ≈0 V potential difference observed between the HOR and ORR in the voltammetry presented in Figure 4.12 (E). These calculations can therefore give an approximation of the likely cell potential. It should also be noted that unlike the voltammetry presented which is subject to ORR and HOR overpotentials, the calculations above consider only thermodynamics and therefore theoretical maximum cell potentials and not the effects of reaction rate.

$$\Delta_r G^{\ominus}_{Total} = -nFE^{\ominus}_{cell}$$

$$E^{\ominus}_{cell} = \frac{\Delta_r G^{\ominus}_{Total}}{-nF} \qquad (48)$$

$$E^{\ominus}_{cell} = \frac{87404.58}{-4 \times 96484.56}$$

$$E^{\ominus}_{cell} = -0.23\ V$$

Since a maximum E_{cell} value can be approximated for a pure PIL electrolyte fuel cell based on the $\Delta_r G^{\ominus}$ of PIL synthesis and $\Delta_r G^{\ominus}$ of H_2O formation, and since $\Delta_r G^{\ominus}$ of PIL synthesis can be related to the difference in pK_a between the parent acid and base of the PIL ($\Delta pK_a \equiv pK_{eq}$), this relationship can be expressed in the form of Figure 4.13.

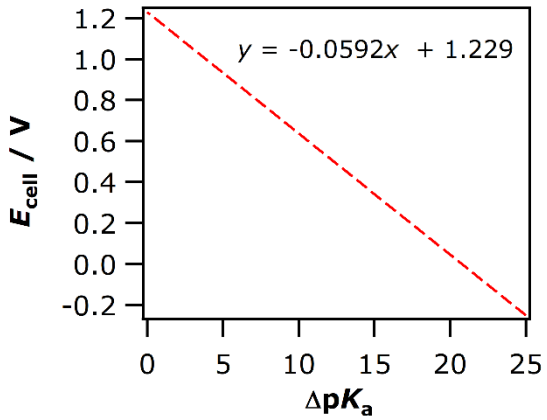


Figure 4.13 Relationship between the difference in pK_a of the parent acid and base in a protic ionic liquid (PIL) and maximum cell potential of a pure PIL-electrolyte H_2/O_2 fuel cell operating under standard conditions from thermodynamic calculations shown in equations 43 to 48.

From Figure 4.13 it can been seen that a pure PIL H_2/O_2 fuel cell system with a parent acid and base ΔpK_a of 20.76 or greater, will be electrolytic, requiring a potential to be applied for the reaction to proceed. Conversely, a ΔpK_a less than 20.76 will result in the fuel cell functioning galvanically with an increasing E_{cell} as

PILs with an increasingly lower ΔpK_a are chosen as the fuel cell electrolyte. A problem arises however in choosing PILs with increasingly low ΔpK_as, because the concentrations of neutral species will increase as the PIL synthesis equilibrium shifts away from product formation, resulting in volatile and toxic base and acid which would likely prevent the use of these low-ΔpK_a electrolytes at elevated temperatures, as intended for PIL electrolytes. Previous studies have suggested that a ΔpK_a of 10 or more is required for a high-ionicity PIL in which case 'complete' proton transfer from the acid to base has occurred[39]; this would result in a PIL-electrolyte fuel cell with an E_{cell} of 0.637 V and would be the highest theoretical E_{cell} possible using a pure PIL as an electrolyte. The gradient of the ΔpK_a / E_{cell} relationship is -0.0592 V per unit ΔpK_a and is Nernstian in origin.

Using the principles of thermodynamics, the cell potential of an hypothetical pure[dema][TfO] fuel-cell device has been calculated and is found to be close to that observed in the experimental voltammetry. Can this be repeated for [dema][TfO] with added triflic acid or dema, which have each been shown by voltammetric methods to have a cell potential of ≈0.9 V? Unfortunately, the case is not the same as in pure [dema][TfO] since neither proton shuttling species, $[TfO]^-$/TfOH in the acidified PIL and dema/$[dema]^+$ in the basified PIL (see Figure 4.12 (B) and (D)), are consumed or changed in the overall fuel-cell reaction which reverts to Equation 41 in the presence of a suitable proton shuttle. The combination of the ORR and HOR fuel cell half reactions in Equations 49 and 50 for acidified and basified [dema][TfO] respectively, confirm the overall fuel-cell reaction is that of $2H_2$ and O_2 making $2H_2O$, the same as in conventional fuel-cell systems.

$$2H_2 + 4[TfO]^- + O_2 + 4TfOH + 4e^- \rightarrow 2H_2O + 4TfOH + 4[TfO]^- + 4e^- \quad (49)$$

$$2H_2 + 4dema + O_2 + 4[dema]^+ + 4e^- \rightarrow 2H_2O + 4[dema]^+ + 4dema + 4e^- \quad (50)$$

A consequence of the overall reaction being the formation of water, is that the E_{cell} of an acidified or basified PIL fuel cell system is limited to 1.229 V from the −474.26 kJ mol^{-1} O_2 $\Delta_f G^{\ominus}$ of water. Furthermore, it indicates that the chemical identity of the added proton shuttle (either TfOH or dema) will not affect the overall E_{cell} of a PIL-based fuel cell. For example, for [dema][TfO] acidified with triflic acid to provide a $[TfO]^-$/TfOH proton-acceptor/proton-donor shuttle, the thermodynamically favourable $-\Delta G$ of deprotonation of the triflic acid (arising from the -14 pK_a to TfOH) in the ORR, is negated by the equally positive ΔG of re-protonation of $[TfO]^-$ at the HOR. This leaves only the $-\Delta G$ of water formation as the driving force for the fuel cell. The same can be said of basified [dema][TfO] but the $-\Delta G$ of protonation of dema of the HOR is negated by the equally positive ΔG of deprotonation of $[dema]^+$ of the ORR, again leaving the $-\Delta G$ of water formation as the only driving force for the fuel cell. Also, were an acid weaker than triflic acid be added to pure [dema][TfO] to make the ORR onset occur at a more positive potential (see Figure 4.8), but less positive than in the presence of TfOH, the overall theoretical E_{cell} would be less than 1.229 V because the $-\Delta G$ of proton donation from the weak acid in the ORR would be less than the $+\Delta G$ of re-protonating $[TfO]^-$, which would still be the HOR reaction. It would be expected that the E_{cell} would be dependent on the pK_a of the acid or base species added. A maximum theoretical E_{cell} of 1.229 V could therefore only be achieved if the added acid or base was TfOH or dema to [dema][TfO]. More generally, based on thermodynamic calculations for a PIL-based fuel cell with an added proton shuttle,

the chemical identity of the added species must either be the parent acid or base of the PIL if a maximum theoretical E_{cell} value of 1.229 V (determined by $\Delta_r G^{\ominus}$ of H_2O formation) is to be achieved.

To ensure that the voltammetric comparisons of the HOR and ORR in the presence and absence of acid or base presented in Figure 4.11 and Figure 4.12 were accurate, CVs were recorded in O_2-saturated [dema][TfO] containing added dema, and in H_2-saturated [dema][TfO] containing added TfOH. The presence of dema was not expected to affect the ORR potential since dema is not a proton donor; this is confirmed by Figure 4.14 (B). Here the ORR onset potential is only affected by the presence of TfOH (green CV), and not dema (turquoise CV). A notable effect of the presence of dema on the ORR is that the j_L has dropped to approximately half its value at ≈1.8 mA cm^{-2}. This loss of current density is indicative of dema poisoning the Pt electrode surface, inhibiting the availability of Pt sites to O_2 and lowering the electrochemically active surface area of the electrode. The electrode-poisoning effect of dema has been proven at a GC electrode and shown in Figure 4.10 (D). The addition of dema as a proton shuttle to a [dema][TfO] fuel-cell electrolyte is not a viable solution to pure [dema][TfO]'s innate lack of a proton conduction mechanism, because of the observed electrode-poisoning effect and dema's high volatility.

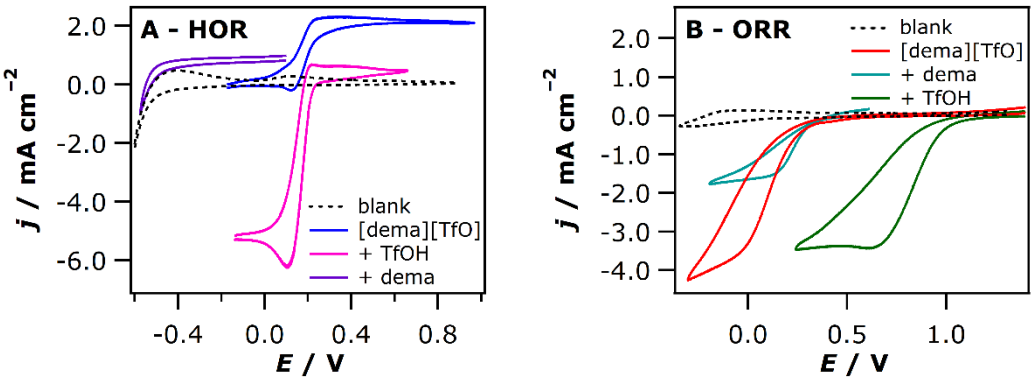


Figure 4.14 (A) - Voltammograms recorded in H_2-saturated [dema][TfO] in the absence or presence of either triflic acid or dema in a 0.1 mol dm^{-3} concentration at a Pt RDE rotating at 1,600 rpm. (B) – Voltammograms recorded in O_2-saturated [dema][TfO] in the absence or presence of either triflic acid or dema at a Pt RDE rotating at 1,600 rpm. The scan rate is 100 mV s^{-1}.

The presence of TfOH was not expected to affect the HOR as TfOH is not a proton acceptor; this is confirmed by the voltammograms in Figure 4.14 (A). Here the HOR onset potential is only affected by the presence of dema (purple CV), and not TfOH (pink CV). The HOR j_L is notably smaller in the presence of TfOH, however, this is most likely a result of a loss of H_2 saturation and lower H_2 concentration due to fast H_2 diffusion in the PIL. The large cathodic (negative) current observed in the pink CV in Figure 4.14 (A) is the reduction of TfOH to $[TfO]^-$ and H_2 (see Equation 38). The negligible effect of the presence of TfOH on the HOR onset potential and dema on the ORR onset potential validate the description of the ORR/HOR potential difference in Figure 4.12.

4.3.2 Oxygen-reduction and hydrogen-oxidation in [dema][NTf_2]

The effect of the presence of added acid or base on the ORR and HOR, respectively, has been shown in the PIL, [dema][TfO]. However, to confirm whether the observed effects are also observed in other PILs, the ORR and HOR in the presence and absence of acid and base were studied in [dema][NTf_2]. [dema][NTf_2] has the same cation as [dema][TfO] but a different anion, and was chosen because it has

also been studied as a possible H_2/O_2 fuel-cell electrolyte and showed favourable properties.[20,12] The electrochemical breakdown of [dema][NTf_2] is shown voltammetrically in Figure 4.15 recorded at both Pt and GC electrodes. At negative potentials the $[dema]^+$ cation is reduced to H_2 and dema and at positive potentials, the $[NTf_2]^-$ anion is oxidised. At a platinum electrode, H_2 and dema are oxidised to $[dema]^+$ at ≈−0.5 V (Figure 4.15 (A)); this does not occur at the GC electrode which is a poor hydrogen oxidation electrocatalyst. The anodic current peak at ≈1 V in Figure 4.15 (B) is from the oxidation of dema which is present due to the prior reduction of the $[dema]^+$ cation. Like [dema][TfO], the electrochemical window of [dema][NTf_2] is greater at a GC electrode than at Pt because cation reduction occurs at a more negative potential at the GC electrode.

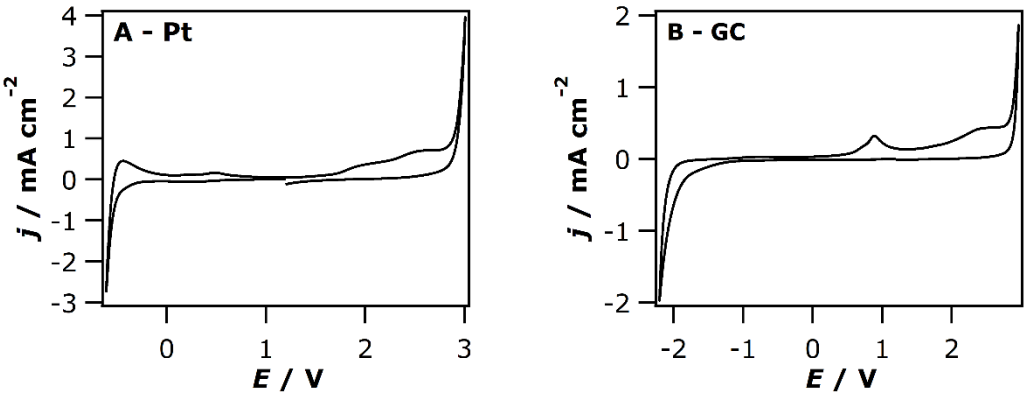


Figure 4.15 CVs of deaerated [dema][NTf_2] recorded at Pt (A) and GC (B) electrodes. Potential cycles begin in a negative-going direction at 100 mV s^{-1} beginning at 1.2 V.

The voltammograms in Figure 4.16 are recorded in O_2-saturated pure [dema][NTf_2] at stationary and rotating Pt and GC electrodes with blanks recorded in deaerated [dema][NTf_2] at each electrode. Oxygen is reduced from ≈0.3 V at Pt and −0.2 V at GC and is very similar to the ORR onset potentials observed in [dema][TfO] (see Figure 4.1). The ORR j_Ls recorded at Pt and GC in [dema][NTf_2]

is slightly greater in [dema][NTf_2], possibly due to a lower viscosity or higher O_2-saturation concentration of [dema][NTf_2], but importantly the ratio of the j_L at Pt and GC is approximately 2:1 as expected, since $[dema]^+$ is the cation donating the proton for the ORR in both PILs (Pt: ≈5 mA cm^{-2}, GC: 2.5 mA cm^{-2}), meaning that H_2O and H_2O_2 are the likely ORR products at Pt and GC respectively (see Equations 16 and 17). Figure 4.1 (A) and (B) also show the oxidation of dema at ≈1.0 V on the positive potential sweeps, after the ORR, at stationary electrodes. The presence of a dema oxidation current at the same potential as observed in [dema][TfO], independent of electrode material, confirms the expectation that the ORR mechanism and products are the same in both PILs.

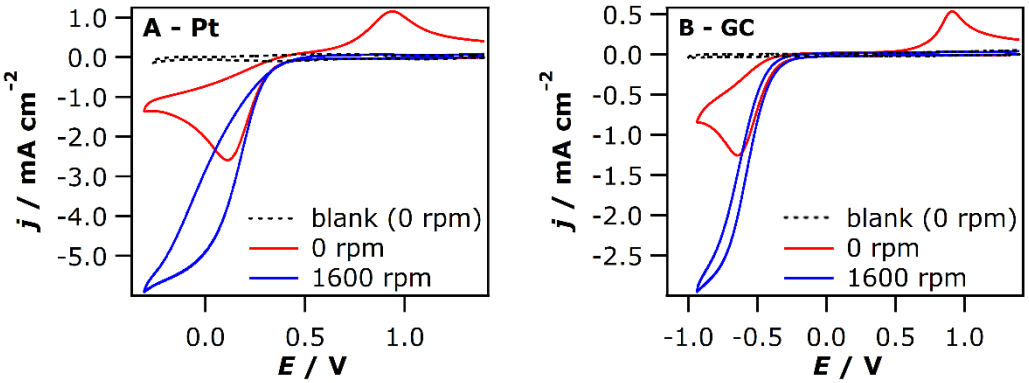


Figure 4.16 Voltammograms of O_2-saturated [dema][NTf_2] at a Pt (A) and GC (B) RDE at 0 and 1,600 rpm. The scan rate is 100 mV s^{-1}. The blanks are recorded in deaerated [dema][NTf_2].

Hydrogen bis(trifluoromethanesulfonyl)imide ($HNTf_2$) was added to [dema][NTf_2] to a concentration of 0.1 mol dm^{-3} and saturated with O_2. CVs were then recorded in the acidified liquid and compared with those in the unacidified liquid as shown in Figure 4.17. The presence of the strong acid, $HNTf_2$ (aqueous pK_a ≈−14) causes the ORR to shift to a more positive potential by ≈0.8 V at Pt and ≈0.7 at GC. This shift in ORR onset potential, like that observed in [dema][TfO], is caused by the change in ORR proton donor from the weakly proton-donating

cation ($[dema]^+$) to strongly proton-donating $HNTf_2$ as shown in Equations 51 and 52 for Pt and GC, respectively. The peak ORR current density in acidified $[dema][NTf_2]$ recorded at Pt and GC remains similar to that observed in pure $[dema][NTf_2]$ at both electrodes, indicating that the reaction stoichiometry has not changed upon acidification. However, despite being similar, there is an observable increase in peak ORR current density at Pt of ≈1 mA cm^{-2} upon acidification observed in $[dema][NTf_2]$ and [dema][TfO]; this could be explained by the dema produced by the ORR in the pure PILs inhibiting the ORR as the potential is swept negative with dema having a greater affinity for Pt than GC. The absence of a dema oxidation peak at 1.0 V also suggests that the dominant ORR mechanism has changed such that dema is not a product, however, it must be noted that if any dema was produced it would be short-lived in the acidified PIL due to chemical proton-transfer reaction with the acid, reducing the chances of an observable oxidation wave.

At Pt:

$$O_2 + 4HNTf_2 + 4e^- \rightarrow 2H_2O + 4[NTf_2]^- \quad (51)$$

At GC:

$$O_2 + 2HNTf_2 + 2e^- \rightarrow H_2O_2 + 2[NTf_2]^- \quad (52)$$

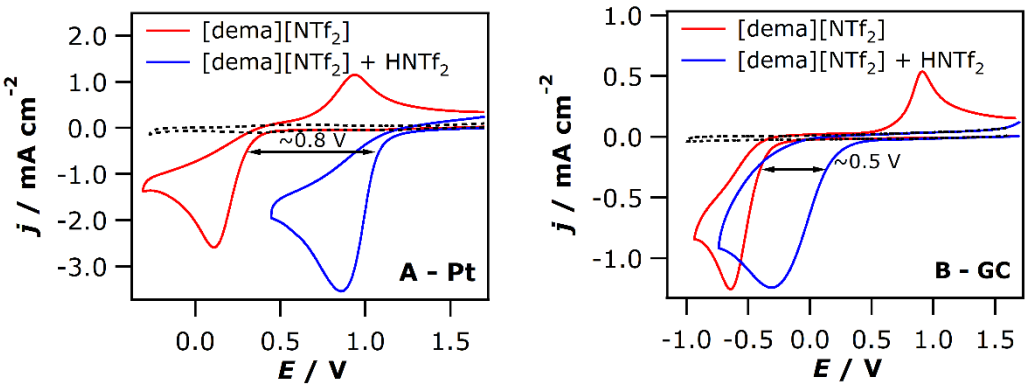


Figure 4.17 Cyclic voltammograms (CVs) recorded in O_2-saturated [dema][NTf_2] at Pt (A) and GC (B) electrodes at 0 rpm in the presence and absence of 0.1 mol dm^{-3} $HNTf_2$. The scan rate is 100 mV s^{-1}. The blanks (black-dotted CVs) are recorded in deaerated, acid-free [dema][NTf_2].

To assess [dema][NTf_2]'s suitability as a fuel-cell electrolyte, and to compare with the ORR voltammetry in the pure and acidified PIL, the HOR has been studied in [dema][NTf_2]. The CVs in Figure 4.18 (A) are of H_2-saturated [dema][NTf_2] recorded at a stationary and rotating Pt electrode. The HOR onset potential is ≈0.2 V, about 0.2 V more positive than the oxidation of H_2 in [dema][TfO], with a j_L of ≈2.25 mA cm^{-2}, a very similar value of j_L to H_2 oxidation in [dema][TfO]. The HOR, as in [dema][TfO], is highly reversible and proceeds according to Equation 53 with the reduction of $HNTf_2$ described by Equation 54.

$$2[NTf_2]^- + H_2 \rightarrow 2HNTf_2 + 2e^- \quad (53)$$

$$2HNTf_2 + 2e^- \rightarrow 2[NTf_2]^- + H_2 \quad (54)$$

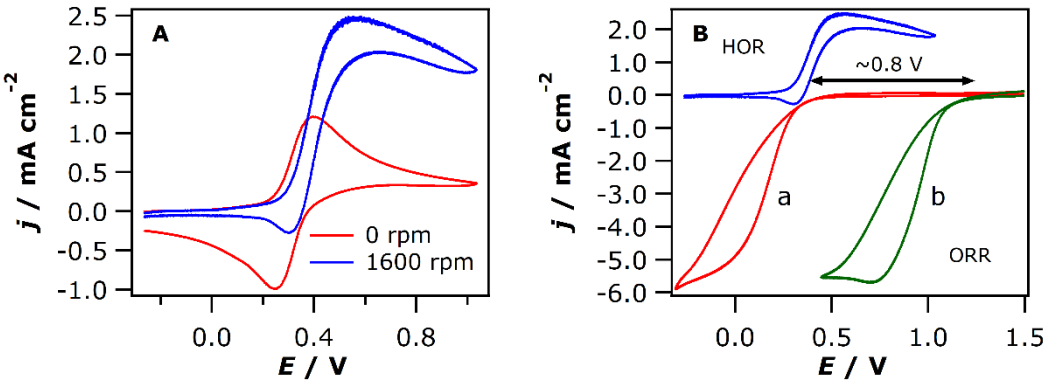


Figure 4.18 (A) – Cyclic voltammograms (CVs) recorded in H_2-saturated [dema][NTf_2] at a Pt electrode at 0 and 1,600 rpm. (B) – CVs recoded in either H_2-saturated pure [dema][NTf_2] (positive current) or O_2-saturated [dema][NTf_2] in the absence (a) and presence (b) of 0.1 mol dm^{-3} $HNTf_2$ (negative currents). The scan rate is 100 mV s^{-1}.

The HOR and ORR, in acidified and pure [dema][NTf_2], are compared in Figure 4.18 (B) and show a potential difference of ≈ 0.8 V when [dema][NTf_2] contains 0.1 mol dm^{-3} $HNTf_2$, causing the ORR to shift to a more positive potential (see ORR CV (b)), an effect described in Figure 4.17. Any PIL-PEM fuel cell device containing [dema][NTf_2] acidified with a strong acid would therefore have a likely maximum E_{cell}, at OCP, of around 0.8 V. In pure [dema][NTf_2], the onset potentials of the HOR and ORR overlap as shown by ORR CV (a) recorded in O_2-saturated [dema][NTf_2] and the HOR CV recorded in H_2-saturated [dema][NTf_2], resulting in what would be a PIL-PEM E_{cell} potential at OCP of 0 V; meaning no power could be drawn from the fuel-cell at any current density. The previously reported E_{cell} of ca. 0.7 V recorded in [dema][NTf_2] is therefore likely due to the presence of acid.[12] The observation that the HOR/ORR potential difference in pure [dema][NTf_2] is very similar to that in pure [dema][TfO], suggests that acidified-PIL electrolytes may be necessary in many (or all) cases for PEMFC applications.

4.4 Conclusions

The electrochemical behaviour of the ORR and HOR has been studied in the PILs [dema][TfO] and [dema][NTf_2] in the presence or absence of either added acid or base. These studies have revealed that the presence of highly proton-donating species, such as the parent acid of the PILs, causes the ORR to shift by ≈0.9 V to a significantly more positive potential, and with no effect on the HOR. Similarly, the presence of a strongly proton-accepting species, such as the parent base of the PILs, causes the HOR to shift by ≈0.9 V to a significantly more negative potential. The ORR $E_{1/2}$ potential changed linearly with the aqueous pK_a of the acid used to acidify the PIL by 50 mV per unit pK_a in the range –3< pK_a <10, which is similar to that expected for a general proton donor and as observed in an aprotic ionic liquid.[16]

The main ORR product, particularly important in fuel cell operation due to the corrosive effects of peroxides, was H_2O at Pt and Pd, and H_2O_2 at GC and Au. The presence of acid or base did not affect the ORR or HOR reaction stoichiometry. The other ORR product, in the absence of added acid and also the PIL cation reduction product, was dema which oxidised irreversibly at Pt and GC at ≈1.0 V in both [dema][TfO] and [dema][NTf_2], likely making a highly reactive radical species. Electrochemically-generated dema was also found to adsorb to Pt and GC electrodes, inhibiting other reactions until removed from the electrode surface by oxidation.

The synthesis of pure PILs, containig no electrochemically detectable concentrations of acid or base, has led to the discovery that the HOR and ORR onset potentials in pure PILs are very similar, making the potential difference

between them (and that of a fuel cell device) ≈0 V. The only way to achieve a potential difference between the HOR and ORR was by adding a strong acid of pK_a ≥−3 or a strong base, such as dema, to shift the HOR or ORR to more negative or positive potentials respectively. The cause of the 0 V HOR/ORR potential difference in pure PILs is the exergonic formation of H_2O from H_2 and O_2, being offset by the endergonic electrolysis of the PIL cation and anion. Furthermore, in the absence of added acid or base, there exists no viable mechanism by which protons can shuttle from the anode to the cathode (while simultaneously shuttling proton acceptors to the anode from the cathode), sustaining the water-forming fuel-cell reaction. The favourable fuel-cell OCPs that have been reported in pure PILs such as [dema][TfO] (1.03 V)[20] and [dema][NTf_2] (0.77 V)[20] at elevated temperatures by Watanabe *et al*. will be explored in Chapter 7.

The consequence of the discoveries presented in this chapter is that for use as PEM fuel-cell electrolytes, PILs require the addition of a proton-shuttling species. The nature of the additive proton shuttle could cause additional problems to PIL-PEM fuel-cell development; dema has been shown to posion electrode materials, is toxic, and highly volatile, and strong acids can cause cell corrosion and may limit the use of new non-noble metal ORR catalysts due to corrosive effects. New challenges now arise to identify electrolyte compositions that retain the advantages offered by PILs (non-volatility and non-corrosivity), while supporting fast proton transport between the anode and cathode of fuel cells.

4.5 References

1. Barbir, F. *PEM Fuel Cells Theory and Practice*. 2nd Edition; Elsevier: United States of America, 2013

2. Ge, X.; Sumboja, A.; Wuu, D.; An, T.; Li, B.; Goh, F. W. T.; Hor, T. S. A.; Zong, Y.; Liu, Z. Oxygen Reduction in Alkaline Media: From Mechanisms to Recent Advances of Catalysts. *ACS Catal.* **2015,** *5* (8), 4643-4667.

3. Bard, A. J.; Faulkner, L. R. *Electrochemical Methods: Fundamentals and Applications*. 2nd Edition; John Wiley & Sons, Inc.: 2001.

4. Yannick Garsany; Olga A. Baturina; Karen E. Swider-Lyons; Kocha, S. S. Experimental Methods for Quantifying the Activity of Platinum Electrocatalysts for the ORR. *Anal. Chem. (Washington, DC, U. S.)* **2010,** *82* (15), 6321–6328.

5. Bautista-Martinez, J. A.; Tang, L.; Belieres, J.-P.; Zeller, R.; Angell, C. A.; Friesen, C. Hydrogen Redox in Protic Ionic Liquids and a Direct Measurement of Proton Thermodynamics. *J. Phys. Chem. C* **2009,** *113*, 12586–12593.

6. Sheng, W.; Gasteiger, H. A.; Shao-Horn, Y. Hydrogen Oxidation and Evolution Reaction Kinetics on Platinum: Acid vs Alkaline Electrolytes. *J. Electrochem. Soc.* **2010,** *157* (11), B1529.

7. Marbán, G.; Valdés-Solís, T. Towards the hydrogen economy? *Int. J. Hydrogen Energy* **2007**, *32* (12), 1625-1637.

8. Colella, W. G.; Jacobson, M. Z.; Golden, D. M. Switching to a U.S. hydrogen fuel cell vehicle fleet: The resultant change in emissions, energy use, and greenhouse gases. *J. Power Sources* **2005**, *150*, 150-181.

9. Ogden, J. M. Prospects for Building a Hydrogen Energy Infrastructure. *Annu. Rev. Energy* **1999,** *24*, 227-279.

10. Walsh, D. A.; Ejigu, A.; Smith, J.; Licence, P. Kinetics and mechanism of oxygen reduction in a protic ionic liquid. *Phys. Chem. Chem. Phys.* **2013,** *15* (20), 7548.

11. Johnson, L.; Ejigu, A.; Licence, P.; Walsh, D. A. Hydrogen Oxidation and Oxygen Reduction at Platinum in Protic Ionic Liquids. *J. Phys. Chem. C* **2012,** *116*, 18048−18056.

12. Lee, S. Y.; Ogawa, A.; Kanno, M.; Nakamoto, H.; Yasuda, T.; Watanabe, M. Nonhumidified Intermediate Temperature Fuel Cells Using Protic Ionic Liquids. *J. Am. Chem. Soc.* **2010,** *132* (28), 9764-9773.

13. Zhang, Y.; Pozo-Gonzalo, C. Variations and applications of the oxygen reduction reaction in ionic liquids. *Chem. Commun. (Cambridge, UK)* **2018,** *54* (31), 3800-3810.

14. Katayama, Y.; Onodera, H.; Yamagata, M.; Miura, T. Electrochemical Reduction of Oxygen in Some Hydrophobic Room-Temperature Molten Salt Systems. *J. Electrochem. Soc.* **2004,** *151* (1), A59.

15. René, A.; Hauchard, D.; Lagrost, C.; Hapiot, P. Superoxide Protonation by Weak Acids in Imidazolium Based Ionic Liquids. *J. Phys. Chem. B* **2009,** *113* (9), 2826–2831.

16. Switzer, E. E.; Zeller, R.; Chen, Q.; Sieradzki, K.; Buttry, D. A.; Friesen, C. Oxygen Reduction Reaction in Ionic Liquids: The Addition of Protic Species. *J. Phys. Chem. C* **2013,** *117* (17), 8683-8690.

17. Yoshizawa, M.; Xu, W.; Angell, C. A. Ionic Liquids by Proton Transfer: Vapor Pressure, Conductivity, and the Relevance of ΔpK_a from Aqueous Solutions. *J. Am. Chem. Soc.* **2003,** *125* (125), 15411-15419.

18. Yasuda, T.; Kinoshita, H.; Miran, M. S.; Tsuzuki, S.; Watanabe, M. Comparative Study on Physicochemical Properties of Protic Ionic Liquids Based on Allylammonium and Propylammonium Cations. *J. Chem. Eng. Data* **2013,** *58* (10), 2724-2732.

19. Khan, A.; Lu, X.; Aldous, L.; Zhao, C. Oxygen Reduction Reaction in Room Temperature Protic Ionic Liquids. *J. Phys. Chem. C* **2013,** *117* (36), 18334-18342.

20. Nakamoto, H.; Watanabe, M. Brønsted acid-base ionic liquids for fuel cell electrolytes. *Chem. Commun. (Cambridge, UK)* **2007,** (24), 2539-2541.

21. Mori, K.; Kobayashi, T.; Sakakibara, K.; Ueda, K. Experimental and theoretical investigation of proton exchange reaction between protic ionic liquid diethylmethylammonium trifluoromethanesulfonate and H_2O. *Chem. Phys. Lett.* **2012,** *552*, 58-63.

22. Wang, L.; Advani, S. G.; Prasad, A. K. Ionic Liquid-Based Composite Membrane for PEMFCs Operating under Low Relative Humidity Conditions. *Electrochem. Solid-State Lett.* **2012,** *15* (4), B44.

23. Miran, M. S.; Yasuda, T.; Susan, M. A. B. H.; Dokko, K.; Watanabe, M. Binary Protic Ionic Liquid Mixtures as a Proton Conductor: High Fuel Cell Reaction Activity and Facile Proton Transport. *J. Phys. Chem. C* **2014,** *118* (48), 27631-27639.

24. Stamenkovic, V. R.; Fowler, B.; Mun, B. S.; Wang, G.; Ross, P. N.; Lucas, C. A.; Markovic, N. M. Improved Oxygen Reduction Activity on $Pt_3Ni(111)$ via Increased Surface Site Availability. *Science (Washington, DC, U. S.)* **2007,** *315* (5811), 493-497.

25. Xie, G.; Okada, T. Water Transport Behavior in Nafion-117 Membranes. *J. Electrochem. Soc.* **1995,** *142* (9), 3057-3062.

26. Zawodzinski, J. T. A.; Derouin, C.; Radzinski, S.; Sherman, R. J.; Smith, V. T.; Springer, T. E.; Gottesfeld, S. Water Uptake by and Transport Through Nafion® 117 Membranes. *J. Electrochem. Soc.* **1993,** *140* (44), 1041-1047.

27. Mack, F.; Heissler, S.; Laukenmann, R.; Zeis, R. Phosphoric acid distribution and its impact on the performance of polybenzimidazole membranes. *J. Power Sources* **2014,** *270*, 627-633.

28. Chandan, A.; Hattenberger, M.; El-Kharouf, A.; Du, S.; Dhir, A.; Self, V.; Pollet, B. G.; Ingram, A.; Bujalski, W. High temperature (HT) polymer electrolyte membrane fuel cells (PEMFC)–A review. *J. Power Sources* **2013,** *231*, 264-278.

29. Zhou, R.; Zheng, Y.; Jaroniec, M.; Qiao, S.-Z. Determination of the Electron Transfer Number for the Oxygen Reduction Reaction: From Theory to Experiment. *ACS Catal.* **2016,** *6* (7), 4720-4728.

30. Biao Liu; Bard, A. J. Scanning Electrochemical Microscopy. 45. Study of the Kinetics of Oxygen Reduction on Platinum with Potential Programming of the Tip. *J. Phys. Chem. B* **2002,** *106* (49), 12801-12806.

31. Williams, R.; Jencks, W. P.; Westheimer, F. H. pK_a Data Listing (Bordwell pK_a Table). University of Wisconsin-Madison [Online], pp 1-33. http://www.chem.wisc.edu/areas/organic/index-chem.htm

32. Ripin, D. H.; Evans, D. A. pKas of Inorganic and Oxo-Acids. http://evans.rc.fas.harvard.edu/pdf/evans_pKa_table.pdf.

33. Nørskov, J. K.; Rossmeisl, J.; Logadottir, A.; Lindqvist, L.; Kitchin, J. R.; Bligaard, T.; Jonsson, H. Origin of the Overpotential for Oxygen Reduction at a Fuel-Cell Cathode. *J. Phys. Chem. B* **2004,** *108*, 17886-17892.

34. Wroblowa, H. S.; Yen-Chi-Pan; Razumney, G. Electroreduction Of Oxygen A New Mechanistic Criterion. *J. Electroanal. Chem.* **1976,** *69*, 195-201.

35. Luo, P.; Zhang, F.; Baldwin, R. P. Comparison of metallic electrodes for constant-potential amperometric detection of carbohydrates, amino acids and related compounds in flow systems. *Anal. Chim. Acta* **1991,** *244*, 169-178.

36. Bentley, C. L.; Bond, A. M.; Hollenkamp, A. F.; Mahon, P. J.; Zhang, J. Mass Transport Studies and Hydrogen Evolution at a Platinum Electrode Using Bis(trifluoromethanesulfonyl)imide as the Proton Source in Ionic Liquids and Conventional Solvents. *J. Phys. Chem. C* **2014,** *118* (51), 29663-29673.

37. Walsh, D. A.; Ejigu, A.; Muhammad, S.; Licence, P. The Formation and Role of Oxide Layers on Pt during Hydrazine Oxidation in Protic Ionic Liquids. *ChemElectroChem* **2014,** *1* (1), 281-288.

38. Atkins, P. W.; De Paula, J. *Atkins' Physical Chemistry*. 9th Edition; Oxford University Press: 2010.

39. Yoshizawa, M.; Xu, W.; Angell, C. A. Ionic Liquids by Proton Transfer: Vapor Pressure, Conductivity, and the Relevance of ΔpK_a from Aqueous Solutions. *J. Am. Chem. Soc.* **2003,** *125*, 15411-15419.

5 Oxygen-Reduction and Hydrogen-Oxidation Reactions in Aprotic Ionic Liquids

5.1 Introduction

The oxygen-reduction reaction (ORR) and hydrogen-oxidation reactions (HOR) in aprotic media have been studied for many years.[1] In recent years, the ORR in aprotic ionic liquids (AILs) has been studied, because of their unique physiochemical properties such as very low volatility and thermal stability.[2] The absence of proton-donating species yields new insights into this well-studied electrocatalytic reaction.[3,4]

AILs differ from protic ionic liquids (PILs) in that AILs do not have a labile proton on the IL cation and instead (typically) have quaternary ammonium or phosphonium cations.[5] This greatly affects the physiochemical and electrochemical properties of AILs because there is no acid-base equilibrium reaction involving transfer of a proton between the IL cation and anion, as occurs in PILs.[6] AILs are therefore typically less volatile and are more electrochemically stable than PILs, with wider electrochemical windows due to the quaternary IL cations being notably harder to reduce than ternary ones.[7,8]

The ORR in AILs follows a quasi-reversible 1-electron reduction O_2 to superoxide, possible because of the absence of a protic IL cation.[9,10] The reversibility of the reaction in Equation 1 decreases as proton-donating species are added.[4]

$$O_2 + e^- \rightarrow O_2^{\bullet -} \qquad (1)$$

The HOR in AILs is similar to that observed in PILs since the electrogenerated protons are only able to sit on the IL anion in both cases, as per the reaction in Equation 2.[11]

$$H_2 + 2A^- \rightarrow 2AH + 2e^- \quad (2)$$

This thesis has thus far been concerned with oxygen and hydrogen electrochemistry in protic ionic liquids (PILs), because of their potential applications in intermediate-temperature (100-300 °C) polymer electrolyte membrane fuel-cells (PEMFCs).[12,13,14,15] However, the work presented in chapters 4 and 7 of this study confirms their unsuitability for the application without the addition of another protic species, either the parent acid or base of the PIL.[16,17] This knowledge makes the use of AILs with an added protic species, the protonated AIL anion in particular, another candidate for intermediate-temperature ionic liquid (IL) PEMFCs. As such, a discussion of the ORR and HOR in AILs, as well as a comparison of the ORR between ammonium and phosphonium AIL analogues, is presented. Phosphonium-based ILs have previously been shown to have lower viscosities, higher conductivities and higher thermal stabilities than their ammonium-based analogues.[18]

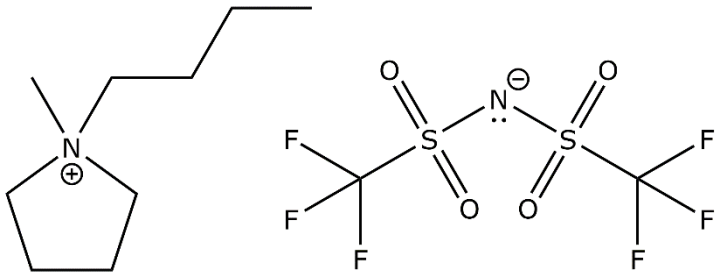
5.2 Experimental Section

5.2.1 Materials and apparatus

All chemicals were obtained from Acros Organics, Sigma Aldrich, Merck, or Iolitech, and were used as received. O_2 (99.95%) and H_2 (99.999%), were from BOC gases (Nottingham, UK). Ar (99.999%) was from CryoService (Worcester, UK). Pd wire (0.5 mm diameter, 99.99%) was from Alfa Aesar. A modulated speed rotator and platinum and glassy-carbon rotating disk electrodes (RDEs) were

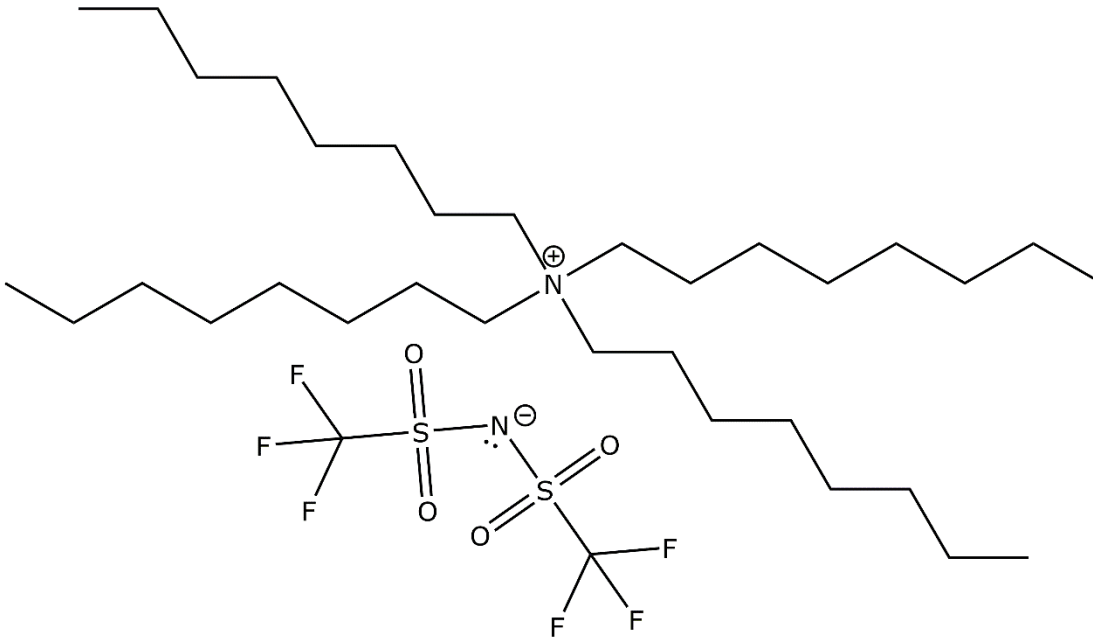
from Pine Research Instrumentation, Inc (Durham, NC, USA). Electrochemical measurements were performed using a model CHI760C potentiostat from CH Instruments, Austin, TX, USA.

The AILs chosen for this study are 1-methyl,1-butylpyrrolidinium bis(trifluoromethanesulfonyl)imide ([pyrr][NTf_2]),



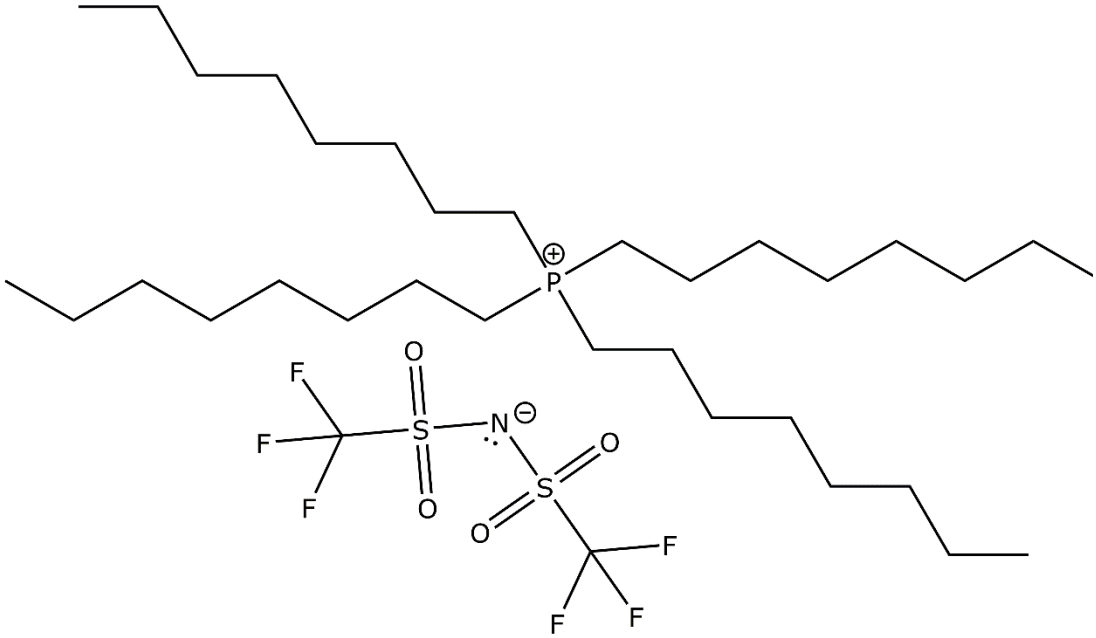
Scheme 5.1 Pyrrolidinium bis(trifluoromethanesulfonyl)imide.

N,N,N,N-tetraoctylammonium bis(trifluoromethanesulfonyl)imide ([N8888][NTf_2]),



Scheme 5.2 N,N,N,N-tetraoctylammonium bis(trifluoromethanesulfonyl)imide.

and N,N,N,N-tetraoctylphosphonium bis(trifluoromethanesulfonyl)imide ([P8888][NTf_2]).



Scheme 5.3 N,N,N,N-tetraoctylphosphonium bis(trifluoromethanesulfonyl)imide.

The three AILs were used as provided. AILs are typically synthesised by a metathesis reaction described in reference.[19]

5.2.2 Characterisation of aprotic ionic liquids

[pyrr][NTf_2], [N8888][NTf_2] and [P8888][NTf_2] were characterized by ^{1}H, ^{13}C and ^{19}F NMR spectroscopy (Bruker Ascend™ 400 MHz NMR Spectrometer) using a hexadeuterodimethyl sulfoxide solvent. Attenuated total reflection Fourier-transform infrared spectroscopy was carried out using a Bruker Alpha Platinum-ATR FTIR spectrometer at 30 °C. Thermogravimetric analysis (TGA) and differential scanning calorimetry (DSC) was carried out using a TA Instruments Discovery instrument under a N_2 atmosphere, and water concentrations were

determined using Karl-Fischer titrations (Mitsubishi CA-200 Moisturemeter). Characterisation data is presented in Chapter 3 and Appendix I.

5.2.3 Electrode fabrication and electrochemical measurements

Pd-H reference electrodes have previously been used in ILs.[19] A Pd-H reference electrode was fabricated by sealing a 0.5 mm diameter Pd wire (≈2.7 cm long) into borosilicate glass using a butane flame. Approximately 1.5 cm of the Pd wire was left protruding from the glass sheath to form a Pd rod electrode. A polished Ag contact wire was attached to the Pd wire inside the glass sheath using Ag epoxy (Chemtronics, Kennesaw, GA, USA). The Pd rod was then annealed in a butane flame and immersed in water before H_2 was bubbled over the Pd metal surface for 30 minutes. The rod was then rinsed with deionised water and either dried under a flow of N_2 or Ar, or left covered in air until dry.

A three-electrode electrochemical cell either a 4.6 mm diameter Pt disk or 5.6 mm diameter glassy-carbon (GC) working electrode, a Pt flag counter electrode (A ≈0.70 cm^2) and a Pd-H reference electrode, were used for all electrochemical measurements, unless otherwise stated. Prior to use, the Pt or GC disk electrode was polished using an aqueous suspension of 0.05 μm α-alumina (Buehler, Lake Bluff, Illinois) on felt polishing pads, and rinsed thoroughly with deionized water. The Pt flag counter electrode was flame annealed in a butane flame before being rinsed with deionised water. All working and counter electrodes were dried in a glassware oven before use. The cell was charged with 2 mL of AIL, sealed using rubber septa and bubbled with O_2, H_2 or Ar through a needle for a minimum of 40 minutes, while being stirred by a magnetic stirrer. During voltammetric measurements, a blanket of the appropriate gas was maintained above the AIL. All

voltammograms were *iR*-corrected unless otherwise stated. To mitigate for changes in the potential of the Pd-H reference electrode upon addition of acid or gasses to the AILs, potentials were adjusted such that the electrochemical window was the same during each analysis.

5.3 Results and Discussion

5.3.1 Oxygen-reduction and hydrogen-oxidation in [pyrr][NTf_2]

Cyclic voltammograms of [pyrr][NTf_2] recorded using Pt and GC electrodes are presented in Figure 5.1. The electrochemical window is ≈5 V wide at both Pt and GC electrodes, typical for a dry AIL.[8,20,21] The cathodic current from 1.5 V on the positive-going cycle recorded at both electrodes is water oxidation, as observed in PILs, since it is not possible to remove water completely from ILs.[20,22] The electrochemical stability of [pyrr][NTf_2] is notably greater than that of PILs (see Chapter 4) at negative potentials as predicted, due to the more stable quaternary ammonium cation of the AIL. The electrochemical oxidation of the PIL anion $[NTf_2]^-$ occurs at similar potentials to that observed in the PILs [dema][NTf_2] and [dema][TfO], as expected.[22,23]

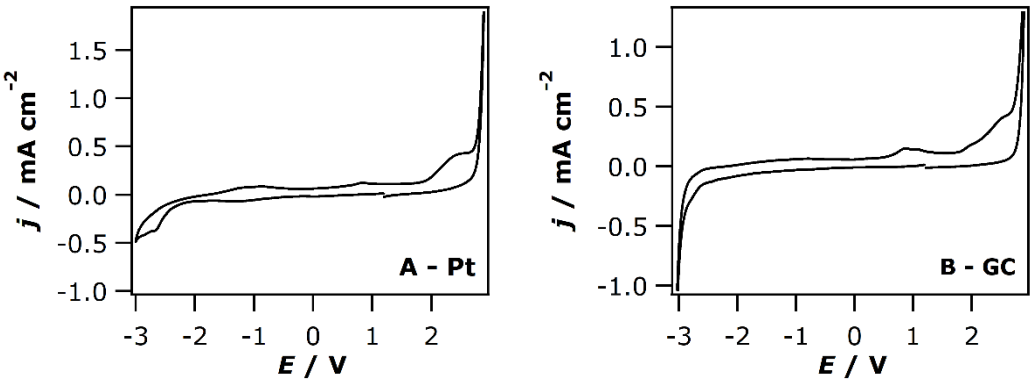


Figure 5.1 Cyclic voltammograms of deaerated [pyrr][NTf_2] recorded at Pt (A) and GC (B) electrodes. Potential cycles begin in a negative-going direction at 100 mV s^{-1} beginning at 1.2 V.

To investigate the ORR in an AIL, [pyrr][NTf_2] was saturated with O_2 and voltammograms were recorded. Figure 5.2 shows that reduction of O_2 at Pt (A) and GC (B) electrodes had onset potentials of −0.5 V and −0.65 V, respectively. A quasi-reversible oxidation of the ORR product also occurred at both electrodes. The peak-to-peak separation was ≈0.3 V and 0.1 V at Pt and GC respectively, indicating that O_2 reduction is quasi-reversible in both cases, as previously observed when using an Au electrode.[10]

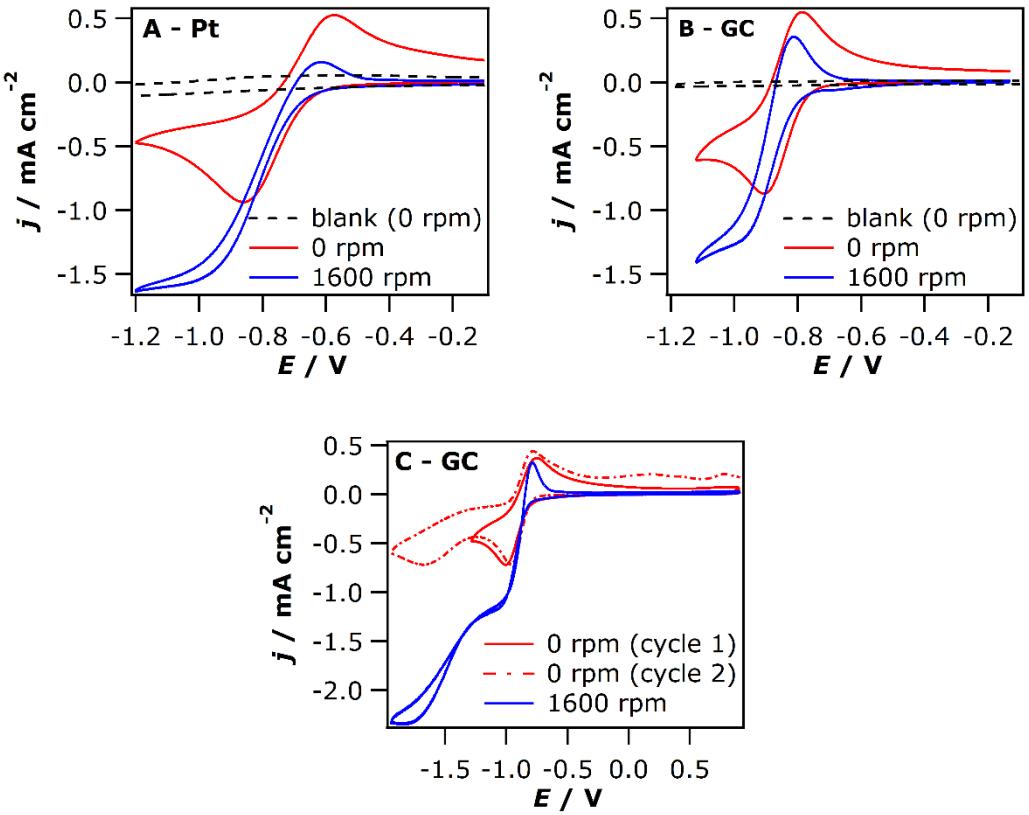


Figure 5.2 Cyclic voltammograms of [pyrr][NTf_2] recorded using stationary and rotating (A) Pt and (B)/(C) glassy-carbon (GC) electrodes. Voltammograms recorded at a GC electrode over a wider potential range are presented in (C). The voltammograms were recorded at 100 mV s^{-1} and the initial sweep was in the negative direction. Blanks are recorded at 0 rpm in deaerated [pyrr][NTf_2]. Where the electrode is rotating the rotation rate is 1,600 rpm.

The mass transport-limited current density (j_L) recorded at Pt and GC electrodes rotating at 1,600 rpm is similar at both electrodes, at around 1.5 mA cm^{-2}; this suggests that the ORR product is the same at both Pt and GC electrodes. Given that

the ORR in [pyrr][NTf_2] is considerably more reversible than in PILs (see Chapter 4, Figure 4.1), and that j_L is close to ¼ of that observed in the 4-electron ORR to make H_2O at Pt in diethylmethylammonium trifluromethanesulfonate ([dema][TfO]), the ORR in [pyrr][NTf_2] is ascribed to the reduction of O_2 to superoxide as shown in Equation 1, and is consistent with previous reported observations.[10] Using a GC electrode, if the potential is cycled more negative, a second, this time irreversible, ORR process occurs as shown by the red dot-dashed data (0 rpm), and blue data (1,600 rpm) in Figure 5.2 (C). This second ORR process has double the j_L (≈2.5 mA cm^{-2}) of the first (≈1.25 mA cm^{-2}) suggesting the simultaneous 1-electron reduction of superoxide, which has been reported in other $[NTf_2]^-$-based AILs with very similar voltammetry.[4,9]

$$O_2^{\bullet -} + e^- \rightarrow O_2^{-2} \qquad (3)$$

The electrochemical reduction of superoxide to peroxide (Equation 3) has previously been observed in other dry aprotic solvents at GC and Pt electrodes, such as liquid ammonia (1.12 mol dm^{-3} H_2O)[1], and at Pt, Au and Hg electrodes in dimethylsulfoxide[24], at negative potentials. The irreversibility of the second ORR wave has previously been attributed to the highly reactive O_2^{-2} species either reacting with the solvent, or with the carbon electrode.[1] When superoxide is irreversibly reduced to peroxide on the negative-going potential sweep, the red dot-dashed CV in Figure 5.2 (C) shows an anodic peak corresponding to superoxide oxidation. This has been observed in other AILs and is attributed either to oxidation $O_2^{\bullet -}$ not reduced to O_2^{-2} in the preceding cathodic potential sweep, or oxidation of $O_2^{\bullet -}$ present due to the comproportionation reaction of O_2^{-2} and O_2 as described in Equation 4.[4,9]

$$O_2^{-2} + O_2 \rightarrow 2O_2^{\bullet -} \quad (4)$$

When water is present in AILs, electrogenerated superoxide reacts according to Equation 5.[25,26]

$$2O_2^{\bullet -} + H_2O \rightarrow O_2 + HOO^- + HO^- \quad (5)$$

To determine the effect of an added protic species on the ORR in an AIL, hydrogen bis(trifluoromethanesulfonyl)imide ($HNTf_2$) was added to [pyrr][NTf_2] to a 0.1 mol dm^{-3} concentration and voltammograms recorded in the acidified liquid. The voltammograms in Figure 5.3 (A) and (C), recorded using stationary and rotating Pt electrodes respectively, show a clear and significant positive shift in the ORR onset potential of ≈1.6 V. A similar effect is observed at stationary and rotating GC electrodes but with a positive shift in ORR potential of ≈1 V, shown in Figure 5.3 (B) and (D) respectively. The j_Ls in acidified [pyrr][NTf_2] are ≈3.0 mA cm^{-2} and 2.5 mA cm^{-2} at Pt and GC, respectively, suggesting that the dominant ORR product is the same at both electrode materials. Also, given that j_L approximately doubles when acid is present, at both Pt and GC electrodes, it suggests that the 1-electron ORR to superoxide has become a 2-electron ORR to H_2O_2 upon addition of $HNTf_2$ (see Equation 6) as has been observed when protic species are added to other AILs.[4] This is different to the PILs studied in Chapter 4 where H_2O is the dominant ORR product at Pt and H_2O_2 at GC.

$$O_2 + 2HNTf_2 + 2e^- \rightarrow H_2O_2 + 2[NTf_2]^- \quad (6)$$

A possible reason for this could be the highly protic environment in PILs, aiding the 4-electron reduction of O_2 to H_2O. In AILs, even with an added protic species, there is no such intrinsically protic environment comparable to PILs.

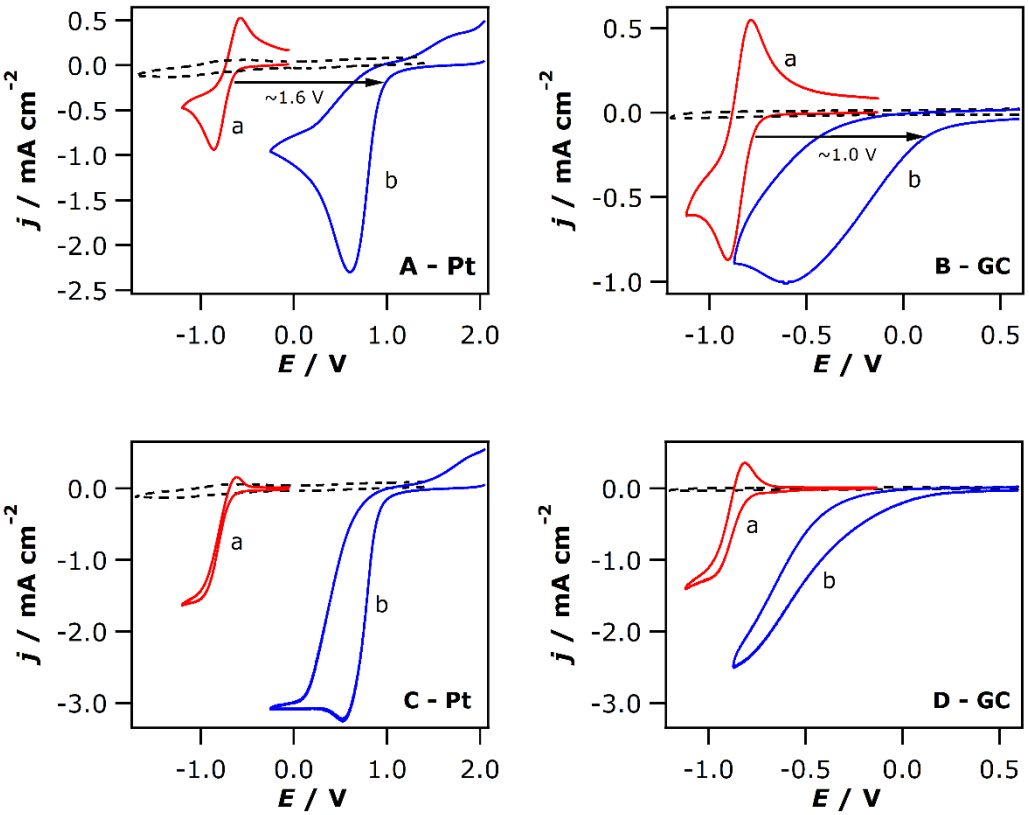


Figure 5.3 Cyclic voltammograms (CVs) recorded in O_2-saturated [pyrr][NTf_2] and O_2-saturated [pyrr][NTf_2] containing 0.1 mol dm^{-3} $HNTf_2$ using stationary (A)/(B) and rotating (C)/(D) Pt and glassy-carbon (GC) electrodes at 100 mV s^{-1}. Rotating electrodes ae at 1,600 rpm. In each frame CV (a) is acid-free and CV (b) contains acid. The initial sweeps were in the negative direction. Blanks are recorded in deaerated [pyrr][NTf_2] at stationary Pt or GC electrodes as appropriate.

The ORR at a GC electrode in [pyrr][NTf_2] containing 0.1 mol dm^{-3} $HNTf_2$ did not always produce a consistent voltammetric response as the CVs transitioned from a single wave ORR to a double wave ORR as the experiment progressed (as shown in Figure 5.4 (A) and (B)). The cause of this effect cannot be stated unequivocally, however, likely causes are electrode surface contaminants forming or being removed by potential cycling. Nevertheless, the ORR onset potential is unaffected by the effect and remains consistent. If it is the case that the removal of contaminants on the GC electrode's surface results in a multi-step ORR to form H_2O_2, then it likely proceeds according to Equations 7–10, as has been observed in ethylammonium nitrate (EAN).[27] The separation of the two electrochemical steps

into two distinct waves suggests that the first and second electron transfer constants are (or become) substantially different, while the overall charge transferred remains similar in both cases.

E $O_2 + e^- \rightarrow O_2^{\bullet -}$ (7)

C $O_2^{\bullet -} + HNTf_2 \rightarrow HO_2^{\bullet} + [NTf_2]^-$ (8)

E $HO_2^{\bullet} + e^- \rightarrow HO_2^{\bullet -}$ (9)

C $HO_2^{\bullet -} + HNTf_2 \rightarrow H_2O_2 + [NTf_2]^-$ (10)

The magnitudes of j_L for the first and second ORR process presented in Figure 5.4 (B) are in a roughly 1:2 ratio, suggesting the $1e^- + 1e^-$ mechanism as described above. Regardless of how the ORR voltammetry changes at GC between Figure 5.4 (A) and (B), the ultimate j_L is ≈ 2.5 mA cm^{-2} in both cases, indicating that the final ORR product is the same (H_2O_2).

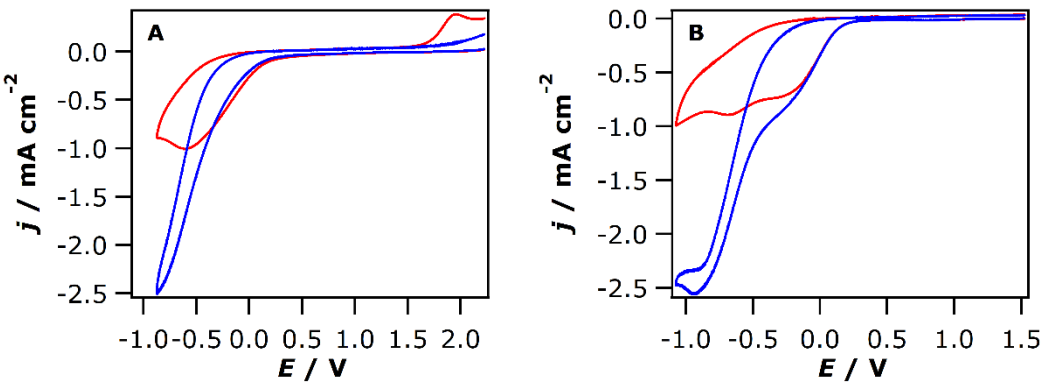


Figure 5.4 Cyclic voltammograms recorded in O_2-saturated [pyrr][NTf_2] containing 0.1 mol dm^{-3} $HNTf_2$ using stationary (red CVs) and rotating (blue CVs) glassy-carbon electrodes at 100 mV s^{-1}. The initial sweeps were in the negative direction. A shows the voltammetric response consistent for ≈16 minutes, and five CVs, from when the GC electrode is first introduced to the electrolyte; B shows the voltammetric response after 26 minutes.

The oxidation peak at ≈ 1.9 V in Figure 5.4 (A) is most likely H_2O_2 oxidation which proceeds according to Equation 11.[28]

$$H_2O_2 + 2[NTf_2]^- \rightarrow O_2 + 2HNTf_2 + 2e^- \quad (11)$$

To further investigate the identity of the ORR product in [pyrr][NTf_2], rotating-ring-disk electrode (RRDE) voltammetry was used to calculate the electron transfer number, *n*. Greater detail about the method of calculating *n* is provided in Chapter 2 and Chapter 4. Figure 5.5 (A) shows an ORR current in O_2-saturated [pyrr][NTf_2] at Pt and GC disk electrodes rotating at 1,600 rpm, and the concomitant oxidation of the ORR product at Pt rings. The two ORR waves at the GC disk (blue linear-sweep voltammogram (LSV) are described by Equations 1 and 3 respectively. Unlike the voltammetry at a GC electrode in Figure 5.2 (C), which shows an irreversible reduction of superoxide to peroxide as the electrode potential is scanned negative of the first (reversible) reduction of O_2 to superoxide, the second ORR wave in Figure 5.5 (A) results in a significant increase in the oxidation current at the Pt ring. This increase in oxidation current at the ring is unexpected due to the irreversibility of the second ORR process at GC which has previously been explained by the highly reactive peroxide reacting with the GC electrode. A possible explanation for the increase in current at the Pt ring while superoxide is reduced at the GC disk, is that the force of the rotation of the electrode prevents some (or most) of the produced peroxide from sticking to (and reacting with) the carbon electrode and forces it out over the Pt ring, where it is oxidised back to superoxide and then to oxygen.

The LSVs in Figure 5.5 (B) show an ORR current in O_2-saturated [pyrr][NTf_2] containing 0.1 mol dm^{-3} $HNTf_2$ at Pt and GC disk electrodes rotating at 1,600 rpm and the concomitant oxidation of the ORR product at each electrode's Pt ring. The oxidation current at the GC disk's Pt ring is significantly higher than that at the Pt

disk's Pt ring, suggesting that the ORR products are different at each electrode material. The lower oxidation ring current resulting from the ORR at the Pt disk suggests that the ORR product at Pt is less easily oxidised than the ORR product at GC; this indicates that H_2O could be the dominant ORR product at Pt (Equation 12) in acidified [pyrr][NTf_2] and H_2O_2 at GC (Equation 6) and is consistent with others' observation in acidified AILs.[3]

$$O_2 + 4HNTf_2 + 4e^- \rightarrow 2H_2O + 4[NTf_2]^- \qquad (12)$$

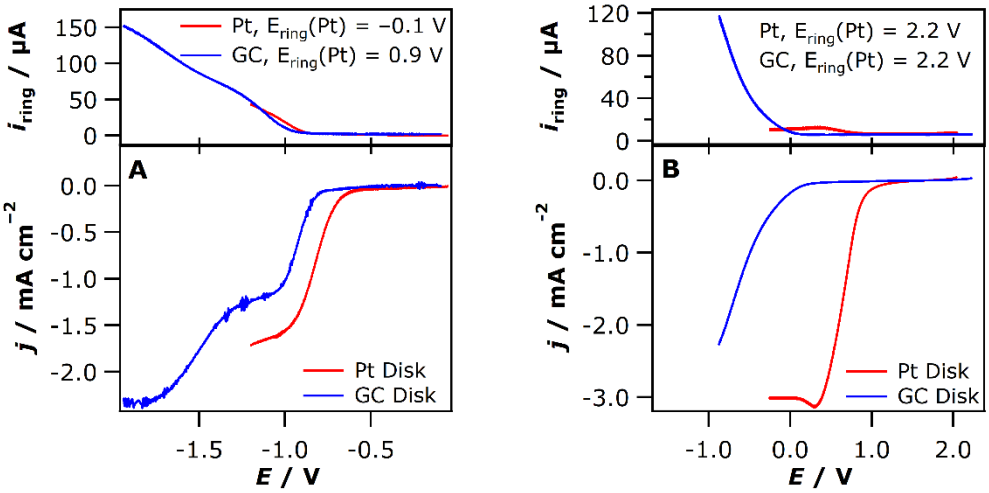


Figure 5.5 Linear sweep voltammograms (LSVs) recorded in O_2-saturated [dema][TfO] in the absence (A) and presence (B) of added hydrogen bis(trifluoromethanesulfonyl)imide to a 0.1 mol dm^{-3} concentration recorded at either a Pt-ring/Pt-disk or Pt-ring/GC-disk rotating ring disk electrode (RRDE). A fixed potential was maintained at the Pt rings of the Pt and GC-disk RRDEs such that the ORR product at the Pt and GC disk electrodes, is oxidised. Pt/GC disk LSVs, are recorded at 4.57 mm diameter Pt and 5.61 mm diameter GC disks. The Pt ring of the Pt RRDE has an area of 0.037 cm^2 and the Pt ring of the GC RRDE has an area of 0.1866 cm^2. All LSVs are recorded at a 100 mV s^{-1} scan rate with the electrodes rotating at 1,600 rpm. The GC disk LSV in (A) has undergone smoothing due to noisy data. The potential sweeps begin in a negative-going direction.

Unfortunately, the values of *n* obtained from the voltammetry were not reliable so no firm conclusions can be drawn. The values of *n* for acid-free and acidified [pyrr][NTf_2] at a Pt electrode were 14 and 4.5 respectively. The values of *n* obtained in acid-free [pyrr][NTf_2] at a GC electrode were 8.7 followed by 14, and 9 for acidified [pyrr][NTf_2]. Any value of *n* significantly above 4 is highly

questionable, leaving the n = 4.5 for acidified [pyrr][NTf_2] as the only sensible value and suggests that H_2O is the dominant ORR product at Pt. Given the very high likelihood, considering the reversible voltammetry and others' experiments using O_2-saturated AILs, that superoxide is the ORR product at both Pt and GC electrodes in acid-free[pyrr][NTf_2], it could partly explain why impossibly high values of n were obtained using the RRDE method that typically discerns between 2- and 4-electron processes.

To examine whether AILs such as [pyrr][NTf_2] could be suitable electrolytes for PEMFCs, the HOR also needs to be investigated in AILs. Figure 5.6 (A) shows voltammetry of H_2-saturated [pyrr][NTf_2] at a stationary and rotating (1,600 rpm) Pt electrode. The anodic current density onset at ≈0.25 V corresponds to the electrooxidation of H_2 and protons formed siting on the $[NTf_2]^-$ anion (the only proton acceptor) of [pyrr][NTf_2] to make $HNTf_2$ (Equation 13).

$$H_2 + 2[NTf_2]^- \rightarrow 2HNTf_2 + 2e^- \quad (13)$$

A reverse wave corresponding to the reduction of $HNTf_2$ to make H_2 and $[NTf_2]^-$ is observed at a stationary Pt electrode in Figure 5.6 (A) (red CV), and is described by Equation 14.

$$2HNTf_2 + 2e^- \rightarrow H_2 + 2[NTf_2]^- \quad (14)$$

Unlike in the PIL [dema][NTf_2], the HOR in the aprotic [pyrr][NTf_2] appears to be quasi-reversible, rather than reversible, with a peak-to-peak potential separation of around 0.96 V. Also, the HOR j_L is low at about 0.36 mA cm^{-2} compared with ≈2 mA cm^{-2} in [dema][TfO] (see Chapter 4). The low j_L and quasi-reversibility could be due to the $[pyrr]^+$ cation having a passivating effect on the Pt electrode

but also the possibility of a lower H_2 saturation concentration and higher viscosity of [pyrr][NTf_2] could result in the lower j_L. In addition, cyclic cations, most notably imidazoles, have been shown to have a significant electrode-passivating effect and will be discussed further in Chapter 6.[29]

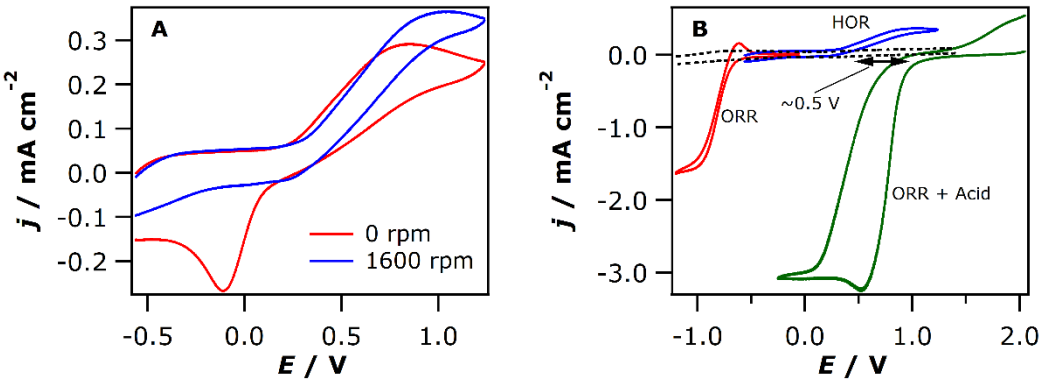


Figure 5.6 (A) – Cyclic voltammograms recorded in H_2-saturated [pyrr][NTf_2] at stationary and rotating Pt electrodes, at 100 mV s^{-1}. (B) – Cyclic voltammograms recorded in O_2-saturated [pyrr][NTf_2] and O_2-saturated [pyrr][NTf_2] containing 0.1 mol dm^{-3} hydrogen bis(trifluoromethanesulfonyl)imide ($HNTf_2$) using stationary Pt and glassy-carbon electrodes at 100 mV s^{-1}. The initial sweeps were in the negative direction. The blank is recorded in deaerated [pyrr][NTf_2].

Figure 5.6 (A) compares the potential difference between the HOR in H_2-saturated [pyrr][NTf_2] and the ORR in O_2-saturated [pyrr][NTf_2] with and without added $HNTf_2$. In the absence of acid, the ORR is ≈1 V more negative that the ORR, due to the lack of a proton donor, meaning that a fuel-cell device containing pure [pyrr][NTf_2] could not function as a fuel cell since an energy input would be required for the anodic and cathodic reactions to progress (see Figure 5.7 (B)). This lack of driving force for the fuel-cell reaction becomes clearer when considering the overall reaction of a pure (and dry) [pyrr][NTf_2]-electrolyte fuel cell.

$$\text{Overall: } H_2 + 2[NTf_2]^- + 2O_2 \rightarrow 2HNTf_2 + 2O_2^{\bullet -} \qquad (15)$$

Rather than being the reaction of H_2 and O_2 to make water (or hydrogen peroxide), the overall reaction in [pyrr][NTf_2] (or any pure and dry AIL), would result in the endergonic re-protonation of the AIL anion to make acid and the endergonic synthesis of superoxide from oxygen. These two species would react as they diffuse through the bulk of the electrolyte to make H_2O_2 or H_2O by disproportionation but, electrochemically speaking, it makes no difference to the overall electrochemical reaction being highly endergonic.

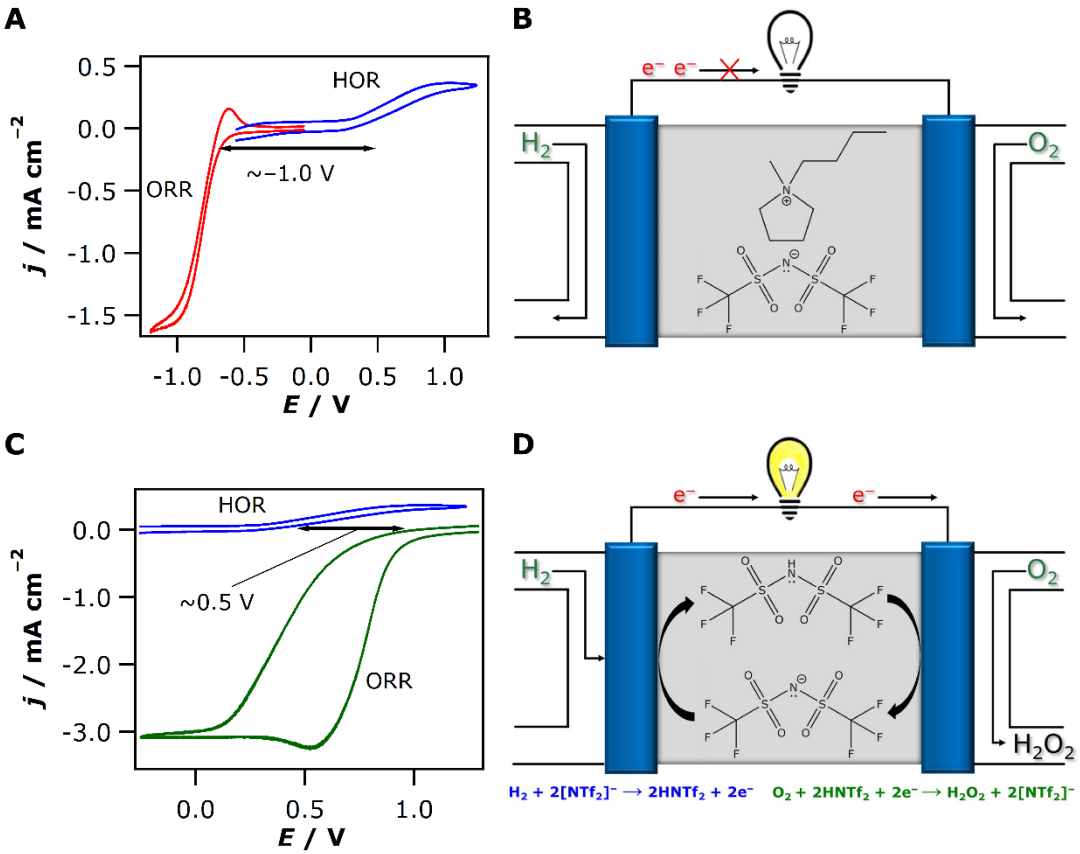


Figure 5.7 (A) cyclic voltammograms (CVs) of H_2- and O_2-saturated [pyrr][NTf_2] with (B) accompanying fuel cell schematic. (C) CVs of H_2-saturated [pyrr][NTf_2] and O_2-saturated [pyrr][NTf_2] containing 0.1 mol dm^{-3} hydrogen bis(trifluoromethanesulfonyl)imide ($HNTf_2$) with (D) accompanying fuel cell schematic. CVs were recorded using a 5-mm diameter Pt electrode rotating at 1,600 rpm and at 100 mV s^{-1}.

By adding a strong proton donor such as $HNTf_2$, the ORR shifts a significantly more positive potential relative to the HOR, giving a potential difference of around 0.5 V

(see Figure 5.7 (C)). This is a lower potential difference between the HOR and ORR than observed in the PIL [dema][NTf_2] (see Figure 5.8 (B)), which is around 0.8 V, and results from the formation of water (see Equation 17), and suggests that the dominant fuel-cell reaction in acidified [pyrr][NTf_2] results in the formation of H_2O_2 as per Equation 16. Only when a proton donor is available so that H_2O_2 synthesis is the overall reaction, and a viable proton acceptor/donor shuttling mechanism is present, is there a driving force resulting in a viable (galvanic) fuel cell (see Figure 5.7 (D)). Also, similar to acidified PILs, adding anything other than the parent acid to AILs would not result in a sustainable proton shuttling mechanism since the added protic species would be consumed as part of the fuel-cell reaction and, unless the pK_a of the added species was the same or greater than that of the parent acid (protonated AIL anion), then the maximum fuel cell potential would be decreased.

Overall: $H_2 + O_2 \rightarrow H_2O_2$ 0.70 V *vs.* SHE[30] (16)

Overall: $2H_2 + O_2 \rightarrow 2H_2O$ 1.229 V *vs.* SHE[30] (17)

A comparison of H_2 and O_2 voltammetry in [pyrr][NTf_2] (an AIL) and [dema][NTf_2] (a PIL) where $HNTf_2$ has been added as a strong proton donor, is presented in Figure 5.8 and shows the higher predicted fuel-cell potential (E_{cell}) in [dema][NTf_2] and [pyrr][NTf_2] where acid is present. Given that $[NTf_2]^-/HNTf_2$ is the proton acceptor/donor for the HOR/ORR in both acidified [pyrr][NTf_2] and acidified [dema][NTf_2], it would be expected that the predicted E_{cell} is the same if the reaction mechanisms are the same. However, since the hypothetical E_{cell} values are approximately 0.5 V and 0.8 V in [pyrr][NTf_2] and [dema][NTf_2] respectively,

it suggests that the overall fuel-cell reaction in [pyrr][NTf_2] results in H_2O_2 formation, rather than H_2O formation.

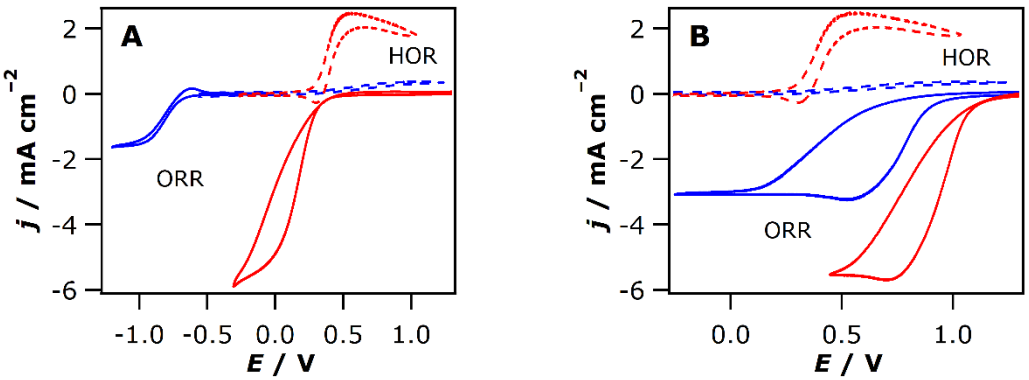


Figure 5.8 (A) cyclic voltammograms (CVs) of H_2- and O_2-saturated [pyrr][NTf_2] (an AIL) and [dema][NTf_2] (a PIL). (B) CVs of H_2-saturated [pyrr][NTf_2] and [dema][TfO], and O_2-saturated [pyrr][NTf_2] and [dema][NTf_2] containing 0.1 mol dm^{-3} hydrogen bis(trifluoromethanesulfonyl)imide ($HNTf_2$). Blue and red CVs are recorded in [pyrr][NTf_2] and [dema][NTf_2], respectively. CVs were recorded using a 5-mm diameter Pt electrode rotating at 1,600 rpm and at 100 mV s^{-1}.

Furthermore, the ORR j_L in acidified [pyrr][NTf_2] being approximately half that in [dema][NTf_2], where the ORR results in H_2O formation (see Chapter 4), could indicate that the dominant ORR process in acidified [pyrr][NTf_2] is a 2-electron reduction to H_2O_2. However, this could be a result of different O_2-saturation concentrations and diffusion coefficients in the two ILs.

5.3.2 Oxygen-reduction in [P8888][NTf_2] and [N8888][NTf_2]

Cyclic voltammograms recorded in deaerated [P8888][NTf_2] and [N8888][NTf_2] are shown in Figure 5.9 at both Pt and GC electrodes. Both AILs have very wide electrochemical windows of ≈8–12 V (Pt) and ≈9 V (GC) in [P8888][NTf_2] and ≈6 V (Pt/GC) in [N8888][NTf_2]. The wide electrochemical window of [N8888][NTf_2] is comparable to other quaternary ammonium-based AILs.[8,21] The exceptionally wide electrochemical window of [P8888][NTf_2] is greater than most reported

values for quaternary phosphonium-based AILs, and results from electrode passivation.[18,31] The unusual voltammetric shapes at the extreme positive and negative potentials in [N8888][NTf_2] recorded at Pt and GC electrodes, and in [P8888][NTf_2] at extreme positive potentials, are likely diffusional effects caused by the very high viscosity of the AILs. The anodic peak recorded in [P8888][NTf_2] at around 5 V and in [N8888][NTf_2] at around 2 V is likely oxidation of water.

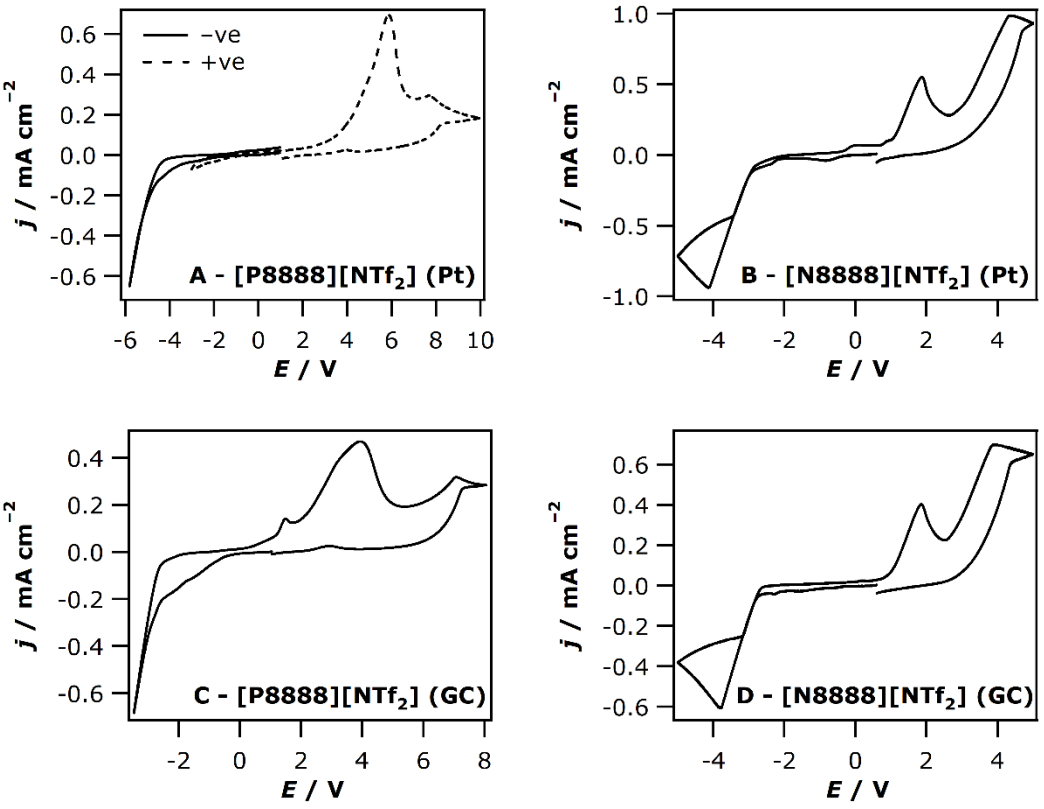


Figure 5.9 Cyclic voltammograms of deaerated [P8888][NTf_2] and [N8888][NTf_2] recorded at Pt (A)/(B) and GC (C)/(D) electrodes, respectively. Potential cycles begin in a negative-going direction at 100 mV s^{-1}. The dashed line CV in (A) was recorded separately to the solid line CV as the potentiostat software limited the potential range for a single CV to 13 V.

The CVs in Figure 5.10 are recorded in O_2-saturated [P8888][NTf_2] and [N8888][NTf_2] at Pt and GC electrodes. In [P8888][NTf_2], O_2 is reduced negative of ≈−0.8 V at both Pt and GC. At a Pt electrode (Figure 5.10 (A)) a reversible voltammogram is observed, similar to that observed in [pyrr][NTf_2], in which O_2

is reduced to superoxide on the negative-going potential sweep and superoxide is oxidised to O_2 in the positive-going sweep. Figure 5.10 (C) shows voltammograms of O_2-saturated [P8888][NTf_2] recorded at a GC electrode recorded at 0 and 1,600 rpm. Two cathodic peaks are observed that correspond to the ORR which is similar to that observed by others in quaternary alkyl-phosphonium cation AILs.[32] The first peak at ≈−1.5 V is O_2-reduction to superoxide and the second peak at −3.0 V, it has been proposed, is the reduction of superoxide to peroxide.[32] The superoxide anion is shown to be stable in phosphonium-based quaternary ILs, even in the presence of small amounts of water, due to bonding with the AIL cation.[32] Furthermore, phosphonium-based cations have a greater stabilising effect on superoxide than ammonium-based cation analogues.[33]

Voltammetry recorded in O_2-saturated [N8888][NTf_2] showing reversible O_2-reduction to superoxide is shown in Figure 5.10 (B) and (D) recorded at Pt and GC electrodes, respectively. The peak separation recorded in [N8888][NTf_2] at a Pt electrode is greater than that recorded in [P8888][NTf_2] which is likely a reflection of a higher water content in the [N8888][NTf_2] sample. The CVs recorded at rotating Pt and GC electrodes in Figure 5.10 (B) and (D) show an anodic peak on the return sweep suggesting a species has adsorbed onto the electrode. In all cases, rotating the Pt or GC electrode at 1,600 rpm produces an unusual voltammetric peak instead of a mass-transport limited current; this is most likely an artefact of a rotating electrode in a very viscous IL.

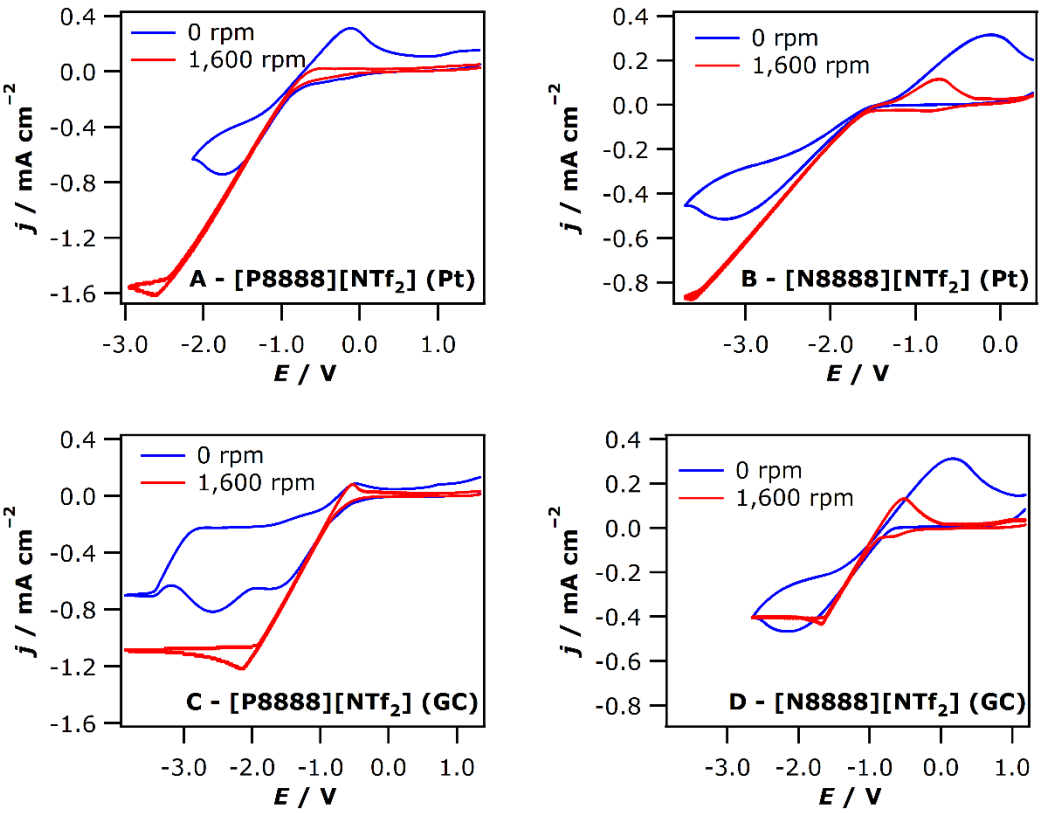


Figure 5.10 Cyclic voltammograms of O_2-saturated [P8888][NTf_2] and [N8888][NTf_2] recorded at stationary and rotating Pt (A)/(B) and GC (C)/(D) electrodes, respectively. Potential cycles begin in a negative-going direction at 100 mV s^{-1}.

To determine the effect of the presence of acid on the ORR in [P8888][NTf_2] and [N8888][NTf_2], $HNTf_2$ was added to each IL to a 0.1 mol dm^{-3} concentration and saturated with oxygen. Voltammograms were then recorded in the acidified, O_2-saturated liquids. Figure 5.11 compares voltammetry of acidified and non-acidified, O_2-saturated [P8888][NTf_2] and [N8888][NTf_2], recorded at stationary and rotating Pt electrodes. The ORR onset potential in [P8888][NTf_2] and [N8888][NTf_2] shifts notably positive in the presence of the strong proton donor, $HNTf_2$ as observed in [pyrr][NTf_2] and PILs (see Chapter 4), and as reported by others when studying oxygen reduction in quaternary phosphonium-based AILs with added HCl.[33] Curiously, the magnitude of the ORR peaks at stationary electrodes and j_L at rotating electrode, is lower when acid is present. This

observation runs contrary to the hypothesis that the presence of a strong proton donor should shift the ORR mechanism from a 1-electron reduction to a 2- or 4-electron reduction to H_2O_2 or H_2O at GC or Pt electrodes.[28] However, due to the very high viscosity and limited volume of the IL available for testing, it is possible that the lower j_{max} of the ORR peaks and j_L is a product of the high viscosity of the IL and experimental limitations. Another possible explanation is that the Pt electrode has been passivated, either by the IL due to exposure over time, or by the added $HNTf_2$, although the later is unlikely due to no previous observations of electrode passivation by $HNTf_2$. Pozo-Gonzalo *et al.* have reported 4-electron ORR in quaternary alkyl-phosphonium-based AILs containing a weak proton donor via a two 2-electron reaction mechanism.[28]

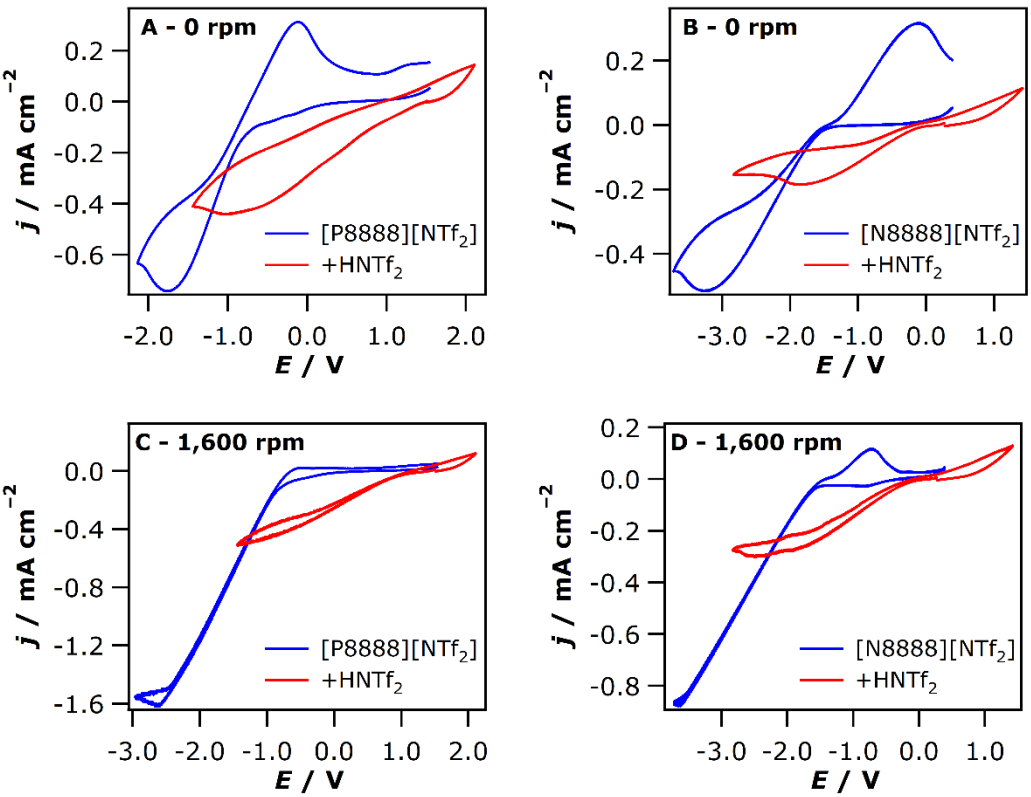


Figure 5.11 Cyclic voltammograms of O_2-saturated [P8888][NTf_2] and [N8888][NTf_2], with and without 0.1 mol dm^{-3} $HNTf_2$, recorded at stationary (A)/(B) and rotating (C)/(D) electrodes, respectively. Potential cycles begin in a negative-going direction at 100 mV s^{-1}.

Recording and aligning CVs of the electrochemical windows of [P8888][NTf_2] and [N8888][NTf_2] were used to avoid shifts in the potential of the reference electrode when the AILs were saturated with O_2 or H_2, or when acidified. While this reference method was successful in PILs and [pyrr][NTf_2], in [P8888][NTf_2] and [N8888][NTf_2] the electrochemical windows changed upon addition of acids and gases such that a fixed reference point in the electrochemical window CVs was difficult to obtain and could lead to errors in the potentials reported. In support of the data presented in Figure 5.11 showing a positive shift in the ORR potential upon addition of acid in both AILs, all reference points in the electrochemical window CVs of pure and acidified AILs showed a positive shift in the ORR potential upon acidification; there is, however, notable error in the reported extent that the ORR potential shifts positive.

5.4 Conclusions

The addition of the strong acid $HNTf_2$ to AILs shifts the ORR to more positive potentials. In [pyrr][NTf_2] this positive shift is ≈1.6 V at a Pt electrode. Without a proton source, the ORR is a 1-electron reduction to make superoxide. Where there is a proton source, the ORR is most likely a 2-electron reduction to make H_2O_2, and supports observations by others.[4] Since the HOR occurs at a more positive potential than the ORR in pure [pyrr][NTf_2], there would be no driving force for the reaction of H_2 and O_2 in a fuel cell or a viable proton shuttling mechanism. If a strong acid is added to [pyrr][NTf_2] the potential difference between the HOR and ORR becomes ≈0.5 V as the ORR shifts positive; this would be a galvanic system if used as

a fuel-cell electrolyte but would have a significantly lower open-circuit potential than a conventional fuel cell.

The addition of $HNTf_2$ to O_2-saturated $[P8888][NTf_2]$ and $[N8888][NTf_2]$ also shifts the ORR to a more positive potential however, the degree to which this shift occurs is uncertain due to problems with the reference potential system. $[P8888][NTf_2]$ and $[N8888][NTf_2]$ exhibit similar ORR electrochemistry except for the observation of the oxidation of an adsorbed species, after oxygen reduction, in $[N8888][NTf_2]$ only. Oxygen electrochemistry in $[P8888][NTf_2]$ with and without a proton donor appears similar to that observed in other quaternary alkyl-ammonium-based AILs.[28,32,33] Finally, $[P8888][NTf_2]$ has a wider electrochemical window than that of $[N8888][NTf_2]$ recorded at a Pt electrode, although this could be due to passivation of the electrode.

5.5 References

1. Uribe, F. A.; Bard, A. J. Electrochemistry in liquid ammonia. 5. Electroreduction of oxygen. *Inorg. Chem.* **1982,** *21* (8), 3160-3163.

2. Esperança, J. M. S. S.; Lopes, J. N. C.; Tariq, M.; Santos, L. M. N. B. F.; Magee, J. W.; Rebelo, L. P. N. Volatility of Aprotic Ionic Liquids s A Review. *J. Chem. Eng. Data* **2010,** *55* (1), 3-12.

3. Switzer, E. E.; Zeller, R.; Chen, Q.; Sieradzki, K.; Buttry, D. A.; Friesen, C. Oxygen Reduction Reaction in Ionic Liquids: The Addition of Protic Species. *J. Phys. Chem. C* **2013,** *117* (17), 8683-8690.

4. René, A.; Hauchard, D.; Lagrost, C.; Hapiot, P. Superoxide Protonation by Weak Acids in Imidazolium Based Ionic Liquids. *J. Phys. Chem. B* **2009,** *113* (9), 2826–2831.

5. Mirjafari, A.; Pham, L. N.; McCabe, J. R.; Mobarrez, N.; Salter, E. A.; Wierzbicki, A.; West, K. N.; Sykora, R. E.; Jr., J. H. D. Building a bridge between aprotic and protic ionic liquids. *RSC Adv.* **2013,** *3*, 337-340.

6. Angell, C. A.; Byrne, N.; Belieres, J.-P. Parallel Developments in Aprotic and Protic Ionic Liquids: Physical Chemistry and Applications. *Acc. Chem. Res.* **2007,** *40* (11), 1228-1236.

7. Earle, M. J.; Esperanca, J. M.; Gilea, M. A.; Lopes, J. N.; Rebelo, L. P.; Magee, J. W.; Seddon, K. R.; Widegren, J. A. The distillation and volatility of ionic liquids. *Nature (London, U. K.)* **2006,** *439* (7078), 831-4.

8. Buzzeo, M. C.; Hardacre, C.; Compton, R. G. Extended electrochemical windows made accessible by room temperature ionic liquid/organic solvent electrolyte systems. *ChemPhysChem* **2006,** *7* (1), 176-80.

9. Katayama, Y.; Onodera, H.; Yamagata, M.; Miura, T. Electrochemical Reduction of Oxygen in Some Hydrophobic Room-Temperature Molten Salt Systems. *J. Electrochem. Soc.* **2004,** *151* (1), A59.

10. Katayama, Y.; Sekiguchi, K.; Yamagata, M.; Miura, T. Electrochemical Behavior of Oxygen/Superoxide Ion Couple in 1-Butyl-1-methylpyrrolidinium Bis(trifluoromethylsulfonyl)imide Room-Temperature Molten Salt. *J. Electrochem. Soc.* **2005,** *152* (8).

11. Bentley, C. L.; Bond, A. M.; Zhang, J. Voltammetric Perspectives on the Acidity Scale and H^+/H_2 Process in Ionic Liquid Media. *Annu. Rev. Anal. Chem.* **2018,** *11* (1), 397-419.

12. Nakamoto, H.; Noda, A.; Hayamizu, K.; Hayashi, S.; Hamaguchi, H.-o.; Watanabe, M. Proton-Conducting Properties of a Brønsted Acid-Base Ionic Liquid and Ionic Melts Consisting of Bis(trifluoromethanesulfonyl)imide and Benzimidazole for Fuel Cell Electrolytes. *J. Phys. Chem. C* **2007,** *111*, 1541-1548.

13. Yasuda, T.; Ogawa, A.; Lee, S.-Y.; Watanabe, M. Protic Ionic Liquid as an Electrolyte for Non-humidified Intermediate Temperature Fuel Cells. *Electrochemical Society Meeting Abstracts* **2008,** *MA2008-02 3043*.

14. Lee, S. Y.; Ogawa, A.; Kanno, M.; Nakamoto, H.; Yasuda, T.; Watanabe, M. Nonhumidified Intermediate Temperature Fuel Cells Using Protic Ionic Liquids. *J Am. Chem. Soc.* **2010,** *132* (28), 9764-9773.

15. Miran, M. S.; Yasuda, T.; Susan, M. A. B. H.; Dokko, K.; Watanabe, M. Binary Protic Ionic Liquid Mixtures as a Proton Conductor: High Fuel Cell Reaction Activity and Facile Proton Transport. *J. Phys. Chem. C* **2014,** *118* (48), 27631-27639.

16. Goodwin, S. E.; Smith, D. E.; Gibson, J. S.; Jones, R. G.; Walsh, D. A. Electroanalysis of Neutral Precursors in Protic Ionic Liquids and Synthesis of High-Ionicity Ionic Liquids. *Langmuir* **2017,** *33* (34), 8436−8446.

17. Smith, D. E.; Walsh, D. A. The Nature of Proton Shuttling in Protic Ionic Liquid Fuel Cells. *Adv. Energy Mater.* **2019,** *9* (24).

18. Tsunashima, K.; Sugiya, M. Physical and electrochemical properties of low-viscosity phosphonium ionic liquids as potential electrolytes. *Electrochem. Commun.* **2007,** *9*, 2353-2358.

19. Bautista-Martinez, J. A.; Tang, L.; Belieres, J.-P.; Zeller, R.; Angell, C. A.; Friesen, C. Hydrogen Redox in Protic Ionic Liquids and a Direct Measurement of Proton Thermodynamics. *J. Phys. Chem. C* **2009,** *113*, 12586−12593.

20. Schröder, U.; Wadhawan, J. D.; Compton, R. G.; Marken, F.; Suarez, P. A. Z.; Consorti, C. S.; de Souza, R. F.; Dupont, J. Water-induced accelerated ion diffusion: voltammetric studies in 1-methyl-3-[2,6-(S)-dimethylocten-2-yl]imidazolium tetrafluoroborate, 1-butyl-3-methylimidazolium tetrafluoroborate and hexafluorophosphate ionic liquids. *New J. Chem.* **2000,** *24* (12), 1009-1015.

21. Silvester, D. S.; Compton, R. G. Electrochemistry in Room Temperature Ionic Liquids: A Review and Some Possible Applications. *Z. Phys. Chem.* **2006,** *220* (10), 1247-1274.

22. O'Mahony, A. M.; Silvester, D. S.; Aldous, L.; Hardacre, C.; Compton, R. G. Effect of Water on the Electrochemical Window and Potential Limits of Room-Temperature Ionic Liquids. *J. Chem. Eng. Data* **2008,** *53* (12), 2884-2891.

23. Johnson, L.; Ejigu, A.; Licence, P.; Walsh, D. A. Hydrogen Oxidation and Oxygen Reduction at Platinum in Protic Ionic Liquids. *J. Phys. Chem. C* **2012,** *116*, 18048−18056.

24. Sawyer, D. T.; Roberts Jr., J. L. Electrochemistry of Oxygen and Superoxide Ion in Dimethylsulfoxide at Platinum, Gold and Mercury Electrodes. *J. Electroanal. Chem.* **1966,** *12*, 90-101.

25. Barnes, A. S.; Rogers, E. I.; Streeter, I.; Aldous, L.; Hardacre, C.; Wildgoose, G. G.; Compton, R. G. Unusual Voltammetry of the Reduction of O_2 in $[C_4dmim][N(Tf)_2]$ Reveals a Strong Interaction of $O_2^{\bullet-}$ with the $[C_4dmim]^+$ Cation. *J. Phys. Chem. C* **2008,** *112* (35), 13709−13715.

26. Zhang, Y.; Pozo-Gonzalo, C. Variations and applications of the oxygen reduction reaction in ionic liquids. *Chem. Commun. (Cambridge U. K.)* **2018,** *54* (31), 3800-3810.

27. Khan, A.; Lu, X.; Aldous, L.; Zhao, C. Oxygen Reduction Reaction in Room Temperature Protic Ionic Liquids. *J. Phys. Chem. C* **2013,** *117* (36), 18334-18342.

28. Pozo-Gonzalo, C.; Virgilio, C.; Yan, Y.; Howlett, P. C.; Byrne, N.; MacFarlane, D. R.; Forsyth, M. Enhanced performance of phosphonium based ionic liquids towards 4 electrons oxygen reduction reaction upon addition of a weak proton source. *Electrochem. Commun.* **2014,** *38*, 24-27.

29. Yang, C.; Costamagna, P.; Srinivasan, S.; Benziger, J.; Bocarsly, A. B. Approaches and technical challenges to high temperature operation of proton exchange membrane fuel cells. *J. Power Sources* **2001,** *103*, 1-9.

30. Song, C.; Zhang, J. Electrocatalytic Oxygen Reduction Reaction. In *PEM Fuel Cell Electrocatalysts and Catalyst Layers*, Springer: 2008; pp 89-134.

31. Zhang, S.; Sun, N.; He, X.; Lu, X.; Zhang, X. Physical Properties of Ionic Liquids: Database and Evaluation. *J. Phys. Chem. Ref. Data* **2006,** *35* (4).

32. Pozo-Gonzalo, C.; Torriero, A. A.; Forsyth, M.; MacFarlane, D. R.; Howlett, P. C. Redox Chemistry of the Superoxide Ion in a Phosphonium-Based Ionic Liquid in the Presence of Water. *J. Phys. Chem. Lett.* **2013,** *4* (11), 1834-7.

33. Pozo-Gonzalo, C.; Howlett, P. C.; Hodgson, J. L.; Madsen, L. A.; MacFarlane, D. R.; Forsyth, M. Insights into the reversible oxygen reduction reaction in a series of phosphonium-based ionic liquids. *Phys. Chem. Chem. Phys.* **2014,** *16* (45), 25062-70.

6 Formic Acid Oxidation in Protic Ionic Liquids

6.1 Introduction

The electro-oxidation of formic acid (FAO), along with oxygen reduction and hydrogen oxidation, are receiving renewed attention as interest in fuel-cell devices increases.[1,2,3] Formic acid is also the simplest carboxylic acid and there has been great interest in understanding its electro-oxidation as a template for the oxidation of larger oxygen-containing organic molecules, and carboxylic acids specifically.

FAO is known to progress via two pathways (direct and indirect) on Pt electrocatalysts in acidic media, as first proposed by Erich Müller, and later confirmed by Capon & Parsons.[4,5,6,7] The direct mechanism was thought to progress via a 'reactive' adsorbed intermediate and the indirect mechanism via a chemisorbed 'electrode-poisoning' intermediate, both ultimately resulting in CO_2 evolution.[1,4] The use of novel electrochemical techniques in the 1960s, such as cyclic voltammetry (CV), which resulted from the invention of the three-electrode potentiostat by Archie Hickling in 1942,[8] led to further confirmation of the duel-pathway FAO mechanism and the characteristic CV associated with it.[3,9,10] The exact natures and identities of the adsorbed intermediates has long been debated. Candidates for the adsorbed species have included CO_{ad}, $HCOOH_{ad}$, $HCOO^-_{ad}$, COH_{ad} and $C(OH)OH_{ad}$.[1,9,11,12] Direct evidence of Pt-adsorbed CO as the electrode-poisoning species in methanol oxidation and indirect FAO was provided by Beden *et al.*, using electrochemically modulated infra-red reflectance spectroscopy (EMIRS).[13,14] More recently, however, compelling work by Osawa *et al.* using surface-enhanced infra-red absorption spectroscopy (SEIRAS), detected

the presence of adsorbed formate[15] and elucidated a more complex relationship between adsorbed species and the two FAO pathways; their FAO mechanism requires adsorbed formate in all cases.[16,17] According to Osawa *et al.*, both direct and indirect pathways begin with the spontaneous electro-adsorption of HCOOH on Pt to make an adsorbed, bridge-bonded, formate species and H^+. Bridge-bonding in this case refers to the two oxygen atoms of the formate anion each bonding with an adjacent Pt atom on the electrode surface.[18] The proton produced would likely sit either on H_2O or exist bound to Pt prior to the next reaction step.

$$\text{A) Common I: } HCOOH + 2Pt \rightarrow HCOO_{ad}\text{-}Pt + H^+ + e^- \quad (1)$$

The pathways then diverge (2), with the indirect pathway continuing with the electro-reduction of adsorbed formate and the proton from (1), giving H_2O and adsorbed CO (2). The net effect of these reactions is dehydration of formic acid to form adsorbed CO. The electro-reduction in (2) will only occur if the adsorbed formate is surrounded by three contiguous Pt atoms with which it can interact by flattening its bond geometry, which allows the simultaneous rupture of the C-H bond, one of the two C-O bonds, and the subsequent electron transfer.

$$\text{A) Indirect II: } HCOO_{ad}\text{-}Pt + H^+ + e^- \rightarrow CO_{ad}\text{-}Pt + H_2O \quad (2)$$

A notable feature of the proposed FAO mechanism above is the spontaneous electro-oxidation of formic acid to adsorbed formate (1), followed by the spontaneous electro-reduction of adsorbed formate to adsorbed CO (2). This is thermodynamically possible, as the standard potential for formic acid oxidation is lower than the standard potential of adsorbed formate reduction.[18]

The final step (3) of the indirect pathway, as proposed by Osawa *et al.*, is the electro-oxidation of adsorbed CO to give CO_2, clean Pt, and two protons which will sit either on H_2O in acidic aqueous systems or adsorbed to Pt.[16,17]

$$\text{A) Indirect III: } CO_{ad}\text{-Pt} + H_2O \rightarrow Pt + CO_2 + 2H^+ + 2e^- \quad (3)$$

The direct pathway is described as follows and only occurs uninhibited on a clean electrode (Pt) surface. The first step in the direct pathway is common to the indirect pathway, shown in (1), and results in the formation of adsorbed formate on the Pt surface and is followed by

$$\text{A) Direct II: } HCOO_{ad}\text{-Pt} \rightarrow Pt + CO_2 + H^+ + e^- \quad (4)$$

The net reaction of both pathways is the 2-electron oxidation of formic acid to carbon dioxide, as suggested by Müller in the 1920s.[19]

$$\text{A) Net: } HCOOH \rightarrow CO_2 + 2H^+ + 2e^- \quad (5)$$

An alternative FAO mechanism proposed by Chen *et al.* (2006) contains three reaction pathways with weakly adsorbed HCOOH being the adsorbed species common to all three pathways, and adsorbed formate being a spectator species.[12,20] This alternative pathway is described below. Chen *et al*. proposes that formic acid weakly adsorbs to sites on the surface of the Pt electrode (6) prior to any of the three pathways.

$$\text{B) Common: } HCOOH \rightleftharpoons HCOOH_{ad} \quad (6)$$

The direct pathway proceeds by 2-electron oxidation of adsorbed HCOOH to CO_2 and protons (7).

B) Direct: $HCOOH_{ad} \rightarrow CO_2 + 2e^- + 2H^+$ (7)

The 2-step formate pathway begins with oxidation of adsorbed formic acid to adsorbed formate and a proton (8).

B) Formate I: $HCOOH_{ad} \rightleftharpoons HCOO_{ad} + H^+ + e^-$ (8)

The second step in the formate pathway is oxidation of formate to CO_2 and a proton (9).

B) Formate II: $HCOO_{ad} \rightarrow CO_2 + H^+ + e^-$ (9)

The indirect pathway begins with adsorbed formic acid spontaneously dehydrating to adsorbed CO and H_2O (10).

B) Indirect I: $HCOOH_{ad} \rightarrow CO_{ad} + H_2O$ (10)

The second step in the indirect pathway proposed by Chen *et al.* involves oxidation of adsorbed CO and H_2O to CO_2 and protons.[12,20]

B) Indirect II: $CO_{ad} + H_2O \rightarrow CO_2 + 2H^+ + 2e^-$ (11)

There has been debate about which of the two FAO mechanisms, Equations 1–4 or 6–11, and the identity of the active adsorbed species, is correct, although work by Osawa *et al.* (2011) suggests it is the former and that adsorbed, bridge-bonded Pt-$COOH_{ad}$ is the active species.[17,18]

Most recently, however, it has been demonstrated that while bridge-bonded Pt-$COOH_{ad}$ does form spontaneously on Pt in acidic media, it is not the active species in FAO, and is thought to suppress FAO until highly positive potentials are reached, where it enhances FAO by suppressing Pt-oxide formation.[21] In their 2013 paper

Joo *et al.* explored the pH-dependence of FAO and concluded that formate ($HCOO^-$), formed in the equilibrium with water (Equation 12), is the dominant active species in FAO over the pH range studied (0–12).[22] Their voltammetry showed a clear increase in FAO current density with decreasing pH, with a maximum current density when pH is closest to the pK_a of formic acid (3.75); this corresponds with an increase in FAO current as formate concentration increases (as pH decreases).[22,23] The same group provided further evidence that $HCOO^-$ is the active species (going via a transient, weakly adsorbed $HCOO^-$ species) using attenuated total reflection-SEIRAS and cyclic voltammetry over a wide pH range.[21]

$$HCOOH + H_2O \rightleftharpoons HCOO^- + H_3O^+ \quad (12)$$

A subsequent computational study considering $HCOO^-$ as the active species, concludes that formate would react in an H-down configuration to form CO_2 and adsorbed protons at a clean Pt surface without the need for adsorption.[24] The study also concluded that any adsorbed species would inhibit the oxidation of formate limiting access to a clean Pt surface.[24]

$$\text{C) Direct: } HCOO^- \rightarrow CO_2 + H^+ + 2e^- \quad (13)$$

With the discovery that formate is most likely the active species in FAO (see Equation 13), my analysis will incorporate this premise and that of indirect FAO from CO_{ad} formed from the oxidation of adsorbed bridge-bonded formate (notated b-COOH) described in Equations 1 to 3.

Voltammetry of formic acid in ILs has been reported and provides similar voltammetric features to those observed in aqueous media.[9,25,26] In particular, the large anodic current observed on the negative-going potential sweep after Pt

oxide removal has occurred, corresponding to direct FAO, occurs in both aqueous and IL systems (see Chapter 1.3.6).[25,27]

Pt oxides are generally thought to inhibit FAO either in alkaline media or acidic media formed at high potentials by competitively binding to active Pt sites.[9,22] Interactions between Pt-adsorbed oxygen species – oxide formation on metals being worthy of further study in its own right – and formate/formic acid (adsorbed or otherwise) is more complex than first thought. Samjeské *et al.* suggest that the identity of certain voltammogram peaks representing FAO are the result of active sites created from surface rearrangement, or 'place swapping', of Pt oxides.[16] A detailed discussion of oxide formation on Pt electrodes in aqueous and ionic liquid electrolytes is beyond the scope of this study, but it is important to discuss in brief because of surface-adsorbed species' effect on FAO. Oxide formation on Pt electrodes in acidic aqueous media at increasingly positive potentials (between Equations 14 and 18) is described below.[28]

$$Pt + H_2O \rightleftharpoons Pt\text{-}OH_{ad} + H^+ + e^- \quad (14)$$

$$Pt + H_2O \rightarrow Pt_4OH + H^+ + e^- \quad (15)$$

$$Pt_4OH + H_2O \rightarrow Pt_2OH + H^+ + e^- \quad (16)$$

$$Pt_2OH + H_2O \rightarrow PtOH + H^+ + e^- \quad (17)$$

$$Pt\text{-}OH \rightarrow Pt\text{-}O + H^+ + e^- \quad (18)$$

It should also be noted that different Pt oxides form at different Pt crystal facets than those presented in Equations 15 to 17 but it is sufficient for this study to consider Equations 14 and 18 as general equations for a multi-crystalline surface

with Equation 14 occurring at a lower potential than Equation 18.[27] As potential becomes more positive, in the broad oxide formation region of a CV prior to oxygen evolution in an aqueous acidic electrolyte, the Pt-oxide layer thickens and atom displacement can occur with surface oxides swapping with pristine Pt atoms in the underlayer creating a multilayer of Pt-oxides and a roughening of the electrode surface.[29]

The study of FAO in ionic liquids (ILs) and protic ionic liquids (PILs) specifically, is a new area of research. As discussed in other chapters of this work, PILs have been studied for use in hydrogen-fuel fuel cells for ultimate use at elevated temperatures, due to the enhanced electrokinetics; this would also apply to formic acid-fuel fuel cells. Furthermore, the effect of CO poisoning on Pt surfaces that greatly inhibits the FAO reaction (anodic fuel-cell reaction) at room temperature, could be ameliorated by the lessened poisoning effect of CO on Pt at elevated temperatures. PILs are good electrolyte candidates as they have very low vapour pressures and are commonly thermally stable between 100 and 200 °C.[30] Existing voltammetric assessment of FAO in PILs is limited and includes studies of Pd-nanoparticles on glassy-carbon (GC) electrodes in butylammonium nitrate (BAN)[26] and FAO in diethylmethylammonium trifluromethanesulfonate ([dema][TfO]) at Pt electrodes.[25] Work concerning the oxidation of CO to CO_2 , particularly important in indirect FAO, and methanol oxidation, has also been conducted using [dema][TfO] and Pt electrodes.[31]

To give an indication of whether formate or HCOOH is the active species in FAO in [dema][TfO], the parent base, diethylmethylamine (dema), was added to [dema][TfO] in addition to formic acid. In the presence of dema, the direct FAO

current on the negative-going sweep is significantly greater than in the presence of formic acid only.[25] This suggests that it is formate which is the active species, since adding a strong base such as dema, would readily deprotonate HCOOH to dema-H^+ and $HCOO^-$. This is in agreement with the experimental evidence for formate being the active species in aqueous systems provided by Joo *et al.* and computational work by Schwartz *et al*.[22,24]

Elsewhere in this thesis, there has been a discussion of proton activity (approximated by aqueous pK_a) and the potential at which the oxygen-reduction reaction occurs. There is ongoing interest in establishing meaningful definitions of pH and pK_a in ionic liquids with which accurate predictions can be made for proton activity.[32,33,34,35] While oxygen can act as a probe molecule to assess acidity in ILs,[36,37] the results of Goodwin *et al.* suggest that FA could be a probe molecule for basicity in ILs.[25] In this chapter, a range of bases with different aqueous pK_as were added to [dema][TfO] containing formic acid in an equimolar concentration to create a range of electrolytes that contained different concentrations of $HCOO^-$, relating to the basicity of the added base in the PIL. Cyclic voltammograms were then recorded at a Pt electrode in each of the electrolytes and the maximum current density of (uninhibited) direct formate oxidation, on the reverse (negative-going) potential sweep, compared with the aqueous pK_a of the base. The hypothesis that formic acid can be used as a probe molecule to determine basicity in PILs is tested.

6.2 Experimental Section

6.2.1 Materials and apparatus

All chemicals were obtained from Acros Organics (thiazole 99%), Sigma Aldrich (imidazole 99.5 %, pyridine 99.5 %), Merck (formic acid 98%), and were used as received. Ar (99.999%) was from CryoService (Worcester, UK). Pd wire (0.5 mm diameter, 99.99%) was from Alfa Aesar. A modulated speed rotator and platinum and glassy-carbon (GC) rotating disk electrodes (RDEs) and rotating ring-disk electrodes (RRDEs) were from Pine Research Instrumentation, Inc (Durham, NC, USA). Electrochemical measurements were performed using either a model CHI760C or CHI700D potentiostat from CH Instruments, Austin, TX, USA.

6.2.2 Synthesis and characterisation of [dema][TfO]

Diethylmethylammonium trifluoromethanesulfonate, [dema][TfO], was prepared by the dropwise addition of 1 mol dm^{-3} aqueous trifluoromethanesulfonic acid (abbreviated to triflic acid or sometimes TfOH) to 1 mol dm^{-3} aqueous N,N-diethylmethylamine (dema) with a 5% molar excess of the base. The reaction mixture was cooled in an ice bath. Excess water was removed using rotary evaporation. The product was then held under vacuum (5×10^{-2} mbar) at 40 °C for between 5 and 10 days, to remove residual water and base. The liquid was then transferred under vacuum to a glovebox containing a dry N_2 atmosphere (<0.1 ppm O_2 and <0.4 ppm H_2O). [dema][TfO] was characterized by ^{1}H, ^{13}C and ^{19}F NMR spectroscopy (Bruker Ascend™ 400 MHz NMR Spectrometer) using a hexadeuterodimethyl sulfoxide solvent. Attenuated total reflection Fourier-transform infrared spectroscopy was carried out using a Bruker Alpha Platinum-ATR FTIR spectrometer at 30 °C. Thermogravimetric

analysis (TGA) was carried out using a TA Instruments Discovery instrument under a N_2 atmosphere, and residual water contents were determined using Karl-Fischer titrations (Mitsubishi CA-200 Moisturemeter. Residual water contents were below 50 ppm. Characterisation data is presented in Chapter 3 and Appendix I.

6.2.3 Electrochemical measurements

A three-electrode electrochemical cell containing either a 4.6 mm diameter Pt disk or 5.6 mm diameter glassy-carbon working electrode, a Pt flag counter electrode (A ≈0.70 cm^2) and a Pd-H reference electrode, were used for all electrochemical measurements. The fabrication and use of Pd-H reference electrodes for electrochemistry are discussed in the experimental section in Chapter 4. Prior to use, the Pt or GC disk electrode was polished using an aqueous suspension of 0.05 μm α-alumina (Buehler, Lake Bluff, Illinois) on felt polishing pads, and rinsed thoroughly with deionized water. The Pt flag counter electrode was flame annealed in a butane flame before being rinsed with deionised water. All working and counter electrodes were dried in a glassware oven before use. Where electrochemical experiments have been conducted in a dry N_2-atmosphere glovebox (<0.1 ppm O_2 and <0.4 ppm H_2O) this will be stated in the corresponding figure legend. The cell was charged with 4 mL of [dema][TfO], sealed using rubber septa and, except when experiments were conducted in a glovebox, a blanket of Ar was maintained above the PIL during experiments to reduce contamination from atmospheric water and to keep oxygen from dissolving in the electrolyte. All voltammograms were *iR*-corrected unless otherwise stated. To mitigate for changes in the potential of the Pd-H reference electrode upon addition of acid and

base to [dema][TfO], potentials were adjusted such that the electrochemical window was the same during each analysis. For the formic acid (also denoted as HCOOH) oxidation experiments, HCOOH was added to 4 mL of [dema][TfO] using a micropipette to achieve a 0.1 mol dm^{-3} acid in the PIL. When a base was added to [dema][TfO] after formic acid addition, the volume of dema, imidazole, pyridine or thiazole added achieved a 0.1 mol dm^{-3} of base in [dema][TfO]. The aqueous pK_as of the conjugate acids of the bases added are 2.52 (thiazole),[23] 5.23 (pyridine),[23] 6.99 (imidazole)[23] and 10.6 (diethylmethylamine).[37] The aqueous pK_a of formic acid is 3.75.[23]

6.3 Results and Discussion

6.3.1 Electrochemical window studies

To understand the electro-oxidation of formic acid in a PIL electrolyte, pure formic acid was added to [dema][TfO] so that voltammetric experiments could be undertaken. Experiments with pure [dema][TfO] and [dema][TfO] containing formic acid were conducted in a dry N_2-atmophere glovebox to maintain a fixed water content. Figure 6.1 shows cyclic voltammograms of [dema][TfO], with and without formic acid, recorded at both stationary and rotating Pt and GC electrodes over a wide potential range.

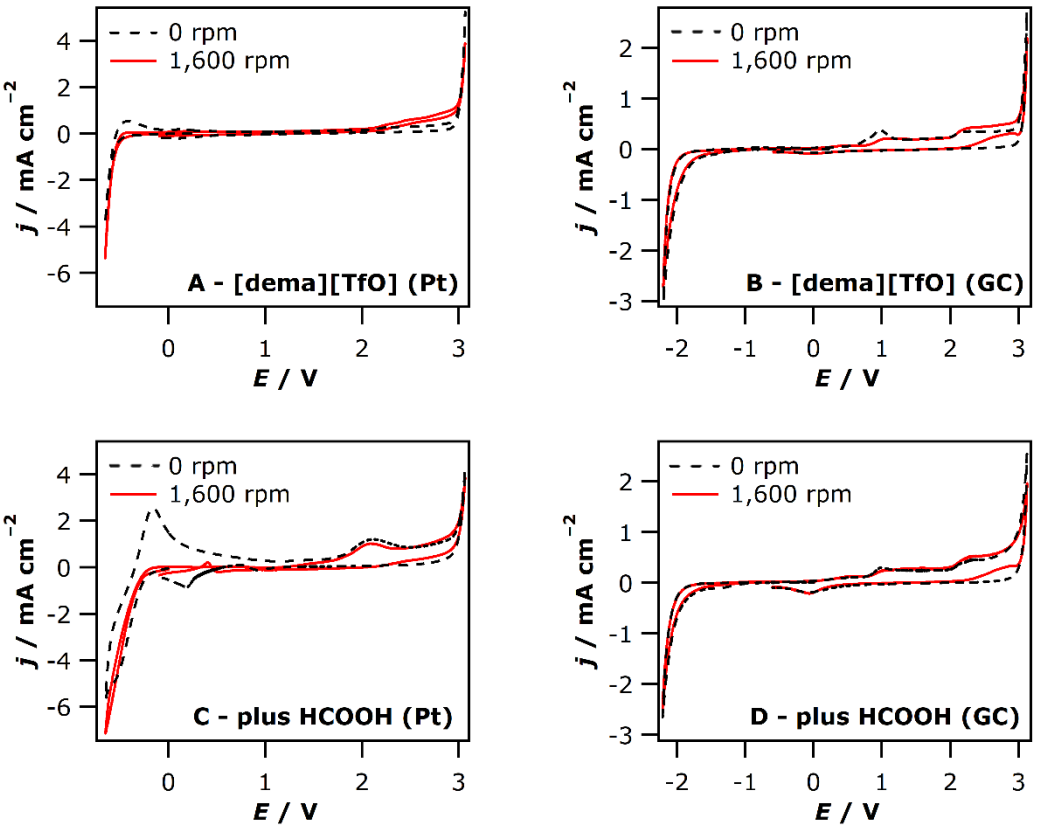


Figure 6.1 Cyclic voltammograms (CVs) of deaerated, dry (≈10 ppm H_2O) [dema][TfO] (A)/(B) and [dema][TfO] containing 0.1 mol dm^{-3} formic acid (C)/(D) recorded at Pt (A)/(C) and GC (B)/(D) stationary and rotating electrodes. Potential cycles begin in a negative-going direction at 100 mV s^{-1} beginning at ≈0 V. All CVs are recorded in a nitrogen-atmosphere glovebox with an atmospheric O_2 and H_2O concentration of <0.1 and <0.4 ppm respectively.

Figure 6.1 (A) shows cyclic voltammetry of [dema][TfO] containing ≈10 ppm H_2O recorded at a stationary and rotating Pt electrode. The electrochemical windows of [dema][TfO] are 3.5 V and 4.5 V at Pt and GC (see Figure 6.1 (B)) respectively, and the PIL-breakdown reactions are as follows.

$$\text{Negative of } -0.45\text{ V}/-1.6\text{ V (Pt/GC): } [\text{dema}]^+ + e^- \rightarrow \text{dema} + H_2 \qquad (19)$$

$$\text{Positive of 2.95 V (Pt \& GC): } [\text{TfO}]^- \rightarrow [\text{TfO}]^-_{\text{fragment}} + e^- \qquad (20)$$

The electrolytic breakdown of the PIL anion at highly oxidising potentials, shown in Equation 20, has been previously studied by Goodwin *et al.* In their work, it was

found that $[TfO]^-$ breaks down into the following ion fragments following mass spec.; CF_3^+, SO_2^+, SO^+, CF_2^+ and $CF_3SO_2^+$.[38]

Since some water is always present in PILs, due to their high hygroscopicity, water is oxidised at high positive potentials but lower potentials than that at which the $[TfO]^-$ anion is oxidised.[38] The oxidation of water in PILs has been shown to form oxides on Pt electrodes similar to those observed in aqueous systems.[39]

Since the water concentration remained ≈10 ppm in Figure 6.1 (A) because the experiments were conducted in a dry N_2 glovebox, the oxidation of the low concentration of water present is only clearly visible when the Pt electrode is rotated, increasing the mass transport of H_2O to the electrode surface resulting in an anodic current positive of around 2.1 V. At a GC electrode (see Figure 6.1 (B)), a similar observation is made, with water oxidation occurring positive of 2.1 V with a greater *j* when the electrode is rotated. The oxidation peak at 1.0 V recorded only at a GC electrode, is the oxidation of dema produced by the prior reduction of $[dema]^+$ at negative potentials (Equation 19). dema oxidation is only observed at GC because the H_2 produced in the negative voltammetric sweep is not re-oxidised back to the $[dema]^+$ cation at GC, which is a very poor hydrogen oxidation electrocatalyst, unlike Pt. The re-oxidation of H_2 to give $[dema]^+$ at Pt, the peak at −0.4 V on the positive-going sweep in Figure 6.1 (A), means that no neutral dema is left at the electrode surface to be oxidised.

$$2dema + H_2 \rightarrow 2[dema]^+ + 2e^- \qquad (21)$$

A more detailed discussion of neutral dema oxidation and evidence for the electrode-passivating effect of dema can be found in Chapter 4 and Chapter 7, respectively.

The CVs in Figure 6.1 (C) and (D) are recorded at Pt and GC electrodes, respectively, in [dema][TfO] containing 0.1 mol dm^{-3} HCOOH. The CVs recorded at a GC electrode in pure [dema][TfO] (Figure 6.1 (D)) and [dema][TfO] containing HCOOH (Figure 6.1 (B)), are nearly identical except for a greater water oxidation current in the acidified PIL and the presence of a reduction peak at about −0.1 V. The reduction peak is likely to be the removal of an oxide layer, formed on the GC electrode surface at water-oxidising potentials, because rotating the electrode has no effect on the presence of the peak or its magnitude (j_{max}). The higher water oxidation current and (likely) oxide removal current, are a result of an increase in water concentration caused by the addition of formic acid to the PIL. Despite being of a high purity (98 %), the added formic acid would have contained some water. Furthermore, the addition of the concentrated acid had to occur outside of the glovebox, and although every effort was taken to minimise exposure to air, some atmospheric water would have dissolved in the highly hygroscopic PIL before being transferred back to the glovebox for electroanalysis. No neutral dema oxidation current is observed when HCOOH has been added to [dema][TfO] because any electrogenerated dema (base) reacts with acid present in the bulk electrolyte. Since the CVs recorded at GC in the absence and presence of acid are so similar, except for effects caused by a slightly increased water concentration, formic acid oxidation in [dema][TfO] will be studied exclusively at a Pt electrode.

Figure 6.1 (C) shows voltammetry of [dema][TfO] containing 0.1 mol dm^{-3} HCOOH recorded using a Pt electrode. A formic acid reduction current is observed negative of −0.15 V and peaks at −0.5 V (stationary electrode),

$$2HCOOH + 2e^- \rightarrow H_2 + 2HCOO^- \quad (22)$$

and a corresponding quasi-reversible electrooxidation of H_2 and formate to formic acid, peaks at about −0.15 V (stationary electrode).

$$H_2 + 2HCOO^- \rightarrow 2HCOOH + 2e^- \quad (23)$$

On the positive-going potential sweep in Figure 6.1 (C), an anodic peak at ≈2.1 V is recorded at a stationary Pt electrode but does not reach a discernible j_L when the electrode is rotated; this is because of the formation of a Pt-oxide layer decreasing the area of Pt accessible to FA or H_2O at potentials positive of 2.1 V (the same reason as for the HOR phenomenon described in Chapter 4). On the negative-going sweep, an anodic (positive) current is observed at ≈0.8 V at a stationary electrode and at ≈0.4 V at an electrode rotating at 1,600 rpm. This is clearly attributable to FAO oxidation and will be discussed further. The reduction peak observed at around 0.2 V in Figure 6.1 (C) at a stationary Pt electrode, on the negative-going sweep after the positive electrochemical limit has been reached, is likely the reduction of triflic acid (TfOH) that has been made by the electrooxidation of water on the prior positive-going potential sweep. With the context of the electrochemical potential window of [dema][TfO], with and without HCOOH, now established, there remains only a voltammetric study of water oxidation in PILs (water always present at some concentration) before a detailed

study of FAO over the appropriate potential range can be undertaken, because of the overlapping potentials of H_2O and FAO redox events.

6.3.2 Water oxidation in [dema][TfO]

The voltammograms in Figure 6.2 are recorded in wet (≈2,388 ppm H_2O) and dry (≈10 ppm H_2O) [dema][TfO] at stationary and rotating Pt and GC electrodes in a glovebox. The CVs recorded at a GC electrode in Figure 6.2 (B) show an increase in anodic current positive of 1.5 V in the presence of a higher water concentration. Also, in both wet and 'dry' [dema][TfO] there is an increase in anodic current when the mass transport of H_2O to the GC electrode is increased by rotating the electrode at 1,600 rpm. Another notable difference in the CVs recorded in wet and 'dry' [dema][TfO] is the reduction peak at ≈−0.25 V on the negative-going potential sweep only present in wet [dema][TfO]; this is only observed after the electrode potential has been swept to water-oxidising potentials on the previous potential sweep. Given that a cathodic peak at ≈−0.25 V is observed at both a stationary and rotating GC electrode, it suggests that this reduction is the removal of an adsorbed species from the surface of the GC electrode – possibly an oxide formed through water oxidation.

The CVs recorded at a Pt electrode comparing 'dry' and wet [dema][TfO] electrolytes in Figure 6.2 (A) show a number of notable differences attributable to the difference in water concentration. Rotating the Pt electrode in 'dry' [dema][TfO] containing ≈10 ppm H_2O (black line) makes little difference to the stationary CV other than an increase in cathodic current positive of 2.0 V. Where water is present in a significantly higher concentration (2,388 ppm), shown by the dashed red (0 rpm) and solid red (1,600 rpm) CVs, clear anodic currents are

observed positive of 1.1 V and 2.0 V on the positive-going potential sweep, and cathodic currents observed on the subsequent negative-going potential sweep with peaks at around 0.75 V and 0.4 V. The CV of a rotating Pt electrode in wet [dema][TfO] contains the same features as that recorded at a stationary electrode (albeit at lower current maxima) but the cathodic peaks on the negative-going potential sweep at about 0.8 V and 0.4 V are still present, suggesting the removal of an adsorbed oxygen species, but with a significantly lower j_{max}. The lower j_{max} in this case suggests the reduction of a non-adsorbed species produced by an electro-oxidation on the preceding positive-going potential sweep, which would only be observed at a stationary electrode. The significant increase in j of both oxidation features on the positive-going potential sweep (the shoulder positive of 1.1 V and peak positive of 2.0 V) where the water content of [dema][TfO] is high, indicate that both these processes are oxidation of H_2O. This is consistent with previous reports of water oxidation occurring in PILs, forming adsorbed Pt-oxides and Pt-oxide electro-reduction.[39,38]

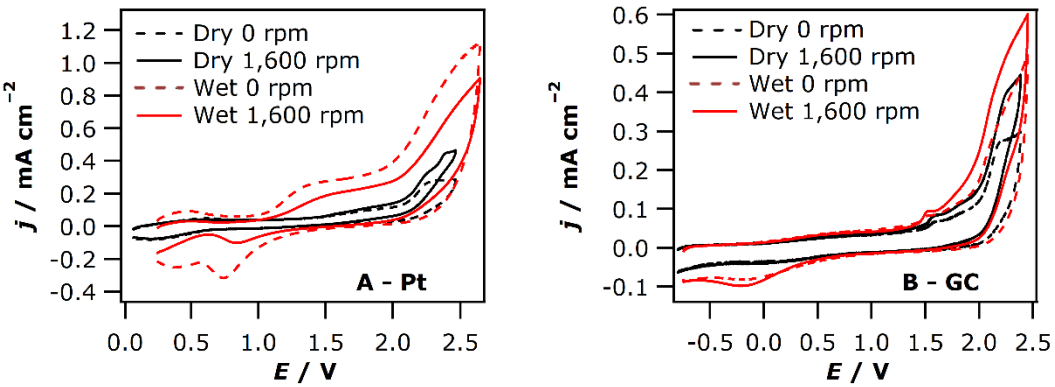


Figure 6.2 Cyclic voltammograms (CVs) of dry (≈10 ppm H_2O) and wet (≈2,388 ppm H_2O) deaerated [dema][TfO] recorded at Pt (A) and GC (B) stationary and rotating electrodes. Potential cycles begin in a positive-going direction at 100 mV s^{-1} beginning at ≈0.2 V or ≈−0.8 V. CVs are recorded in a nitrogen-atmosphere glovebox with an atmospheric O_2 and H_2O concentration of <0.1 and <0.4 ppm respectively.

The oxidation of water at a Pt electrode in PILs such as [dema][TfO] clearly involves two or more distinct processes (see Figure 6.2). To investigate water oxidation at Pt further, and identify which redox events are coupled, a Pt electrode was initially potential-cycled between −0.1 V and 0.9 V and then with each successive cycle, the upper potential limit was increased by 0.1 V until the final cycle between −0.1 V and 3.0 V (Figure 6.3 (A)); this was then repeated at a Pt electrode rotating at 1,600 rpm (Figure 6.3 (B)) to see if the cathodic currents recorded are the reduction of Pt-adsorbed species. Each successive CV in Figure 6.3 has been coloured chromatically with the shortest potential range CV (and first recorded) in red, and the second largest in pink. The largest potential range (and last recorded) CV is in black for clarity.

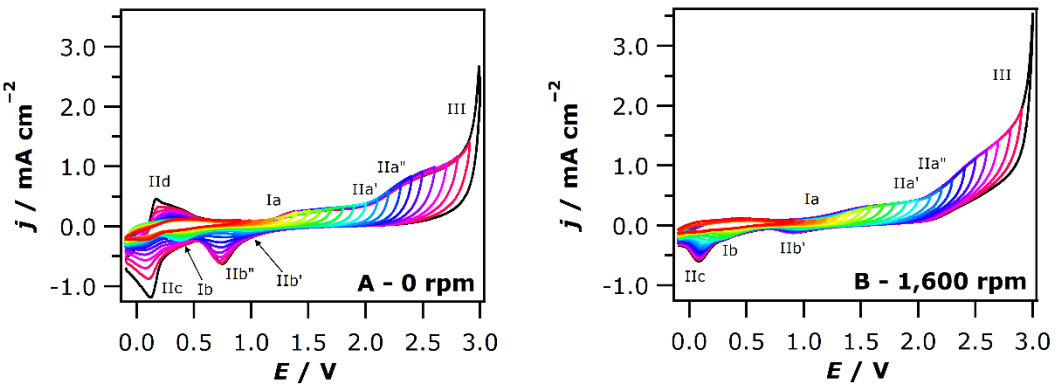


Figure 6.3 Cyclic voltammograms (CVs) of wet (≈2,388 ppm H_2O) deaerated [dema][TfO] recorded at stationary (A) and rotating (B) Pt electrodes. Potential cycles begin in a positive-going direction at 100 mV s^{-1} from ≈0 V. Potential cycles increase by 0.1 V in the positive direction with each successive cycle. CVs are recorded in a nitrogen-atmosphere glovebox with an atmospheric O_2 and H_2O concentration of <0.1 and <0.4 ppm respectively.

The CVs in Figure 6.3 (A) show no features distinct from the dry [dema][TfO] blank (see Figure 6.1 (A)) until the potential cycle goes positive of 1.2 V where the first anodic current, attributable to water oxidation, is recorded (denoted process I_a). Between 1.2 V and 2.0 V, the voltammetry of process I_a takes the 'shoulder' profile

of oxide formation on Pt as previously observed.[39] Accompanying the onset of oxidation process I_a positive of 1.2 V is a reduction denoted I_b which has an onset potential negative of 0.6 V and a peak at ≈0.4 V. If I_a is the oxidation of water and the formation of a Pt-oxides, then I_b must be the removal of the Pt-oxide layer. The I_b peak occurs at increasingly negative potentials, and j_{max} increases, as the upper potential is increased between 1.2 V and 2.1 V, and is likely the result of a more complete oxide layer covering of the Pt electrode, or possibly multi-layers of Pt-oxide as the potential approaches 2.1 V. If the upper potential is increased beyond 2.1 V the I_b reduction peak stops growing and by an upper cycle potential of 2.4 V, a clear peak disappears and is subsumed by the onset of the II_c reduction. The disappearance of a clear I_b peak coincides with the onset of process II_a which begins positive of 1.9 V and suggests that the Pt-oxide formed in process I_a, which is reduced in process I_b, is being further oxidised to a different Pt-oxide species. The process labelled II_a which occurs between 1.9 V and 2.8 V is also accompanied by two distinct reduction processes denoted II_b and II_c. Reduction II_b begins negative of 1.3 V and results in a peak which shifts to increasingly negative potentials, with j_{max} also increasing, as the upper potential of the cycle increases up to 2.8 V. This shifting in peak potential and increase in j_{max} (II_b) at both a rotating and stationary electrode, suggests that II_a is also forming a Pt-oxide layer that covers a greater proportion of the Pt electrode as the potential is scanned increasingly positive; a Pt-oxide which is then removed in II_b. However, reduction II_b is more complex than first considered because the potential of j_{max} at stationary and rotating electrodes are different (see Figure 6.3). At a stationary electrode (see Figure 6.3 (A)) the II_b j_{max} of the widest potential cycle is at ≈0.75 V and ≈−0.6 mA cm^{-2} whereas the same at a rotating electrode (see Figure 6.3 (B)) is

≈0.9 V at a much lower j_{max} ≈0.15 mA cm^{-2}; this suggests that II_b is actually two distinct processes, one the removal of a surface oxide and the second, at a more negative potential, the reduction of a non-adsorbed species at the electrochemical double layer. The II_b reduction peak recorded at a rotating Pt electrode in Figure 6.3 (B) must be the reduction of an adsorbed Pt-oxide species made in the II_a oxidation process. Upon closer inspection, the II_b reduction at a stationary electrode in Figure 6.3 (A) contains two features, a 'shoulder'-like reduction negative of 1.3 V (denoted II_b') which changes to a different process negative of 0.95 V (denoted II_b") giving a peak at 0.75 V. At a stationary electrode, the II_b' reduction occurs as the cycle potential maximum increases past 1.9 V, coinciding with the onset of the II_a oxidation process. However, it is not until the cycle potential maximum increases past 2.2 V that reduction II_b", the electroreduction of a non-adsorbed species, is observed with a peak around 0.75 V. The identity of the non-adsorbed species reduced in II_b" is explored in Figure 6.4. The onset and peak potentials of redox processes labelled in Figure 6.3 (A) and (B) are presented in Table 6.1 and Table 6.2, respectively.

Table 6.1 Additional information on the labelled voltammetric features in Figure 6.3 (A) showing voltammetry at a stationary Pt electrode. +ve = positive, −ve = negative.

CV Feature	≈ Onset Potential (V)	Peak Potential (V)	Description
I_a	+ve of 1.20	N/A	Oxide formation 1
I_b	−ve of 0.60	≈0.40	Oxide removal 1
II_a'	+ve of 1.90	≈2.60 (broad)	Oxide formation 2
II_b'	−ve of 1.30	≈0.95	Oxide removal 2
II_a''	+ve of 2.20	≈2.60 (broad)	Oxygen evolution
II_b''	−ve of 0.95	≈0.75	Oxygen-reduction (TfOH-coupled)
II_c	−ve of 0.20	≈0.10	Hydrogen evolution
II_d	+ve of 0.10	≈0.20	Hydrogen oxidation
III	+ve of 2.80	N/A	Electrolysis of $[TfO]^-$

As well as the II_b reductions, another reduction process also accompanies the II_a oxidation. The reduction labelled II_c is immediately preceded by a 'shoulder'-like reduction negative of ≈0.5 V, likely to be reduction I_b, but has a clear onset negative of 0.2 V. Despite the II_c reduction being observed as the II_a oxidation onset positive of 1.9 V occurs, it is not until the cycle potential maximum increases past 2.2 V that a significant increase in II_c j_{max} occurs; this suggests that the species reduced in II_c is produced via the II_a process, occurring positive of 2.2 V, shown to also produce the non-adsorbed species reduced in the II_b'' process. Furthermore, when comparing the II_c reduction at stationary and rotating electrodes in Figure 6.3 (A) and (B) respectively, the significantly lower II_c j_{max} in the cycle with the widest potential range at the rotating electrode (0.6 mA cm^{-2}), compared with the stationary electrode (−1.2 mA cm^{-2}), strongly suggests that, as well as an adsorbed

component being reduced in II_c, there is also a non-adsorbed species at the electrochemical double layer being reduced at the same potential.

Table 6.2 Additional information on the labelled voltammetric features in Figure 6.3 (B) showing voltammetry at a Pt electrode rotating at 1,600 rpm. +ve = positive, −ve = negative.

CV Feature	≈ Onset Potential (V)	Peak Potential (V)	Description
I_a	+ve of 1.1	N/A	Oxide formation 1
I_b	−ve of 0.60	≈0.25	Oxide removal 1
II_a'	+ve of 1.90	≈2.60 (broad)	Oxide formation 2
II_b'	−ve of 1.30	≈0.90	Oxide removal 2
II_a''	+ve of 2.20	≈2.60 (broad)	Oxygen evolution
II_b''	N/A	N/A	TfOH-coupled ORR not observed
II_c	−ve of 0.20	≈0.10	Hydrogen evolution
II_d	N/A	N/A	Hydrogen oxidation not observed
III	+ve of 2.80	N/A	Electrolysis of $[TfO]^-$

Following reduction II_c, there is a reversible oxidation (denoted II_d) coupled to it with a 0.075 V peak-to-peak separation. This oxidation is only observed at a stationary electrode however, confirming that II_c and II_d are a redox couple and indicating that the product of reduction II_c is not adsorbed to the surface of the electrode. At potentials positive of 2.8 V the $[TfO]^-$ anion is electrolysed and the upper potential limit of the [dema][TfO] solvent is reached; this process is labelled III in Figure 6.3. There is no new reduction process that accompanies oxidation process III but it is of note that the II_c j_{max} is significantly increased at a stationary electrode (see black CV in Figure 6.3 (A)); this suggests that the product of oxidation III is reduced in reduction II_c, and is not adsorbed to the Pt electrode.

With the redox processes described, and the coupled processes established, determining the identity of the reactant and products was paramount.

Given that oxidations I_a and II_a are water oxidation reactions that form different adsorbed oxides on Pt, and reductions I_b and II_b' are the respective Pt-oxide removal reactions, the II_b'' reduction of a non-adsorbed species and II_c simultaneous reduction of an adsorbed and non-adsorbed species (and its oxidation couple, II_d) remain to be explained. However, some tentative, novel, solutions will be posited that are consistent with all other voltammetric observations presented in this thesis and with others' observations of water oxidation in [dema][TfO] at a Pt electrode.

Firstly, the reduction of a non-adsorbed species in II_b'' is only observed if the potential has been swept positive of 2.2 V; this suggests the II_a oxidation produces an adsorbed oxide between 1.9 V and 2.2 V (reduced in II_b') and continues to produce an adsorbed oxide positive of 2.2 V, but also produces the non-adsorbed species reduced in II_b'' – this second oxidative process positive of 2.2 V is evidence of complete water splitting.

$$\text{OER: } (II_a''): 2H_2O + 4[TfO]^- \rightarrow O_2 + 4TfOH + 4e^- \qquad (24)$$

To test the hypothesis that oxygen is evolved from Pt in [dema][TfO] positive of 2.2 V, [dema][TfO] was saturated with oxygen and acidified to a 0.1 mol dm^{-3} concentration of triflic acid (TfOH) and a CV recorded. [dema][TfO] was acidified with TfOH to approximate the conditions at the electrode surface after the OER, as hypothesised in Equation 24. The effect of the presence of acids on the oxygen-reduction reaction (ORR) is well documented elsewhere in this thesis

(see Chapter 4) with the ORR onset potential roughly proportional to the pK_a of the acid added, within specific pK_a limits. The red CV in Figure 6.4 (A) shows the onset of ORR in a TfOH-present environment (see Equation 25) to be negative of ≈0.95 V – identical to that of the reduction of the non-adsorbed species in reduction IIb". Furthermore, both acid-ORR and II_b" have a similar j_{max} peak potential of ≈0.75 V. These results suggest that oxygen is evolved from H_2O positive of 2.2 V at a Pt electrode and also produces triflic acid.

$$\text{ORR } (II_b\text{"}): O_2 + 4TfOH + 4e^- \rightarrow 2H_2O + 4[TfO]^- \quad (25)$$

The high overpotential for the oxygen-evolution reaction (OER) at Pt in [dema][TfO] can be explained by considering the thermodynamics of the PIL anion. $[TfO]^-$ being a very poor base (very strong conjugate acid, TfOH, with a pK_a of −14), would only accept the protons from the OER at a very high overpotential. A method of lowering the OER overpotential in PILs could therefore be to add a base to the PIL, which would more readily accept protons, or use a PIL with a weaker parent acid.

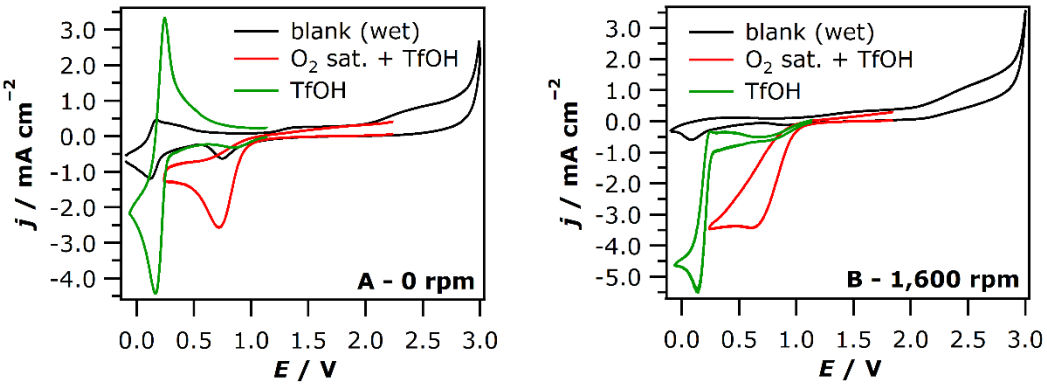


Figure 6.4 Cyclic voltammograms (CVs) of wet (≈2,388 ppm H_2O) deaerated [dema][TfO], deaerated [dema][TfO] containing 0.1 mol dm^{-3} triflic acid (TfOH), and O_2-saturated [dema][TfO] containing 0.1 mol dm^{-3} TfOH recorded at stationary (A) and rotating (B) Pt electrodes. The CVs of wet [dema][TfO] are taken from Figure 6.3 at the widest potential range after potential cycling with incrementally increasing upper potential. CVs are recorded at 100 mV s^{-1}. CVs of wet [dema][TfO] are recorded in a nitrogen-atmosphere glovebox with an atmospheric O_2 and H_2O concentration of <0.1 and <0.4 ppm respectively. CVs in oxygenated and acidified [dema][TfO] were conducted in ambient atmosphere in a fumehood.

If Equation 24 is correct, and the OER occurs positive of 2.2 V and makes triflic acid as well as O_2, reduction II_c can also be explained. As mentioned above, II_c includes the reduction of both an adsorbed and non-adsorbed species at the same potential, is coupled with oxidation II_d, and is kinetically fast – this is indicative of H_2 electrochemistry. To test whether II_c is triflic acid/proton reduction, [dema][TfO] was deaerated and acidified with TfOH to a 0.1 mol dm^{-3} concentration and a CV recorded. The green CV in Figure 6.4 (A) shows triflic acid reduction and hydrogen oxidation at a potential very close to that of the II_c/II_d redox couple, strongly suggesting that II_c/II_d is acid/proton reduction and hydrogen oxidation. A consequence of II_c being observed at a rotating electrode indicates that, if the assumption of TfOH/proton reduction is correct, TfOH must be made positive of 1.9 V (II_a' onset) and must adsorb to Pt (either as Pt-TfOH or Pt-H) at this potential with non-adsorbed TfOH being made positive of 2.2 V (II_a" onset). Non-adsorbed TfOH reduction and adsorbed TfOH reduction in II_c is

described by Equations 26 and 27, respectively. Equation 27 assumes that reduction of adsorbed TfOH produces a non-adsorbed triflate anion.

$$II_c: 2TfOH + 2e^- \rightarrow 2[TfO]^- + H_2 \quad (26)$$

$$II_c: 2Pt\text{-}TfOH_{ads} + 2e^- \rightarrow 2Pt + 2[TfO]^- + H_2 \quad (27)$$

The oxidation corresponding to the II_c reduction is II_d, and is described by Equations 28 and 29 depending on whether $[TfO]^-$ remains adsorbed to Pt after adsorbed TfOH reduction. It is unknown if the adsorbed TfOH is removed by reduction or if a hypothetical adsorbed $[TfO]^-$ is removed through H_2 oxidation in II_d.

$$II_d: 2[TfO]^- + H_2 \rightarrow 2TfOH + 2e^- \quad (28)$$

$$II_d: 2Pt\text{-}[TfO]^- + H_2 \rightarrow 2Pt\text{-}TfOH + 2e^- \quad (29)$$

It has been deduced from the voltammetry in Figure 6.3 and previous work[39] that I_a produces a Pt oxide which is reduced in I_b. While Pt-OH, Pt-O and Pt-O_2 adsorbed oxide species have been identified on Pt in acidic aqueous systems which form from the oxidation of water at increasingly positive potentials, the only Pt oxide species directly observed spectroscopically in [dema][TfO] are Pt-O and Pt-O_2 and so the following equations discussing oxide formation and removal will proceed on the assumption that these are the two principal oxide species formed on Pt in [dema][TfO].[28,39,38,40] Possible mechanisms for the first Pt oxide formation reaction positive of 1.2 V, labelled I_a in Figure 6.4, are presented below.

$$I_a: 3Pt + 3H_2O \rightarrow 3Pt\text{-}O_{ads} + 2H_3O^+ + 2e^- \quad (30)$$

The formation of Pt-O_{ads} in Equation 30 does not require a base other than H_2O to accept the proton produced by water oxidation, however, an alternative to Equation 30 could include the proton being adsorbed to Pt. The proton could not sit on the $[TfO]^-$ to make TfOH at these potentials because I_a (1.2 V to 1.9 V) does not produce any detectable TfOH. The removal of surface oxide (process I_b) produced in I_a is described by two possible pathways in Equations 31 and 32 and requires the donation of a proton either from the PIL cation $[dema]^+$ or from H_2O.

$$I_b: Pt\text{-}O_{ads} + 2[dema]^+ + 2e^- \rightarrow Pt + H_2O + 2dema \quad (31)$$

$$I_b: Pt\text{-}O_{ads} + 2H_2O + 2e^- \rightarrow Pt + H_2O + 2OH^- \quad (32)$$

It has not yet been determined which of the two species $[dema]^+$ or H_2O provide the proton for oxide removal I_b. H_2O is more likely the proton donor over the potential range of reduction I_b (negative of 0.6 V), since proton reduction of $[dema]^+$ to evolve H_2 is negative of ≈−0.45 V however, it is not inconceivable that Pt-O_{ads} is more active toward $[dema]^+$ reduction than clean Pt.

The final water oxidation to Pt-oxide process is that labelled II_a' in Figure 6.3 from which it has been deduced that II_a' produces a Pt oxide (a different oxide to that made in I_a) as well as likely producing Pt-adsorbed TfOH for its part in reduction II_c (see above). A possible reaction mechanism for the further oxidation of Pt-O_{ads}, made in I_a (Equation 30), by oxidation II_a' positive of 1.9 V is presented below.

$$II_a': Pt\text{-}O_{ads} + H_2O + 2[TfO]^- \rightarrow Pt\text{-}O_{2,ads} + 2Pt\text{-}TfOH_{ads} + 2e^- \quad (33)$$

Here Pt-O_{ads} is oxidised to Pt-O_2 positive of 1.9 V with the proton sitting on $[TfO]^-$ which co-adsorbs to Pt as Pt-$TfOH_{ads}$. The high water oxidation overpotential is likely the result of the $[TfO]^-$ being a very poor base and so high overpotentials are

required for it to accept a proton; this is the same reason for the even higher overpotential for the OER (≈2.2 V) described previously in this chapter. The onset of II_a' is also accompanied by reduction II_b' and reduction II_c. II_b' is the reduction of Pt-O_2 formed in II_a' either to Pt-O_{ads} or Pt, and II_c is the reduction of adsorbed TfOH formed in II_a'. Positive of 2.2 V, II_a' coincides with the onset of II_b' which results in oxygen evolution and non-adsorbed triflate production (see Equation 24).

The reduction of Pt-O_{2ads} in II_b' negative of 1.3 V is described by Equation 34 and requires the Pt-$TfOH_{ads}$ species also made in II_a'; this is supported by II_b' occurring at the same potential at a rotating electrode as well as a stationary one.

$$II_b': \text{Pt-}O_{2,ads} + 2\text{Pt-TfOH}_{ads} + 2e^- \rightarrow \text{Pt-}O_{ads} + H_2O + 2[TfO]^- \quad (34)$$

The oxide formation/removal redox couples, I_a/I_b and II_a'/II_b', are kinetically slow processes with onset potential separations of 600 mV for both redox couples which is significantly less electrochemically reversible than that observed at a Pt electrode in aqueous systems. The apparent high overpotential for water oxidation in [dema][TfO] is likely also caused by the high electrode potential required for protonating triflate in oxidation II_a'.[28]

6.3.3 Formic acid oxidation in [dema][TfO]

With the voltammetry of water in [dema][TfO] and the associated redox process better understood, a discussion of FAO in [dema][TfO] can begin. The voltammograms presented in Figure 6.5 are recorded at rotating and stationary Pt and GC electrodes in dry [dema][TfO] (≈10 ppm H_2O), wet [dema][TfO] (≈2,388 ppm), and dry [dema][TfO] containing 0.1 mol dm^{-3} HCOOH. The near-identical

CVs recording at GC electrodes in dry [dema][TfO] and dry [dema][TfO] with HCOOH in Figure 6.5 (B) and (D) provide no evidence for FAO at GC. The difference between the CVs recorded in wet and dry [dema][TfO] electrolytes at GC electrodes identifies the oxidation of H_2O positive of about 1.5 V with the removal of surface oxides in the wet electrolyte negative of 0.5 V. The presence of surface oxides is supported by the cathodic current peak at ≈0.2 V having very similar magnitudes at both a stationary and rotating electrode, and that this peak is only observed in wet [dema][TfO]. Because GC is not active for FAO, as previously stated, the discussion will only be concerned with FAO at a Pt electrode.

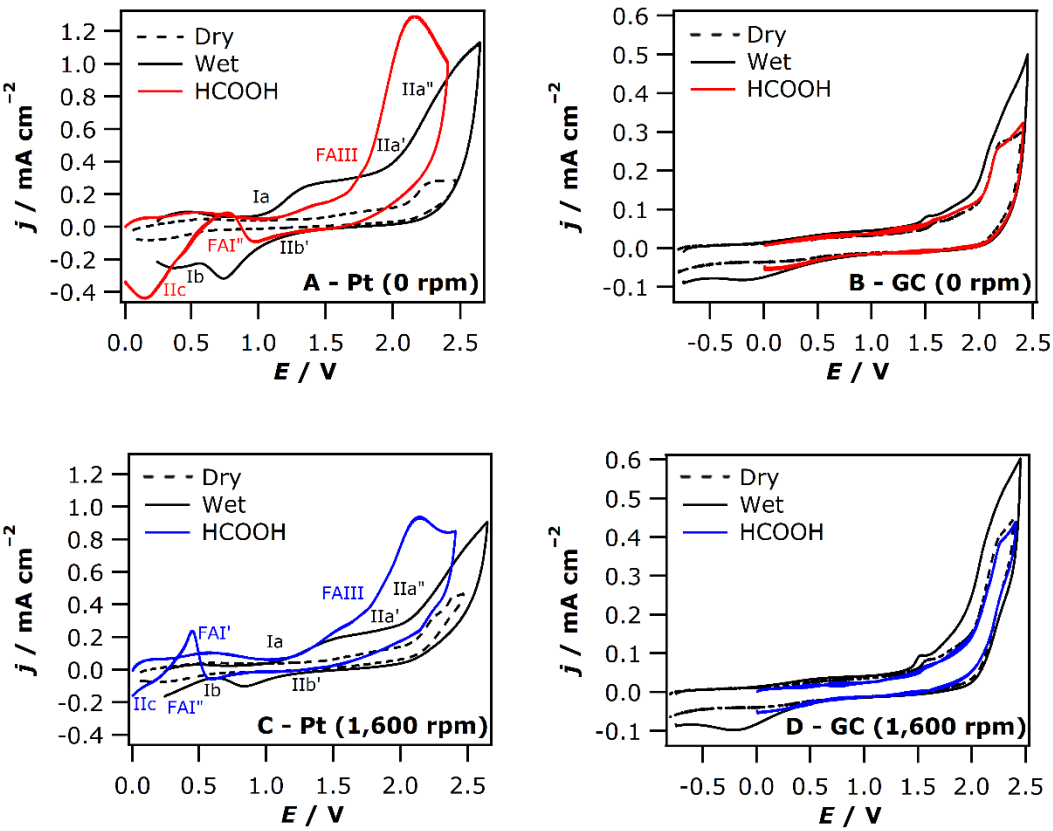


Figure 6.5 Cyclic voltammograms (CVs) of deaerated [dema][TfO] containing 0.1 mol dm^{-3} formic acid recorded at Pt (A)/(C) and GC (B)/(D) stationary and rotating electrodes. Potential cycles begin in a positive-going direction at 100 mV s^{-1} beginning at ≈0 V or ≈−0.8 V. Blanks are recorded in dry (≈10 ppm H_2O) and wet (≈2,388 ppm H_2O) [dema][TfO]. CVs are recorded in a nitrogen-atmosphere glovebox with an atmospheric O_2 and H_2O concentration of <0.1 and <0.4 ppm respectively.

The voltammograms in panels A and C in Figure 6.5 compare HCOOH-containing dry [dema][TfO] with wet and dry [dema][TfO] over a similar potential range recorded at a stationary and rotating Pt electrode. Redox processes only observed when HCOOH is present, are labelled with the prefix 'FA' in red (Figure 6.5 (A), 0 rpm) and blue (Figure 6.5 (B) 1,600 rpm). The voltammetric profile of HCOOH in [dema][TfO] is near identical to that previously recorded in the PIL at a Pt electrode and is also similar to that of HCOOH in an acidic aqueous system albeit with some differences which will be discussed.[7,25] On the positive-going potential sweep in [dema][TfO] containing HCOOH, the first oxidation occurs positive of ≈1.1 V and coincides with water oxidation I_a (Equation 30) but at a much lower j_{max} than the wet blank likely because of a significantly lower water content. However, it is still possible that this is a FAO process – possibly CO_{ads} oxidation and will be considered. Positive of 1.5 V, a second oxidation process occurs labelled FAIII which obscures any water oxidation current from processes II_a' (Equation 33) and II_a" (Equation 25) present in the wet blank.

On the negative-going potential sweep at a stationary Pt electrode, surface oxides are reduced in process IIb' (Equation 34) negative of 1.3 V, which immediately precedes oxidation FAI" (peak at ≈0.7 V) widely considered to be direct FAO on the clean Pt surface after CO_{ads} and Pt-oxide removal.[7,17,22,25] On a stationary electrode, the reduction negative of 0.7 V is likely oxide removal I_b (Equation 31 or 32) which precedes the reduction of an adsorbed protic species (likely TfOH) in II_c which forms at positive potentials in the preceding positive-going potential sweep. At a rotating Pt electrode on the negative-going potential sweep, the removal of surface oxides shifts to a more negative potential with either IIb'

(Equation 34) shifting to an onset negative of 0.9 V or IIb' not occurring and reduction I_b (Equation 31 or 32) occurring instead. The negative shift in oxide removal at a rotating electrode has the effect of shifting direct FAO in FAI" to a more negative potential with a peak at ≈0.4 V.

In order to better understand the coupled processes in FAO and the inextricable Pt oxide formation and removal, similar to wet [dema][TfO] in Figure 6.3, successive potential cycles each more positive than the previous cycle, were recorded in [dema][TfO] containing 0.1 mol dm^{-3} HCOOH, and is shown in Figure 6.6 (E) and (F). Table 6.3 and Table 6.4 present the onset and peak potentials of redox events in Figure 6.6 (E) and (F), respectively.

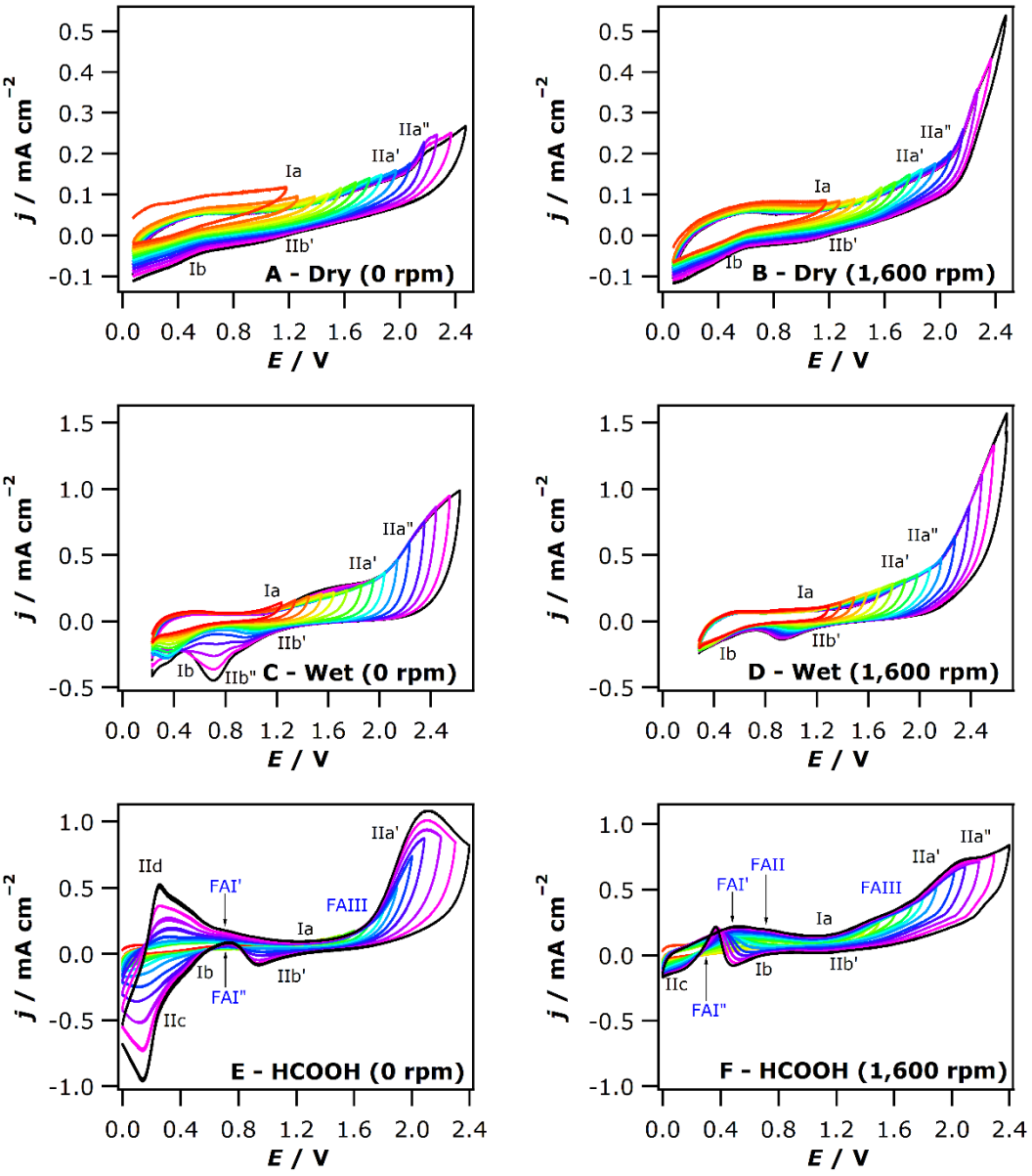


Figure 6.6 Cyclic voltammograms (CVs) of dry (≈10 ppm H_2O) and wet (≈2,388 ppm H_2O) deaerated [dema][TfO] (A/B/C/D), and deaerated [dema][TfO] containing 0.1 mol dm^{-3} formic acid (E/F), recorded at stationary and rotating Pt electrodes. Potential cycles begin in a positive-going direction at 100 mV s^{-1} from ≈0 V. Potential cycles increase by 0.1 V in the positive direction with each successive cycle. CVs are recorded in a nitrogen-atmosphere glovebox with an atmospheric O_2 and H_2O concentration of <0.1 and <0.4 ppm respectively. CVs in frames (D), (E) and (F) are not *iR*-corrected however, the small solution resistance does not affect the CVs at these current densities (CVs with and without *iR*-correction show no significant differences).

Table 6.3 Additional information on the labelled voltammetric features in Figure 6.6 (E) showing voltammetry at a stationary Pt electrode. +ve = positive, −ve = negative.

CV Feature	≈ Onset Potential (V)	Peak Potential (V)	Description
FAI'	+ve of 0.2	≈0.7	Direct formic acid oxidation (FAO) (inhibited)
FAII	N/A	N/A	FAO (not resolved at stationary electrode)
I_a	N/A	N/A	Oxide formation 1 (likely obscured by FAIII)
I_b	−ve of 0.7	≈0.5	Oxide removal 1
FAIII	+ve of 1.5	≈2.1	Formic acid oxidation
II_a'	+ve of 1.9	N/A	Oxide formation 2 (likely obscured by FAIII)
II_a''	+ve of 2.2	N/A	Oxygen evolution (likely obscured by FAIII)
II_b'	−ve of 1.3	≈0.95	Oxide removal 2
FAI"	−ve of 0.9	≈0.7	Direct formic acid oxidation (uninhibited)
II_c	−ve of 0.3	≈0.1	Hydrogen evolution
II_d	+ve of 0.1	≈0.3	Hydrogen oxidation

Table 6.4 Additional information on the labelled voltammetric features in Figure 6.6 (F) showing voltammetry at a Pt electrode rotating at 1,600 rpm. +ve = positive, −ve = negative.

CV Feature	≈Onset Potential (V)	Peak Potential (V)	Description
FAI'	+ve of 0.2	0.5	Direct formic acid oxidation (inhibited)
FAII	+ve of 0.6	0.7	Formic acid oxidation
I_a	+ve of 1.1	N/A	Oxide formation 1
I_b	−ve of 0.7	0.5	Oxide removal 1
FAIII	+ve of 1.5	2.1	Formic acid oxidation
II_a'	+ve of 1.9	N/A	Oxide formation 2 (obscured by FAIII)
II_a"	+ve of 2.2	N/A	Oxygen evolution
II_b'	−ve of 1.3	≈1.1	Oxide removal 2
FAI"	−ve of 0.9	≈0.4	Direct formic acid oxidation (uninhibited)
II_c	−ve of 0.3	≈0.1	Hydrogen evolution
II_d	N/A	N/A	Hydrogen oxidation (not observed)

The cyclic voltammetry in Figure 6.6 (E) recorded at a stationary Pt electrode shows three distinct FAO events. The first occurs positive of 1.5 V with a peak at ≈2.1 V and is labelled FAIII. This first FAO peak coincides with Pt oxide formation I_b' and II_b' in the wet [dema][TfO] blank. Since water cannot be eliminated from [dema][TfO] completely, and the 98% formic acid used contains some water, there will be water oxidation (oxide formation) also occurring at FAIII oxidation potentials. The oxide formation, although obscured by FAIII, is detectable indirectly by its reductions in II_b' negative of 1.3 V and I_b negative of 0.7 V. Water oxidation I_a does not appear at a stationary electrode but does at a rotating one due to the low water content of the FA-containing [dema][TfO]. By rotating the electrode, mass transport of H_2O to the electrode surface is greatly increased

causing a greater I_a water oxidation current in Figure 6.6 (F) than in Figure 6.6 (E). With the removal of the Pt-oxide (Pt-O_{2ads}) in II_b', direct FAO (labelled FAI') can take place at negative of 0.9V on the negative-going potential sweep on the newly clean Pt surface. Residual Pt oxides (Pt-O_{ads}) are then removed in I_b before the reduction of a protic species in II_c to evolve H_2; this H_2 is then oxidised onto $[TfO]^-$ to likely make TfOH (see Figure 6.3 and Figure 6.4) similar to that observed in wet [dema][TfO].

It is possible that there is a link between FAIII and II_c as the reduction of the protic species formed in FAIII is reduced at the same potential as that formed by water oxidation in IIa' at a higher potential. See previous pages (and Figure 6.3 and Figure 6.4) for a discussion of the water redox couple IIa'/II_c and the evidence for TfOH being a water oxidation product. Water is oxidised in wet [dema][TfO] to form a Pt-oxide and adsorbed TfOH positive of 1.9 V (non-adsorbed TfOH is produced when OER starts positive of 2.2 V) which causes the II_c reduction to grow in magnitude at stationary and rotating electrodes. When FA is present (and water content is low) the II_c reduction grows in magnitude positive of 1.5 V, the onset of FAIII. However, unlike in II_a', any TfOH produced by FAIII is not adsorbed to Pt as the significantly lower II_c j_{max} at the rotating electrode in Figure 6.6 (F) would suggest. Some adsorbed TfOH/protons must be formed as evidenced by the presence of the II_c reduction at a rotating electrode and is likely formed by water oxidation process II_a', which would still occur as some water will be present in the dry [dema][TfO] containing formic acid. As described in the introduction, there is no consensus on the active species in direct FAO with b-COOH, HCOOH and $HCOO^-$ all being possible candidates; $HCOO^-$ is the most likely as a result of work done by

Joo *et al*. [22] However, it is also known that b-COOH and CO_{ads} do form spontaneously on Pt in aqueous systems and can be oxidised.[17] Assuming that $HCOO^-$ is the active species and is oxidised by the direct FAO mechanism at more negative potentials (0.4–0.7 V), it is possible that HCOOH or b-COOH can be oxidised directly at more positive potentials >1.5 V. Possible reaction mechanisms for FAIII are below.

$$HCOOH + 2[TfO]^- \rightarrow CO_2 + 2TfOH + 2e^- \quad (35)$$

$$b\text{-}COOH + [TfO]^- \rightarrow CO_2 + TfOH + e^- \quad (36)$$

Direct FAO is observed at a rotating Pt electrode on the negative-going potential sweep with a peak at ≈0.4 V (labelled FAI" in Figure 6.6 (F)) after the preceding positive-going potential sweep reaches potentials >1.5 V. As the positive potential increases beyond 1.5 V the FAI" peak shifts increasingly negative as oxide removal current increases due to greater Pt-oxide coverage at higher potentials. A possible direct FAO mechanism is presented below on the basis that $HCOO^-$ is the active species and the protons produced sit on the triflate PIL anion to make triflic acid.

$$FAI": HCOO^- + [TfO]^- \rightarrow CO_2 + TfOH + e^- \quad (37)$$

At a stationary Pt electrode, direct $HCOO^-$ oxidation on the negative-going potential sweep occurs at a more positive potential, with a peak at ≈0.7 V (FAI"), than is observed at a rotating electrode. While FAI" is observed at a rotating electrode when the positive going potential-sweep exceeds 1.5 V, at a stationary electrode a clear FAI" peak only appears after the positive-going potential sweep exceeds 1.9 V. This discrepancy in the upper potential reached after which FAI" occurs is possibly due to lower $HCOO^-$ mass transport at the stationary electrode.

The shift negative in direct $HCOO^-$ on clean Pt (FAI") at a rotating electrode is due to the shift negative in oxide removal processes at a rotating electrode. The negative shift in oxide removal process could be due to a couple of factors. Firstly, the identity of the protic species available at the electrode to remove the surface oxides Pt-O and Pt-O_2 could affect the potential of oxide removal, or secondly, the increased current of the first water oxidation process (I_a) at a rotating electrode (likely due to increased mass transport of H_2O) could require the corresponding I_b oxide removal process, occurring at a more negative potential than IIb', to occur before $HCOO^-$ oxidation.

Considering the protic species involved in oxide removal, at a stationary electrode the TfOH likely produced by water oxidation processes II_a', making Pt-O_2, will remain at the electrode surface (some of which from II_a' possibly adsorbed to Pt). TfOH is a highly protonating species of pK_a −14, so will likely reduce oxides at a more positive potential than a less protonating species. At a rotating electrode, TfOH produced in water oxidation would be removed from the diffusion layer which means the most protonating species present in the bulk electrolyte and at the electrode surface is equilibrium HCOOH with a pK_a of 3.75. "Equilibrium HCOOH" referring to the equilibrium concentration of HCOOH in [dema][TfO] (with some water present). The second possible cause for the negative shift in direct FAO at a rotating electrode could be the increase in Pt-O formation observed only at a rotating electrode, which is not reduced to clean Pt until a more negative potential than the II_b" reduction of Pt-O_2 at a stationary electrode.

After the first potential cycle at a rotating electrode exceeds 1.5 V, marking the onset of FAIII, direct $HCOO^-$ oxidation (FAI') and a cleaning of the Pt electrode

though oxide removal, a new FAO process on the positive-going potential sweep occurs with a j_{max} growing as the maximum positive potential of the previous positive-going potential sweep increases. This new process is labelled FAI' in Figure 6.6 (F) and occurs at a similar potential to direct $HCOO^-$ oxidation (FAI") on the negative-going potential sweep. FAI' is therefore likely to be direct $HCOO^-$ oxidation identical to FAI" except for being partially inhibited by spontaneously forming adsorbed species such as CO_{ads} and b-COOH, which result in the broad, low j_{max} FAI' peak observed. As the positive-going potential sweep exceeds 1.9 V, the broad direct $HCOO^-$ oxidation (FAI') peak at 0.5 V resolves into two distinct peaks, the first labelled FAI' at 0.5 V and the second labelled FAII with a peak at 0.7 V. A possible cause of this peak could be b-COOH oxidation of possibly CO_{ads} oxidation although the latter is unlikely.

The discussion so far has been primarily concerned with direct FAO however, it is known that FAO can also proceed via an indirect method through the oxidation of a spontaneously forming adsorbed species which passivates the Pt electrode, inhibiting direct FAO – this species is most commonly thought to be adsorbed CO.[7,17,20] Oxidation of adsorbed CO at Pt electrodes has been studied in both acidic aqueous systems and PILs by saturating the respective electrolyte with CO gas. It was found that CO is oxidised in aqueous systems at ≈0.8 V vs. saturated calomel electrode (≈0.55 vs. SHE) and [dema][TfO] at ≈1.2 V vs. Ag/Ag^+ (≈0.56 V vs. SHE).[31,41] Studies of FAO in acidic aqueous systems suggest that the peak at ≈0.9 V (vs. RHE) is CO_{ads} oxidation,[7,25] whereas a study of FAO in [dema][TfO] does not show a CO_{ads} peak at the same potential and is very similar to the voltammetry presented in Figure 6.5 (A) and (C).[25] An oxidation positive of 1.2 V has been

observed when using [dema][TfO] containing HCOOH, which coincides with water oxidation and could be FAIII as described in this work.[25] If CO_{ads} is oxidised in [dema][TfO] positive of 1.2 V, notably higher than in aqueous systems, then it could be due to the low availability of H_2O at the electrode requiring the formation of oxides from what water there is positive of 1.2 V in order to be oxidised to CO_2. Also, any protons produced from CO_{ads}/H_2O oxidation would protonate $[TfO]^-$, a very poor base, which could also raise the oxidation overpotential of CO_{ads}.

Further work concerning CO adsorption and oxidation in PILs is needed because of the requirement for H_2O (see Equations 3 and 11), which is not necessarily abundant in dried PILs.[17,20] Furthermore, the spontaneous oxidation of HCOOH to b-COOH and spontaneous reduction of b-COOH to CO_{ads} proposed by Osawa *et al.*, is likely only possible if protons are readily available (see Equation 2) and the most available proton in [dema][TfO] is $[dema]^+$ which, unlike H_3O^+, is a very poor acid.[17] Also, the 'common pathway' described by Osawa *et al*. (see Equation 1) may not be thermodynamically possible as a spontaneous reaction in PILs because the protons produced along with b-COOH would be sitting on the very poor base $[TfO]^-$ in [dema][TfO] rather than H_2O as H_3O^+ in acidic aqueous systems.[17,18,42] In this work, any CO oxidation that occurred, did so at high overpotentials (E >1.5 V) as shown in Figure 6.6 (E) and (F).

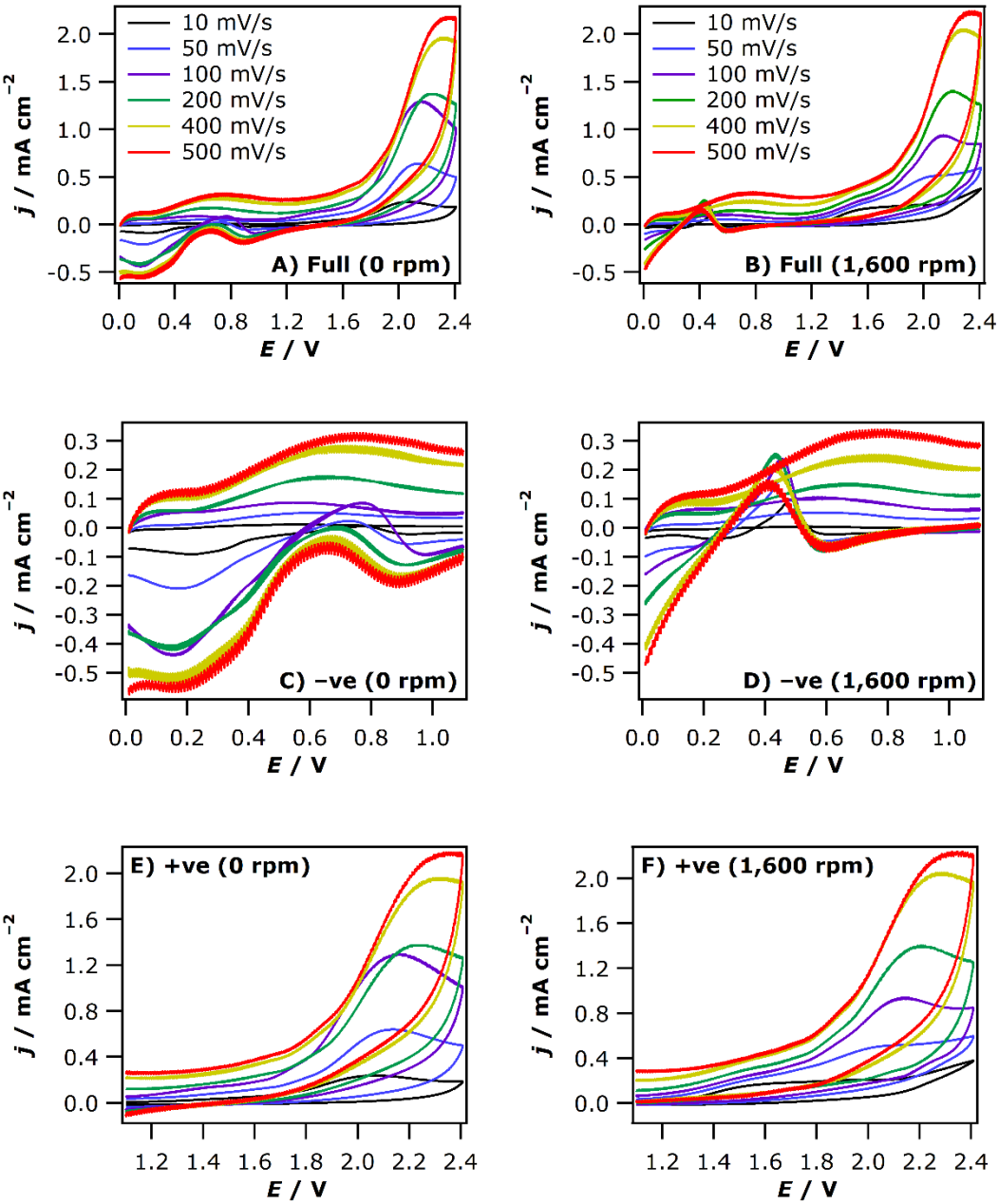


Figure 6.7 Cyclic voltammograms (CVs) of deaerated [dema][TfO] containing 0.1 mol dm^{-3} formic acid recorded at stationary (A/C/E) and rotating (B/D/F) Pt electrodes. Potential cycles begin in a positive-going direction beginning at ≈0 V at a series of increasing scan rates from 10 mV s^{-1} to 500 mV s^{-1}. CVs C) and D) are a magnification of the negative potential range and CVs E) and F) are a magnification of the positive potential range. CVs are recorded in a nitrogen-atmosphere glovebox with an atmospheric O_2 and H_2O concentration of <0.1 and <0.4 ppm respectively.

Direct FAO on the negative-going potential sweep does not change greatly with increasing scan rate (Figure 6.7). However, direct FAO j_{max} on the positive-going potential sweep does increase with scan rate at both stationary and rotating

electrodes (Figure 6.7 (C) and (D), respectively). At potentials positive of 1.5 V, FAIII/water oxidation j_{max} does increase with scan rate but rotating the electrode does not increase j_{max} significantly suggesting that the oxidation positive of 1.5 V could be that of an adsorbed FA-based species (Figure 6.7 (E) and (F)).

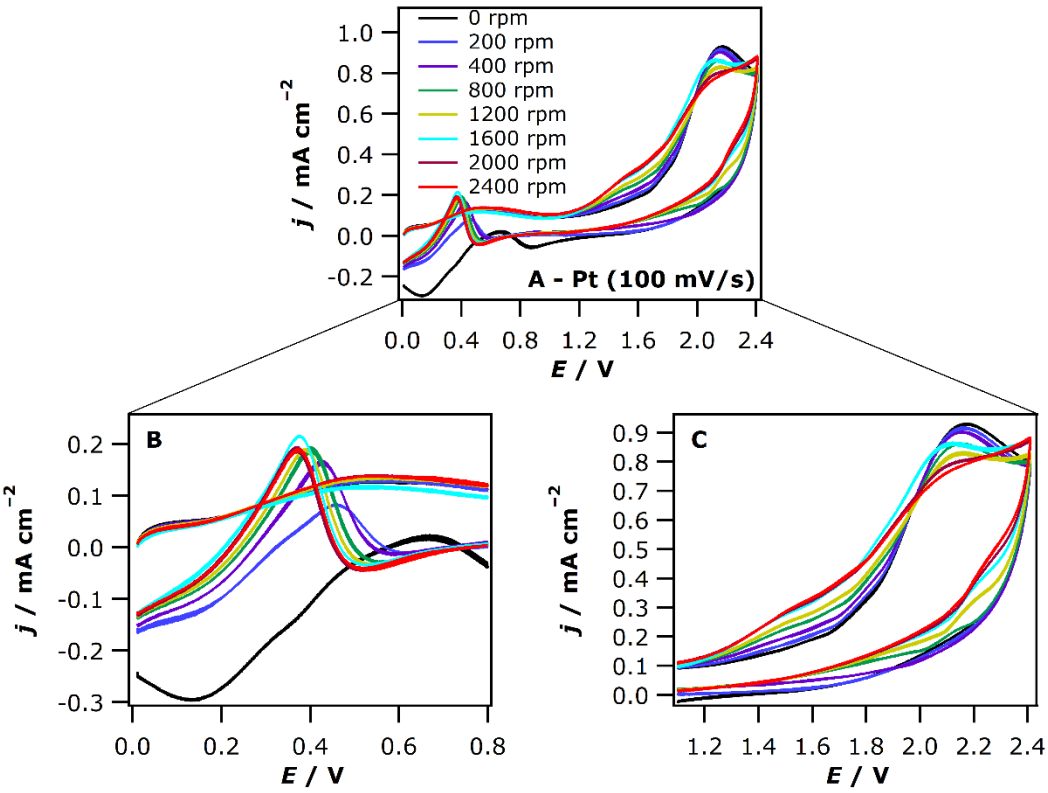


Figure 6.8 Cyclic voltammograms (CVs) of deaerated [dema][TfO] containing 0.1 mol dm^{-3} formic acid recorded at Pt electrodes over a range of rotation rate from 0 rpm to 2,400 rpm. Potential cycles begin in a positive-going direction beginning at ≈0 V. CVs B) and C) are magnifications of the negative and positive potential range respectively. CVs are recorded in a nitrogen-atmosphere glovebox with an atmospheric O_2 and H_2O concentration of <0.1 and <0.4 ppm respectively.

Increasing the rotation rate at a fixed scan rate does not have a great effect on j_{max} of FAO either at negative potentials (FAI'/FAI") or positive of 1.6 V (FAIII). However, the anodic current with an onset positive of 1.2 V, likely water oxidation (I_a) does increase with increased rotation rate as the rate of H_2O mass transport increases; this is supported by the oxide removal current (I_b) also increasing with rotation rate as more Pt-oxide would form as H_2O mass transport increases (see Figure 6.8 and Figure 6.10).

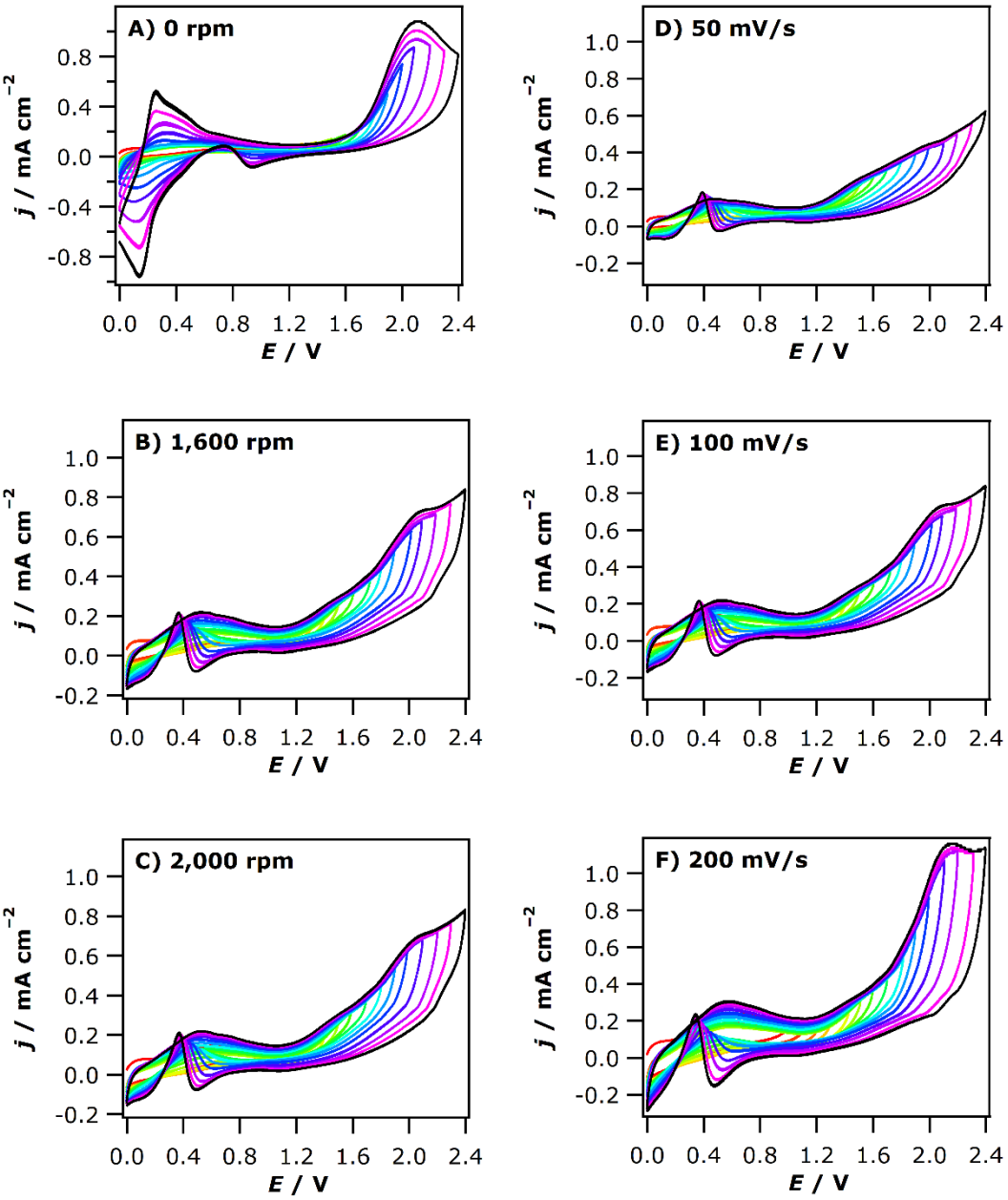


Figure 6.10 Cyclic voltammograms (CVs) of deaerated [dema] containing 0.1 mol dm^{-3} formic acid, recorded at stationary and rotating Pt electrodes. Potential cycles begin in a positive-going direction from ≈0 V. The CVs presented in A), B) and C) are recorded at 100 mV s^{-1} with a stationary Pt electrode (A) or a Pt electrode rotating at 1,600 (B) and 2,000 rpm (C). The CVs presented in D) E) and F) are recorded at a Pt electrode rotating at 1,600 rpm at a 50, 100 and 200 mV s^{-1} respectively. Potential cycles increase by 0.1 V in the positive direction with each successive cycle. CVs are recorded in a nitrogen-atmosphere glovebox with an atmospheric O_2 and H_2O concentration of <0.1 and <0.4 ppm respectively. CVs are not *iR*-corrected however, the small solution resistance does not affect the CVs at these current densities (CVs with and without *iR*-correction show no significant differences).

The reduction of HCOOH to $HCOO^-$ and the subsequent oxidation of H_2 to HCOOH in [dema][TfO] is shown by the voltammetry in Figure 6.9. The onset of formic acid reduction is negative of −0.1 V and the onset of H_2 oxidation onto $HCOO^-$ is positive of −0.35 V.

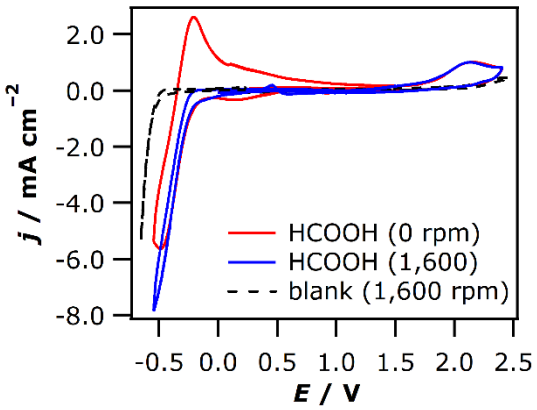


Figure 6.9 Cyclic voltammograms (CVs) of deaerated [dema][TfO] containing 0.1 mol dm^{-3} formic acid recorded at a stationary and rotating Pt electrode. Potential cycles begin in a positive-going direction at 100 mV s^{-1} beginning at ≈0 V. The potential is then swept to negative potentials at which the reduction of formic acid is observed. The blank is recorded in dry (≈10 ppm H_2O) [dema][TfO]. CVs are recorded in a nitrogen-atmosphere glovebox with an atmospheric O_2 and H_2O concentration of <0.1 and <0.4 ppm respectively.

6.3.4 Addition of bases to [dema][TfO] containing formic acid

To test whether FA can be used as a test molecule for basicity in PILs, dema was added to [dema][TfO] containing 0.1 mol dm^{-3} HCOOH, to achieve a 0.1 mol dm^{-3} concentration of dema. If Joo *et al.* are correct and $HCOO^-$ is the active species in FAO, then the addition of dema, a strong base, will shift the HCOOH/$HCOO^-$ equilibrium in favour of $HCOO^-$, increasing $HCOO^-$ concentration and the j_{max} of the FAO voltammetric peak.[22,21] Specifically, if $HCOO^-$ is the active species in FAO the corresponding anodic peak j_{max} on the negative-going potential sweep in the voltammetry in Figure 6.6 (F) (FAI") should increase in the presence of base.

Furthermore, the strength of the base added should affect j_{max}, with stronger bases resulting in a greater $HCOO^-$ concentration and greater j_{max}.

The voltammetry in Figure 6.11 shows a significant increase in direct FAO j_{max} in the presence of dema, which is consistent with $HCOO^-$ being the active species in FAO.[22,25] At a rotating electrode (Figure 6.11 (B)), the direct FAO peak on the negative-going potential sweep has a j_{max} of ≈0.2 mA cm^{-2} and ≈0.7 mA cm^{-2} in the absence and presence of 0.1 mol dm^{-3} dema, respectively. It is known from studies of dema in [dema][TfO] in the absence of HCOOH (see Chapter 4) that dema is oxidised at ≈1.0 V, it is therefore possible that the increase in oxidation current density positive of ≈1.1 V is oxidation of dema not protonated by HCOOH. Another explanation for the increase in anodic current positive of 1.1 V is water oxidation due to an increased water concentration resulting from the experiment being conducted outside of a glovebox. As well as direct formic acid oxidation j_{max} on the negative-going sweep increasing significantly in the presence of dema (FAI"), so too does the broad FAO peak positive of 0.2 V on the forward-going sweep (FAI'); this is also consistent with $HCOO^-$ being the active species in direct FAO.

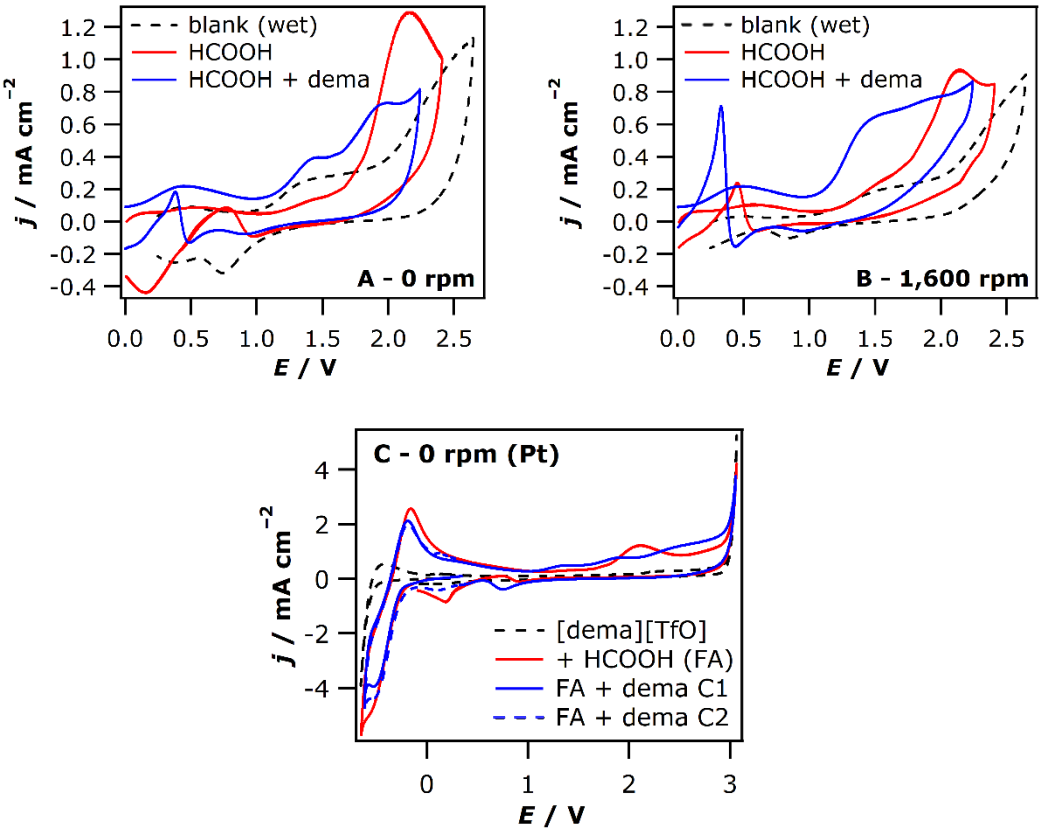


Figure 6.11 Cyclic voltammograms (CVs) of wet (≈2,388 ppm H_2O) deaerated [dema][TfO], [dema][TfO] containing 0.1 mol dm^{-3} formic acid (FA), and [dema][TfO] containing both 0.1 mol dm^{-3} formic acid and diethylmethylamine (dema) recorded at stationary (A)/(C) and rotating (B) Pt electrodes. Potential cycles in (A) and (B) begin in a positive-going direction at 100 mV s^{-1} from ≈0 V. CVs in (C) are recorded in a negative-going direction from around 0.2 V at 100 mV s^{-1}. The blue and blue-dashed CVs in (C) are the first and second potential cycles respectively. All CVs except for those where dema has been added, are recorded in a nitrogen-atmosphere glovebox with an atmospheric O_2 and H_2O concentration of <0.1 and <0.4 ppm respectively.

Figure 6.11 (C) presents full electrochemical window voltammograms recorded in dry [dema][TfO], [dema][TfO] containing FA and [dema][TfO] containing FA and dema. The cathodic peak negative of 0.0 V in the presence of FA is FA reduction and the coupled oxidation positive of −0.1 V is H_2 oxidation onto $HCOO^-$. The FA reduction j_{max} is lower in the presence of dema than without, which is consistent with the expectation that adding dema increases the concentration of $HCOO^-$ (and decreases the concentration of HCOOH).

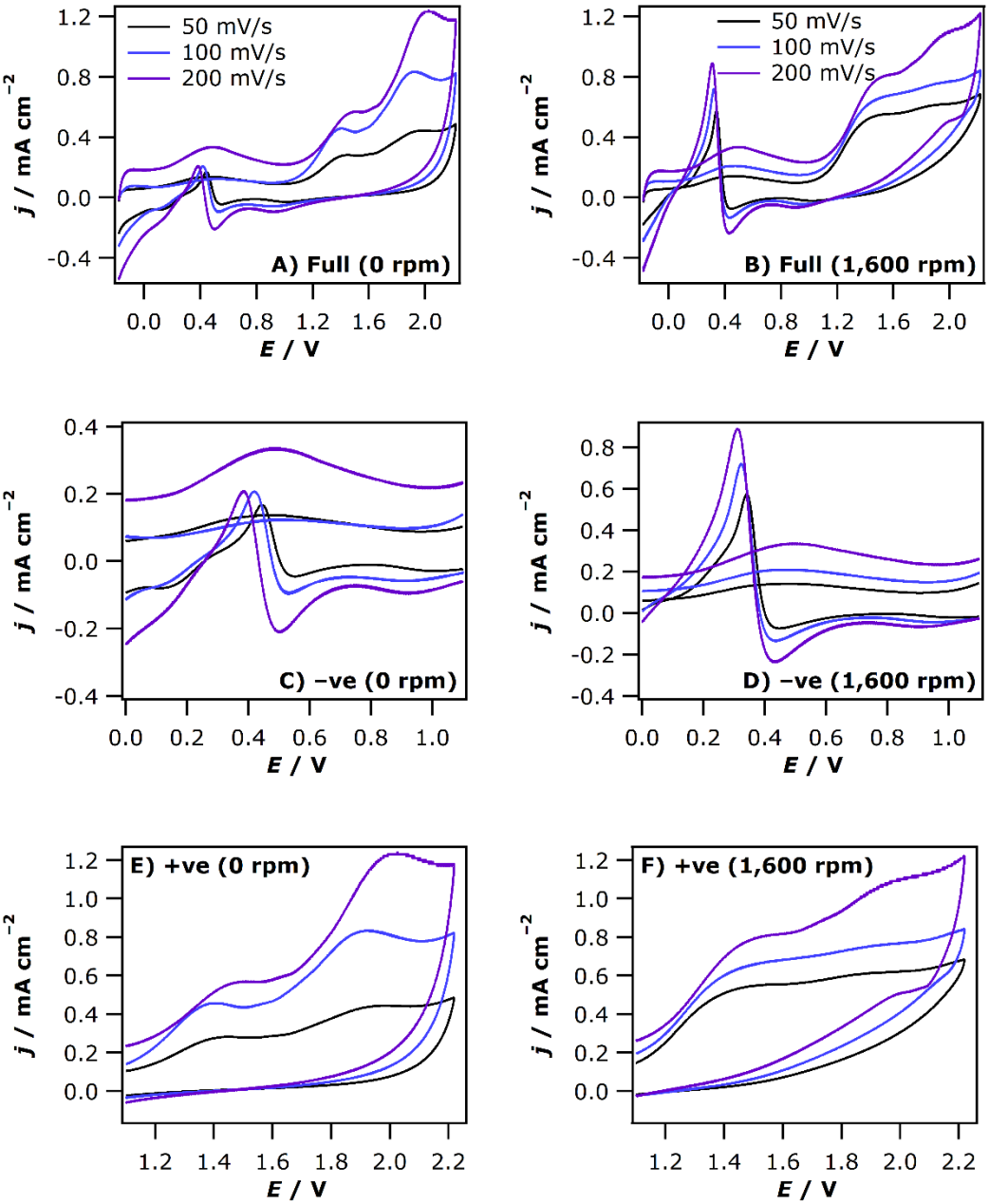


Figure 6.12 Cyclic voltammograms (CVs) of deaerated [dema][TfO] containing both 0.1 mol dm^{-3} formic acid and diethylmethylamine (dema) recorded at stationary (A) and rotating (B) Pt electrodes. Potential cycles in begin in a positive-going direction at 50, 100, and 200 mV s^{-1} from ≈0 V. Frames (C) and (E) are a magnification of the negative and positive potential regions, respectively, of the CVs shown in (A). Frames (D) and (F) are a magnification of the negative and positive potential regions, respectively, of the CVs shown in (B).

The j_{max} of the FAO peak on the negative-going potential sweep increases with scan rate (see Figure 6.12 (D)) at a rotating electrode but not at a stationary electrode (see Figure 6.12 (C)), and is likely due to the constant supply of $HCOO^-$ to the

rotating electrode. Also the oxidation of dema/water oxidation/FAO (FAIII) at potentials positive of ≈1.2 V increases with scan rate at both rotating and stationary electrodes (see Figure 6.12 (E) and (F)).

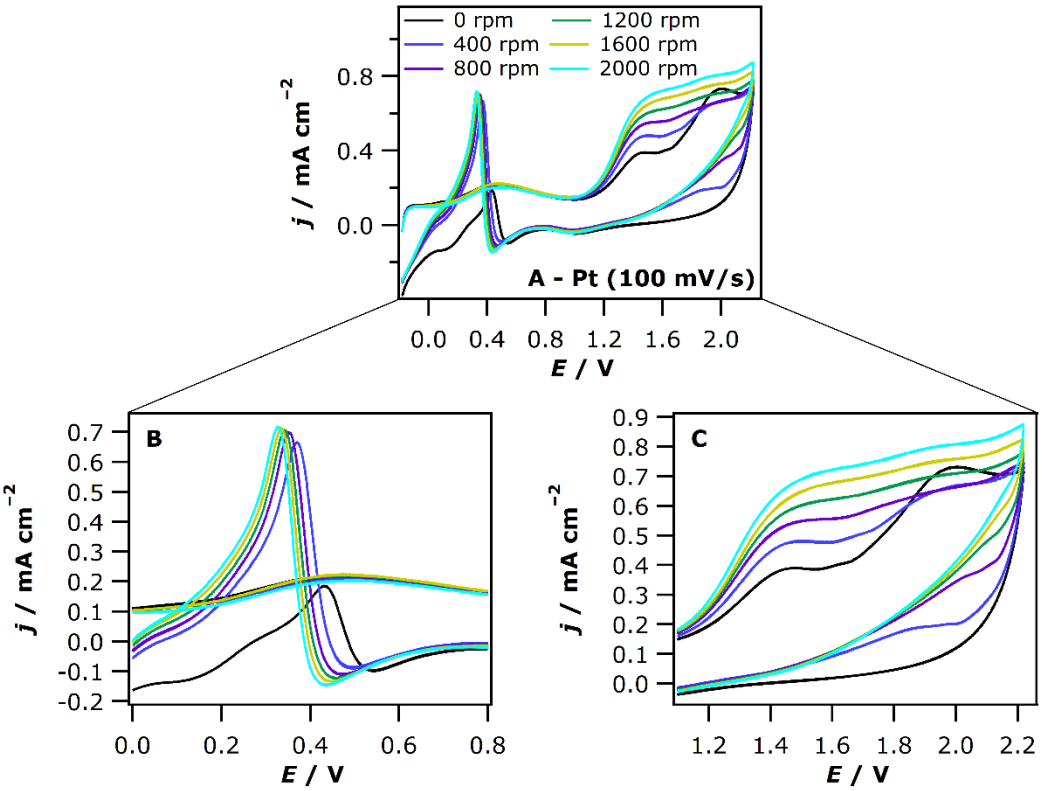
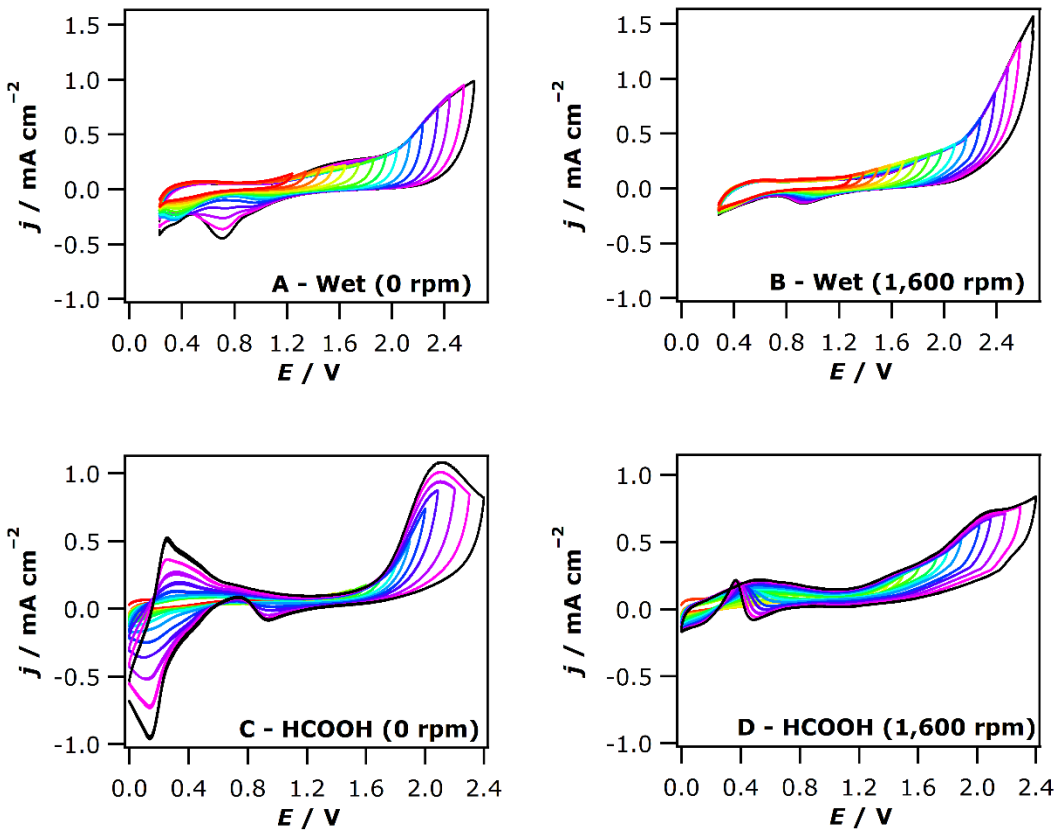


Figure 6.13 Cyclic voltammograms (CVs) of deaerated [dema][TfO] containing both 0.1 mol dm^{-3} formic acid and diethylmethylamine (dema) recorded at a stationary Pt electrode and Pt electrodes rotating at 400, 800, 1,200, 1,600 and 2,000 rpm. Potential cycles in begin in a positive-going direction at 100 mV s^{-1} from ≈0 V. Frames (B) and (C) are a magnification of the negative and positive potential regions, respectively, of the CVs shown in (A).

The j_{max} corresponding to direct FAO in the presence of dema is not greatly affected by increasing electrode rotation rate except for a very slight peak shift to more negative potentials (see Figure 6.13 (B)); this suggests that increasing mass transport to the Pt electrode, above an undetermined rotation rate, has little effect on maximum current density. In contrast, FAO/water oxidation/dema oxidation current density recorded positive of 1.2 V (see Figure 6.13 (C)), does increase with

increasing rotation rate, suggesting that these processes are not oxidation of adsorbed species but oxidations of species in the bulk electrolyte.

The voltammograms in Figure 6.14 compare increasingly positive potential cycles in dry [dema][TfO], wet [dema][TfO], [dema][TfO] containing FA, [dema][TfO] containing FA and dema (0.2 mol dm^{-3}) and [dema][TfO] containing FA and ≈0.2 mol dm^{-3} dema. When the dema concentration is doubled to ≈0.2 mol dm^{-3} the FAO current on the negative-going potential sweep also doubles to ≈1.0 mA cm^{-2}, confirming the link between $HCOO^-$ concentration and direct FAO j_{max}. FAO positive of 0.2 V on the positive-going potential sweep (broad peak) also increases in peak magnitude similarly, when the dema concentration is doubled. Additionally, the oxidation current positive of 1.2 V approximately doubles when dema concentration is doubled, suggesting that this could be dema oxidation.



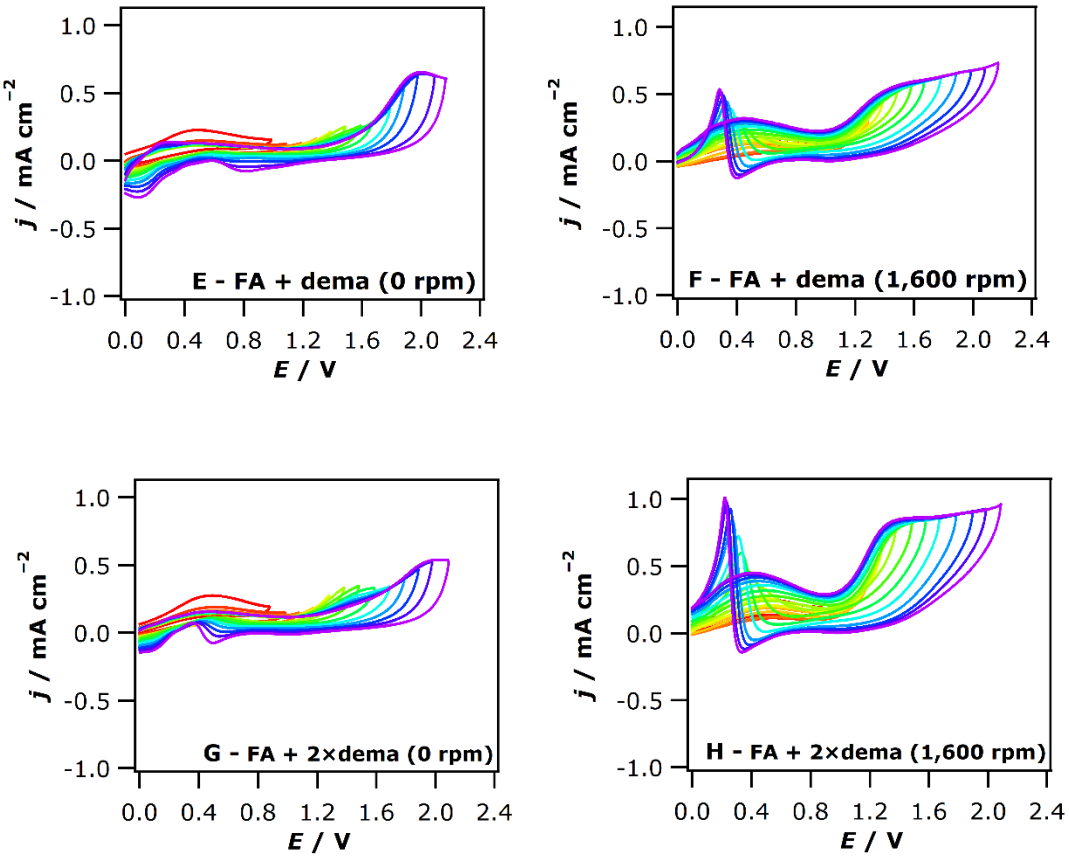


Figure 6.14 Cyclic voltammograms (CVs) of wet (≈2,388 ppm H_2O) deaerated [dema][TfO] (A/B), deaerated [dema][TfO] containing 0.1 mol dm^{-3} formic acid (C/D), deaerated [dema][TfO] containing 0.1 mol dm^{-3} formic acid and diethylmethylamine (dema) (E/F), and deaerated [dema][TfO] containing 0.1 mol dm^{-3} formic acid and ≤0.2 mol dm^{-3} dema (G/H) recorded at stationary and rotating Pt electrodes. Potential cycles begin in a positive-going direction at 100 mV s^{-1} from ≈0 V. Potential cycles increase by 0.1 V in the positive direction with each successive cycle. CVs in (A),(B),(C), and (D) are recorded in a nitrogen-atmosphere glovebox with an atmospheric O_2 and H_2O concentration of <0.1 and <0.4 ppm respectively. CVs in frames (B), (C) and (D) are not *iR*-corrected however, the small solution resistance does not affect the CVs at these current densities (CVs with and without *iR*-correction show no significant differences).

The aqueous pK_a of the conjugate acid of dema is 10.6, to test the effect on FAO of a weaker base, imidazole was added to [dema][TfO] containing 0.1 mol dm^{-3} FA to achieve a 0.1 mol dm^{-3} concentration of imidazole. The aqueous pK_a of the conjugate acid of imidazole is 6.99. Unfortunately, the presence of imidazole appears to passivate the Pt electrode with no obvious direct FAO peak on the negative-going potential sweep although there may be a slight FAO peak on the positive-going potential sweep (see Figure 6.15). Evidence of the irreversible

passivation of Pt by the oxidation of imidazole is shown in Figure 6.15 (E) and (F). The first cycle (solid green CV) shows an unusual and large peak at around 0.3 V which disappears on the second cycle (dashed green CV); this oxidation must be imidazole oxidation. Furthermore, the presence of imidazole also impedes formic acid reduction and hydrogen oxidation as shown by the solid green CVs in Figure 6.15 (E) and (F). After imidazole is oxidised on the first cycle, some acid reduction and hydrogen oxidation is shown in the second cycle. Passivation of Pt electrocatalysts by imidazole and voltammetric oxidation of imidazole at positive potentials has been previously reported.[43] The passivating effect of imidazole makes it an unsuitable candidate to assess basicity in PILs using formic acid as a test molecule.

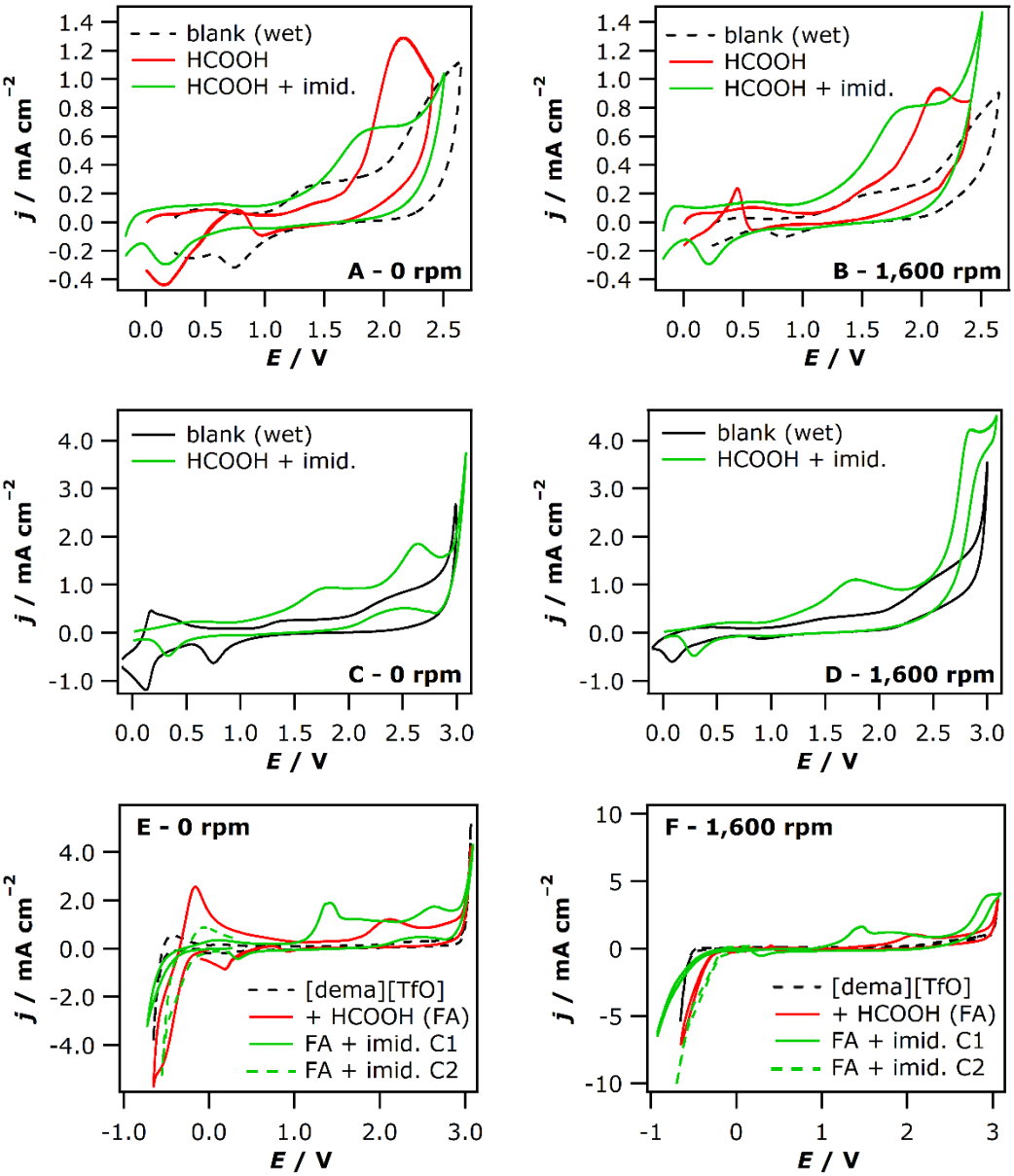


Figure 6.15 Cyclic voltammograms (CVs) of wet (≈2,388 ppm H_2O) deaerated [dema][TfO], [dema][TfO] containing 0.1 mol dm^{-3} formic acid (FA), and [dema][TfO] containing both 0.1 mol dm^{-3} formic acid and imidazole (imid.) recorded at stationary (A)/(C)/(E) and rotating (B)/(D)/(F) Pt electrodes. Potential cycles in (A), (B), (C) and (D) begin in a positive-going direction at 100 mV s^{-1} from ≈0 V. CVs in (E) and (F) are recorded in a negative-going direction from around 0.2 V at 100 mV s^{-1}. The green and green-dashed CVs in (E) and (F) are the first and second potential cycles respectively. The blank (black) CVs in (C) and (D) are taken from the last cycles of Figure 6.3 (A) and (B) respectively. All CVs except for those where imidazole has been added, are recorded in a nitrogen-atmosphere glovebox with an atmospheric O_2 and H_2O concentration of <0.1 and <0.4 ppm respectively.

The voltammograms in Figure 6.16 show the oxidation of imidazole at around 1.3–1.5 V and its appearance/disappearance between cycles.

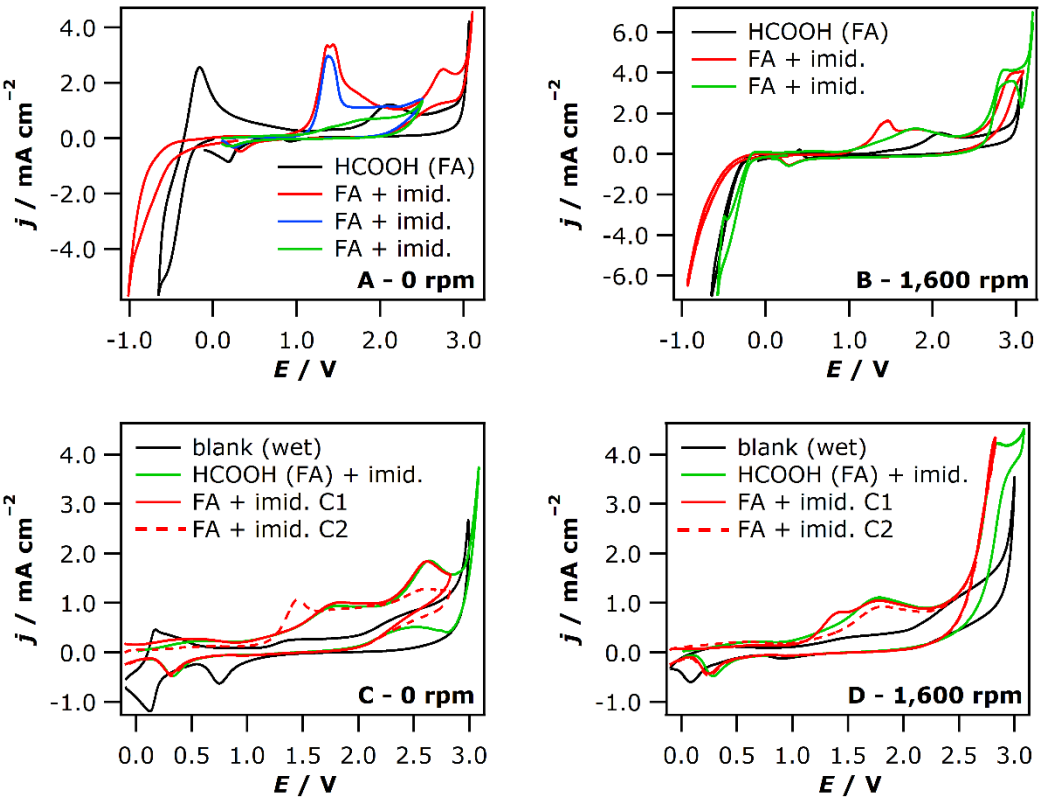


Figure 6.16 Cyclic voltammograms (CVs) of wet (≈2,388 ppm H_2O) deaerated [dema][TfO], [dema][TfO] containing 0.1 mol dm^{-3} formic acid (FA), and [dema][TfO] containing both 0.1 mol dm^{-3} formic acid and imidazole (imid.) recorded at stationary (A)/(C) and rotating (B)/(D) Pt electrodes. Potential cycles in (A) and (B) begin in a negative-going direction at 100 mV s^{-1} from ≈0.2 V. CVs in (C) and (D) are recorded in a positive-going direction from around 0.0 V at 100 mV s^{-1}. The red and red-dashed CVs in (C) and (D) are the first and second potential cycles respectively. The blank (black) CVs in (C) and (D) are taken from the last cycles of Figure 6.3 (A) and (B) respectively. All CVs except for those where imidazole has been added, are recorded in a nitrogen-atmosphere glovebox with an atmospheric O_2 and H_2O concentration of <0.1 and <0.4 ppm respectively.

Another base added to [dema][TfO]-containing 0.1 mol dm^{-3} HCOOH was pyridine, with an aqueous pK_a of 5.23. The solid purple and dashed purple CVs in Figure 6.17 (A) show the two voltammetric profiles recorded at Pt when both pyridine and FA are present in [dema][TfO]. The solid purple CV shows a large, abrupt anodic current positive of 1.0 V which can be attributed to pyridine oxidation – little to no direct FAO is observed. However, the dash purple CV, in which pyridine oxidation is largely absent, shows the broad FAO peak positive on 0.2 V on the positive-going potential sweep. At a rotating electrode the solid purple CV shows pyridine oxidation and dash purple CV does not. At 1,600 rpm (Figure 6.17 (B)) there is a direct FAO peak negative of 0.3 V on the negative-going potential sweep with j_{max} of ≈0.15 mA cm^{-2}. The lower j_{max} when pyridine is present, compared to when dema is present, can be explained as pyridine is a weaker base than dema, hence there will be a lower $HCOO^-$ concentration when pyridine is present than when dema is present. The direct FAO peak on the negative-going potential sweep occurs whether or not pyridine oxidation also occurs, however, the FAO on the positive going potential sweep positive of 0.2 V is only observed if pyridine oxidation is not observed (see dashed purple CV). Pyridine therefore also has an electrode-passivating effect which inhibits FAO in some instances.

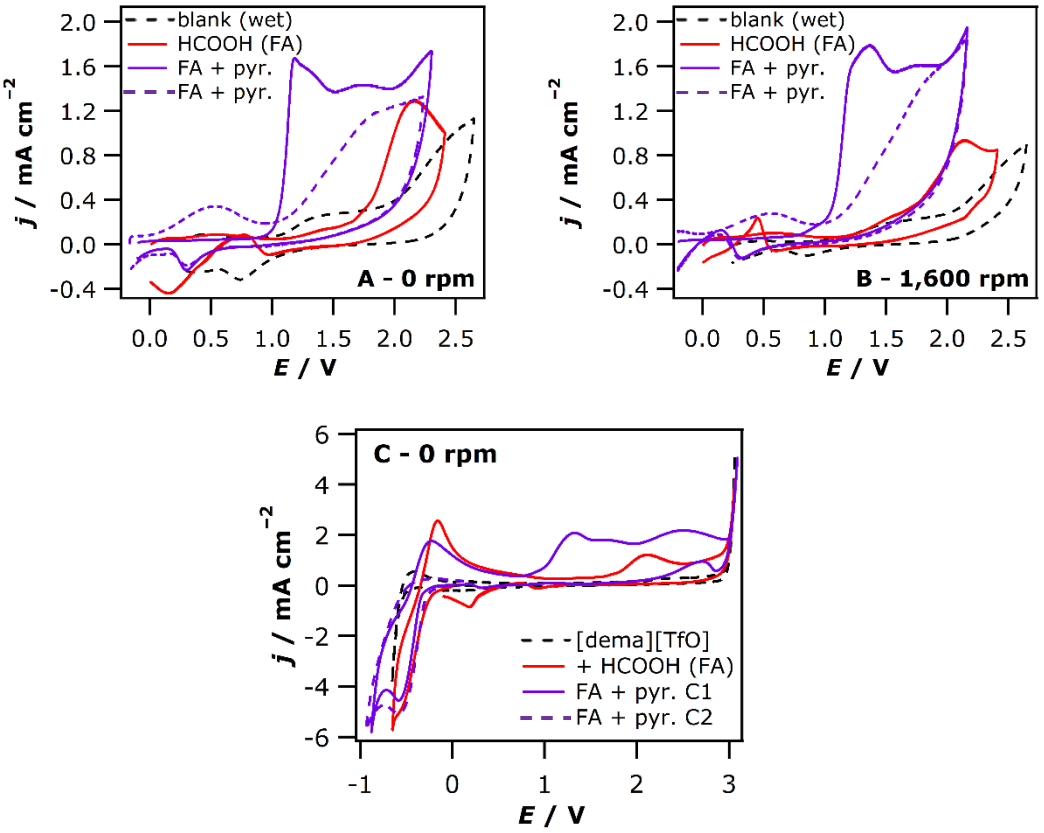


Figure 6.17 Cyclic voltammograms (CVs) of wet (≈2,388 ppm H_2O) deaerated [dema][TfO], [dema][TfO] containing 0.1 mol dm^{-3} formic acid (FA), and [dema][TfO] containing both 0.1 mol dm^{-3} formic acid and pyridine (pyr.) recorded at stationary (A)/(C) and rotating (B) Pt electrodes. Potential cycles in (A) and (B) begin in a positive-going direction at 100 mV s^{-1} from ≈0 V. CVs in (C) are recorded in a negative-going direction from around 0.2 V at 100 mV s^{-1}. The purple and purple-dashed CVs in (C) are the first and second potential cycles respectively. All CVs except for those where pyridine has been added, are recorded in a nitrogen-atmosphere glovebox with an atmospheric O_2 and H_2O concentration of <0.1 and <0.4 ppm respectively.

The purple and purple dashed CVs Figure 6.17 (C) show that H_2 onto $HCOO^-$ only occurs before pyridine is oxidised (solid purple CV – cycle 1). After pyridine is oxidised in cycle 1 at high potentials, while HCOOH is reduced, H_2 oxidation is inhibited (dashed purple CV – cycle 2), confirming that pyridine does passivate Pt electrodes.

The final base added to [dema][TfO] containing FA was thiazole, which has a conjugate acid aqueous pK_a of 2.52. Unfortunately, no direct FAO was observed when compared with the blanks in Figure 6.18 (A) and (B). What was observed however, was oxidation of thiazole positive of 2.25 V as shown by the mustard CVs in Figure 6.18 (C) and (D) at stationary and rotating electrodes respectively. It is clear from Figure 6.18 (E) and (F) that thiazole has a passivating effect on Pt as hydrogen oxidation is not observed at a stationary electrode and HCOOH reduction on the first potential cycle is shifted to a more negative potential than when thiazole is absent. Oxidising thiazole at high potentials does cause the HCOOH reduction potential to become more positive (closer to that without the presence of thiazole) but H_2 oxidization is not observed in any instance.

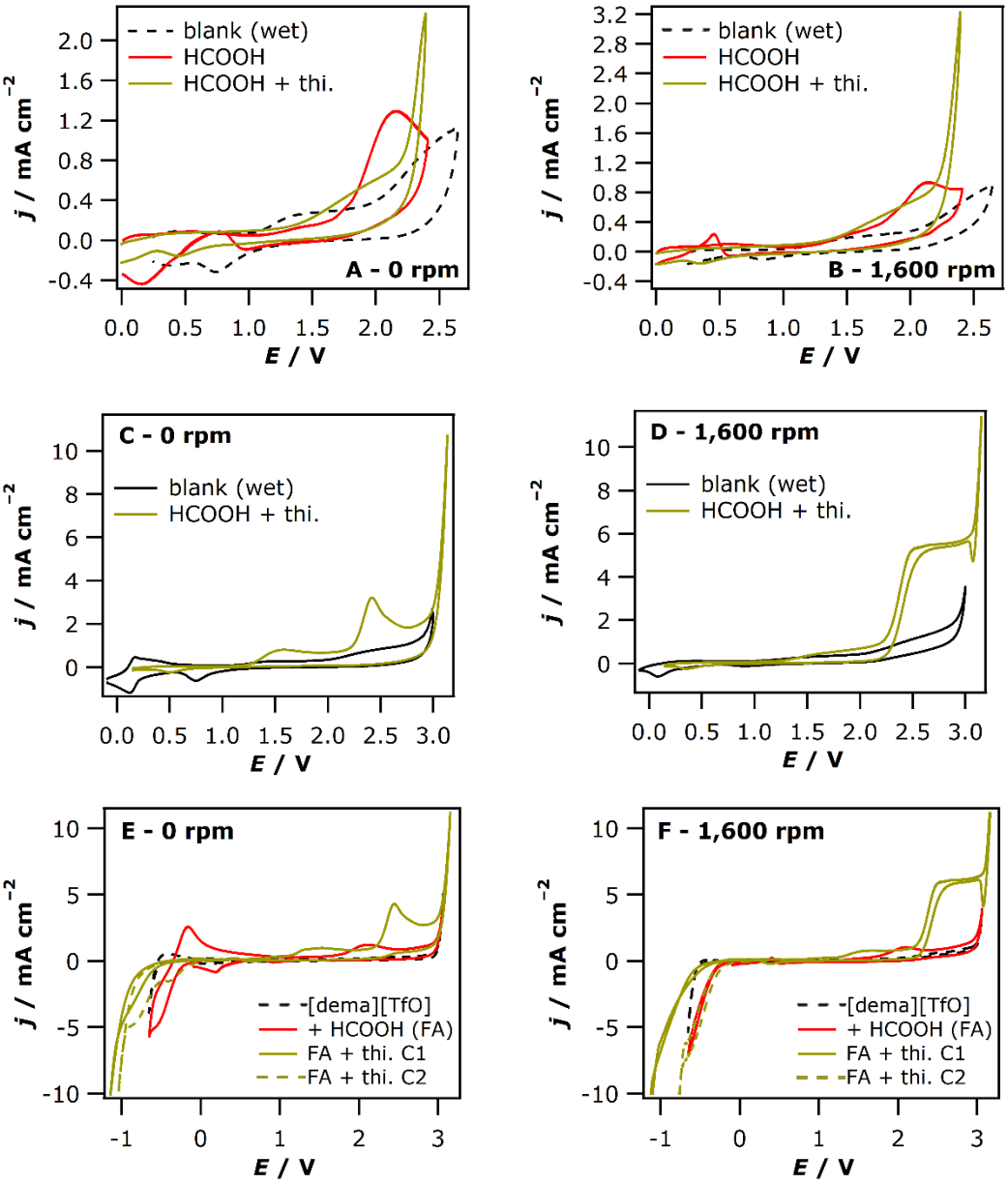


Figure 6.18 Cyclic voltammograms (CVs) of wet (≈2,388 ppm H_2O) deaerated [dema][TfO], [dema][TfO] containing 0.1 mol dm^{-3} formic acid (FA), and [dema][TfO] containing both 0.1 mol dm^{-3} formic acid and thiazole (thi.) recorded at stationary (A)/(C)/(E) and rotating (B)/(D)/(F) Pt electrodes. Potential cycles in (A), (B), (C) and (D) begin in a positive-going direction at 100 mV s^{-1} from ≈0 V. CVs in (E) and (F) are recorded in a negative-going direction from around 0.2 V at 100 mV s^{-1}. The mustard and mustard-dashed CVs in (E) and (F) are the first and second potential cycles respectively. The blank (black) CVs in (C) and (D) are taken from the last cycles of Figure 6.3 (A) and (B) respectively. All CVs except for those where thiazole has been added, are recorded in a nitrogen-atmosphere glovebox with an atmospheric O_2 and H_2O concentration of <0.1 and <0.4 ppm respectively.

The voltammograms in Figure 6.19 compare all bases added to [dema][TfO] containing FA, [dema][TfO] containing FA without added base, and wet [dema][TfO]. Direct FAO is only observed when bases are absent or when either dema or pyridine is added to [dema][TfO]. While thiazole and imidazole have the greatest electrode-passivating effects inhibiting FAO, all added bases, except dema, showed the effects of electrode passivation toward hydrogen electrochemistry, so it is likely that this may also affect FAO.

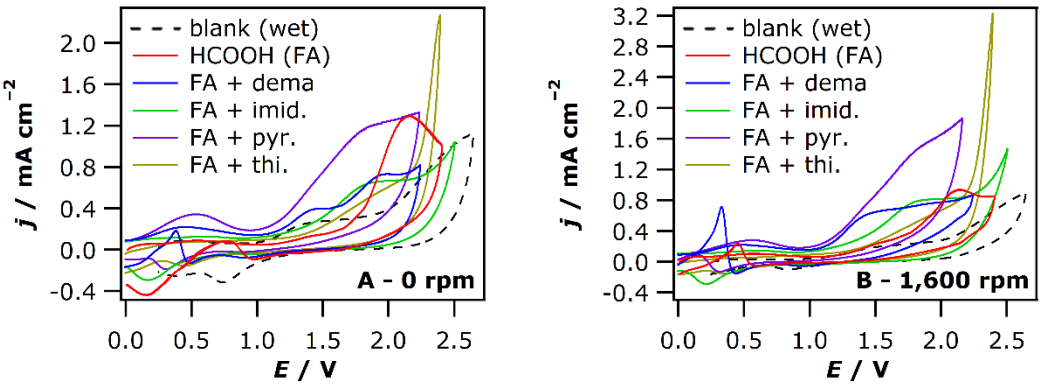


Figure 6.19 Cyclic voltammograms (CVs) of wet (≈2,388 ppm H_2O) deaerated [dema][TfO], [dema][TfO] containing 0.1 mol dm^{-3} formic acid (FA), and [dema][TfO] containing both 0.1 mol dm^{-3} formic acid and base recorded at stationary (A) and rotating (B) Pt electrodes. The bases added to [dema][TfO] containing 0.1 mol dm^{-3} formic acid, are diethylmethylamine (dema), imidazole (imid.), pyridine (pyr.) or thiazole (thi.). Potential cycles in (A) and (B) begin in a positive-going direction at 100 mV s^{-1} from ≈0 V. CVs, except those recorded in the presence of an added base which are recorded in a fumehood, are recorded in a nitrogen-atmosphere glovebox with an atmospheric O_2 and H_2O concentration of <0.1 and <0.4 ppm respectively.

Due to the significant Pt-passivating effects of most of the added bases inhibiting FAO, it was not possible to quantitatively relate direct FAO j_{max} with the aqueous pK_a of the base added. In the cases of dema and pyridine it was observed that j_{max} was greatest when the stronger base (dema) was added. However, pyridine electrode-passivating effects cannot be completely discounted. Of the base chosen, most produced electrode-passivating effects – this suggests that it may not

be possible to use FAO as a test reaction for basicity in PILs by adding bases unless bases that do not adsorb to Pt, or otherwise inhibit FAO, can be found.

6.4 Conclusions

Water oxidation and formic acid oxidation have been studied in the PIL, [dema][TfO] at Pt electrodes using cyclic voltammetry. Although, GC electrodes were also used, no evidence of FAO was found with any difference in the voltammetry caused by an increase in water concentration upon addition of the acid.

Water was found to be oxidised at Pt positive of 1.2 V with a second water oxidation process positive of 1.9 V which is indicative of two different Pt-oxide species, possibly Pt-O or Pt-O_2, which have been previously detected after water oxidation in [dema][TfO].[39] The two distinct oxide species were found to be removed at different potentials, negative of 1.3 V and 0.6 V, respectively. If the potential was cycled positive of 2.2 V, oxygen and triflic acid is likely evolved as the corresponding reduction was observed at the same potential oxygen is reduced in the presence of triflic acid, and only at a stationary electrode. In addition, when water was oxidised at potentials greater than 1.9 V a reduction of an adsorbed and non-adsorbed protic species was observed at the same potential that triflic acid is reduced. A corresponding oxidation was also observed at the same potential hydrogen is oxidised onto $[TfO]^-$. This suggests that water oxidation at highly oxidising potentials produces adsorbed TfOH or protons, and non-adsorbed TfOH. The high overpotential of water oxidation and oxygen evolution can be explained by the $[TfO]^-$ being a very poor proton acceptor.

The voltammetry of formic acid in [dema][TfO] at a Pt electrode produced very similar results to those previously observed with a broad, low j_{max} peak on the positive-going potential sweep, a large peak at more positive potentials (E >1.5 V), and a sharp peak with a large j_{max} on the negative-going potential sweep at around 0.4 V immediately after the removal of surface oxides.[25] Introducing dema to [dema][TfO] and formic acid causes the sharp-peaked oxidation of FA on the negative-going sweep to significantly increase in magnitude; this is consistent with previous observations[25] and the proposal that $HCOO^-$ is the active species in direct FAO.[22,21] $HCOO^-$ being the active species in direct FAO is also supported by the doubling of the oxidation peak j_{max} when the dema concentration was doubled. The oxidation of formic acid at E > 1.5 V also appears to produce adsorbed and non-adsorbed TfOH which is reduced at the same potential as observed in wet [dema][TfO] in the absence of formic acid. No distinct peak attributable to CO oxidation was observed which, because direct FAO is inhibited until potentials greater than 1.5 V have been reached in the positive-going potential sweep, suggests that either b-COOH is the Pt-passivating species and CO_{ads} doesn't form from HCOOH in [dema][TfO], or CO_{ads} does still form but in a dry [dema][TfO] sample in the presence of formic acid, it is not oxidised until around 1.5 V.

The addition bases other than dema were found to heavily inhibit FAO as well as formic acid reduction and hydrogen oxidation (imidazole and thiazole), with FAO only being detected when pyridine or dema were present in [dema][TfO]. Pyridine, as a weaker base than dema, had the predicted effect of a lower direct FAO peak j_{max} however, the possible effect of electrode passivation by pyridine cannot be ruled out entirely since hydrogen oxidation was found to be inhibited

in its presence. The bases themselves could be oxidised with thiazole, imidazole, and pyridine oxidised positive of 2.25 V, 1.0 V and 1.0 V, respectively. However, the oxidation of the added bases was not consistently observed often with the base oxidation current only observed in CVs recorded soon after the bases were added.

Since the bases chosen for this study, with the exception of dema, were found to inhibit direct FAO, it requires further study to determine which bases, if any across a wide conjugate acid pK_a range, are suitable to test the direct FAO reaction as a probe reaction for predicting basicity in PILs. However, despite setbacks, insights into oxide formation/removal, oxygen evolution in [dema][TfO] and their possible mechanisms, have been gained.

6.5 References

1. Capon, A.; Parsons, R. The Oxidation Of Formic Acid On Noble Metal Electrodes I. Review Of Previous Work. *J. Electroanal. Chem. Interfacial Electrochem.* **1973,** *44*, 1-7.

2. Giner, J. The Anodic Oxidation Of Methanol And Formic Acid And The Reductive Adsorption Of CO_2. *Electrochim. Acta* **1964,** *9*, 63-77.

3. Buck, R. P.; Griffith, L. R. Voltammetric and Chronopotentiometric Study of the Anodic Oxidation of Methanol, Formaldehyde, and Formic Acid. *J. Electrochem. Soc.* **1962**.

4. Müller, E. Zur Elektrolytischen Oxydation Der Ameisensäure. *Z. Elektrochem. Angew. Phys. Chem.* **1927,** *33*, 561-568.

5. Müller, E.; Schwabe, K. Katalytische Spaltung Und Oxydation Der Ameisensäure. *Z. Elektrochem. Angew. Phys. Chem.* **1928,** *34* (4), 170-185.

6. Müller, E.; Tanaka, S. Über Die Pulsierende Elektrolytische Oxydation Der Ameisensäure. *Z. Elektrochem. Angew. Phys. Chem.* **1928,** *34* (5).

7. Capon, A.; Parsons, R. The Oxidation Of Formic Acid On Noble Metal Electrodes II. A Comparison Of The Behaviour Of Pure Electrodes. *J. Electroanal. Chem. Interfacial Electrochem.* **1973,** *44*, 239-554.

8. Hickling, A. Studies in electrode polarisation. Part IV.—The automatic control of the potential of a working electrode. *Trans. Faraday Soc.* **1942,** *38* (0), 27-33.

9. Breiter, M. W. Anodic Oxidation Of Formic Acid On Platinum-I. Adsorption Of Formic Acid, Oxygen, And Hydrogen In Perchloric Acid Solutions. *Electrochim. Acta* **1963,** *8*, 447-456.

10. Crépy, G.; Lamy, C.; Maximovitch, S. Oxydation de l'acide formique sur électrode d'or. *Electroanal. Chem. Interfacial Electrochem.* **1974,** *54*, 161-179.

11. Brummer, S. B.; Makrides, A. C. Adsorption and Oxidation of Formic Acid on Smooth Platinum Electrodes in Perchloric Acid Solutions. *J. Phys. Chem.* **1964,** *68* (6).

12. Chen, Y. X.; Heinen, M.; Jusys, Z.; Behm, R. J. Kinetics and mechanism of the electrooxidation of formic acid - spectroelectrochemical studies in a flow cell. *Angew. Chem. Int. Ed. Engl.* **2006,** *45* (6), 981-5.

13. Beden, B.; C., L. Electrosorption Of Methanol On A Platinum Electrode. IR Spectroscopic Evidence For Adsorbed CO Species. *J. Electroanal. Chem.* **1981,** *121*, 343-347.

14. Beden, B.; Bewick, A.; Lamy, C. A Study By Electrochemically Modulated Infrared Reflectance Spectroscopy Of The Electrosorption Of Formic Acid At A Platinum Electrode. *J. Electroanal. Chem.* **1983,** *148*, 147-160.

15. Miki, A.; Ye, S.; Osawa, M. Surface-enhanced IR absorption on platinum nanoparticles: an application to real-time monitoring of electrocatalytic reactions. *Chem. Commun. (Cambridge, U. K.)* **2002,** (14), 1500-1501.

16. Samjeské, G.; Miki, A.; Ye, S.; Osawa, M. Mechanistic Study of Electrocatalytic Oxidation of Formic Acid at Platinum in Acidic Solution by Time-Resolved Surface-Enhanced Infrared Absorption Spectroscopy. *J. Phys. Chem. B* **2006,** *110* (33), 16559-16566.

17. Osawa, M.; Komatsu, K.; Samjeske, G.; Uchida, T.; Ikeshoji, T.; Cuesta, A.; Gutierrez, C. The role of bridge-bonded adsorbed formate in the electrocatalytic oxidation of formic acid on platinum. *Angew. Chem. Int. Ed. Engl.* **2011,** *50* (5), 1159-63.

18. Cuesta, A.; Cabello, G.; Gutierrez, C.; Osawa, M. Adsorbed formate: the key intermediate in the oxidation of formic acid on platinum electrodes. *Phys. Chem. Chem. Phys.* **2011,** *13* (45), 20091-5.

19. Müller, E. Die Elektrolytische Oxydation Der Ameisensäure. *Z. Elektrochem. Angew. Phys. Chem.* **1923,** *23*, 264-274.

20. Chen, Y.-X.; Heinen, M.; Jusys, Z.; Behm, R. J. Bridge-Bonded Formate: Active Intermediate or Spectator Species in Formic Acid Oxidation on a Pt Film Electrode? *Langmuir* **2006,** *22*, 10399-10408.

21. Joo, J.; Uchida, T.; Cuesta, A.; Koper, M. T. M.; Osawa, M. The effect of pH on the electrocatalytic oxidation of formic acid/formate on platinum: A mechanistic study by surface-enhanced infrared spectroscopy coupled with cyclic voltammetry. *Electrochim. Acta* **2014,** *129*, 127-136.

22. Joo, J.; Uchida, T.; Cuesta, A.; Koper, M. T.; Osawa, M. Importance of acid-base equilibrium in electrocatalytic oxidation of formic acid on platinum. *J. Am. Chem. Soc.* **2013,** *135* (27), 9991-4.

23. CRC, *CRC Handbook of Chemistry and Physics*. 96th ed.; CRC Press: 2015; p 2677.

24. Schwarz, K. A.; Sundararaman, R.; Moffat, T. P.; Allison, T. C. Formic acid oxidation on platinum: a simple mechanistic study. *Phys. Chem. Chem. Phys.* **2015,** *17* (32), 20805-13.

25. Goodwin, S. E.; Muhammad, S.; Tuan, L.-P.; Walsh, D. A. The contrasting effects of diethylmethylamine during reduction of protons and oxidation of formic acid in diethylmethylammonium-based protic ionic liquids. *J. Electroanal. Chem.* **2018,** *819*, 187-192.

26. Feng, Y.-Y.; Yin, Q.-Y.; Lu, G.-P.; Yang, H.-F.; Zhu, X.; Kong, D.-S.; You, J.-M. Enhanced catalytic performance of Pd catalyst for formic acid electrooxidation in ionic liquid aqueous solution. *J. Power Sources* **2014,** *272*, 606-613.

27. Capon, A.; Parsons, R. The Oxidation Of Formic Acid On Noble Metal Electrodes III. Intermediates And Mechanism On Platinum Electrodes. *Electroanal. Chem. Interfacial Electrochem.* **1973,** *45*, 205-231.

28. Angerstein-Kozlowska, H.; Conway, B. E.; Sharp, W. B. A. The Real Condition Of Electrochemically Oxidized Platinum Surfaces Part I. Resolution Of Component Processes. *Electroanal. Chem. Interfacial Electrochem.* **1973,** *43*, 9-36.

29. Tilak, B. V.; Conway, B. E.; Angerstein-Kozlowska, H. The Real Condition Of Oxidized Pt Electrodes Part III. Kinetic Theory Of Formation And Reduction Of Surface Oxides. *Electroanal. Chem. Interfacial Electrochem.* **1973,** *48*, 1-23.

30. Zhang, G.-R.; Etzold, B. J. M. Ionic liquids in electrocatalysis. *J. Energy Chem.* **2016,** *25* (2), 199-207.

31. Ejigu, A.; Johnson, L.; Licence, P.; Walsh, D. A. Electrocatalytic oxidation of methanol and carbon monoxide at platinum in protic ionic liquids. *Electrochem. Commun.* **2012,** *23*, 122-124.

32. Barhdadi, R.; Troupel, M.; Comminges, C.; Laurent, M.; Doherty, A. Electrochemical determination of pKa of N-bases in ionic liquid media. *J. Phys. Chem. B* **2012,** *116* (1), 277-82.

33. Millan, D.; Rojas, M.; Santos, J. G.; Morales, J.; Isaacs, M.; Diaz, C.; Pavez, P. Toward a pK(a) scale of N-base amines in ionic liquids. *J. Phys. Chem. B* **2014,** *118* (16), 4412-8.

34. Kanzaki, R.; Kodamatani, H.; Tomiyasu, T.; Watanabe, H.; Umebayashi, Y. A pH Scale for the Protic Ionic Liquid Ethylammonium Nitrate. *Angew. Chem., Int. Ed. Engl.* **2016,** *55* (21), 6266-6269.

35. Bentley, C. L.; Bond, A. M.; Zhang, J. Voltammetric Perspectives on the Acidity Scale and H^+/H_2 Process in Ionic Liquid Media. *Annu. Rev. Anal. Chem.* **2018,** *11* (1), 397-419.

36. Smith, D. E.; Walsh, D. A. The Nature of Proton Shuttling in Protic Ionic Liquid Fuel Cells. *Adv. Energy Mater.* **2019,** *9* (24).

37. Switzer, E. E.; Zeller, R.; Chen, Q.; Sieradzki, K.; Buttry, D. A.; Friesen, C. Oxygen Reduction Reaction in Ionic Liquids: The Addition of Protic Species. *J. Phys. Chem. C* **2013,** *117* (17), 8683-8690.

38. Goodwin, S. E.; Gibson, J. S.; Jones, R. G.; Walsh, D. A. An ultra-high vacuum electrochemical/mass spectrometry study of anodic decomposition of a protic ionic liquid. *Electrochem. Commun.* **2018,** *90*, 111-115.

39. Walsh, D. A.; Ejigu, A.; Muhammad, S.; Licence, P. The Formation and Role of Oxide Layers on Pt during Hydrazine Oxidation in Protic Ionic Liquids. *ChemElectroChem* **2014,** *1* (1), 281-288.

40. Conway, B. E.; Gottesfe, S. Real Condition of Oxidized Platinum Electrodes Part 2.-Resolution of Reversible and Irreversible Processes by Optical and Impedance Studies. *J. Chem. Soc., Faraday Trans. 1* **1973,** *69*, 1090-1107.

41. Rhodes, D. R.; Steigelmann, E. F. Catalytic Decomposition of Aqueous Formic Acid on Platinum Electrodes. *J. Electrochem. Soc.* **1965,** *112* (1), 16-21.

42. Cuesta, A.; Cabello, G.; Osawa, M.; Gutiérrez, C. Mechanism of the Electrocatalytic Oxidation of Formic Acid on Metals. *ACS Catal.* **2012,** *2* (5), 728-738.

43. Yang, C.; Costamagna, P.; Srinivasan, S.; Benziger, J.; Bocarsly, A. B. Approaches and technical challenges to high temperature operation of proton exchange membrane fuel cells. *J. Power Sources* **2001,** *103*, 1-9.

7 Protic Ionic Liquids as Fuel-Cell Electrolytes

7.1 Introduction

Polymer electrolyte membrane fuel cells (PEMFCs) remain the most promising type of fuel cell for vehicular transport and portable applications.[1] However, the electrocatalysis driving the oxygen reduction and hydrogen oxidation fuel cell reactions, even at the most effective platinum catalysts, is affected by slow electrode kinetics which hampers fuel-cell performance.[2] The oxygen-reduction reaction (ORR) is particularly prone to slow electrode kinetics, which has necessitated the use of high Pt-loading electrocatalysts in an attempt to increase the rate of the ORR; this has resulted in higher costs of PEMFCs.[3] Furthermore, Pt-based electrocatalysts can be susceptible to passivation by CO found in hydrogen produced from fossil fuel sources[4] by processes such as steam methane reforming (SMR).[5] Hydrogen produced by SMR requires expensive gas separation/purification processes to remove the CO and other contaminant gases for use in fuel cells.[6,7]

A possible solution to the problems of slow ORR kinetics, high platinum loadings, and the requirement for ultra-pure H_2, is to increase the operating temperature of the fuel cell.[8,9,10,11] This would reduce the binding affinity of contaminants to the electrocatalysts, increasing the rate of the ORR, potentially reducing the Pt-loading requirement or even making possible the use of non-noble metal catalysts.[8,12] However, fuel cell operating temperatures are currently limited to <100 °C because the polymer electrolyte membrane, most commonly Nafion®, requires hydration (liquid water) to facilitate proton transport across the membrane.[13,14] Water management in the fuel cell is therefore very important to ensure

membrane hydration and prevent fuel-cell flooding which greatly reduces performance.[15] One approach to intermediate-temperature (120 to 200 °C) PEMFCs involve the use of proton-conducting acid-doped polymers such as phosphoric acid-doped polybenzimidazole but these have encountered problems of the acid leeching out of the membrane and corrosion effects from the presence of the acid.[16,17]

A different approach is to use protic ionic liquids (PILs) as fuel-cell electrolytes as they are ionically conductive, are thermally stable at temperatures elevated above 100 °C, and have low volatility.[18,19] Diethylmethylammonium trifluoromethanesulfonate ([dema][TfO]), in particular, has been suggested as a good candidate for incorporation into a fuel cell membrane, because of its good proton conductivity, thermal stability and high open circuit potential (OCP) (greater than 1.0 V at 150 °C).[20,21] The high OCP reported by Watanabe and co-workers was attributed to fast ORR and HOR kinetics in the PIL. The ORR and HOR has been extensively studied as half cell reactions using voltammetric methods and is presented in Chapter 4. This chapter tests the conclusions of Chapter 4 by making a fuel cell with an acidified, basified and pure [dema][TfO] electrolyte, and recording fuel cell polarisation curves for each using a Grove-type cell. A discussion of the interpretation of fuel-cell polarization curves is found in Chapter 2.

Also investigated in this chapter is the effect of elevated temperature on the [dema][TfO] electrolyte in terms of PIL ionicity and physical appearance. The favourable fuel-cell potentials (E_{cell}) observed by others in [dema][TfO] at temperatures of 150 °C is explained in terms of physical changes to the PIL.[20,22]

The results presented in this chapter confirm the predications made in Chapter 4 regarding the effect of the presence of acid or base on E_{cell} in a fuel cell using an established method.[23,24] Finally, using the findings of Chapter 4 and this chapter, a single H_2/O_2 fuel cell with an E_{cell} significantly greater than the thermodynamically determined theoretical maximum of 1.229 V in a conventional fuel cell is presented, and the mechanism explained.[2]

7.2 Experimental Section

7.2.1 Materials and apparatus

All chemicals were obtained from Acros Organics, Sigma Aldrich, Merck, VWR Chemicals, or Fischer Scientific, and were used as received. O_2 (99.95%) and H_2 (99.999%), were from BOC gases (Nottingham, UK). Ar (99.999%) was from CryoService (Worcester, UK). Pd wire (0.5 mm diameter, 99.99%) and Pt wire (0.5 mm diameter, 99.997%) was from Alfa Aesar. A modulated speed rotator and Pt and glassy-carbon rotating disk electrodes (RDEs) and rotating ring-disk electrodes (RRDEs) were from Pine Research Instrumentation, Inc (Durham, NC, USA). Electrochemical measurements were performed using a model CHI760C or model CHI700D potentiostat from CH Instruments, Austin, TX, USA. Ultra-violet/visible light spectroscopy (UV-Vis.) was carried out used an Ocean Optics UV-Vis. spectrometer. UV-Vis. coupled with hydrophilic-interaction liquid ion chromatography (HILIC) and mass spectrometry (mass spec.) was carried out using a Thermoscientific Dionex Ultimate 3000 UHPLC and Bruker MicroTOF II in reverse phase mode.

7.2.2 Synthesis and Characterisation of [dema][TfO]

Diethylmethylammonium trifluoromethanesulfonate, [dema][TfO], was prepared by the dropwise addition of 0.1 mol dm^{-3} aqueous trifluoromethanesulfonic acid to 0.1 mol dm^{-3} aqueous N,N-diethylmethylamine with a 5% molar excess of the base. The reaction mixture was cooled in an ice bath. Excess water was removed using rotary evaporation. The product was then held under vacuum (5×10^{-2} mbar) at room temperature for 24 h and then at 40 °C at 5×10^{-2} mbar for about 10 days, to remove residual water and base. The liquid was then transferred under vacuum to a glovebox containing a dry N_2 atmosphere (<0.1 ppm O_2 and <0.4 ppm H_2O). [dema][TfO] was characterized by ^{1}H, ^{13}C and ^{19}F NMR spectroscopy (Bruker Ascend™ 400 MHz NMR Spectrometer) using a hexadeuterodimethyl sulfoxide solvent. Attenuated total reflection Fourier-transform infrared spectroscopy was carried out using a Bruker Alpha Platinum-ATR FTIR spectrometer at 30 °C. Residual water contents were determined using Karl-Fischer titrations (Mitsubishi CA-200 Moisturemeter). Residual water contents were below 50 ppm. Characterisation data is presented in Chapter 3 and Appendix I.

7.2.3 Cell setup and electrochemical measurements

Fuel-cell polarisation curves were recorded using a H-cell from Pine Research Instrumentation, Inc. (Durham, NC, USA), in which a glass frit separated the two chambers. Each chamber of the cell was filled with 8 mL of [dema][TfO]. H_2 and O_2 was flowed over the negative and positive electrodes, respectively, and each electrolyte was stirred at 650 rpm during measurements. 0.5 mm-diameter Pt wire electrodes were used as the anode and cathode. The current was increased from ≈0 A at a rate of 0.25 μA s^{-1} and cell potential was recorded.

The 3-electrode ORR experiments with heated and unheated [dema][TfO] were conducted as follows: A 50 mL three-necked round-bottomed flask was charged with 5 mL of [dema][TfO] and bubbled with O_2 for 40 minutes while the liquid was magnetically stirred at 500 rpm. A 4.6 mm Pt disk RDE or 0.2356 cm^2 Pt ring RDE working electrode, Pt flag counter electrode (A ≈0.70 cm^2), and Pd-H reference electrode were immersed in the cell. During voltammetric measurements, a blanket of the appropriate gas was maintained above the PIL. Prior to use, the Pt disk electrode was polished using an aqueous suspension of 0.05 μm α-alumina (Buehler, Lake Bluff, Illinois) on felt polishing pads, and rinsed thoroughly with deionized water. The Pt flag counter electrode was flame annealed in a butane flame before being rinsed with deionised water. All working and counter electrodes were dried in a glassware oven before use. To mitigate for changes in the potential of the Pd-H reference electrode upon heating or saturation with O_2, potentials were adjusted such that the electrochemical window was the same during each analysis. The fabrication and use of Pd-H reference electrodes for electrochemistry are discussed in the experimental section in Chapter 4.

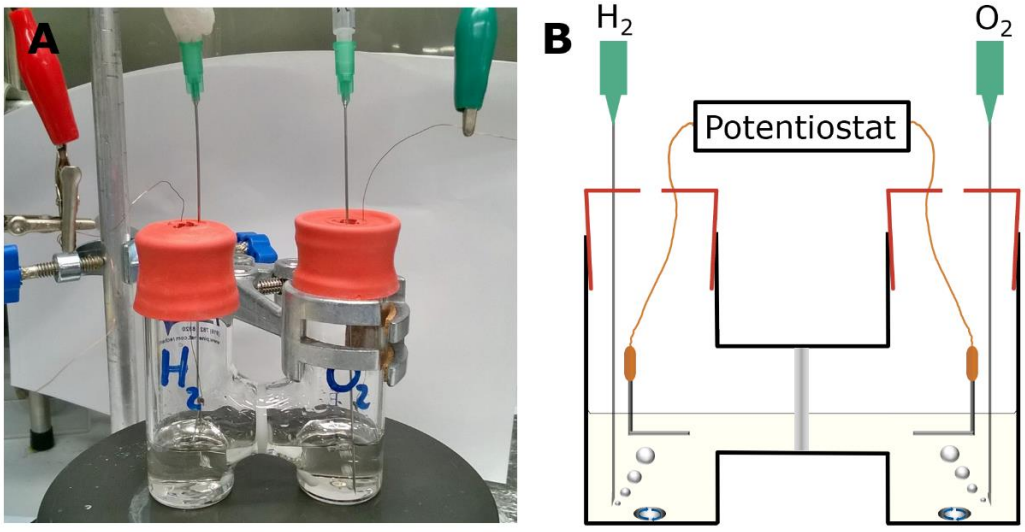


Figure 7.1 The Grove-type electrochemical cell setup used to test a [dema][TfO]-H_2/O_2 fuel cell. (A) Photograph. (B) Schematic diagram of the experimental setup.

CVs of O_2-saturated [dema][TfO] were recorded before heating the sample to 80 °C using a flask size-specific heating block, and recording voltammograms at this elevated temperature. The same [dema][TfO] electrolyte was then heated to 150 °C in air for approximately 64 hours using a heating block. After heating, the sample was left to cool to room temperature and was re-saturated with O_2 by bubbling with the gas for 40 minutes while stirring the liquid.

7.3 Results and Discussion

7.3.1 Polarisation of a PIL-based fuel cell

An H_2/O_2 fuel-cell experiment using a Grove-type cell was set up using 16 mL of pure [dema][TfO] electrolyte as presented in Figure 7.1. The left-hand side of the cell was saturated with H_2 and the right-hand side with O_2 by bubbling with the respective gases for 40 minutes prior to measurements. All polarisation curve measurements were at room temperature. During fuel-cell polarisation experiments, the electrolyte on each side of the cell was continuously bubbled with the respective gas, and stirrer bars were set to 650 rpm to ensure efficient mass transport of dissolved gases to each Pt electrode during measurements.

The fuel-cell polarisation curves in Figure 7.2 compare results obtained in a pure [dema][TfO] electrolyte with [dema][TfO] either acidified with triflic acid or basified with dema, the parent acid and base of the PIL respectively. In a pure [dema][TfO] electrolyte (green polarisation curve), E_{cell} decreases rapidly from ≈1.0 V to 0 V over a small j increase of 0.1 mA cm^{-2}. All initial E_{cell} losses are kinetic but very quickly become mass-transport limited causing the E_{cell} to fall to 0 V. This effect can be explained in part by the HOR and ORR voltammetry in Chapter 4 which showed a hypothetical E_{cell} of 0 V for a pure [dema][TfO] electrolyte because

of the positive $\Delta_r G^{\ominus}$ of returning the PIL to its parent acid and base entirely offsetting the negative $\Delta G^{\ominus}$ of water formation (see Equations 1 and 2). However, this alone does not explain the initial OCP around 1 V; what causes the initial high OCP and rapid drop is very likely the presence of a small equilibrium concentration of acid present in the electrolyte, undetectable by standard voltammetric methods. This small equilibrium concentration of triflic acid would cause the ORR to shift by ≈0.9 V to a more positive potential, thus providing an OCP of ≈0.9 V, but would be depleted as soon as any current density was applied, causing the E_{cell} to rapidly fall to zero, as observed. No ohmic region is observed in pure [dema][TfO] because there are no stable current densities over which a pure [dema][TfO] fuel cell can operate.

$$HOR_{(\text{pure [dema][TfO]})}: 2H_2 + 4[TfO]^- \rightarrow 4TfOH + 4e^- \quad (1)$$

$$ORR_{(\text{pure [dema][TfO]})}: O_2 + 4[dema]^+ + 4e^- \rightarrow 2H_2O + 4dema \quad (2)$$

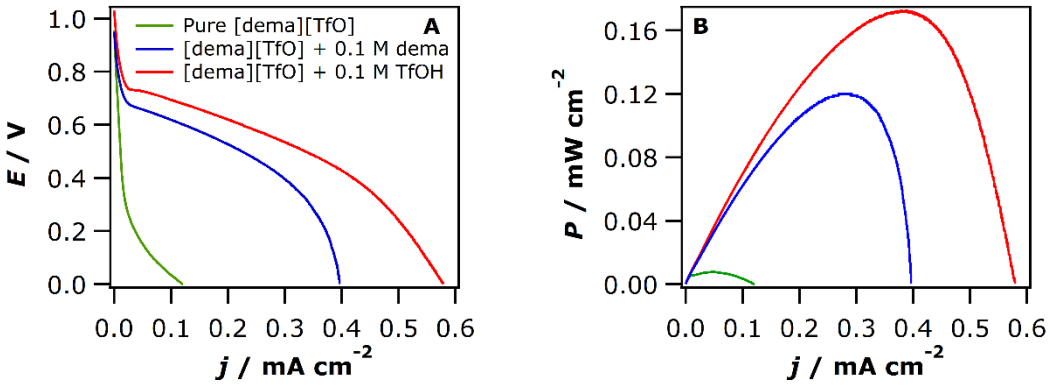


Figure 7.2 (A) Fuel-cell polarisation curves recorded using a Grove-type fuel cell containing H_2- (anolyte) and O_2-saturated (catholyte) [dema][TfO] containing (red line) 0.1 mol dm^{-3} triflic acid, and (blue line) 0.1 mol dm^{-3} diethylmethylamine. The current was ramped at 0.25 μA s^{-1}. H_2 and O_2 were bubbled into the anolyte and catholyte, respectively, throughout the experiments and the electrolytes were stirred using magnetic stirrer bars rotating at 650 rpm. (B) Accompanying fuel cell power curves to the polarisation curves presented in (A). Electrodes were cleaned electrochemically by potential cycling prior to each measurement.

The blue polarisation curve in Figure 7.2 (A) is recorded in [dema][TfO] containing 0.1 mol dm^{-3} of dema, the parent base, and has an OCP of ≈0.9 V as predicted by the HOR voltammetry of basified [dema][TfO] in Chapter 4. Unlike in pure [dema][TfO], the added base provides a valid proton shuttling mechanism with dema/$[dema]^+$ acting as a proton acceptor and donor respectively (see Equations 3, 4 and 5). Any mass-transport limitations will be the result of the flux of dema (concentration ≈0.1 mol dm^{-3}) or H_2/O_2, rather than $[dema]^+$ (concentration ≈5.5 mol dm^{-3}), to the respective electrodes' surfaces. As such, an ohmic region is established from ≈0.05 mA cm^{-2} with an E_{cell} starting at ≈0.7 V until mass-transport effects cause a rapid loss in E_{cell} beginning at ≈0.325 mA cm^{-2}.

$$HOR_{(\text{with added dema})}: 2H_2 + 4\text{dema} \rightarrow 4[\text{dema}]^+ + 4e^- \quad (3)$$

$$ORR_{(\text{with added dema})}: O_2 + 4[\text{dema}]^+ + 4e^- \rightarrow 2H_2O + 4\text{dema} \quad (4)$$

$$\text{Overall reaction: } 2H_2 + O_2 \rightarrow 2H_2O \quad (5)$$

Similarly, when [dema][TfO] is acidified with triflic acid to a 0.1 mol dm^{-3} concentration, the fuel cell polarisation curve looks similar to that of [dema][TfO] basified with dema to the same concentration and shown by the red data curve in Figure 7.2 (A). The OCP of the acidified [dema][TfO] fuel cell is ≈1 V as predicted by the HOR and ORR voltammetry presented in Chapter 4 (see Equations 6, 7 and 5). As j is increased activation losses account for a drop in E_{cell} of ≈0.3 V, after which an Ohmic region is established from ≈0.05 mA cm^{-2} with an E_{cell} starting at ≈0.75 V until mass-transport effects cause a rapid loss in E_{cell} beginning at ≈0.45 mA cm^{-2}.

$$HOR_{(\text{with added TfOH})}: 2H_2 + 4[TfO]^- \rightarrow 4TfOH + 4e^- \quad (6)$$

$$ORR_{(\text{with added TfOH})}: O_2 + 4TfOH + 4e^- \rightarrow 2H_2O + 4[TfO]^- \quad (7)$$

The performance of the triflic acid-acidified [dema][TfO] fuel cell was greater than that of the basified [dema][TfO] fuel cell probably because dema is highly volatile and quickly evaporates from the H-cell, lowering the concentration of dema to react in the HOR. Furthermore, dema has been shown to passivate the Pt electrode surface as discussed in Chapter 4 and later in this chapter, which would likely contribute to a loss of fuel-cell performance. Despite the slight difference in performance, both acidified and basified [dema][TfO] electrolytes provided fuel-cell polarisation curves that indicate a functioning system, whereas the pure [dema][TfO] electrolyte performed very poorly with the E_{cell} very quickly dropping to zero once current began to flow. To complement the fuel-cell polarisation curves, power curves are presented in Figure 7.2 (B), calculated using Equation 8, to highlight the considerable difference in performance of the electrolytes with a suitable proton shuttling mechanism and pure [dema][TfO] which does not. The poor performance of the pure [dema][TfO] electrolyte fuel cell at room temperature is significantly different to the performance reported of the same at 150 °C by Watanabe *et al*.[22] and will be explored later in this chapter.

$$\text{power density} = \text{current density} \times \text{cell potential} \ (P = j \times E_{cell}) \quad (8)$$

Evidence of Pt electrode passivation is presented in Figure 7.3 together with the need for an electrode electrochemical cleaning step between each of the polarisation curve measurements. The solid line polarisation curve 1) is recorded before any electrochemical cleaning step has taken place and shows an OCP of

≈0.6 V which very rapidly falls to zero at as soon as a very small current density of 0.005 mA cm^{-2} is applied. Polarisation curve 2), with a dashed line, shows the improvement in fuel-cell performance after an electrochemical cleaning step relative to the polarisation curve recorded before any electrode cleaning step. The cleaning step entailed cycling the Pt electrodes relative to negative and positive potentials over the electrochemical window of [dema][TfO]. Any species formed at the electrodes' surfaces as a result of the potential cycling would be removed due to the constant stirring on both H-cell compartments before the polarisation curve was recorded. The OCP shown by 2) is ≈1.0 V, 0.4 V higher than without a cleaning step, and drops to an E_{cell} of 0 V at ≈0.09 mA cm^{-2} (0.085 mA cm^{-2} higher than without a cleaning step). Polarisation curve 3) (dotted line) is recorded immediately after 2) but without an intervening cleaning step, and shows a drop in performance with an OCP of ≈0.8 V and drops to an E_{cell} of 0 V at ≈0.08 mA cm^{-2}. The drop in performance between 2) and 3) suggests that without a cleaning step, the electrodes will eventually revert to their 'passivated' state with the corresponding fuel cell performance. A likely cause of the apparent passivation of the Pt electrodes is dema sticking to the electrodes' surfaces; dema either being present at a very small equilibrium concentration or as a result of the ORR in Equation 2. Either way, this passivation effect could further impede PILs, and [dema][TfO] specifically, acting as fuel cell electrolytes. However, it is possible that the passivation effect is lessened at elevated temperatures, where these new electrolytes are intended to operate. In order to compare polarisation curve data from all [dema][TfO] electrolytes, basified/acidified or otherwise, an electrochemical cleaning step as described was used prior to recording each polarisation curve.

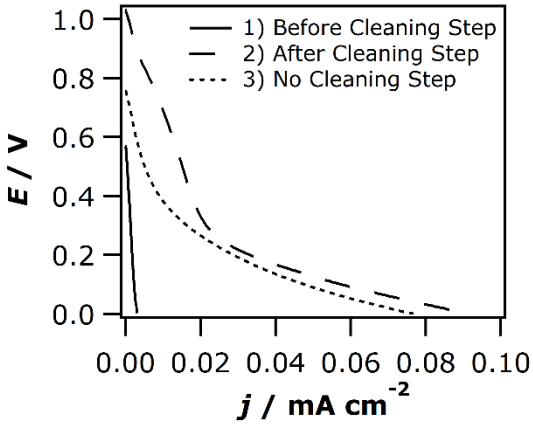
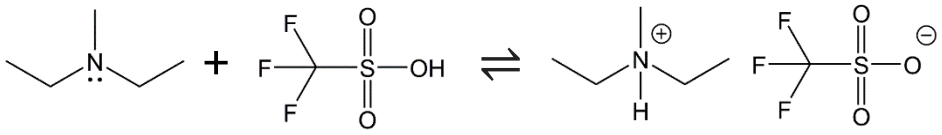


Figure 7.3 Fuel cell polarisation curves recorded using a Grove-type fuel cell containing H_2- (anolyte) and O_2-saturated (catholyte) pure [dema][TfO]. The current was ramped at 0.25 μA s^{-1}. H_2 and O_2 were bubbled into the anolyte and catholyte, respectively, throughout the experiments and the electrolytes were stirred using magnetic stirrer bars rotating at 650 rpm. 1) Is recorded before any electrode potential-cycling cleaning. 2) Is recorded after a potential-cycling electrode cleaning step. 3) Is recorded immediately after 2) but without an intervening potential-cycling electrode cleaning step.

7.3.2 Effect of elevated temperature on [dema][TfO]

To asses the effect, if any, heating the PIL to temperatures they are intended to function at in intermediate-temperature fuel cells,[22] [dema][TfO] was heated to 80 and 150 °C for varying lengths of time. Figure 7.4 shows the colour change in [dema][TfO] when heated. Figure 7.4 (A) and (B) are pictures of unheated [dema][TfO] and [dema][TfO] heated to 80 °C for 2 hours respectively, and there appears to be very little colour change between them as they are both clear and very pale yellow. However, Figure 7.4 (C) shows that heating [dema][TfO] to 150 ° C for 1 hour induces a notable deepening of the yellow colour. This slight colour change is greatly enhanced when the [dema][TfO] sample has been heated to 150 °C for a further 63 hours (Figure 7.4 (D)), where the sample is shown to have gone a deep red/brown. A possible cause of this colour change is the chemical equilibrium of PIL formation shifting to produce a higher concentration of the parent acid and base species (see Equations 9, 10 and 11), the dema could

then oxidise or thermally decompose to some chromophoric species which remains either suspended or dissolved in the PIL, while the TfOH produced would remain unchanged.



(9)

dema triflic acid [dema][TfO]

$$K_{eq} = \frac{([dema][TfO])}{[dema][TfOH]} \quad pK_{eq} = -\log_{10}K_{eq}$$

$$pK_{eq} = pK_{a(TfOH)} - pK_{a([dema]^+)} \tag{10}$$

$$K_{eq}^{\ominus} = e^{-\frac{\Delta_r G^{\ominus}}{RT}} \tag{11}$$

It is well-known that pure, near-colourless, amines oxidise over time in an air environment to yellow/brown liquids[25,26] so dema decomposition/oxidation is a likely candidate for the colour change in [dema][TfO] at elevated temperatures.

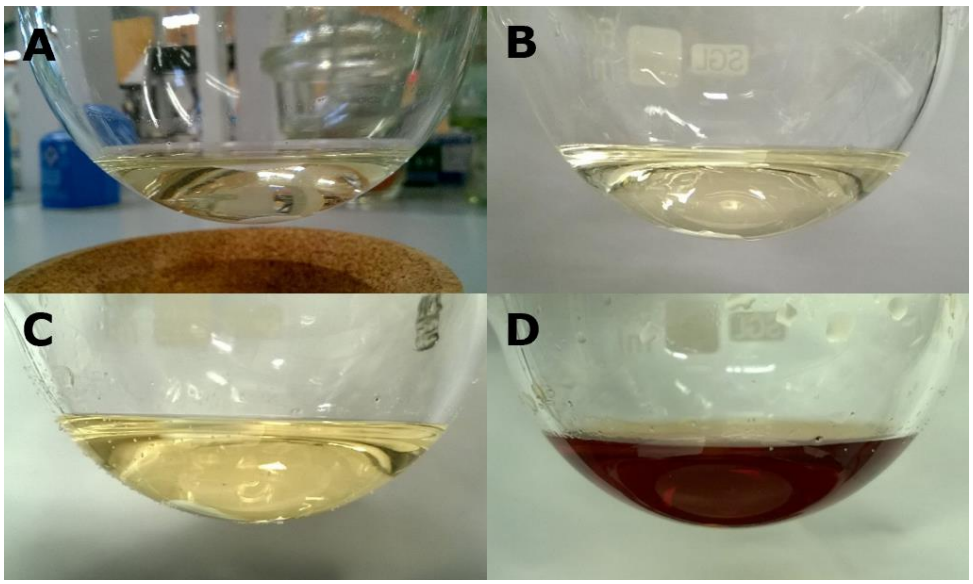


Figure 7.4 (A) Unheated [dema][TfO] as synthesised. (B) [dema][TfO] heated to 80 °C for ≈2 hours. (C) [dema][TfO] heated to 150 °C for 1 hour. (D) [dema][TfO] heated to 150 °C for a further 63 hours. Samples are heated in a flask open to air.

Unlike neutral dema, TfOH is stable in PILs under high vacuums and temperature, likely due to hydrogen bonding in the PIL.[27] If it is the case that dema is lost by oxidation/decomposition and probably some evaporation, it would leave a non-stoichiometric excess stable concentration of neutral TfOH, which as shown in Chapter 4 and in Figure 7.2, has a significant effect on the ORR and fuel cell performance, which should be detectable by voltammetric methods.

To determine the effect of heating on the ORR, O_2-saturated [dema][TfO] was heated to 80 °C and a voltammogram was recorded to compare the ORR at 80 °C with that at room temperature. The red voltammogram in Figure 7.5 is recorded in O_2-saturated [dema][TfO] at 80 °C, and shows the ORR onset at ≈0.6 V, which is ≈0.4 V more positive than at room temperature but ≈0.4 V more negative than at room temperature in the presence of triflic acid. Also, the maximum ORR current density (*j)* achieved at 80 °C is significantly greater than that at room temperature, which were all at ≈0.4 mA cm^{-2}, caused by a decrease in PIL viscosity and increase in diffusion rate to the electrodes greatly outweighing any offset by the reduction in bulk O_2 and H_2 concentrations at 80 °C.[28] When heated at 150 °C for 64 hours, cooled back down to room temperature and re-saturated with O_2, the ORR shifts back to similar potentials and j_L before heating. However, the onset potential after heating is shifted positive by about 0.3 V and a new peak has appeared prior to the main ORR peak.

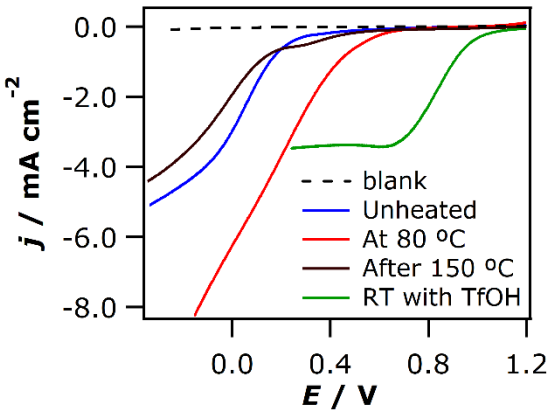


Figure 7.5 Cyclic voltammograms of O_2-saturated [dema][TfO] recorded at a Pt electrode rotating at 1,600 rpm at 0.1 V s^{-1} before, during, and after heating. Voltammograms were recorded at room temperature, at 80 °C and at room temperature after being heated to 150 °C for 64 hours. A voltammograms of O_2-saturated[dema][TfO] containing a 0.1 mol dm^{-3} concentration TfOH at room temperature is presented for comparison. The blank is recorded in deaerated [dema][TfO] containing 10 ppm H_2O, in a nitrogen-atmosphere glove box, at a Pt electrode rotating at 1,600 rpm.

The difference between the ORR in [dema][TfO] before and after heating to 150 °C for 64 hours is shown in Figure 7.6 (A) and (B). The ORR onset potential is ≈0.2 V more positive after the [dema][TfO] has been heated (see Figure 7.6 (B)) and results in an extra ORR peak at ≈0.4 V, as shown at a stationary Pt electrode in Figure 7.6 (A). Furthermore, after [dema][TfO] has been heated for 64 hours at 150 °C, the peak current of dema oxidation at ≈1 V is notably less than observed before heating. This suggests that the process responsible for the new small ORR peak in the heated sample also causes less dema to be made by the ORR in the main peak. Furthermore, the peak ORR current observed after heating is less than that before heating suggesting that the process responsible for the small ORR peak is also consuming oxygen and must be itself, an ORR. This is confirmed by the voltammograms in Figure 7.6 (A) and (D) recorded in deaerated [dema][TfO] recorded after the sample is heated and returned to room temperature heated

which does not show a reduction current corresponding to the one observed in O_2-saturated [dema][TfO].

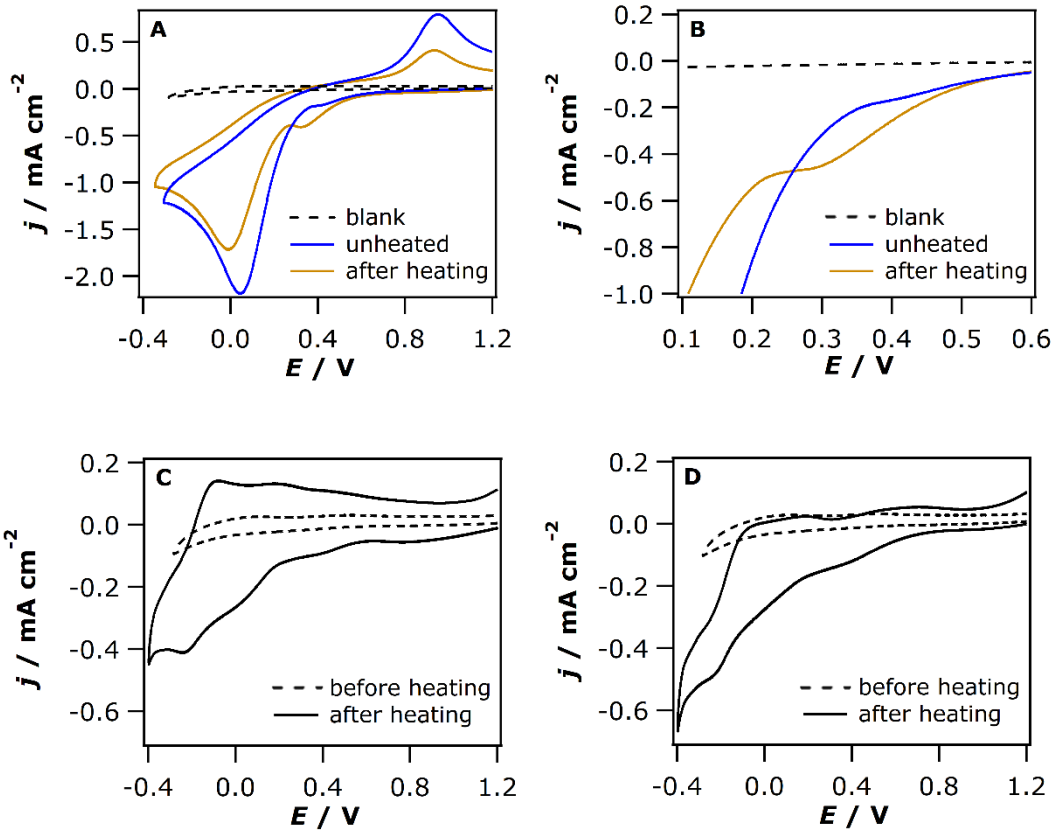


Figure 7.6 Cyclic voltammograms of [dema][TfO] before and after heating to 150 °C for 64 hours recorded at a Pt electrode at 0.1 V s^{-1}. (A) O_2-saturated [dema][TfO] at a stationary Pt electrode. (B) O_2-saturated [dema][TfO] at a Pt electrode rotating at 1,600 rpm. (C) Deaerated [dema][TfO] at a stationary Pt electrode. (D) Deaerated [dema][TfO] at a Pt electrode rotating at 1,600 rpm. Blank CVs were recorded in air-free [dema][TfO] containing 10 ppm H_2O in a nitrogen-atmosphere glovebox at a Pt electrode.

The nature of the small ORR peak only observed after the PIL has undergone prolonged heating can be explained as follows. When heated, the K_{eq} of [dema][TfO] shifts so that there is a higher equilibrium concentration of triflic acid and dema. The dema is then either lost through thermal decomposition, oxidation (causing the colour in the PIL) or evaporation, leaving excess TfOH in the PIL. If the TfOH was responsible for the second ORR peak observed in Figure 7.6 (A) and (B) it would occur around 0.9 V, as shown by the work in Chapter 4 and Figure 7.5.

The reason for the presence of the second ORR peak after heating is likely the presence of water in the highly hygroscopic PIL. Any small concentration of TfOH now 'fixed' in [dema][TfO] by heating the PIL, shifting K_{eq} and then returning to room temperature, would readily donate its proton to any water molecules present to make a PIL within a PIL, hydronium triflate in [dema][TfO] (see Equation 12).

$$TfOH + H_2O \rightleftharpoons [H_3O]^+ + [TfO]^- \quad (12)$$

The hydronium cations present could then take part in the ORR by donating protons as described in Equation 13.

$$O_2 + 4[H_3O]^+ + 4e^- \rightarrow 6H_2O \quad (13)$$

Due to the fact that $[H_3O]^+$ is a significantly weaker acid than TfOH, it is expected that the ORR onset potential from hydronium-donated protons to be significantly less positive than TfOH-donated protons. Furthermore, if the relationship between proton donor pK_a and $E_{½}$ established in Chapter 4 holds, then the $E_{½}$ of a 0 pK_a proton-donating species should be around 0.5 V. This is sufficiently close to the $E_{½}$ of ≈0.4 V observed from the small ORR peak in the O_2-saturated [dema][TfO] sample heated for 64 hours at 150 °C and cooled to room temperature, that $[H_3O]^+$-coupled ORR is the most likely cause. This could have consequences for PIL-based PEMs in that temperature cycling and variations in PIL water content could have a significant effect on the overall cell potential.

The CVs presented in Figure 7.6 (C) and (D) are of deaerated [dema][TfO] before and after the heating process at stationary and rotating Pt electrodes respectively and show what is likely to be hydronium reduction as shown in Equation 14.

$$2[H_3O]^+ + 2e^- \rightarrow 2H_2O + H_2 \quad (14)$$

The small cathodic current which peaks at −0.2 V in Figure 7.6 (C) and precedes hydrogen evolution from $[dema]^+$ at −0.4 V, is likely to be hydrogen evolution from the small hydronium concentration present in [dema][TfO] originating from the heating process. The increase in cathodic current of the process ascribed to hydronium reduction when the electrode is rotating at 1,600 rpm in Figure 7.6 (D) confirms that the process relates to a dissolved species and is not the formation or removal of a species on or from the electrode's surface that may be present in the PIL as a dema decomposition product. It is conceivable that if [dema][TfO] was heated for significantly longer than 64 hours and dried under vacuum then TfOH reduction would be observed in the deaerated PIL and characteristic TfOH-coupled ORR if it were saturated with O_2.

7.3.3 Determination of PIL impurities formed upon heating

Since a both a physical and electrochemical change has been observed in [dema][TfO] after heating the liquid, a quantitative determination of the colour-causing dema-oxidation/decomposition product was undertaken. Figure 7.7 (A) shows the UV-vis. spectrums of [dema][TfO] and [dema][TfO] heated to 150 °C for 64 hours. Photographs of the unheated and heated [dema][TfO] samples are presented in Figure 7.7 (B). In the unheated sample, an absorbance peak in the UV region at about 260 nm is observed; the same peak is observed in heated [dema][TfO] but is much broader, encompassing a range 200-575 nm, corresponding to absorbance of blue and green light, which is as expected from the red/brown IL sample.

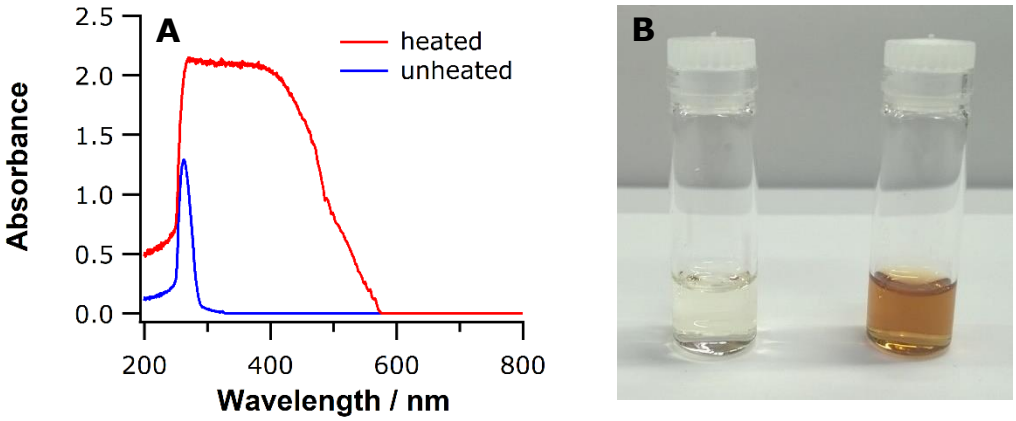


Figure 7.7 (A) ultra-violet/visible light spectrums of unheated [dema][TfO] and heated to 150 °C for 64 hours. (B) vials of unheated [dema][TfO] (left) and [dema][TfO] heated to 150 °C for 64 hours (right).

An attempt to detect protic species in the heated [dema][TfO] sample using universal pH indicator is shown in Figure 7.8. Unfortunately, the slight red colour change of the indicator paper when exposed to heated [dema][TfO] (Figure 7.8 (B)) could have been due to the colour of the ionic liquid, rather than the clear presence of a protic species, so the test is inconclusive. Figure 7.8 (C) is universal indicator paper plus acidified [dema][TfO] and Figure 7.8 (A) is universal indicator paper plus unheated, unacidified [dema][TfO] for comparison.

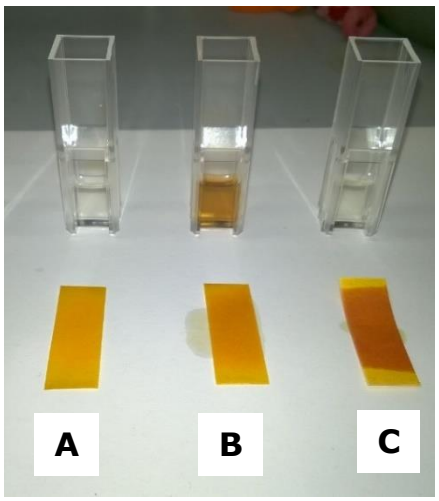


Figure 7.8 Photograph of [dema][TfO] samples on universal pH indicator paper. Water contents provided are starting water contents prior to the photograph being taken. (A) [dema][TfO] (≈8 ppm H_2O), (B) [dema][TfO] heated to 150 °C for 64 hours (≈500 ppm H_2O). (C) [dema][TfO] + 0.1 mol dm^{-3} TfOH.

HILIC coupled with mass spec. was carried out but a mass peak corresponding to a dema-oxide based chromophore, could not be isolated.

7.3.4 Simultaneous acid/base-coupling of ORR/HOR in PIL-based fuel cells

Now that the fuel-cell behaviour of the HOR and ORR in [dema][TfO] with and without added acid or base to act as a proton shuttle is better understood, both experimentally and as a result of basic thermodynamic calculations, this understanding was tested by seeing if it were possible to make a single H_2/O_2 fuel cell that would have an E_{cell} greater than that of the theoretical maximum of 1.229 V of a conventional fuel cell.

The reason that the HOR and ORR in pure [dema][TfO] occur at similar potentials, giving an E_{cell} of ≈0 V is because the exergonic process of water formation from H_2 and O_2 is offset entirely by the endergonic formation of the parent acid and base from the PIL – the fuel-cell reactions in pure [dema][TfO] would use the PIL anion and cation as reactants. When 0.1 mol dm^{-3} TfOH or dema has been added to provide a suitable proton shuttling mechanism, [dema][TfO] is no longer consumed by the HOR and ORR as the overall reaction becomes Equation 5 where the only reactants are H_2 and O_2 and the only product is H_2O – a maximum theoretical E_{cell} of 1.229 V can then be hypothetically achieved. However, what if instead of the endergonic breakdown of the PIL into the parent base and acid, the parent base and acid were provided at the fuel cell anode and cathode respectively so that the exergonic reaction of PIL formation could be utilised in the formation of water from H_2 andO_2? Equation 15 shows such a scheme where the overall fuel cell reaction produces [dema][TfO] and water.

$$2H_2 + 4\text{dema} + O_2 + 4\text{TfOH} \rightarrow 2H_2O + 4[\text{dema}][\text{TfO}] \quad (15)$$

Figure 7.9 (A) and (C) compare the voltammetry of HOR and ORR in pure [dema][TfO], with [dema][TfO] containing 0.1 mol dm^{-3} dema for the HOR experiment and 0.1 mol dm^{-3} TfOH for the ORR experiment. As previously shown, the potential difference between the HOR and ORR in pure [dema][TfO] is ≈0 V whereas in an hypothetical electrolyte containing both dema and TfOH, it is ≈1.8 V. The fuel-cell schematics for a pure [dema][TfO] fuel cell and one containing both dema and TfOH are shown in Figure 7.9 (B) and (D) respectively.

To test the conclusions of the voltammetry and hypothetical E_{cell} of 1.8 V of a [dema][TfO] fuel-cell electrolyte containing both dema and TfOH as suggested by Figure 7.9 (C), an H-cell containing 8 mL of [dema][TfO] in each side of the porous glass cell divide was set up according to Figure 7.1. The left-hand side was saturated with H_2 and the right-hand side was saturated with O_2. Then dema was added to the H_2-containing side and TfOH to the O_2-contaning side both to concentrations of 0.1 mol dm^{-3} and, after a voltammetric electrode cleaning step, a polarisation curve was recorded and is presented in Figure 7.9 (E). The OCP of the fuel cell containing both dema and TfOH (green polarisation curve), at ≈1.8 V, is double that of pure [dema][TfO] (red polarisation curve) and [dema][TfO] with either TfOH or dema added as a proton shuttle in Figure 7.2 (A), as predicted by the voltammetry in Figure 7.2 (C). The ohmic region beginning at 1.5 V from 0.05 mA cm^{-2} is over double that of [dema][TfO] containing either TfOH or dema which start at ≈0.7 V. This confirms that the fuel cell is operating according to Equation 15 and the electrochemical synthesis of [dema][TfO] is contributing to the E_{cell} above that of the reaction of H_2 and O_2.

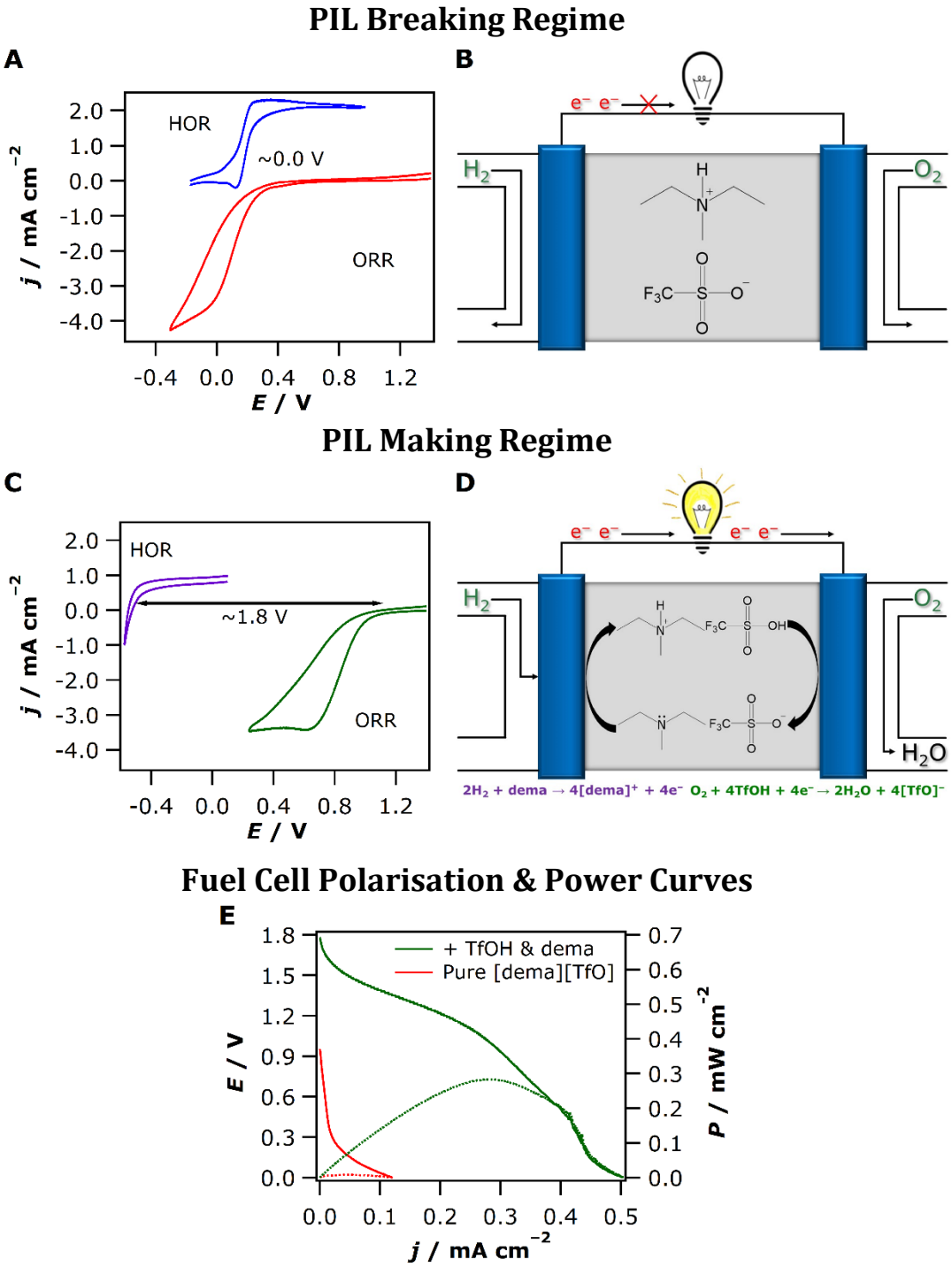


Figure 7.9 (A) HOR and ORR cyclic voltammograms of H_2- and O_2-saturated [dema][TfO] with (B) accompanying fuel cell schematic. (C) HOR and ORR cyclic voltammograms of H_2- and O_2-saturated [dema][TfO] containing 0.1 mol dm^{-3} dema (HOR) or TfOH (ORR) with (D) accompanying fuel cell schematic. Voltammograms were recorded using a 5-mm diameter Pt electrode rotating at 1,600 rpm and at 100 mV s^{-1}. (E) Fuel cell polarisation and associated power curves for a [dema][TfO]-electrolyte fuel cell and a [dema][TfO]-electrolyte fuel cell with a 0.1 mol dm^{-3} dema concentration at the anode (HOR) and 0.1 mol dm^{-3} TfOH at the cathode (ORR). Fuel cell polarisation curves recorded using a Grove-type fuel cell. The current was ramped at 0.25 μA s^{-1}. H_2 and O_2 were bubbled into the anolyte and catholyte, respectively, throughout the experiments and the electrolytes were stirred using magnetic stirrer bars rotating at 650 rpm.

The power curves (dotted lines) presented in Figure 7.9 (E) are intended to highlight the great disparity in fuel cell performance between pure [dema][TfO] and [dema][TfO] containing both dema and TfOH further. The maximum power of the acid and base [dema][TfO] fuel cell is ≈0.3 mW cm^{-2} which is approximately double the 0.12 and 0.16 mW cm^{-2} of [dema][TfO] containing either dema or TfOH respectively.

Using Equations 10, 11 and 16, and the method set out in Chapter 4, an approximation of the maximum E_{cell} from a [dema][TfO]-fuel cell containing added dema and TfOH with a mechanism as described in Equation 15, can be calculated. The combined $\Delta_r G$ of water formation (−474.260 kJ mol^{-1} O_2) and [dema][TfO] synthesis (−561.665 kJ mol^{-1} O_2) is 1035.925 kJ mol^{-1} O_2 which corresponds to an E_{cell} of 2.684 V. This is clearly significantly higher than the OCP of 1.8 V obtained from the green polarisation curve in Figure 7.9 (E), but the difference can likely be attributed to two reasons. Firstly, that the calculations likely only provide an approximation of the true ΔG value because pK_a is defined in terms of an aqueous system and not a PIL, and secondly, because of kinetic limitations that will likely play a part in reducing the experimentally-determined maximum E_{cell} value.

$$\Delta_r G^{\ominus}_{Total} = -nFE^{\ominus}_{cell} \qquad (16)$$

While the polarisation curves in Figure 7.9 (E) demonstrate that a doubling of cell potential is possible by adding both dema and TfOH to a [dema][TfO] electrolyte, the practicality of such system in an actual fuel cell is dubious at best given the chemical reaction that would occur between dema and TfOH eventually returning the PIL-electrolyte to the poor performance of pure [dema][TfO]. However, to see how long, given the H-cell setup, that the enhanced fuel cell performance would

last before complete acid-base neutralisation took place, the OCP was measured for ≈5 hours after an electrode cleaning step as previously described. During measurements both side of the cell were bubbled with their respective H_2 or O_2 gas and stirred with a stirrer bar rotating at 650 rpm likely increasing the rate of acid-base neutralisation. Figure 7.10 (A) shows the OCP dropping from round 1.7 V to ≈1.25 V after only 1 hour. Over the next four hours the OCP remained above the ≈1.0 V OCP recorded in pure [dema][TfO] (see OCP II. in Figure 7.10 (B)). This suggests that the added acid and base has mostly neutralised after 1 hour and the HOR and ORR has reverted back to Equations 1 and 2. However, it is more likely that an excess of TfOH still remains given the high volatility of dema, meaning a loss of dema from the system prior to neutralising with TfOH so that the ORR is likely described by Equation 7.

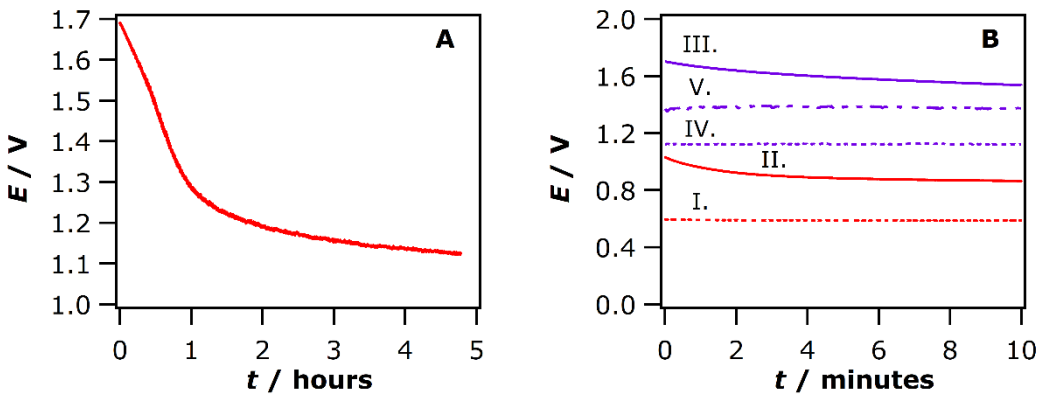


Figure 7.10 Open-circuit potential (OCP) measurements recorded at Pt-wire electrodes in a [dema][TfO] electrolyte in a Grove-type electrochemical cell. An electrochemical window CV was recorded prior to the OCP measurement to clean the surface of the Pt electrodes. (A) [dema][TfO] with an acidified cathode (0.1 mol dm^{-3} TfOH) and basified anode (0.1 mol dm^{-3} dema). (B) I. Pure [dema][TfO] without prior CV cleaning step. II. Pure [dema][TfO] with prior CV cleaning step. III. [dema][TfO] with an acidified cathode (0.1 mol dm^{-3} TfOH) and basified anode (0.1 mol dm^{-3} dema) with a prior CV cleaning step. IV. [dema][TfO] with an acidified cathode (0.1 mol dm^{-3} TfOH) and basified anode (0.1 mol dm^{-3} dema) approximately 5 hours after the addition of the acid and base, and without a prior CV cleaning step. V. see previous entry but after a CV electrode cleaning step.

Another explanation for the drop in OCP shown in Figure 7.10 (A) is demonstrated in Figure 7.10 (B) where after ≈5 hours the OCP has droped from III. (≈1.7 V) to IV. (1.1 V) but after another voltammetric electrode cleaning step, returns to ≈1.4 V in V. A likely cause of the drop in OCP of the acid/base fuel cell, as well as chemical neturalisation of dema and TfOH, is electrode passivation by dema which has been repeatedly demonstrated as sticking to glassy-carbon (GC) and Pt electrodes inhibiting their activity. The electrode-passivating effect of dema, aside from the need to add more PIL precursors as reacants, provides further challenges for the practical use of an acid/base PIL-based fuel cell.

7.4 Conclusions

Protic ionic liquid-based fuel-cells have been shown to be ineffective when a pure PIL electrolyte is used due to an insufficient proton-shuttling mechanism within the PIL. The poor performance of a pure [dema][TfO] electrolyte has been explained in terms of fundamental thermodynamics and experimental voltammetry (Equation 17). A characteristic fuel cell polarisation curve can be obtained but only when either the parent base (dema) or acid (TfOH) of the PIL has been added to facilitate proton-donor and -acceptor shuttling between the fuel-cell electrodes (see Equations 18 and 19 respectively). The conclusions from the experimental voltammetry investigating the effect of the presence of dema and TfOH on the fuel cell half reactions, HOR and ORR, respectively, have been proven correct, given the observations of the fuel-cell experiments. Also, the electrode-passivating effect of dema has been demonstrated, ruling out the addition of the highly volatile base as a solution needing an added proton shuttle for fuel-cell performance.

Furthermore, a 1.8 V OCP from a single H_2/O_2 fuel cell has been achieved and maintained above the conventional fuel-cell maximum OCP of 1.229 V for an hour by the addition of diethylmethylamine to the fuel-cell anode and triflic acid to the fuel-cell cathode, which confirms our understanding of the HOR and ORR mechanism in the presence or absence of added protic species (see Equation 20). The use of such a system is not practical however, given the volatility of the added dema and the competing reaction of chemical neutralisation by the fuel-cell species.

$$\text{Pure [dema][TfO]} \rightarrow \approx 0 \text{ V OCP} \quad (17)$$

$$\text{[dema][TfO] + dema (0.1 mol dm}^{-3}\text{)} \rightarrow \approx 1.0 \text{ V OCP} \quad (18)$$

$$\text{[dema][TfO] +TfOH (0.1 mol dm}^{-3}\text{)} \rightarrow \approx 1.0 \text{ V OCP} \quad (19)$$

$$\text{[dema][TfO] + dema + TfOH} \rightarrow \approx 1.8 \text{ V OCP} \quad (20)$$

The physical and electrochemical changes in [dema][TfO] after heating in the 'intermediate-temperature' regime have indicated that a temperature-induced shift in the PIL reaction equilibrium causes the decomposition of neutral dema and the presence of a protic contaminant which couples with the ORR. The thermal decomposition/oxidation of dema is likely responsible for the observed colour-change in [dema][TfO] upon heating and the protic contaminant is likely stable TfOH which forms hydronium and $[TfO]^-$ in the presence of water. The favourable fuel-cell performance observed by others at 150 °C[22] is therefore likely to be the result of protic contaminants either from the heating itself, or from overheating in the synthesis method[27] used to make [dema][TfO].

The use of pure PILs as fuel-cell electrolytes has been shown not to be viable because of the absence of a proton shuttling mechanism. The only way to achieve a viable PIL-based fuel-cell electrolyte is the addition of a protic species, either the parent acid or base, but this creates significant challenges. These challenges include finding a PIL electrolyte composition that is neither corrosive or volatile (at room temperature or elevated temperatures) while maintaining conductivity and a functional proton shuttling mechanism. The need for added protic species, and the resulting challenges, will likely remove some of the incentives for using PIL-based electrolytes for fuel cells.

7.5 References

1. *Hydrogen and Fuel Cells - A Vision for Our Future*; European Commission: Luxembourg, 2003.

2. Barbir, F. *PEM Fuel Cells Theory and Practice*. Second Edition; Elsevier: United States of America, 2013.

3. Stamenkovic, V. R.; Fowler, B.; Mun, B. S.; Wang, G.; Ross, P. N.; Lucas, C. A.; Markovic, N. M. Improved Oxygen Reduction Activity on $Pt_3Ni(111)$ via Increased Surface Site Availability. *Science (Washington, DC, U. S.)* **2007,** *315* (5811), 493-497.

4. Wee, J.-H.; Lee, K.-Y. Overview of the development of CO-tolerant anode electrocatalysts for proton-exchange membrane fuel cells. *J. Power Sources* **2006,** *157* (1), 128-135.

5. Borup, R.; Meyers, J.; Pivovar, B.; Kim, Y. S.; Mukundan, R.; Garland, N.; Myers, D.; Wilson, M.; Garzon, F.; Wood, D.; Zelenay, P.; More, K.; Stroh, K.; Zawodzinski, T.; Boncella, J.; McGrath, J. E.; Inaba, M.; Miyatake, K.; Hori, M.; Ota, K.; Ogumi, Z.; Miyata, S.; Nishikata, A.; Siroma, Z.; Uchimoto, Y.; Yasuda, K.; Kimijima, K.-i.; Iwashita, N. Scientific Aspects of Polymer Electrolyte Fuel Cell Durability and Degradation. *Chem. Rev.* **2007,** *107*, 3904-3951.

6. Adhikari, S.; Fernando, S. Hydrogen Membrane Separation Techniques. *Industrial & Engineering Chemistry Research* **2006,** *45*, 875-881.

7. Hinchliffe, A. B.; Porter, K. E. A Comparison of Membrane Separation and Distillation. *Chem. Eng. Res. Des.* **2000,** *78* (A2), 255-268.

8. Shao, M.; Chang, Q.; Dodelet, J. P.; Chenitz, R. Recent Advances in Electrocatalysts for Oxygen Reduction Reaction. *Chem. Rev.* **2016,** *116* (6), 3594-657.

9. Uemiya, S. Brief review of steam reforming using a metal membrane reactor. *Top. Catal.* **2004,** *29* (1-2), 79-84.

10. Park, M. J.; Choi, I.; Hong, J.; Kim, O. Polymer Electrolytes Integrated with Ionic Liquids for Future Electrochemical Devices. *J. Appl. Polym. Sci.* **2013,** *129* (5), 2363-2376.

11. Song, C.; Tang, Y.; Zhang, J. L.; Zhang, J.; Wang, H.; Shen, J.; McDermid, S.; Li, J.; Kozak, P. PEM fuel cell reaction kinetics in the temperature range of 23–120 °C. *Electrochim. Acta* **2007,** *52* (7), 2552-2561.

12. Chandan, A.; Hattenberger, M.; El-Kharouf, A.; Du, S.; Dhir, A.; Self, V.; Pollet, B. G.; Ingram, A.; Bujalski, W. High temperature (HT) polymer electrolyte membrane fuel cells (PEMFC)–A review. *J. Power Sources* **2013,** *231*, 264-278.

13. Cappadonia, M.; Erning, J. W.; Niaki, S. M. S.; Stimming, U. Conductance of Nafion 117 Membranes as a Function of Temperature and Water-Content. *Solid State Ionics* **1995,** *77*, 65-69.

14. Sone, Y.; Ekdunge, P.; Simonsson, D. Proton Conductivity of Nafion 117 as Measured by a Four-Electrode AC Impedance Method. *J. Electrochem. Soc.* **1996,** *143* (4), 1254-1259.

15. Hamilton, P. J.; Pollet, B. G. Polymer Electrolyte Membrane Fuel Cell (PEMFC) Flow Field Plate: Design, Materials and Characterisation. *Fuel Cells* **2010,** *10* (4), 489-509.

16. Savinell, R.; Yeager, E.; Tryk, D.; Landau, U.; Wainright, J.; Weng, D.; Lux, K.; Litt, M.; Rogers, C. A Polymer Electrolyte for Operation at Temperatures up to 200°C. *J. Electrochem. Soc.* **1994,** *141*, L46-L48.

17. Mack, F.; Heissler, S.; Laukenmann, R.; Zeis, R. Phosphoric acid distribution and its impact on the performance of polybenzimidazole membranes. *J. Power Sources* **2014,** *270*, 627-633.

18. Greaves, T. L.; Weerawardena, A.; Fong, C.; Krodkiewska, I.; Drummon, C. J. Protic Ionic Liquids: Solvents with Tunable Phase Behavior and Physicochemical Properties. *J. Phys. Chem. B* **2006,** *110*, 22479-22487.

19. Angell, C. A.; Byrne, N.; Belieres, J.-P. Parallel Developments in Aprotic and Protic Ionic Liquids: Physical Chemistry and Applications. *Acc. Chem. Res.* **2007,** *40* (11), 1228-1236.

20. Nakamoto, H.; Watanabe, M. Brønsted acid-base ionic liquids for fuel cell electrolytes. *Chem. Commun. (Cambridge, U. K.)* **2007,** (24), 2539-2541.

21. Lee, S.-Y.; Yasuda, T.; Watanabe, M. Fabrication of protic ionic liquid/sulfonated polyimide composite membranes for non-humidified fuel cells. *J. Power Sources* **2010,** *195* (18), 5909-5914.

22. Lee, S. Y.; Ogawa, A.; Kanno, M.; Nakamoto, H.; Yasuda, T.; Watanabe, M. Nonhumidified Intermediate Temperature Fuel Cells Using Protic Ionic Liquids. *J. Am. Chem. Soc.* **2010,** *132* (28), 9764-9773.

23. Noda, A.; Susan, M. A. B. H.; Kudo, K.; Mitsushima, S.; Hayamizu, K.; Watanabe, M. Brønsted Acid-Base Ionic Liquids as Proton-Conducting Nonaqueous Electrolytes. *J. Phys. Chem. B* **2003,** *107*, 4024-4033.

24. Susan, M. A. B. H.; Noda, A.; Mitsushima, S.; Watanabe, M. Brønsted acid–base ionic liquids and their use as new materials for anhydrous proton conductors. *Chem. Commun. (Cambridge, U. K.)* **2003**, 938–939.

25. Lawrence, S. A. *Amines: Synthesis, Properties and Applications*. Cambridge University Press: 2004.

26. Aleksandrov, A. L. Oxidation Of Amines By Molecular Oxygen. *Bull. Acad. Sci. USSR, Div. Chem. Sci. (Engl. Transl.)* **1980,** *29* (11), 1740-1744.

27. Goodwin, S. E.; Smith, D. E.; Gibson, J. S.; Jones, R. G.; Walsh, D. A. Electroanalysis of Neutral Precursors in Protic Ionic Liquids and Synthesis of High-Ionicity Ionic Liquids. *Langmuir* **2017,** *33* (34), 8436–8446.

28. Johnson, L.; Ejigu, A.; Licence, P.; Walsh, D. A. Hydrogen Oxidation and Oxygen Reduction at Platinum in Protic Ionic Liquids. *J. Phys. Chem. C* **2012,** *116*, 18048–18056.

8 Final Conclusions and Future Outlook

8.1 Final Conclusions

Electrocatalytic reactions pertinent to energy conversion devices have been studied in protic and aprotic ionic liquids. In the protic ionic liquids (PILs) diethylmethylammonium trifluoromethanesulfonate ([dema][TfO]) and diethylmethylammonium bis(trifluoromethanesulfonyl)imide ([dema][NTf_2]), the oxygen-reduction reaction (ORR) shifted to significantly more positive potentials (up to 0.9 V more positive) upon the addition of increasingly strong acids (by aqueous pK_a). The ORR half-wave potential ($E_{½}$) shifted positive by ≈50 mV per pK_a unit in [dema][TfO], close to what would be expected in aqueous systems. A positive shift in ORR potential upon the addition of a strong acid was also observed in the aprotic ionic liquid (AIL) 1-butyl,1-methyl pyrrolidinium bis(trifluoromethanesulfonyl)imide ([pyrr][NTf_2]).

The addition of a strong base, diethylmethylamine (dema), to [dema][TfO], caused a negative shift (≈0.9 V) in the hydrogen-oxidation reaction (HOR) onset potential. The shifts positive and negative of the ORR and HOR respectively, as a result of the added proton-donating/accepting species, are caused by a fundamental change in the mechanisms of these reactions. Where a strong acid is present, the ORR will be acid-coupled, where a strong base is present the HOR will be base-coupled – both confer thermodynamic advantages as they provide ORR and HOR mechanisms that do not involve the destruction of the electrochemically- and thermodynamically-stable PIL.

The electrochemical stability of high-ionicity PILs (with a ΔpK_a greater than 10 between parent acid and cation) makes them unsuitable for use as fuel cell electrolytes, without the addition of a protic species. This was confirmed by fuel-cell testing where the recorded polarisation curves in pure [dema][TfO] rapidly dropped to 0 V once current density was applied. The polarisation curves recorded in [dema][TfO] containing either 0.1 mol dm^{-3} trifluoromethanesulfonic acid (TfOH) or 0.1 mol dm^{-3} dema, however, were characteristic of a functioning H_2/O_2 fuel cell. The reason for the negligible performance of the pure [dema][TfO] fuel cell is a lack of a viable proton-shuttling mechanism. When TfOH is present, the $[TfO]^-$/TfOH shuttle is in effect; when dema is present, the dema/$[dema]^+$ proton shuttle is in effect, allowing the reaction to proceed galvanically.[1] In the absence of both added acid and base, there is no thermodynamic driving force for H_2 to be oxidised onto the very poor base, $[TfO]^-$, or for O_2 to be reduced with the very poor acid $[dema]^+$ – the driving force for the reaction of O_2 and H_2 to make H_2O (1.229 V) is entirely offset by the energy required to protonate a very poor base ($[TfO]^-$) and deprotonate a very weak acid ($[dema]^+$). The fuel-cell test observations are supported by voltammetric measurements which show the HOR and ORR in pure [dema][[TfO] occurring at approximately the same potential – no driving force is provided for the overall reaction.

Given the favourable fuel-cell performance of [dema][TfO] as an electrolyte at elevated temperatures, it was hypothesised that some TfOH/protic species must be present.[2] It was previously found that the PIL synthesis method used can result in non-stoichiometric PILs with an excess of parent acid (TfOH) up to ≈0.2 mol dm^{-3}.[3] In cases where the temperature of the highly exothermic

neutralisation reaction is not adequately controlled, base can either evaporate, or more likely, thermally decompose before reacting, resulting in an excess of acid (TfOH in the case [dema][TfO]). However, by studying the ORR in 'pure' [dema][TfO] and [dema][TfO] heated to 150 °C for 63 hours, the same temperature that favourable fuel-cell performance was reported, and also the temperature at which the PIL was dried under vacuum by Watanabe and co-workers, it was found that a protic species is generated and the PIL discoloured.[2] This is strong evidence that the PIL-synthesis equilibrium moves to produce parent acid and base at 150 °C, with the base then thermally decomposing to produce a red/brown chromophore and excess TfOH, which remains in the PIL. The TfOH produced then either takes part in the ORR, shifting it to a more positive potential or, if water is present, dissociates to form H_3O^+ which itself can couple with the ORR also shifting it to a more positive potential. Although amines are well known to become yellow/red/brown upon oxidation, the exact chemical identity of the chromophore could not be identified using spectroscopic methods. Colour in PILs could however be a likely indication of whether protic impurities are present. It is most likely therefore that any favourable fuel-cell performance at elevated temperatures is a result of protic species generated at those temperatures providing a viable proton shuttling mechanism.

Our understanding of the proton-shutting mechanisms and thermodynamics of PIL-fuel cell reactions was confirmed by the addition of dema and TfOH to the anode and cathode sides respectively, of a [dema][TfO]-electrolyte fuel cell and an open circuit potential (OCP) of 1.8 V being observed as was predicted by voltammetric experiments. In this instance the driving force for PIL synthesis is

added to the driving force for water formation. It would be impractical to use the acid and base system in a device due to uncontrolled chemical neutralisation resulting in PIL synthesis, and because the acid and base, along with H_2, would be consumed as fuel for the reaction. However, it demonstrates a system whereby an H_2/O_2 fuel cell can generate nearly double the cell voltage of a conventional aqueous system, and could be the basis for research into new IL electrolytes that can make use of this effect.

An investigation into the use of formic acid and the direct formic acid oxidation (FAO) reaction as a test reaction for basicity in PILs, was conducted by adding bases of different strengths and observing the change in oxidation peak magnitude. Formate was confirmed as the active species in direct FAO as the addition of dema to [dema][TfO] yielded a greater FAO peak height as a greater concentration of formate was present. Unfortunately, the addition of the other bases, pyridine, imidazole, thiazole caused a passivating effect of the Pt electrode which prevented FAO from being observed. Voltammetric studies of water oxidation in the PIL [dema][TfO] however, did provide insight with oxygen being evolved at potentials greater than 2.2 V (versus Pd-H) and the confirmation of a protic species (likely TfOH) being adsorbed onto Pt at high potentials.

The presence of acids and bases in PILs have a critical effect on the electrocatalysis of O_2, H_2 and HCOOH and the origins of such species are of great importance for synthetic and analytical chemists. Furthermore, the effect of these protic species on fuel-cell reactions in particular, is the crux on which PILs can be used effectively as fuel-cell electrolytes with a viable proton shuttling mechanism available only when acid or base are present. The need for non-volatile protic additives in PIL

electrolytes creates challenges, corrosion etc., that these electrolytes were thought to have avoided. However, with greater understanding of the thermodynamics of the ORR and HOR in PILs, and how cell potential can be manipulated by design, new ILs that use this knowledge could lead to a new class of high-performing IL-based fuel-cell electrolytes.

8.2 Future Work

Given the promising results of a PIL-based fuel cell containing both strong acid and base providing an OCP of ≈1.8 V, at Pt electrodes, it would be of interest to see if this performance could be replicated using non-noble metals or even a carbon cathode for the ORR.

Similarly, if an IL could be synthesised such that it had a strongly acidic proton on a quaternary ammonium cation that would couple to the ORR, no added acid or base would be required to achieve a viable proton shuttling mechanism. Also, if an IL could be synthesised that had a weakly acidic proton on a quaternary ammonium cation and a weakly basic site on the anion, it is possible that more facile proton transport could be achieved as well as some of the thermodynamic advantages of the added acid and base system (see Figure 8.1). While the hypothetical IL in Figure 8.1 might well exist as a dication and dianion at room temperature, at elevated temperatures the proton equilibrium may shift to form the cationic carboxylic acid and anionic amine, lowing the energy for proton hopping and possibly shifting the HOR to negative potentials and ORR to positive potentials. The synthesis of acidic PIL-based electrolyte membranes is also of interest.

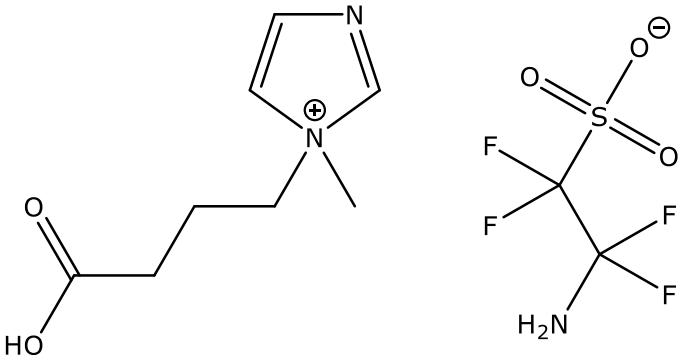


Figure 8.1 Schematic of hypothetical ionic liquid with extra acidic and basic sites.

Determining the exact nature of the protic species made when heating PILs for extended periods would be beneficial, as would identification of the chromophoric species. This work would provide more evidence for the PIL synthesis equilibrium shifting to produce more parent acid and base at elevated temperatures.

Another area of interest is identifying bases over a wide pK_a (conjugate acid) range that do not passivate Pt electrodes. This would allow the FAO reaction to be studied in the presence of those bases to assess basicity voltammetrically in PILs, by comparing the magnitude of the direct formate oxidation current with the pK_a of the added base (conjugate acid). Furthermore, electrospectroscopic experiments to determine reaction intermediates of FAO in PILs would be of great interest.

Finally, since the effect of acids and bases on fuel-cell reactions is now much better understood, it would be of great interest to see how the presence of protic and basic species affect water splitting in PILs as one would expect to observe a similar thermodynamic effect as in fuel cells.

8.3 References

1. Smith, D. E.; Walsh, D. A. The Nature of Proton Shuttling in Protic Ionic Liquid Fuel Cells. *Adv. Energy Mater.* **2019,** *9* (24).

2. Lee, S. Y.; Ogawa, A.; Kanno, M.; Nakamoto, H.; Yasuda, T.; Watanabe, M. Nonhumidified Intermediate Temperature Fuel Cells Using Protic Ionic Liquids. *J. Am. Chem. Soc.* **2010,** *132* (28), 9764-9773.

3. Goodwin, S. E.; Smith, D. E.; Gibson, J. S.; Jones, R. G.; Walsh, D. A. Electroanalysis of Neutral Precursors in Protic Ionic Liquids and Synthesis of High-Ionicity Ionic Liquids. *Langmuir* **2017,** *33* (34), 8436−8446.

Appendix I: Supplementary Characterisation Data

1.1 Nuclear Magnetic Resonance Spectroscopy of Ionic Liquids

1.1.1 Diethylmethylammonium trifluoromethanesulfonate ([dema][TfO])

A ^{1}H NMR spectrum of [dema][TfO] and [dema][TfO] containing 0.1 mol dm^{-3} triflic acid is presented in Figure A1 and A2, respectively. The peaks, peak assignments and splitting patterns are consistent with those in the literature.[1,2,3,4]

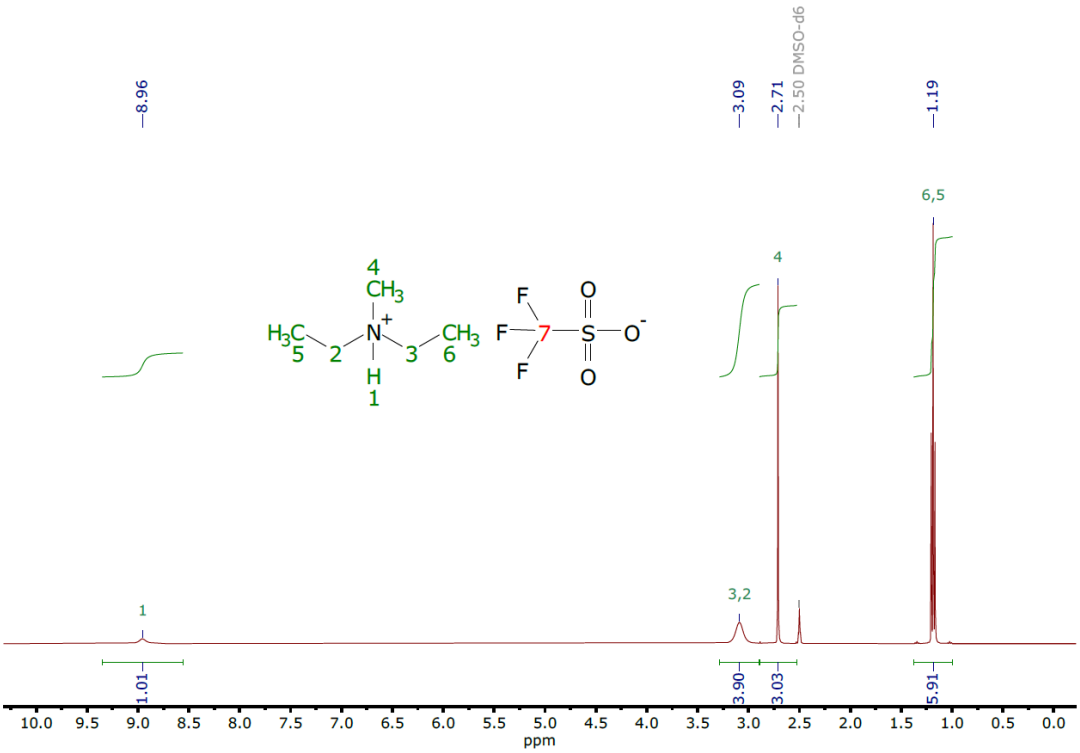


Figure A1 ^{1}H NMR spectrum of [dema][TfO] containing 11.7 ppm H_2O.

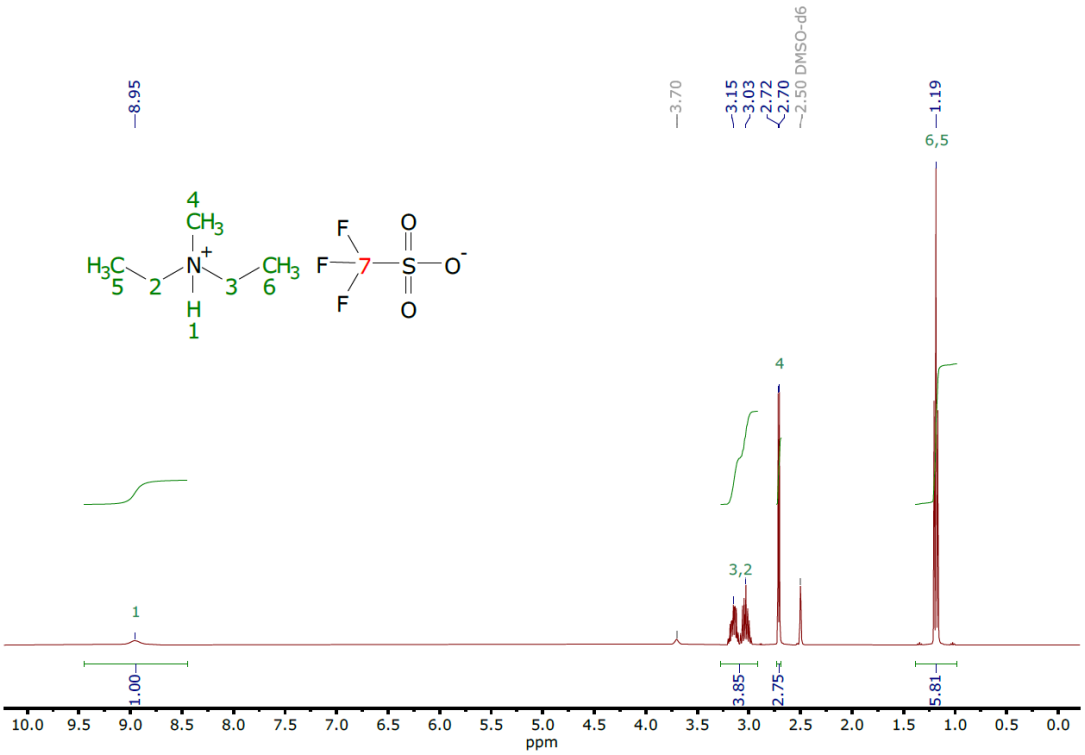


Figure A2 ^{1}H NMR spectrum of [dema][TfO] containing 0.1 mol dm^{-3} triflic acid.

^{13}C NMR spectra of [dema][TfO] and [dema][TfO] containing 0.1 mol dm^{-3} triflic acid are presented in Figure A3 and Figure A4, respectively. The peaks, peak assignments and splitting patterns are consistent with those in the literature.[5]

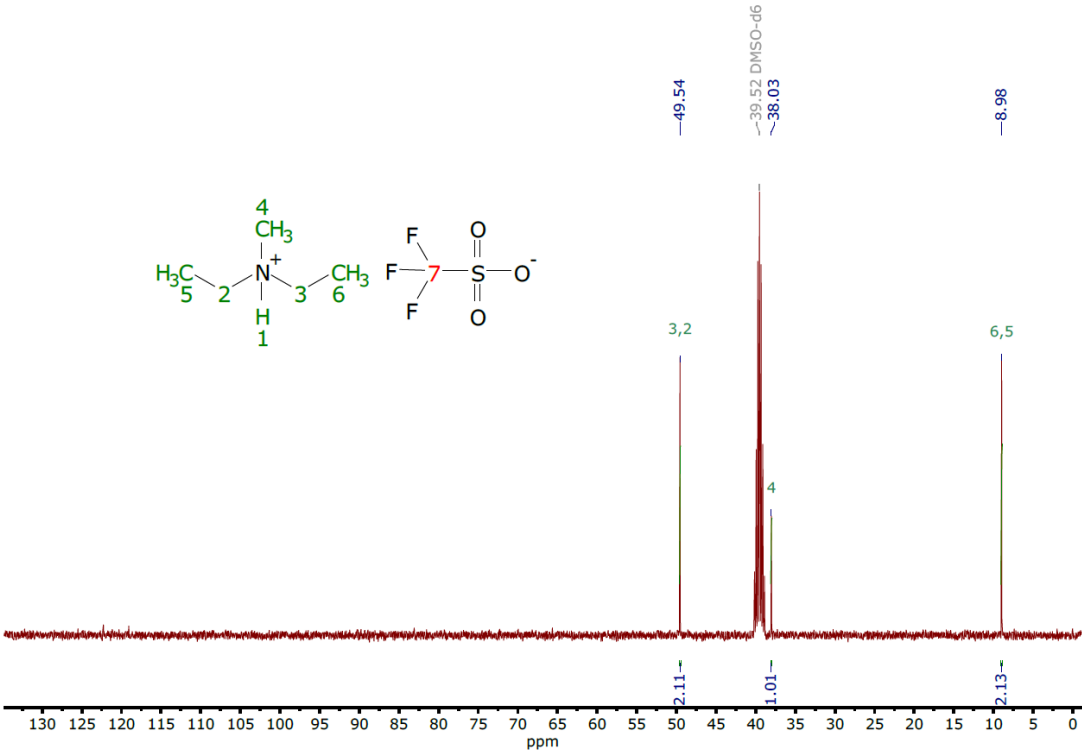


Figure A3 ^{13}C NMR spectrum of [dema][TfO] containing 11.7 ppm H_2O.

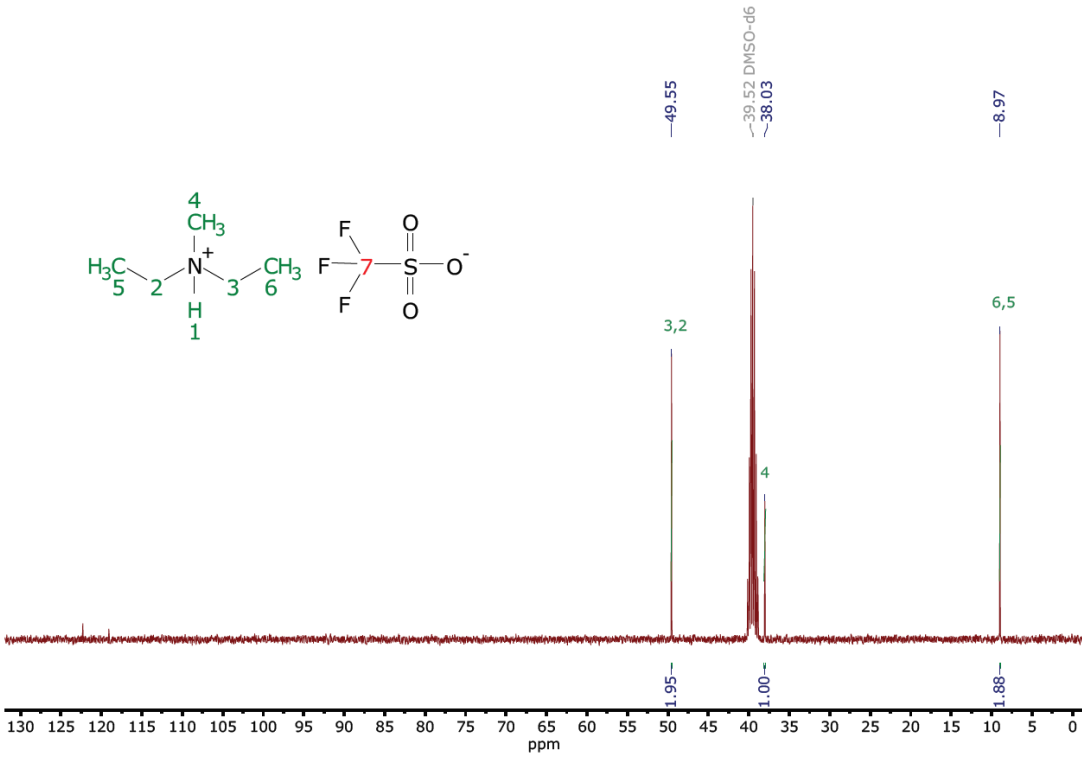


Figure A4 ^{13}C NMR spectrum of [dema][TfO] containing 0.1 mol dm^{-3} triflic acid.

^{19}F NMR spectra of [dema][TfO] and [dema][TfO] containing 0.1 mol dm^{-3} triflic acid are presented in Figure A5 and Figure A6, respectively. The single peak at δ = −77.77 is due to the presence of the [TfO]$^-$ anion in all ILs used in this study.

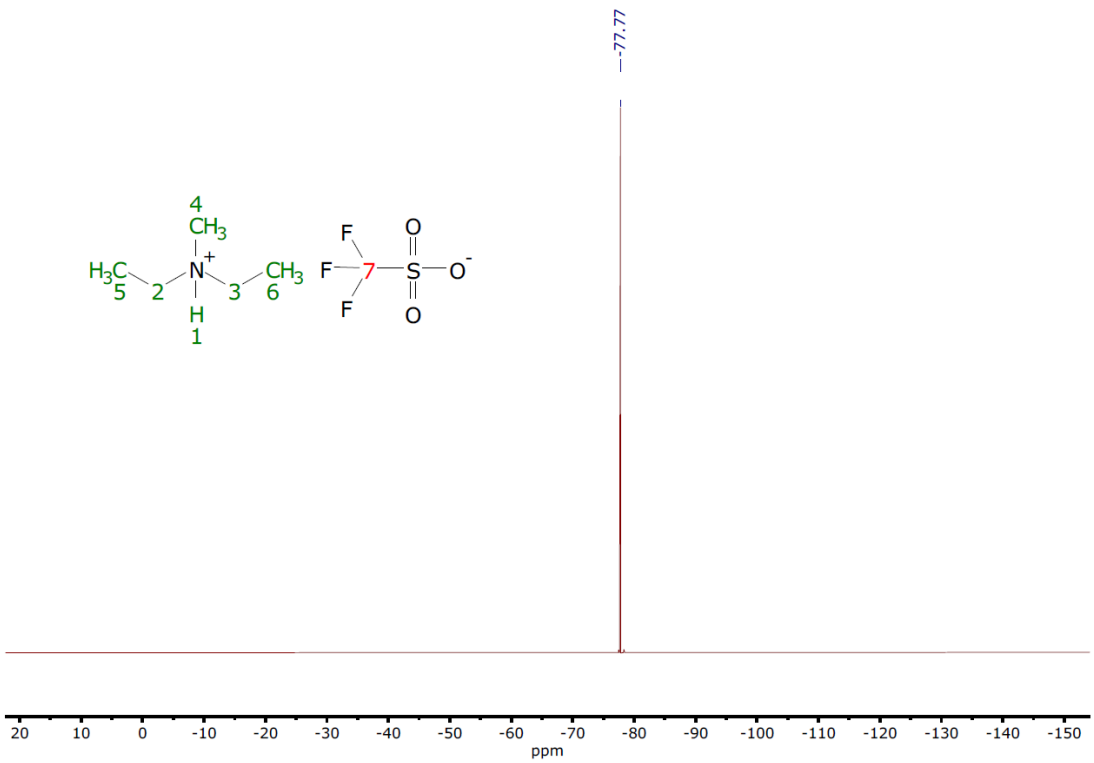


Figure A5 ^{19}F NMR spectrum of [dema][TfO] containing 11.7 ppm H_2O.

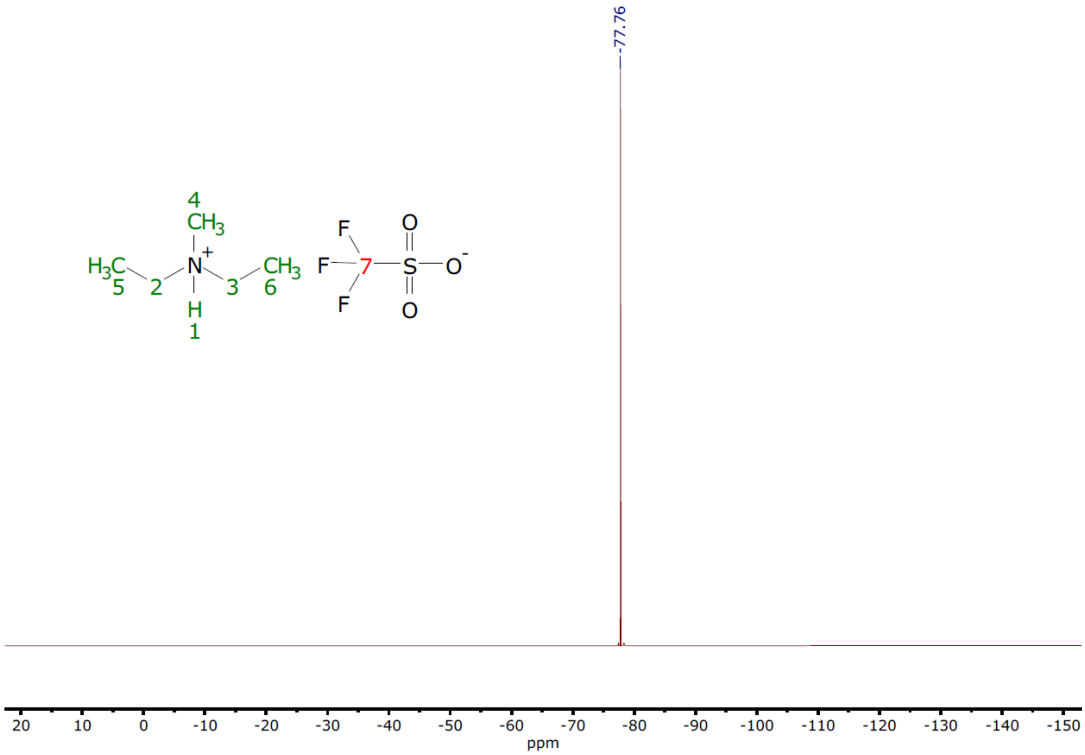


Figure A6 ^{19}F NMR spectrum of [dema][TfO] containing 0.1 mol dm^{-3} triflic acid.

1.1.2 Diethylmethylammonium bis(trifluoromethanesulfonyl)imide ([dema][NTf$_2$])

^{1}H, ^{13}C, and ^{19}F NMR spectra of [dema][NTf$_2$] are presented in Figure A7, Figure A8, and Figure A9, respectively. The peaks, peak assignments and splitting patterns are consistent with literature and the other ionic liquids used in this study.[1] The single 19F peak at δ = −78.72 is consistent with the [NTf$_2$]$^-$ anion in [pyrr][NTf$_2$], [N8888 NTf$_2$] and [P8888][NTf$_2$], also used in this study.

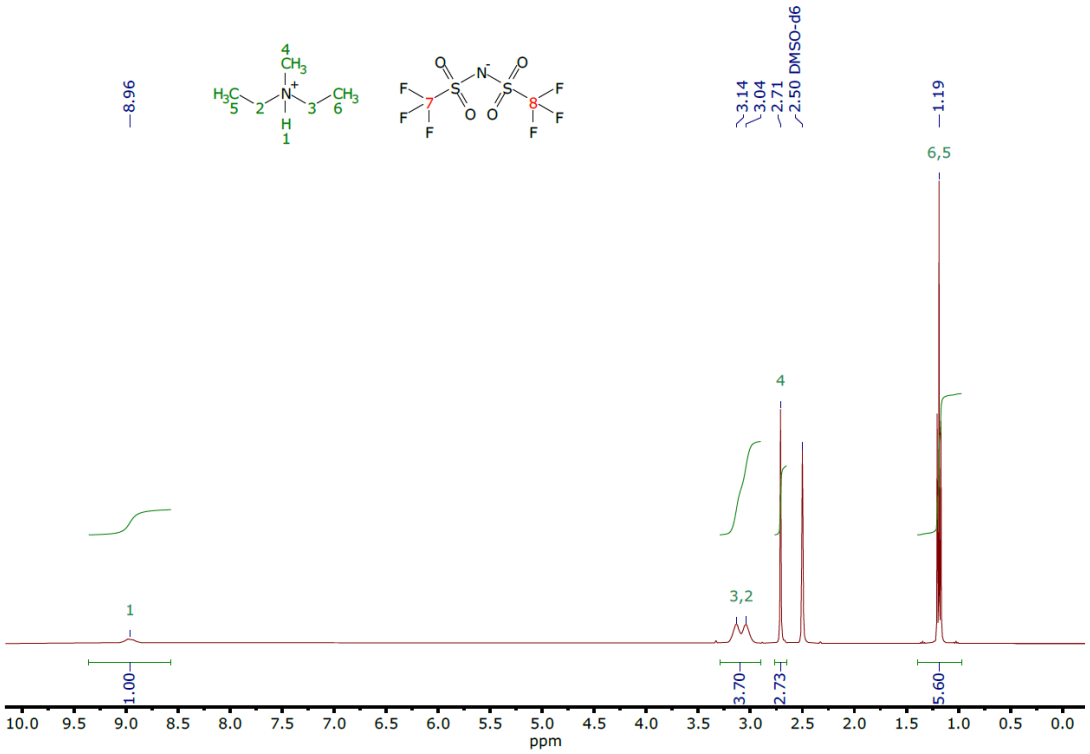


Figure A7 ^{1}H NMR spectrum of [dema][NTf_2] containing 187.8 ppm H_2O.

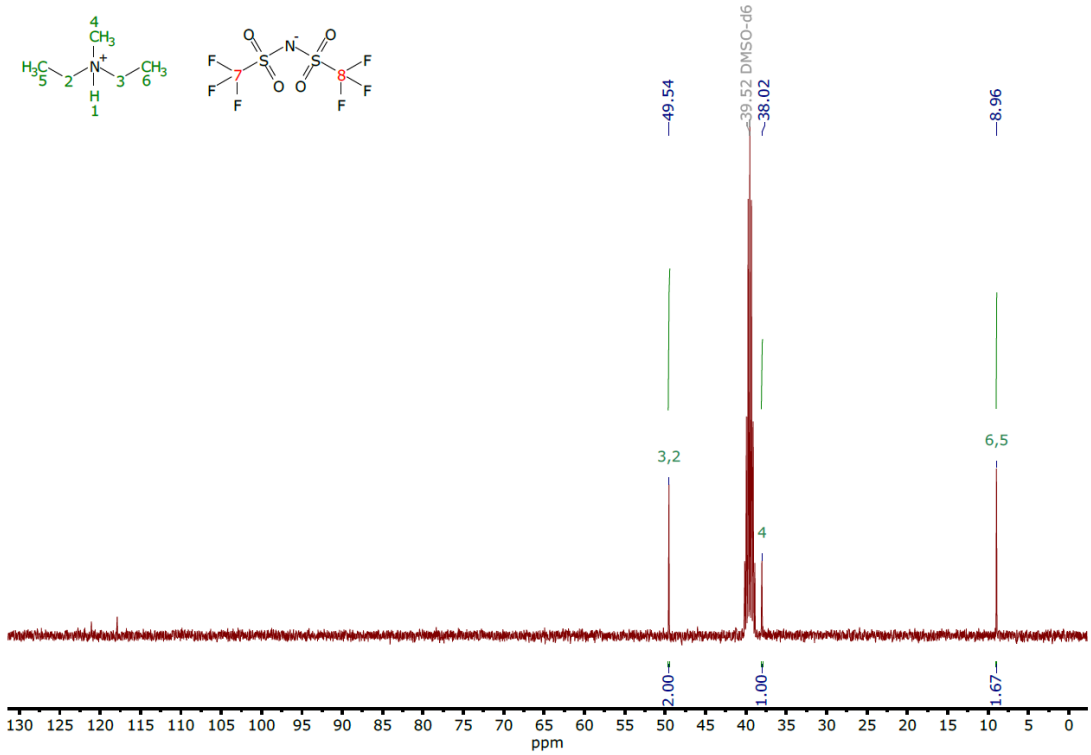


Figure A8 ^{13}C NMR spectrum of [dema][NTf_2] containing 187.8 ppm H_2O.

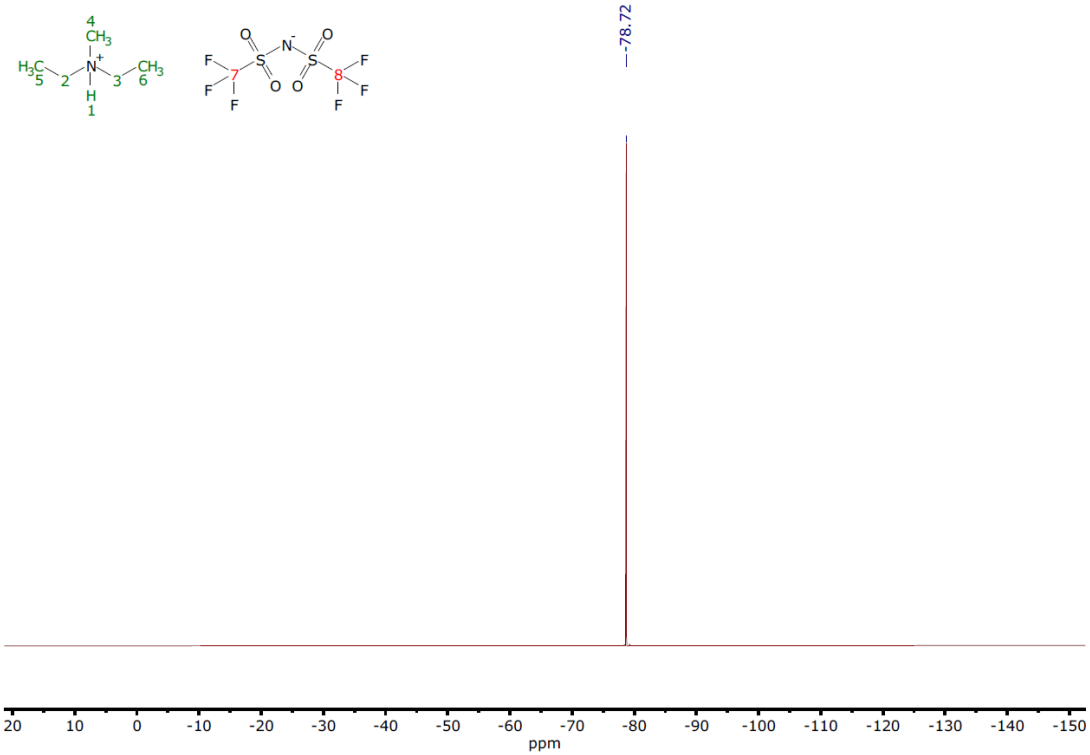


Figure A9 ^{19}F NMR spectrum of [dema][NTf_2] containing 187.8 ppm H_2O.

1.1.3 Dimethylbutylammonium trifluoromethanesulfonate ([dmba][TfO])

^{1}H, ^{13}C, and ^{19}F NMR spectroscopy of [dmba][TfO] is presented in Figure A10, Figure A11, and Figure A12, respectively. The peaks, peak assignments and splitting patterns are consistent with literature and the other ionic liquids used in this study.[2]

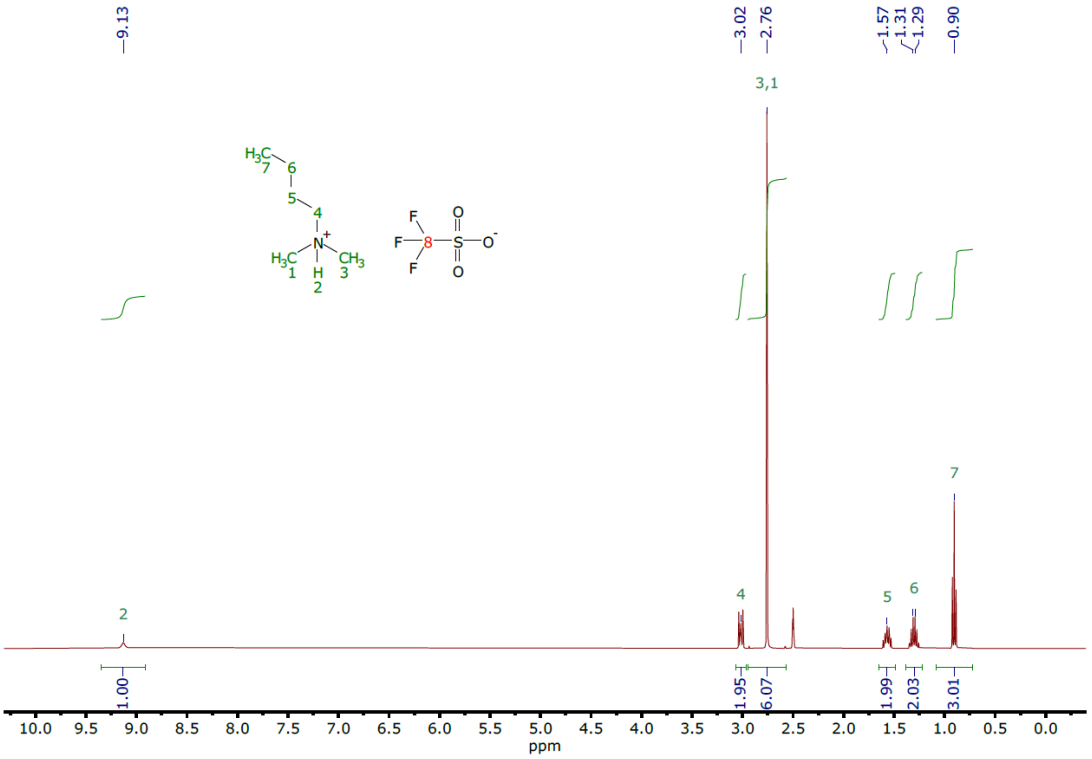


Figure A10 ^{1}H NMR spectrum of [dmba][TfO] containing 16.4 ppm H_2O.

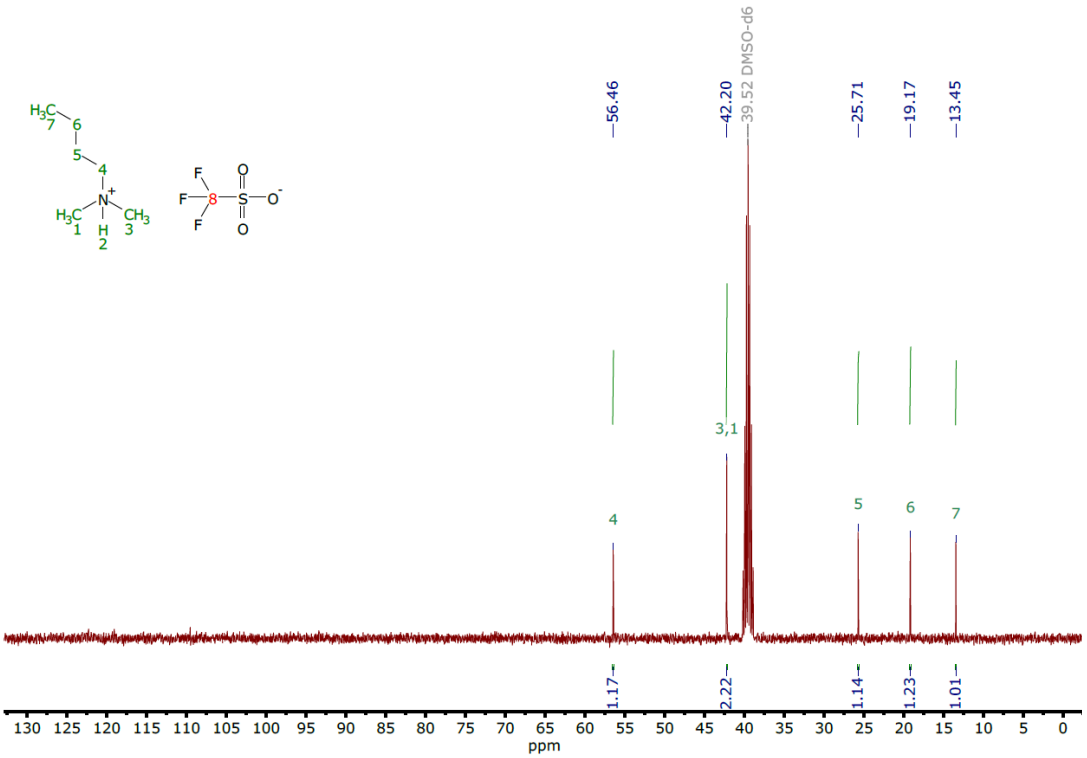


Figure A11 ^{13}C NMR spectrum of [dmba][TfO] containing 16.4 ppm H_2O.

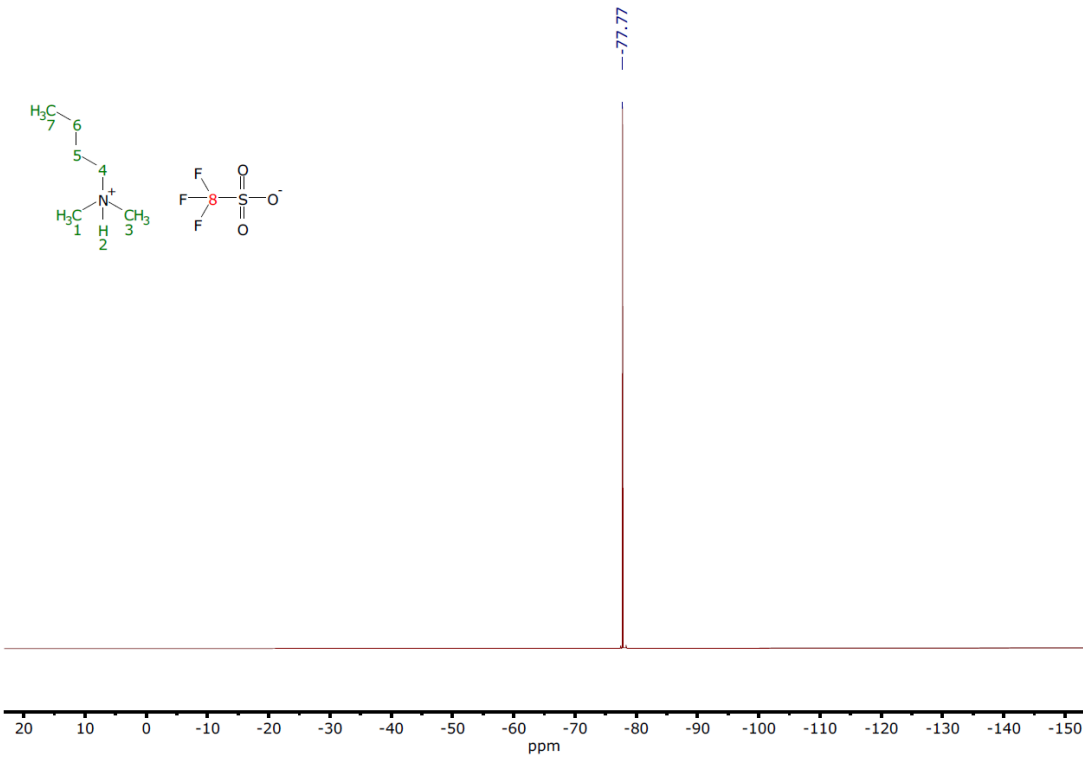


Figure A12 ^{19}F NMR spectrum of [dmba][TfO] containing 16.4 ppm H_2O.

1.1.4 Triethylammonium trifluoromethanesulfonate ([tea][TfAc])

^{1}H, ^{13}C, and ^{19}F NMR spectra of [tea][TfAc] are presented in Figure A13, Figure A14, and Figure A15, respectively. The peaks, peak assignments and splitting patterns are consistent with literature and the other ionic liquids used in this study.[2]

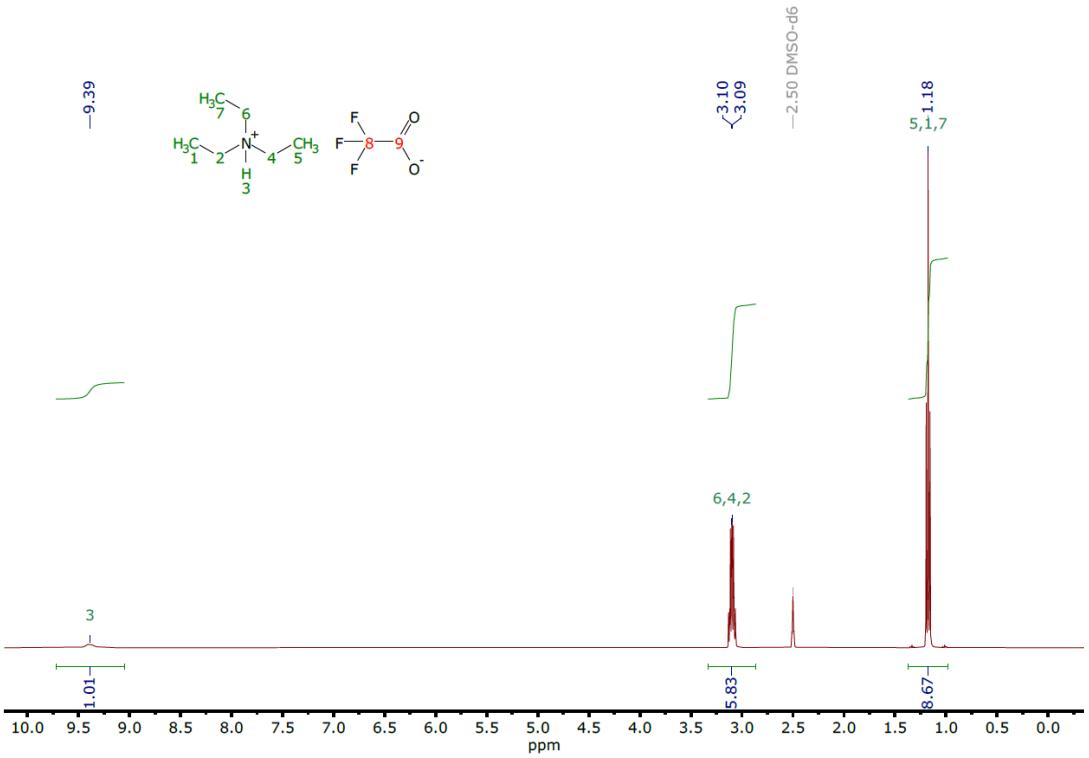


Figure A13 ^{1}H NMR spectrum of [tea][TfAc] containing 1896.2 ppm H_2O.

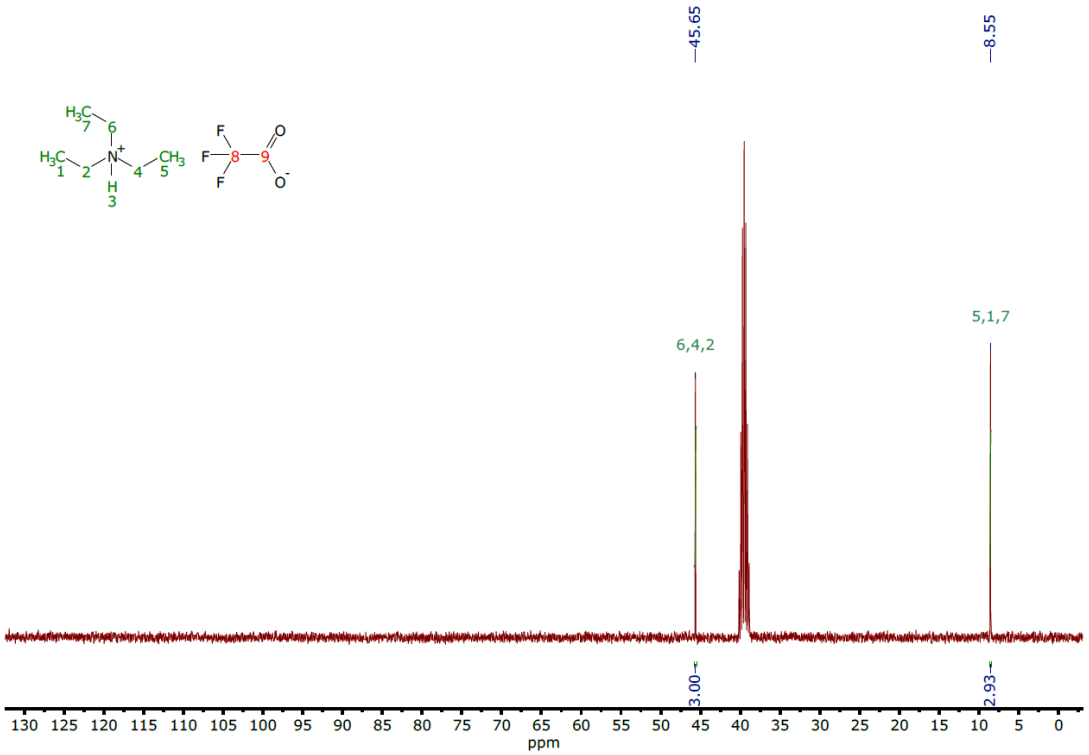


Figure A14 ^{13}C NMR spectrum of [tea][TfAc] containing 1896.2 ppm H_2O.

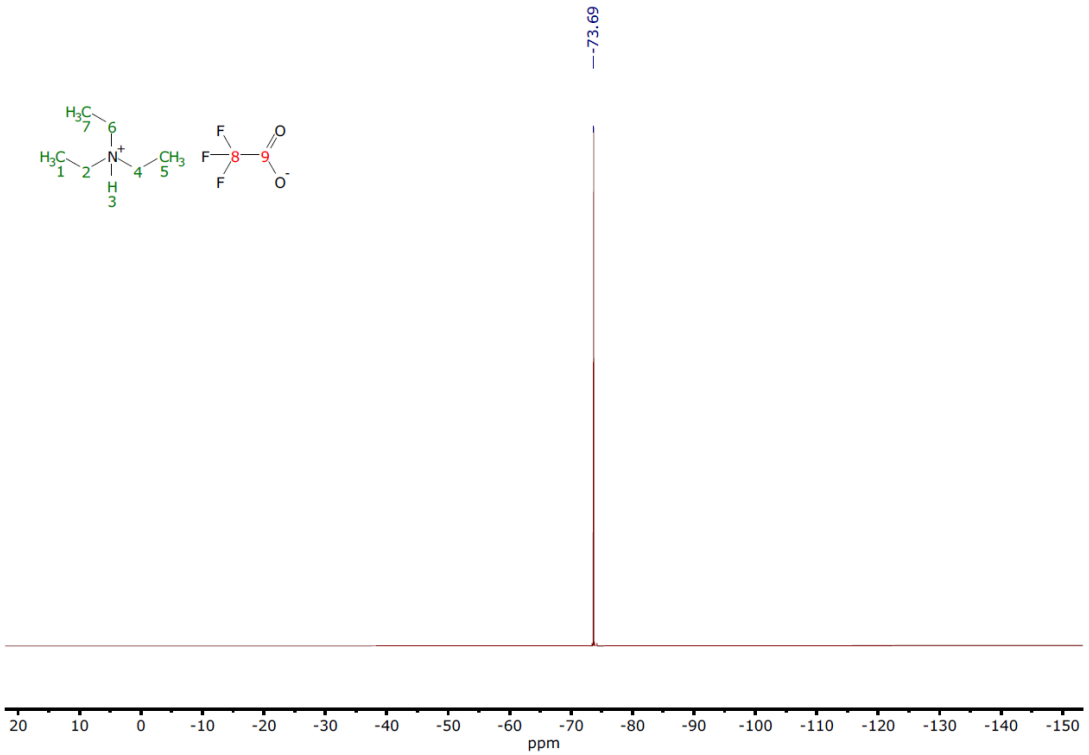


Figure A15 ^{19}F NMR spectrum of [tea][TfAc] containing 1896.2 ppm H_2O.

1.1.5 1-methyl 1-butyl pyrrolidinium bis(trifluoromethanesulfonyl)imide ([pyrr][NTf$_2$])

^{1}H, ^{13}C, and ^{19}F NMR spectra of [pyrr][NTf$_2$] are presented in Figure A16, Figure A17, Figure A18, respectively.

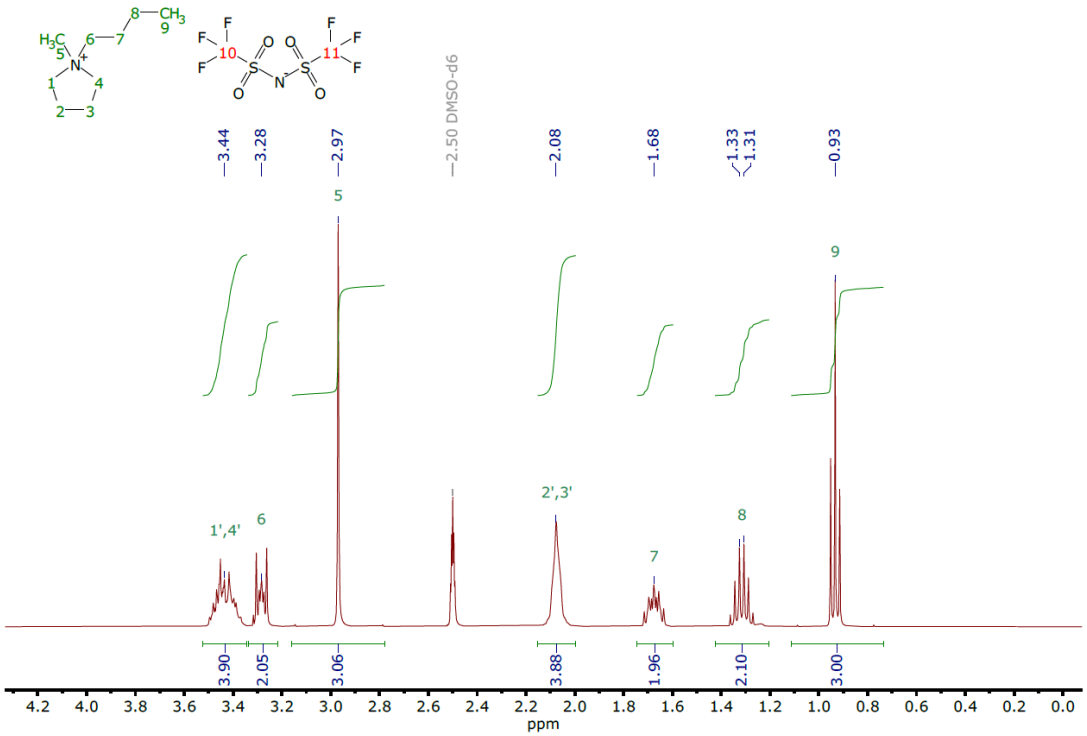


Figure A16 ^{1}H NMR spectrum of [pyrr][NTf$_2$] containing 146.3 ppm H_2O.

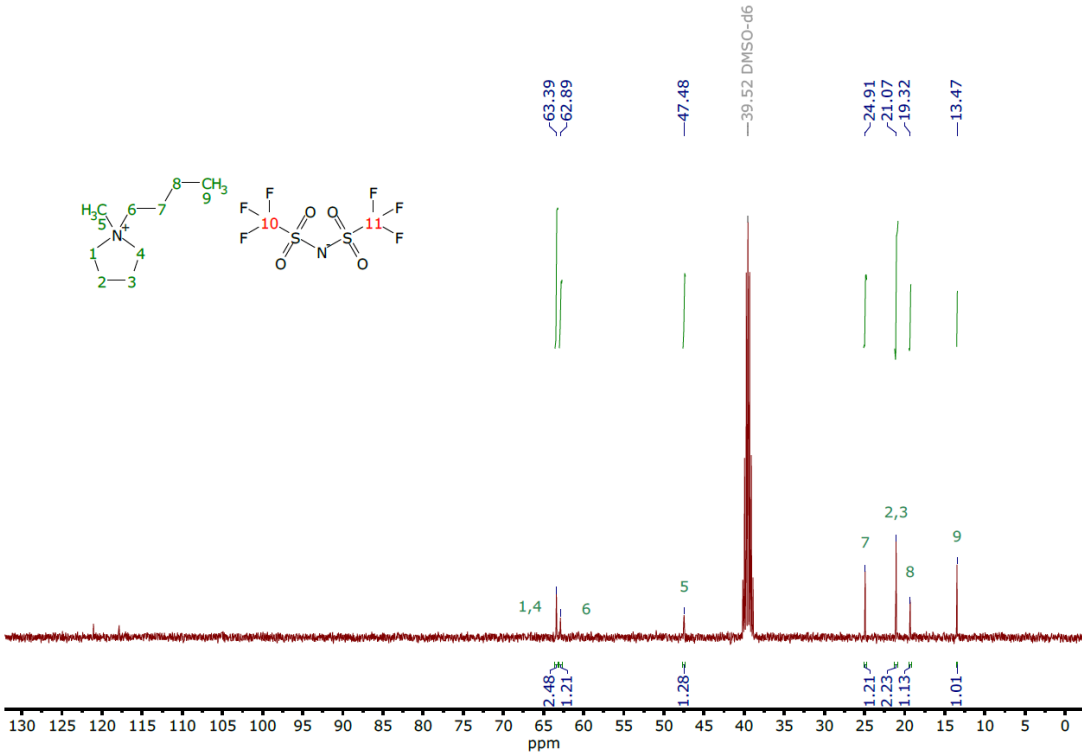


Figure A17 ^{13}C NMR spectrum of [pyrr][NTf_2] containing 146.3 ppm H_2O.

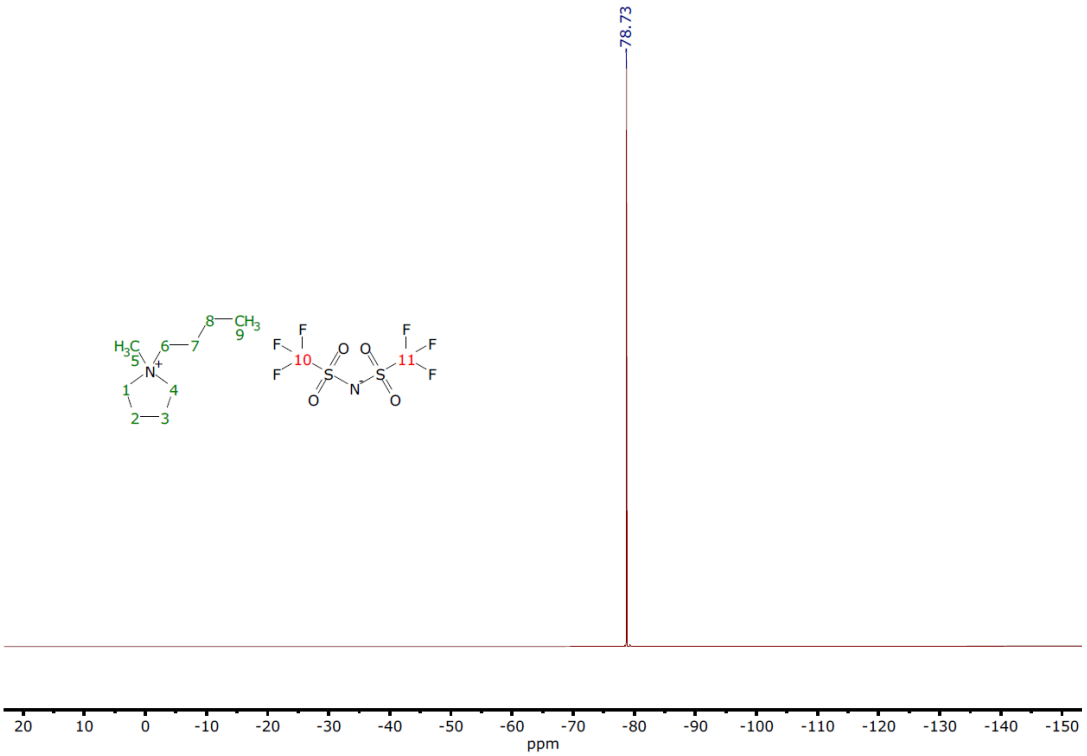


Figure A18 ^{19}F NMR spectrum of [pyrr][NTf_2] containing 146.3 ppm H_2O.

1.1.6 Tetraoctylammonium bis(trifluoromethanesulfonyl)imide ([N8888][NTf$_2$])

^{1}H, ^{13}C, and ^{19}F NMR spectra of [N8888][NTf$_2$] are presented in Figure A19, Figure A20, and Figure A21, respectively.

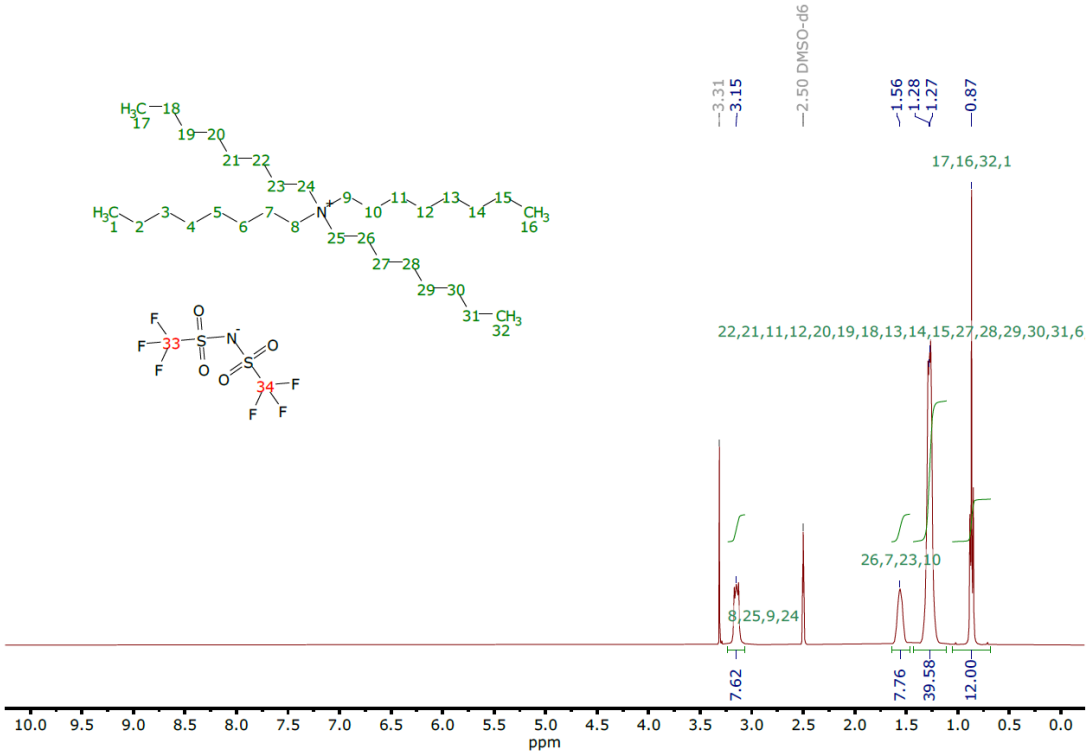


Figure A19 ^{1}H NMR spectrum of [N8888][NTf$_2$].

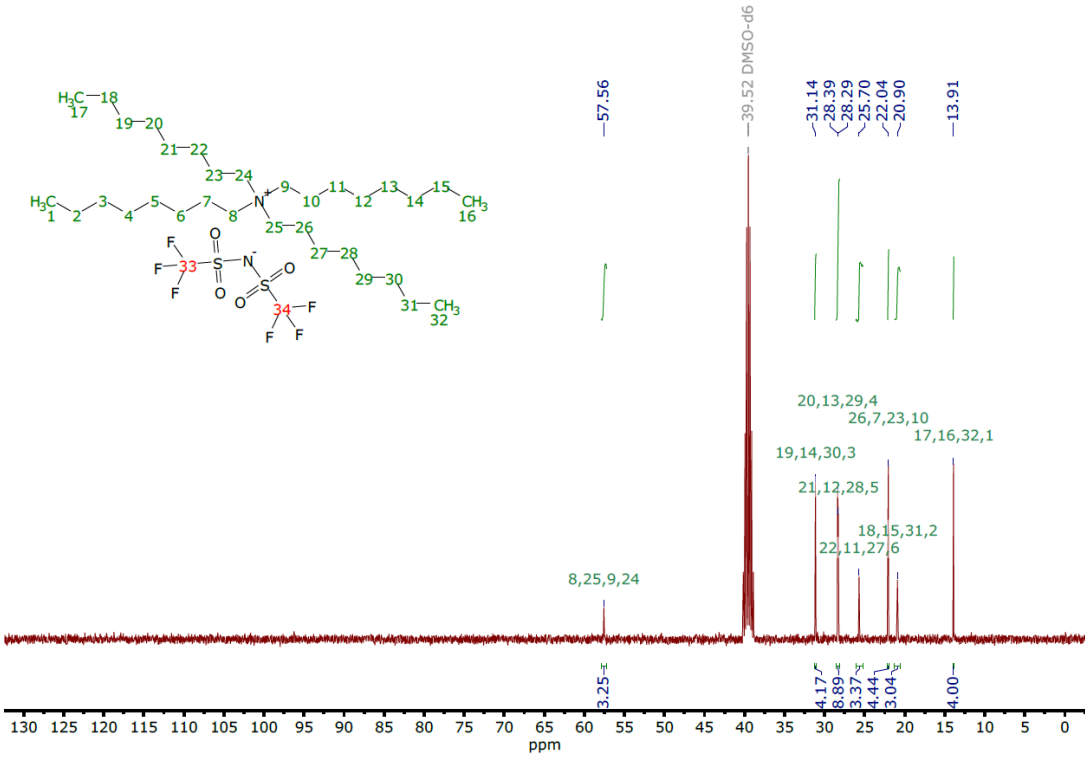


Figure A20 ^{13}C NMR spectrum of [N8888][NTf_2].

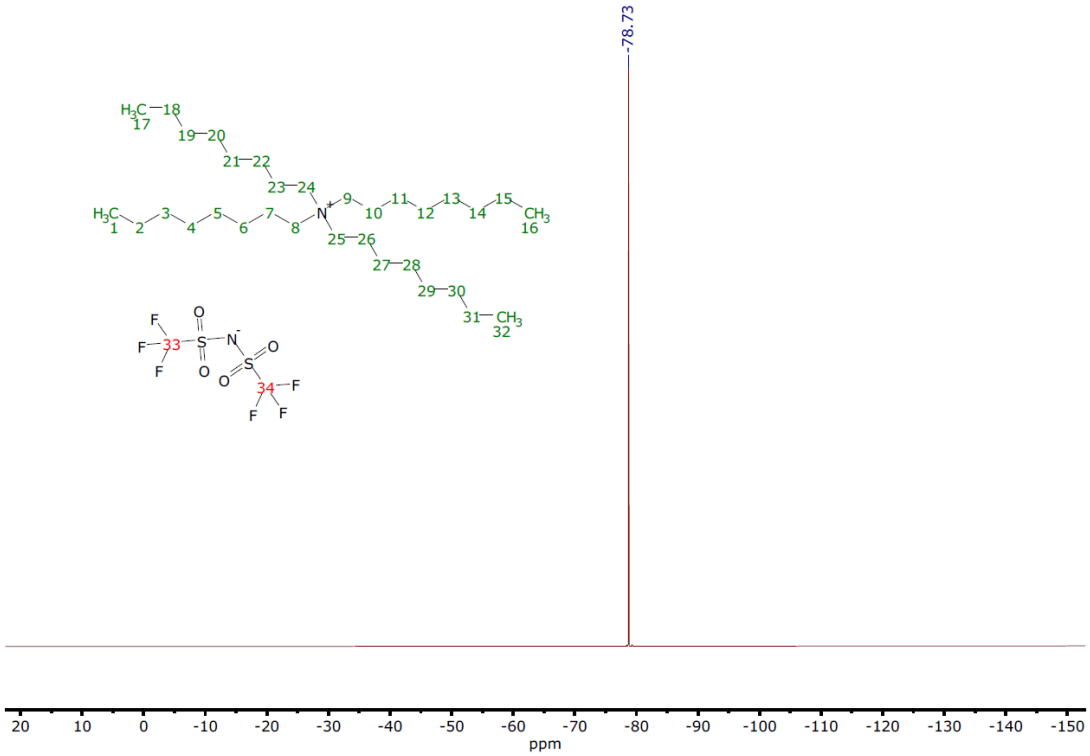


Figure A21 ^{19}F NMR spectrum of [N8888][NTf_2].

1.1.7 Tetraoctylphosphonium bis(trifluoromethanesulfonyl)imide ([P8888][NTf$_2$])

^{1}H, ^{13}C, and ^{19}F NMR spectra of [P8888][NTf$_2$] are presented in Figure A22, Figure A23, and Figure A24, respectively and are comparable to the published literature.[6]

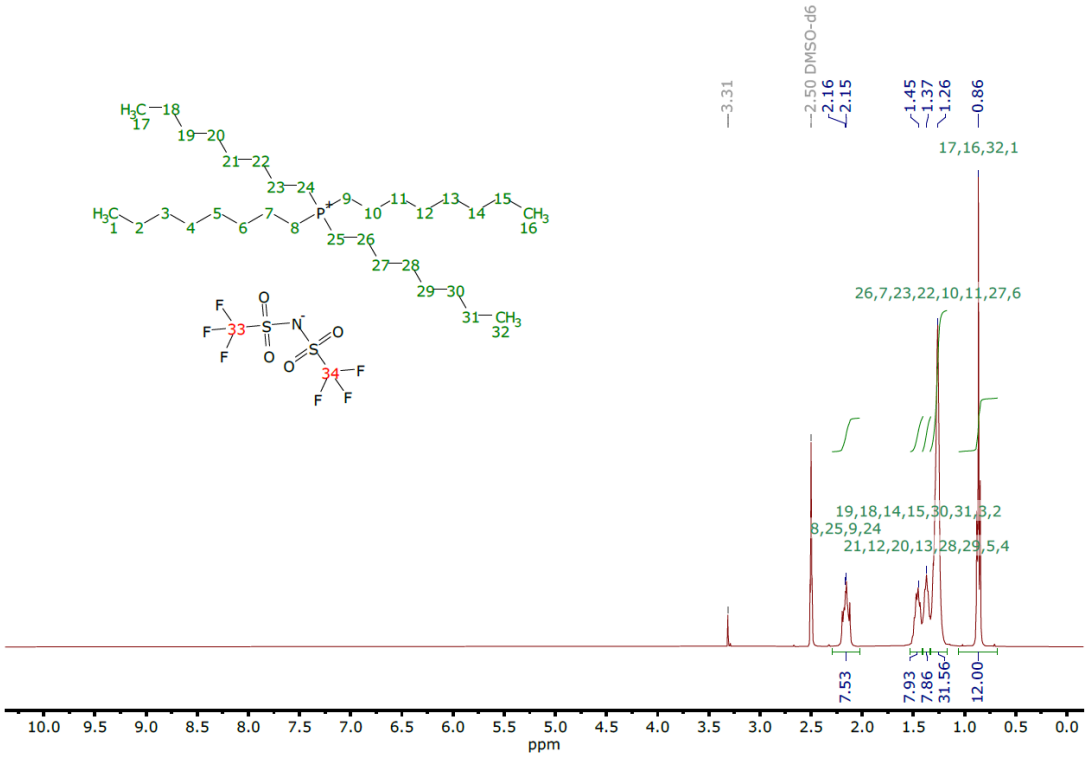


Figure A22 ^{1}H NMR spectrum of [P8888][NTf$_2$].

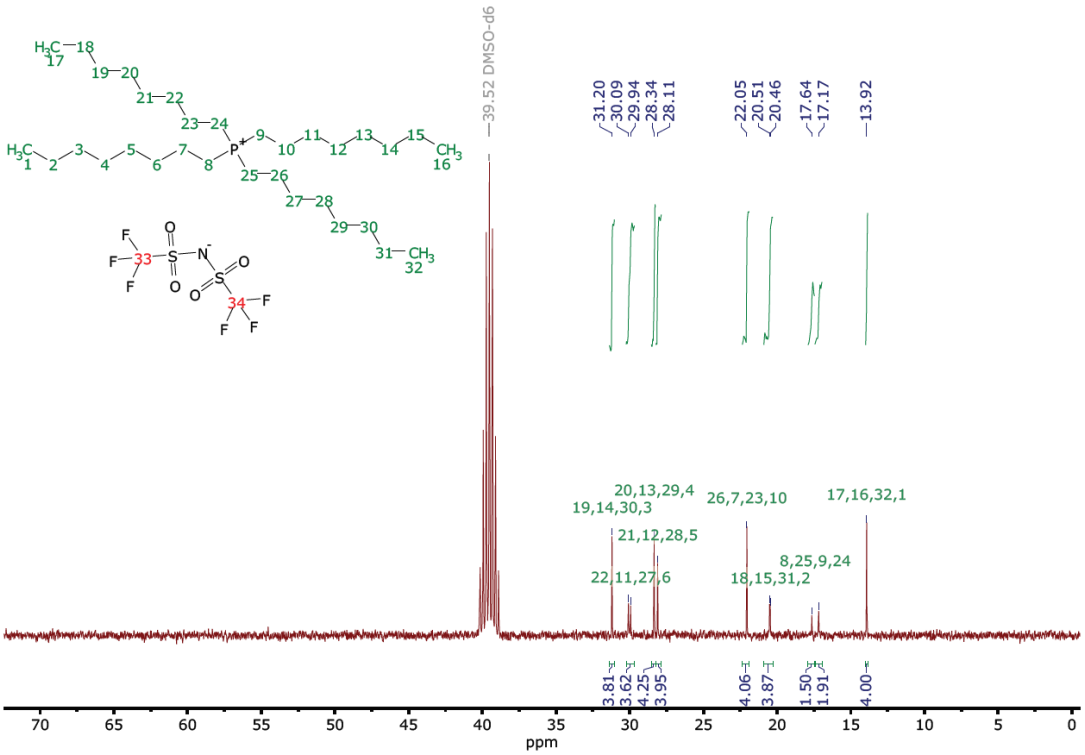


Figure A23 ^{13}C NMR spectrum of [P8888][NTf_2].

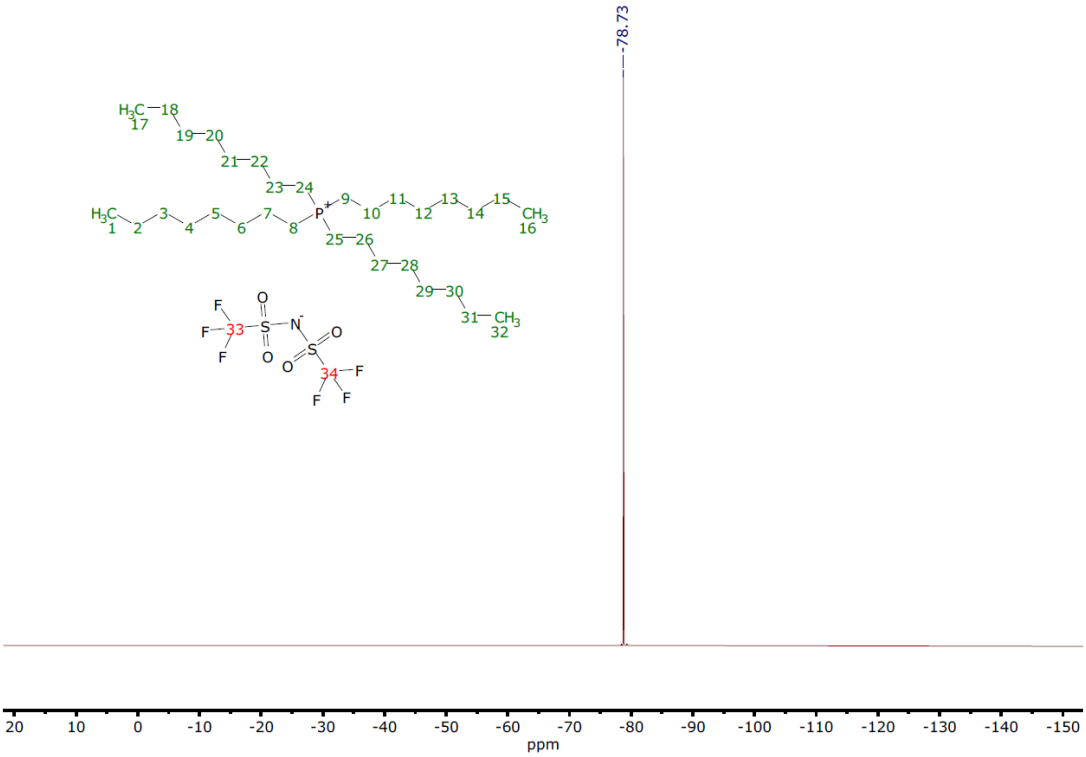


Figure A24 ^{19}F NMR spectrum of [P8888][NTf_2].

1.2 References

1. Mori, K.; Hashimoto, S.; Yuzuri, T.; Sakakibara, K. Structural and Spectroscopic Characteristics of a Proton-Conductive Ionic Liquid Diethylmethylammonium Trifluoromethanesulfonate [dema][TfOH]. *Bull. Chem. Soc. Jpn.* **2010,** *83* (4), 328-334.

2. Goodwin, S. E.; Smith, D. E.; Gibson, J. S.; Jones, R. G.; Walsh, D. A., Electroanalysis of Neutral Precursors in Protic Ionic Liquids and Synthesis of High-Ionicity Ionic Liquids. *Langmuir* **2017,** *33* (34), 8436−8446.

3. Li, H.; Jiang, F.; Di, Z.; Gu, J. Anhydrous proton-conducting glass membranes doped with ionic liquid for intermediate-temperature fuel cells. *Electrochim. Acta* **2012,** *59*, 86-90.

4. Johnson, L.; Ejigu, A.; Licence, P.; Walsh, D. A. Hydrogen Oxidation and Oxygen Reduction at Platinum in Protic Ionic Liquids. *J. Phys. Chem. C* **2012,** *116*, 18048−18056.

5. Bio-Rad Laboratories, Inc. SpectraBase: 1980. http://spectrabase.com/compound/5NeyFUnWfjj (accessed Oct 09, 2019).

6. Domańska, U.; Wlazło, M.; Karpińska, M.; Zawadzki, M. High selective water/butan-1-ol separation on investigation of limiting activity coefficients with [P8,8,8,8][NTf_2] ionic liquid. *Fluid Phase Equilib.* **2017,** *449*, 1-9.

Appendix II: List of Publications

1. Goodwin, S. E.; Smith, D. E.; Gibson, J. S.; Jones, R. G.; Walsh, D. A. Electroanalysis of Neutral Precursors in Protic Ionic Liquids and Synthesis of High-Ionicity Ionic Liquids. *Langmuir* **2017,** *33* (34), 8436–8446.

2. Smith, D. E.; Walsh, D. A. The Nature of Proton Shuttling in Protic Ionic Liquid Fuel Cells. *Adv. Energy Mater.* **2019,** *9* (24).